

Post-translational Regulation of Transcription Factor EB

Supervised by

Professor Colin Goding

This thesis is submitted to Nuffield Department of Medicine, University of Oxford, in partial fulfillment of the requirements for the degree of Doctor of Philosophy in Clinical Medicine.

Linxin Li

Lady Margaret Hall, Oxford

Trinity Term 2018

Disclaimer

I declare that this submission is my own written work. To the best of my knowledge, it contains no material that has been written by another or previously submitted in the same or a different form as academic work, to this or any other university.

The results presented herein derive from my own experiments, with the exception of **Figure 3.2.1.7** by Jagat Chauhan**, Figure 3.2.8 A, B** by Hans Friedrichsen, **Figure 3.2.8 C, D** by Sarah Andrews, **Figure 3.2.10.3 A** by Laurent Volpon and **Figure 4.2.3** by Val Millar.

The results as shown in **Figure 3.2.2.3**, **Figure 3.2.2.4**, **Figure 3.2.3**, **Figure 3.2.4.1 A, B**, **Figure 3.2.4.2**, **Figure 3.2.5.1 A**, **Figure 3.2.5.4**, **Figure 3.2.6**, **Figure 3.2.7.2 A**, **Figure 3.2.7.3**, **Figure 3.2.9.2**, **Figure 3.2.10.1 C**, **Figure 3.2.10.3 C, D**, **Figure 3.2.10.4**, **Figure 3.2.11.1**, **Figure 3.2.11.2** and **Figure 3.2.11.3** are my own data of a published scientific paper (Li et al., 2018). The results in **Figure 3.2.8** are published data by Hans Friedrichsen and Sarah Andrews, and **Figure 3.2.10.3 A** by Laurent Volpon (Li et al., 2018), which are with permission of the co-authors and the supervisor, presented in this thesis.

Linxin Li

Trinity Term 2018

Abstract

Post-translational regulation of transcription factor EB

Linxin Li, Lady Margaret Hall

D.Phil. Clinical Medicine, Trinity Term 2018

The bHLH-LZ transcription factor EB (TFEB) is a master regulator of lysosomal biogenesis and autophagy, it also plays an important role in lipid and glucose metabolism, mitochondrial biogenesis, integrated stress response and immunity. Dysregulation of TFEB family is implicated in cancer as well as neurodegenerative diseases. TFEB subcellular localisation and transcriptional activity are regulated by cellular nutrient and energy status. Elucidating the mechanism of TFEB regulation is the key to understanding its role in maintaining cellular homeostasis as well as providing therapeutic insights. In this study we showed that TFEB subcellular localisation is regulated by both amino acids and glucose availability. Low glucose levels activate mTORC2-AKT signalling, leading to the inactivation of GSK3β, and GSK3β kinase activity is required for TFEB cytoplasmic localisation. We also demonstrated that GSK3β phosphorylates TFEB at S138 only after a priming phosphorylation event at S142. The sequential phosphorylation is required for CRM1-depedent nuclear export of TFEB via a novel nuclear export signal. This mechanism is important for the rapid cytoplasmic relocalisation and inactivation of TFEB upon nutrient replenishment. Additionally, we performed a high-throughput screen of 1,600 FDA-approved drugs and identified around 100 chemical modulators of TFEB and TFE3, of which around 50 % exhibited lysosomal biogenesis promoting potential. In particular, trifluoperazine, pimozide and loperamide induce TFEB nuclear translocation, lysosomal biogenesis and autophagy in an mTORC1- and AMPK- independent manner.

Acknowledgements

I deeply thank Professor Colin Goding who has been wise, resourceful and enlightening for the duration of my DPhil, I really appreciate his supervision and mentorship. I am grateful to my lab partners, Hans Friedrichsen whose catchphrase was 'It's not gonna work', and Sarah Andrews who is always 'concerned', for our bittersweet and fruitful scientific discussion and collaboration. I am thankful to Paola Falletta and Yurena Vivas who are always encouraging and Romuald Binet who is always critical, whom I really enjoyed talking about science with. I also thank Sizhu Lu, Diogo Dias, Beth Henderson, Pakavarin Louphrasitthiphol, Laura Mosteo and Richard Lisle who really made the lab such a friendly and fun place. And how could I forget to mention Kao Chin Ngeow, without whom the foundation of our work would not be possible.

I am hugely thankful to Elena Seraira and Val Millar from Dr. Daniel Ebner's Group who offered tremendous help in the assay development, execution and image analysis of the drug screen, Dr. Katherine Borden and Dr. Laurent Volpon for the timely help with their expertise, and Professor Simon Leedham and Dr. Hayley Davis who generously shared their valuable research materials. And I thank Mark Shipman for his great assistance in microscopy and Jagat Chauhan for the bioinformatics analysis.

Of course, my thanks will go to friends in the Ludwig, Derek Leske, Mattia Zuuca, Felix Zhou, Carlos Ruiz Puig, and to friends in Oxford, Xin Xu, Yuanjie Pang, Wei Wu and Daniel Lee, who have made my life outside research wonderful, especially to Yishan Wang for all the sharing and company of the scientific, the artistic, the philosophical and the anthropological explorations. Lastly but the most importantly, I thank my family for their unreserved support and understanding.

Table of Contents

DISCLAIMER i
ABSTRACT ii
ACKNOWLEDGEMENTS iii
TABLE OF CONTENTS iv
LIST OF ABBREVIATIONS vii
CHAPTER 1 - INTRODUCTION 1
1.1 Glucose and Amino Acid Metabolism in Cancer 2
1.2 mTORC1 and mTORC2 Signalling and Cancer 6
1.2.1 Regulation of mTORC1 and mTORC2 8
1.2.2 Functions of mTORC1 and mTORC2 12
1.2.3 mTOR in Cancer 15
1.3 Transcription Factor EB (TFEB) 18
1.3.1 The MITF/TFE family transcription factors 18
1.3.2 Mechanisms of TFEB regulation 20
1.3.3 Physiological roles of TFE family 25
1.3.4 TFEB and TFE3 in cancer 30
1.3.5 TFE family as therapeutic targets 33
1.4 Summary and aims 35
CHAPTER 2 – METHODS AND MATERIALS 38
2.1 Bacterial methods 39
2.1.1 Growth conditions 39
2.1.2 Bacterial Strains 39
2.2 Mammalian methods 40
2.2.1 Cell culture 40
2.2.2 Transient transfection of Plasmids 42
2.2.3 Generation of stable cell lines 42

2.2.4 Transient transfection of siRNA 42
2.2.5 Virus-mediated transduction of shRNA or DNA 43
2.3 Nucleic acid methods 43
2.3.1 Agarose gel electrophoresis 43
2.3.2 Plasmid purification 44
2.3.3 Polymerase chain reaction 44
2.3.4 Restriction enzyme digestion 45
2.3.5 Ligation 46
2.3.5 Site-directed mutagenesis 46
2.3.6 Quantitative real time PCR 47
2.4 Protein methods 47
2.4.1 Whole cell lysate 47
2.4.2 Subcellular fractionation 48
2.4.3 Immunoprecipitation 48
2.4.4 SDS-PAGE 49
2.4.5 Immunoblotting 50
2.5 Cell biology methods 51
2.5.1 Immunofluorescent microscopy 51
2.5.2 Fluorescent live cell imaging 52
2.5.3 Flow cytometry 52
2.6 Reagents 53
2.6.1 Chemicals 53
2.6.2 Oligonucleotides 57
2.6.3 Plasmids 59
2.6.4 Antibodies 60
2.6.5 siRNA 62
CHAPTER 3 – TFEB SUBCELLULAR LOCALISATION IS REGULATED BY NUTRIENT AVAILABILITY THROUGH NUCLEAR EXPORT 63
3.1 Introduction 64
3.2 Results 66
3.2.1 TFEB/3 expression in different cancer origins and cell types 66
3.2.2 TFEB nuclear translocation is regulated by amino acid and glucose levels 75
3.2.3 TFEB transcriptional activity is induced by glucose deprivation 82

3.2.4 Cellular signalling events under glucose starvation....84
3.2.5 Low glucose activates mTORC2-AKT-GSK3β axis....89
3.2.6 The IRS1 feedback loop does not participate in AKT-GSK3β regulation under glucose starvation....95
3.2.7 GSK3β kinase activity is required for TFEB cytoplasmic localisation....98
3.2.8 TFEB S138 phosphorylation by GSK3β is primed by S142 phosphorylation....103
3.2.9 Phosphorylation of S138 and S142 is required for TFEB nuclear export....105
3.2.10 TFEB contains a NES adjacent to S138 and S142....108
3.2.11 TFEB nuclear export is regulated by glucose....115
3.2.12 TFEB NES mutants exhibit higher levels of autophagy....119
3.3 Discussion....121
CHAPTER 4 – A HIGH-THROUGHPUT SMALL COMPOUND SCREEN TO IDENTIFY TFEB/3 MODULATORS....127
4.1 Introduction....128
4.2 Screen Procedure....130
4.3 Screen Results....133
4.3.1 Image based screen results....133
4.3.2 Functional validation of the hits....139
4.3.3 Cellular signalling events induced by the hits....155
4.4 Discussion....157
CHAPTER 5 – DISCUSSION....161
5.1 TFEB in nutrient and energy homeostasis....162
5.2 TFEB as a therapeutic target....168
5.3 Conclusion....171
REFERENCES....172

List of Abbreviations

Aβ	β-amyloid
AD	Alzheimer's disease
AMP	adenosine monophosphate
AMPK	adenosine monophosphate-activated protein kinase
AKT	RAC-alpha serine/threonine-protein kinase/protein kinase B/AKT
ATG	autophagy related gene
ATF4	activating transcription factor 4
ATP	adenosine triphosphate
bHLH-LZ	basic-helix-loop-helix leucin-zipper
BafA	bafilomycin A
BSA	bovine serum albumin
C-terminal	carboxyl-terminal
CAD	carbamoyl-phosphate synthetase
CDKN1A	cyclin-dependent kinase inhibitor 1A
ChIP-seq	chromatin immunoprecipitation followed by sequencing
CLEAR	coordinated lysosomal expression and regulation
CREB	cAMP response element binding protein
CRM1	chromosomal region maintenance 1
CsA	cyclosporine
DAPI	4′, 6-diamidino-2-phenylindole
DMEM	Dulbecco's modified eagle medium
DMSO	dimethyl sulfoxide
DNA	deoxyribonucleic acid
EGFP	enhanced green fluorescent protein
EGFR	epidermal growth factor receptor
ER	endoplasmic reticulum
ERK2	mitogen-activated protein kinase 1

FDA	food and drug administration
FKBP12	FK506 binding protein 12
FLCN	folliculin
GAP	guanosine triphosphate hydrolase activating protein
GDP	guanosine diphosphate
GEF	guanine-nucleotide exchange factor
GFAT1	glutamine: fructose-6-phosphate amidotransferase 1
GFP	green fluorescent protein
GLUT1	glucose transporter 1
GSK3β	glycogen synthase kinase 3 β
GST	glutathione S-transferase
GTP	guanosine triphosphate
GTPase	guanosine triphosphate hydrolase
HA	human influenza hemagglutinin
HBSS	Hank's balanced salt solution
HD	Huntington's disease
HER2	human epidermal growth factor receptor 2
HK1	hexokinase 1
HIF1α	hypoxia-induced factor 1 subunit α
IF	immunofluorescence
IGF-1	insulin/insulin-like growth factor-1
IPO	nuclear importin
IRS1	insulin receptor substrate 1
kDa	kilodalton
LacR	DeoR family transcriptional regulator
LAMP2	lysosomal associated membrane protein 2
LC3B	microtubule associated protein 1 light chain 3 B
LDL	low-density lipoprotein
LKB1	serine/threonine kinase 11/liver kinase B1
LMB	leptomycin B

LPS	liposaccharide
LSD	lysosomal storage disorder
MAPK	mitogen-activated protein kinase
MAP4K3	mitogen-activated protein kinase kinase kinase kinase 3
MCOLN1	mucolipin 1
MEK	mitogen-activated protein kinase kinase 1
MHC	major histocompatibility complex
MITF	microphthalmia associated transcription factor
mLST8	mammalian lethal with Sec13 protein 8
mRNA	messenger ribonucleic acid
mTOR	mechanistic target of rapamycin
mTORC1	mechanistic target of rapamycin complex 1
mTORC2	mechanistic target of rapamycin complex 2
N-terminal	amine-terminal
NES	nuclear export signal
NLS	nuclear localisation signal
TBST	tris-buffered saline with Tween
TCA	tricarboxylic acid
TCGA	The Cancer Genome Atlas
TFEB	transcription factor EB
TFE3	transcription factor E3
TSC	tuberous sclerosis complex
TYR	tyrosinase
TYRP1	tyrosinase-related protein 1
PBS (T)	phosphate-buffered saline (with Tween)
PCR	polymerase chain reaction
PD	Parkinson’s disease
PDAC	pancreatic ductal adenocarcinoma
PDK1	phosphoinositide-dependent kinase 1
PERK	PRKR-Like Endoplasmic Reticulum Kinase

PFK	phosphofructokinase
PGC1-α	peroxisome proliferator-activated receptor γ coactivator 1 α
PI3K	phosphoinositide 3-kinase
PKB	protein kinase B/AKT
PKC	protein kinase C
PKI	cAMP-dependent protein kinase inhibitor
PP2A	protein phosphatase 2A
PRPS2	phosphoribosyl pyrophosphate synthetase
PRAS40	proline-rich AKT substrate of 40 kDa
PTEN	phosphatase and tensin homolog
qRT-PCR	quantitative real-time PCR
RAN	Ras-related nuclear protein
RRAGD	Ras-related GTP-binding protein D
RANKL	Receptor activator of nuclear factor kappa-B ligand
RAPTOR	regulatory protein associated with TOR
RCC	renal cell carcinoma
Rheb	Ras homologue enriched in brain
RNA	ribonucleic acid
RNAi	RNA interference
RICTOR	rapamycin insensitive companion of mTOR
Rb	retinoblastoma
S6	ribosomal protein S6
S6K	ribosomal protein S6 kinase/p70 S6 kinase
SBMA	spinal and bulbar muscular atrophy
SD	standard deviation
SGK1	glucocorticoid-induced protein kinase 1
shRNA	small hairpin RNA
siRNA	small interfering RNA
SREBP	sterol responsive element binding protein
SSMD	strictly standardised mean difference

ULK1	Unc-51 like autophagy activating kinase 1
UPR	unfolded protein response
v-ATPase	vacuolar-type H^+- adenosine triphosphate hydrolase
WT	wild-type
XPO1	nuclear exportin 1
YWHA	tyrosine 3-monooxygenase/tryptophan 5-monooxygenase activation protein/14-3-3

Chapter 1 - Introduction

1.1 Glucose and Amino Acid Metabolism in Cancer

Cancer is a multitude of diseases that constitute a major global health issue. One of the biggest challenges for anti-cancer therapies is tumour heterogeneity—subpopulations of cells within a certain tumour harbour distinct genetic or epigenetic alterations and display different phenotypes (Hoek and Goding, 2010; Meacham and Morrison, 2013). A melanoma tumour, for instance, typically consists of a combination of cells that are highly proliferative and therapeutically sensitive and cells that are stem cell-like, slowly growing, highly invasive and therapeutically resistant (Hoek and Goding, 2010). The complexity of tumour composition, combined with other microenvironmental stimuli such as nutrient limitation, low levels of oxygen, immune cell infiltration and cytokine secretion from the stroma, often reprogram cancer cell metabolism, considered an emerging hallmark of cancer and allowing sustained proliferation. (Hanahan and Weinberg, 2000, Hanahan and Weinberg, 2011)

The evidence for aberrant metabolism in cancer was first described almost a century ago by the German physiologist Otto Warburg, who observed a considerably increased glucose consumption by tumours compared to normal tissues (Warburg et al., 1923, Warburg, 1924). It was also noted that cancer cells utilise massive amounts of glucose to undergo aerobic glycolysis rather than the TCA cycle to generate ATP, and that cells preferentially convert the pyruvate from glycolysis to lactate, despite the presence of ambient oxygen (Warburg, 1956). Warburg and other researchers concluded that this effect was attributed to the "irreversible injuring of respiration", possibly due to the dysfunction of mitochondria that rendered tumour cells inefficiency for oxidative phosphorylation (Pavlova and Thompson, 2016). However, this assumption was challenged in recent decades by various studies showing that depletion of mitochondrial DNA largely reduced the tumorigenic potential of cancer cells in vitro and in

vivo (Morais et al., 1994, Cavalli et al., 1997, Tan et al., 2015), suggesting that rather than being deficient in mitochondrial respiration, cancer cells harness glucose via a regulated reprogrammed metabolic pathway, which may be beneficial to cope with high demand of nutrients required for tumour progression.

In contrast to normal cells for which the glucose uptake is strictly regulated by growth factors and extracellular matrix (Rathmell et al., 2000, Lindsten et al., 2003, Schafer et al., 2009, Grassian et al., 2011), tumour cells display an considerable independence of external growth cues (Aguirre-Ghiso et al., 2003). Particularly, the phosphoinositide 3-kinase (PI3K)/AKT signalling pathway acts as a central regulator of glucose uptake by promoting both the glucose transporter GLUT1 mRNA expression and the translocation of GLUT1 protein to the cell membrane (Barthel et al., 1999; Wieman et al., 2007). AKT can also phosphorylate hexokinase (HK) and phosphofructokinase (PFK), two kinases that catalyse the first commitment steps of glycolysis (Deprez et al., 1997; Gottlob et al., 2001). The receptors upstream of PI3K/AKT activation such as EGFR, KIT and HER2 are frequently mutated in cancers (reviewed in Hennessy et al., 2005). The negative regulator PTEN which dephosphorylates phosphatidylinositol-3,4,5-trisphosphate (PtdIns(3,4,5)P_3) to PtdIns(4,5)P_3, a reverse process catalysed by PI3K, is also mutated or downregulated in over 50% of tumours across different cancer types (reviewed in Hennessy et al., 2005). These observations support the notion that oncogenic mutations in the PI3K/AKT pathway enable cancer cells to internalise high quantities of glucose (Vander Heiden et al., 2009; Pavlova and Thompson, 2016).

In addition, other oncogenic pathways also play a role in altered glucose metabolism. For instance, cells with KRAS or BRAF mutations displayed consistently upregulated GLUT1 levels and exhibited higher glucose uptake and glycolysis (Murakami et al., 1992; Ying et al.,

2012; Yun et al., 2009). c-Myc overexpression correlates with genes involved in glycolysis using a ^{18}F-fluorodeoxy-glucose positron emission tomography technique in a triple negative breast cancer subtype (Palaskas et al., 2011). Collectively, multiple growth pathways are often aberrantly activated to allow cancer cells to access sufficient glucose.

Although aerobic glycolysis seems inefficient in producing energy, hypothetically it is the glycolytic intermediates that cancer cells really benefit from. For instance, Fructose-6-phosphate can be used to generate hexamine; dihydroxyacetone phosphate (DHAP) is converted into glycerol-3-phosphate to synthesize phospholipids (major component of cell membrane); and 3-phosphoglycerate is utilised as a precursor for the biosynthesis of serine and glycine (Pavlova and Thompson, 2016). Given that proliferative cells need not only ATP but also precursors for a variety of biosynthetic processes, and that glycolysis provides a reservoir for such purpose, it is not surprising that many oncogenic pathways raise the uptake of glucose and feed it into the glycolytic production line in order to meet the high demand for biomolecule synthesis of rapidly growing cancer cells.

The second category of biological substances that support tumour growth are amino acids, of which glutamine is one of the most important. Glutamine not only provides carbon for other amino acid and fatty acid biosynthesis, but also contributes nitrogen to the de novo synthesis of nucleotides, non-essential amino acids and hexosamines (DeBerardinis and Cheng, 2010; Lane and Fan, 2015). More importantly, the efflux of L-glutamine facilitates the cellular uptake of essential amino acids such as L-leucine, L-tryptophan, L-phenylalanine and L-arginine through the L-type amino acid transporter LAT1, a prerequisite process for many cellular functions including protein synthesis and mTORC1 signalling (Kanai et al., 1998; Mastroberardino et al., 1998; Nicklin et al., 2009).

More than 60 years ago the American physiologist Harry Eagle first described that HeLa cells required a 10 to100 fold excess of glutamine in culture conditions (Eagle, 1955). It was later established that glutamine is one of the most depleted amino acids in ascites cell tumours (Roberts et al., 1956), as well as in a range of cancers including pancreatic ductal adenocarcinoma and melanomas (Kamphorst et al., 2015; Pan et al., 2016). Glutamine is also the major nitrogen source and the most rapidly consumed amino acid in Erhlich ascites tumour cells, hepatomas and carcinosarcomas in vivo (Márquez et al., 1989; Sauer et al., 1982). What's more, several cancer types such as pancreatic cancer, glioma and melanoma exhibited a striking glutamine addiction (Baenke et al., 2016; Hernandez-Davies et al., 2015; Wise and Thompson, 2010; Wise et al., 2008).

The oncogenic pathways that lead to aberrant reliance on glutamine in cancer cells are being revealed in recent years. First, the oncogenic RAS mutations impair glucose flux from entering TCA cycle (Fan et al., 2013; Gaglio et al., 2011), thus the RAS-driven pancreatic ductal adenocarcinomas heavily depend on glutamine and its catabolites, glutamate and α-ketoglutarate, as a carbon source to generate ATP via the TCA cycle (Son et al., 2013), and necessitates the ability to scavenge extracellular protein through a process named macropinocytosis to acquire nutrients (Kamphorst et al., 2015). Second, the transcription factor c-Myc, which is frequently up-regulated in various cancer types, induces the transcription of glutamine transporters ASCT2 and SN2, promotes the expression of glutaminase (GLS1), carbamoyl-phosphate synthetase 2 (CAD) and phosphoribosyl pyrophosphate synthetase (PRPS2), therefore enhancing the glutamine import as well as its utilisation for energy production and nucleotide synthesis (Eberhardy and Farnham, 2001; Gao et al., 2009; Wise et al., 2008). Third, the tumour suppressor Retinoblastoma (Rb) negatively regulates ASCT2 and

GLS1 through E2F, a transcription factor critical for cell division along with Rb (Reynolds et al., 2014), thus coupling cell proliferation to the uptake and utilisation of glutamine. Overall, glutamine is not only a fundamental building block for the synthesis of bio-molecules necessary for many cellular functions, also its low availability is involved in inducing melanoma cell phenotype switching from proliferative to invasive (Falletta et al., 2017), as well as it being used as an energy source. It is no wonder that oncogenic alterations tend to prioritise glutamine uptake and utilisation in line with glucose feeding enhanced aerobic glycolysis.

Taken together, an oncogene-driven metabolic shift in glucose and amino acids, especially glutamine, is a highly regulated cellular reprogramming process required for tumour cell adaptation to microenvironmental stresses, such as nutrient limitation, hypoxia, and likely immune surveillance. Therapeutically targeting metabolic enzymes has shown potential in cancer prevention and intervention (Vander Heiden, 2011; Wang et al., 2014; Wise and Thompson, 2010). A deeper understanding of how nutrient balance and cell metabolism is regulated may provide improvement for treating cancer and other diseases.

1.2 mTORC1 and mTORC2 Signalling and Cancer

In the 1960s, in the search for novel antibiotics, a natural compound was isolated from bacteria on the island of Rapa Nui. This compound, named rapamycin or sirolimus, was later found to exhibit immunosuppressive and anti-tumour functions (Eng et al., 1984; Martel et al., 1977; Vézina et al., 1975). It was not until the 1990s that biochemical studies revealed that rapamycin forms a complex with FKBP12 in mammalian cells (Chung et al., 1992), to inhibit a signalling network required for cell growth and proliferation, dictated by a protein kinase later

discovered as the mechanistic/mammalian target of rapamycin (mTOR) (Brown et al., 1994; Sabatini et al., 1994; Sabers et al., 1995).

As a key regulator of cell growth and proliferation, the mTOR protein kinase and other regulatory subunits form two distinct protein complexes, namely mTORC1 and mTORC2 (Laplante and Sabatini, 2012; Saxton and Sabatini, 2017). mTORC1 contains RAPTOR (regulatory protein associated with TOR) (Hara et al., 2002; Kim et al., 2002), mLST8 (mammalian lethal with Sec13 protein 8, or GβL) (Kim et al., 2003), and two inhibitory subunits PRAS40 (proline-rich AKT substrate of 40 kDa) (Haar et al., 2007; Sancak et al., 2007; Wang et al., 2007) and DEPTOR (Peterson et al., 2009). Although the rapamycin-FKBP12 complex can directly bind and inhibit mTORC1, mTORC2 is rapamycin insensitive. It also contains the core kinase mTOR, the regulatory subunit mLST8, and the inhibitory subunit DEPTOR (Peterson et al., 2009). But instead of RAPTOR, mTORC2 is characterized by its regulatory subunits RICTOR (rapamycin insensitive companion of mTOR) (Dos et al., 2004; Jacinto et al., 2004), mSIN1 (Frias et al., 2006; Jacinto et al., 2006; Yang et al., 2006), and Protor1/2 (Pearce et al., 2007; Woo et al., 2007)(**Figure 1.2**). Composed of different regulatory subunits, mTORC1 and mTORC2 display quite distinct yet related regulation as well as cellular functions.

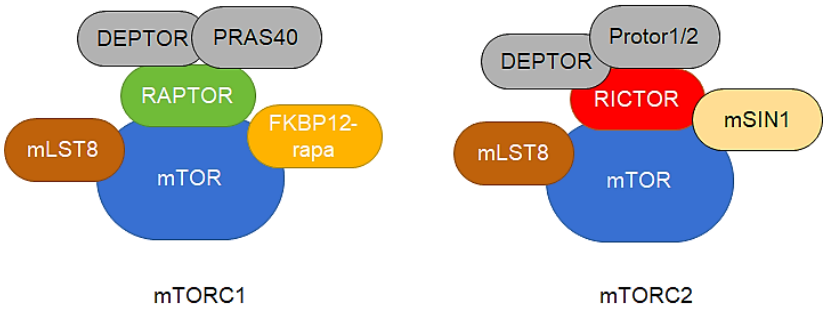


Figure 1.2 Composition of the mTOR complexes. mTORC1 consists of the catalytic subunit mTOR, the positive regulatory subunits mLST8 and RAPTOR, and the negative regulatory subunits DEPTOR, PRAS40 and the FKBP12-rapamycin complex. mTORC2 consists of the core mTOR kinase, the positive regulatory subunits mLST8, RICTOR and mSIN1, and the negative regulatory subunits DEPTOR and Protor1/2.

1.2.1 Regulation of mTORC1 and mTORC2

A number of growth factor pathways converge on mTORC1 signalling, through the inhibition of the Tuberous Sclerosis Complex (TSC), a negative regulator of mTORC1, which consists of TSC1, TSC2 and TBC1D7 (Dibble et al., 2012), that acts as a GTPase activating protein (GAP) for the small GTPase Rheb (Ras homologue enriched in brain) (Garami et al., 2003; Inoki et al., 2003a; Tee et al., 2003; Zhang et al., 2003)(**Figure 1.2.1**). Activated Rheb directly binds mTORC1 and stimulates its activity (Long et al., 2005)(**Figure 1.2.1**). When stimulated with insulin/insulin-like growth factor-1 (IGF-1), AKT downstream of PI3K becomes activated, phosphorylates TSC2 and prevent its GAP function for Rheb by dissociating TSC from the lysosomal surface, thus rendering mTORC1 active (Inoki et al., 2002; Manning et al., 2002)(**Figure 1.2.1**). Simultaneously, insulin/IGF-1-stimulated AKT phosphorylates PRAS40 and attenuates its inhibition on mTORC1 (Sancak et al., 2007). Furthermore, mitogen-activated protein kinase (MAPK) activated p90 ribosomal S6 kinase (RSK), downstream of receptor tyrosine kinase-RAS signalling, also activates mTORC1 by phosphorylation and inhibition of TSC2 (Ma et al., 2005; Roux et al., 2004). Other growth factor or cytokine pathways contributing to mTORC1 activation, including the Wnt and the TNFα inflammatory pathways, involve the phosphorylation of TSC2 and TSC1 by glycogen synthase kinase 3β (GSK3β) and inhibitor of nuclear factor kappa-B (IKKβ), respectively (Inoki et al., 2006; Lee et al., 2007)(**Figure 1.2.1**).

Amino acid availability is another major input for cellular nutrient and energy status sensed by mTORC1. The mechanism involves the heterodimeric Rag GTPases, Rag A or B with Rag C or D (Kim et al., 2008; Sancak et al., 2008), which are tethered to the lysosomal surface through the Ragulator complex (Sancak et al., 2010). When amino acids are present,

through binding to RAPTOR, the active forms of Rag GTPases, RagA/B^{GTP}-RagC/D^{GDP} recruit mTORC1 to the surface of lysosomes, where mTORC1 is activated by Rheb (Sancak et al., 2010). The recruitment itself is independent of growth factors, Rheb or TSC, thus activation of mTORC1 by amino acids requires both Rags and Rheb signalling (**Figure 1.2.1**).

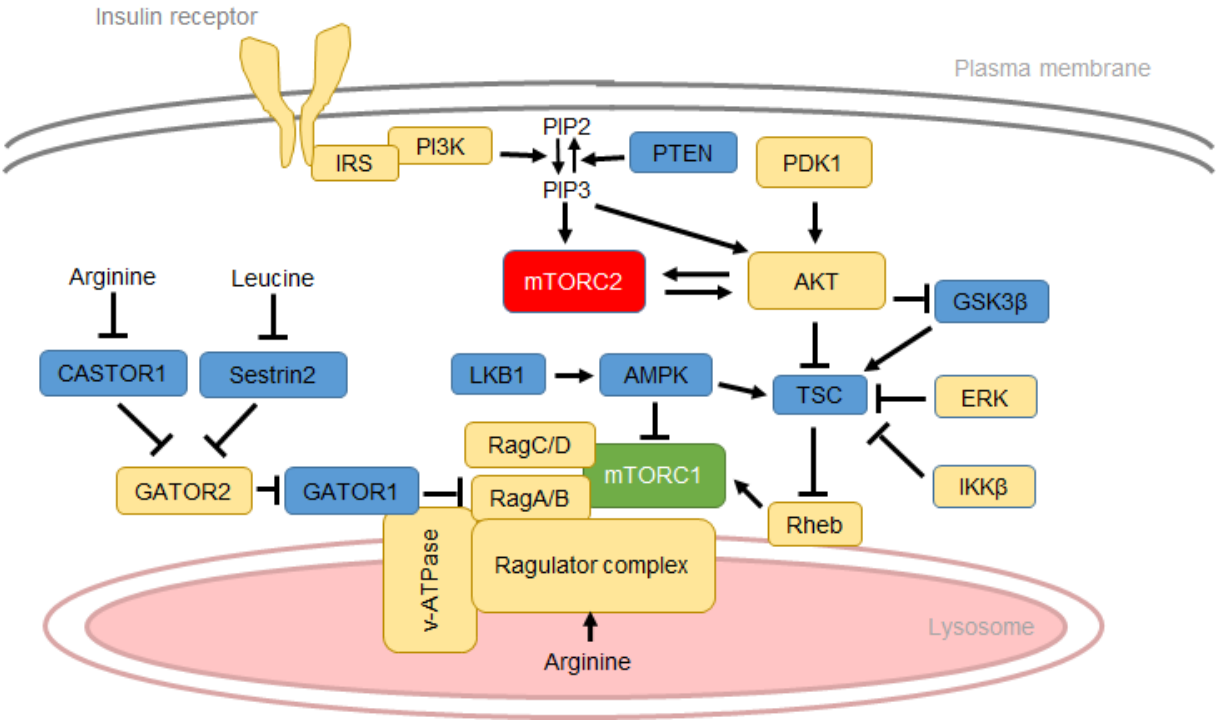


Figure 1.2.1 Upstream signalling network of mTORC1 and mTORC2. mTORC1 and mTORC2 are shown in green and red, respectively. Positive regulators of mTORC1 are shown in yellow, while negative regulators of mTORC2 are shown in blue. This figure was adapted from a review by Saxton and Sabatini, 2017.

Amino acid sensing by Rags and mTORC1 are exerted through both an inside-out lysosomal mechanism and a cytosolic mechanism. Amino acids such as arginine inside the lysosomal lumen, can activate mTORC1 through the lysosomal amino acid transporter SLC38A9 (Jung et al., 2015; Rebsamen et al., 2015; Wang et al., 2015), and is dependent on

the lysosomal v-ATPase which facilitates the guanine-nucleotide exchange factor (GEF) function of the Regulator complex toward Rag A/B (Bar-Peled et al., 2012; Zoncu et al., 2011). In parallel, cytosolic amino acids, precisely leucine and arginine, activate mTORC1 through the GATOR1 and GATOR2 complex. By binding to Sestrin1/2 or CASTOR1, respectively, leucine or arginine promote the inhibition of the GAP function of GATOR1 toward RagA/B via GATOR2. This then enables the Rags to recruit mTORC1 to the lysosomal surface for its activation (Chantranupong et al., 2014, 2016; Parmigiani et al., 2014; Saxton et al., 2016). While RagA/B are regulated by GATOR complexes, the tumour suppressor Folliculin (FLCN) forms a complex with FNIP2 and functions as a GAP for the RagC/D in the presence of amino acids, which is also critical for mTORC1 activation (Petit et al., 2013; Tsun et al., 2013). Furthermore, mTORC1 activation by glutamine is accomplished by adenosine diphosphate ribosylation factor-1 (Arf1) GTPase via the v-ATPase in a Rag or Regulator-independent manner (Jewell et al., 2015), suggesting a differential regulation for different amino acids.

Apart from sensing the nitrogen source availability, mTORC1 also senses the levels of carbon source such as lipids and glucose. Cholesterol is an important type of lipid as it is the precursor of steroid hormones, bile acid and vitamin D, as well as being a key building block of biological membranes. It can be transported throughout the body in low-density lipoprotein (LDL) particles and taken up by cells via endocytosis. When LDLs are dissembled in the lysosomal lumen, cholesterol is exported from the lysosome by the Niemann-Pick C1 (NPC1) protein, which interacts with the amino acid transporter SLC38A9 that senses lysosomal arginine, and regulates mTORC1 activation (Castellano et al., 2017). In such a manner, mTORC1 monitors the lipid levels of the body. Glucose, on the other hand, is the primary fuel for energy production. Its absence is reflected by both the elevation of AMP/ATP ratio (Salt et

al., 1998) and the decrease in glycolytic product fructose-1,6-bisphosphate levels which is sensed by the enzyme aldolase (Zhang et al., 2017), both of which lead to AMP-activated protein kinase (AMPK) activation. Activated AMPK then inhibits mTORC1 signalling by phosphorylation on both RAPTOR and TSC2 (Gwinn et al., 2008; Inoki et al., 2003b). However, AMPK is not the only pathway through which mTORC1 integrates energy stress. Glucose starvation abrogates mTORC1 signalling also through inhibition of the Rag GTPases in cells lacking AMPK (Efeyan et al., 2012; Kalender et al., 2010), suggesting carbon abundance and the cell energy status is sensed and converged to mTORC1 through multiple mechanisms.

Composed of different regulatory subunits, mTORC2 exhibits a quite different regulation from mTORC1. It primarily functions as the downstream effector of the insulin/insulin-like growth factor-1 (IGF-1) signalling. mSIN1, the essential component for mTORC2, contains a pleckstrin homology (PH) domain which inhibits mTOR kinase activity. When stimulated with insulin, PtdIns(3,4,5)P_3, generated by active PI3K, binds to the PH domain and relieves the inhibition to trigger mTORC2 activation (Liu et al., 2015). Furthermore, phosphoinositide-dependent kinase 1 (PDK1)-activated AKT phosphorylates mSIN1 to activate mTORC2, the latter in turn phosphorylates AKT at S473 for its full activation, suggesting a positive feedback loop for mTORC2-AKT signalling (Yang et al., 2015).

Despite lacking direct regulation by nutrients, mTORC2 is indirectly regulated by mTORC1 through a negative feedback loop via insulin receptor substrate 1 (IRS1)-PI3K signalling. S6K1 phosphorylates IRS1 at multiple sites to promote its proteasomal degradation, and therefore attenuates mTORC2 activation (Harrington et al., 2004; Shah et al., 2004). Although amino acid and glucose sensing and signalling is mainly executed by mTORC1, intriguingly, mTORC2 activity is also responsive to levels of glutamine catabolites as well as

glucose through an unknown mechanism independent of mTORC1 (Moloughney et al., 2016). In other words, nutrient and energy status sensing involves the coordination of the mTORC1 and mTORC2 signalling network that integrates multiple inputs to achieve fine-tuned cell growth and proliferation.

1.2.2 Functions of mTORC1 and mTORC2

Despite having the same core catalytic subunit, mTORC1 and mTORC2 have distinct cellular functions. mTORC1 plays a central role in protein synthesis through direct phosphorylation on two critical modulators controlling mRNA translation, p70 S6 Kinase 1 (S6K1) and eIF4E Binding Protein (4EBP) (Burnett et al., 1998). The phosphorylation on T389 enables S6K1 to further phosphorylate its substrates including ribosomal protein S6, promoting mRNA translation (Burnett et al., 1998; Chung et al., 1992; Kuo et al., 1992). S6K1 can also phosphorylate the translation activator eIF4B, resulting in the assembly of a translation initiation complex (Holz et al., 2005). In parallel, mTORC1 phosphorylates the translation inhibitor 4EBP on multiple sites to block its interaction with translation initiation factor eIF4E, thus allowing 5' cap-dependent mRNA translation to occur (Brunn et al., 1997; Burnett et al., 1998).

Growing cells require not only protein but also lipids as the major components of the membrane of the cell and many organelles. The de novo lipid biosynthesis is regulated by the sterol responsive element binding protein (SREBP), a transcription factor family that controls the expression of genes involved in fatty acid and cholesterol anabolism (Eberlé et al., 2004). SREBP activity is also regulated by mTORC1 (Porstmann et al., 2008) in a S6K1 dependent manner (Düvel et al., 2010). In addition, rapamycin-resistant mTORC1 substrate Lipin 1 negatively regulates SREBP transcriptional activity (Peterson et al., 2011).

At the centre for regulation of anabolic processes, mTORC1 is also shown to regulate the de novo biosynthesis of nucleotides. S6K1 directly phosphorylates CAD (carbamoyl-phosphate synthetase 2, aspartate transcarbamoylase, dihydroorotase) and stimulates its activity, which is critical for pyrimidine production (Ben-Sahra et al., 2013; Robitaille et al., 2013). Furthermore, mTORC1 stimulates activation transcription factor 4 (ATF4)-dependent expression of MTHFD2 (methylenetetrahydrofolate dehydrogenase 2), boosting the mitochondrial tetrahydrofolate (mTHF) cycle to produce one-carbon units, therefore enhancing purine production (Ben-Sahra et al., 2016).

mTORC1 also accounts for the glucose metabolic shift from oxidative phosphorylation towards aerobic glycolysis. Hyperactivation of mTORC1 pathway leads to up-regulation of HIF1α (hypoxia-induced factor 1 subunit α), a transcription factor whose levels are often elevated in cancer that drives expression of several glycolytic enzymes (Düvel et al., 2010), allowing abundant glycolytic intermediate products to be incorporated into various anabolic processes, supporting cell growth and proliferation.

Other than being a master activator of anabolism, mTORC1 is also a chief suppressor of catabolic pathways. Autophagy, a highly regulated clearance process that breaks down excessive or damaged cellular compartments and recycles nutrients, requires the activation of ULK1 (homolog to yeast ATG13) for the formation of autophagosomes (He and Klionsky, 2009). mTORC1, under nutrient rich conditions, phosphorylates ULK1 on S757 to prevent its interaction with AMPK and subsequent activation and thereby inhibits the initiation of autophagy (Kim et al., 2011). The later stages of autophagy include the fusion of autophagosomes to lysosomes and the hydrolysis of the autophagic cargo contents in low pH (He and Klionsky, 2009). The expression of genes involved in lysosomal biogenesis and

autophagy machinery is largely regulated by transcription factor EB (TFEB) (Sardiello et al., 2009; Settembre et al., 2011), which is also phosphorylated by mTORC1 at multiple sites, resulting in TFEB's cytoplasmic retention and inactivation (Martina et al., 2012; Roczniak-Ferguson et al., 2012; Settembre et al., 2012; Vega-Rubin-de-Celis et al., 2017). Therefore, mTORC1 activity, determined by nutrient status, also regulates cellular clearance pathways via TFEB-dependent transcription of lysosomal and autophagic genes. Moreover, mTORC1 regulates protein turnover via ubiquitin-proteasome degradation. Inhibition of mTOR rapidly stimulates Lys48-linked ubiquitin conjugation to protein in cells and in vivo, leading to increased proteolysis of growth related proteins independently of protein translation or autophagy (Zhao et al., 2015). One such mechanism is controlled by another mTORC1 phosphorylation substrate Mpk1/ERK5, which regulates the proteasome assembly and this mechanism is evolutionarily conserved from yeast to mammals (Rousseau and Bertolotti, 2016).

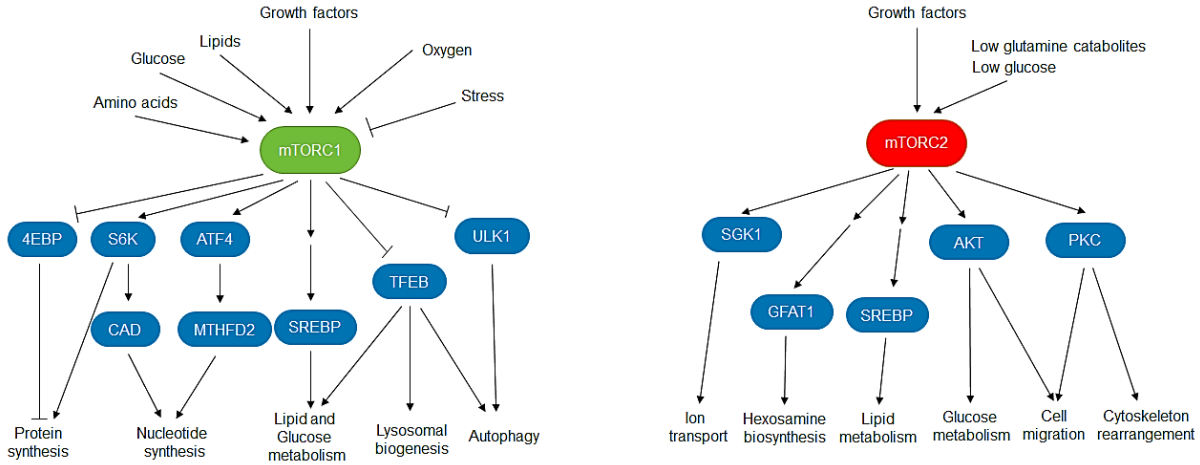


Figure 1.2.2 Summary of the functions of mTORC1 and mTORC2. The known physiological stimuli upstream of mTORC1 and mTORC2 and the cellular functions of the two mTOR complexes. The downstream targets of each mTOR signalling pathways are highlighted in blue. Arrows indicate positive regulation, while arrows with blunt heads indicate negative regulatory function.

Unlike mTORC1 coordinating metabolic homeostasis to support cell growth, mTORC2 promotes cell proliferation and survival through regulating diverse cellular pathways. Perhaps the most important substrate for mTORC2 is AKT, a key effector of the insulin/PI3K signalling pathway. AKT becomes fully activated when phosphorylated by mTORC2 at Ser473, following its phosphorylation by PDK1 at Ser308 (Sarbassov et al., 2005). Once activated, AKT can phosphorylate a variety of downstream targets including glycolytic enzymes HK and PFK (Deprez et al., 1997; Gottlob et al., 2001), the metabolic and transcriptional regulator GSK3β (Cross et al., 1995), transcription factors FoxO1/3a (Brunet et al., 1999) as well as the mTORC1 inhibitor TSC2, to control survival, proliferation and growth. mTORC2 also controls de novo lipid biosynthesis through modulating SREBP1 in liver (Hagiwara et al., 2012; Yuan et al., 2012), as well as the biosynthesis of hexosamine through regulating the expression of the rate limiting enzyme glutamine:fructose-6-phosphate amidotransferase 1 (GFAT1) (Moloughney et al., 2016), although the mechanisms are less clear. Moreover, mTORC2 was originally identified as phosphorylating several members of the protein kinase C (PKC) family to control cytoskeleton arrangement, cell morphology and cell migration (Sarbassov et al., 2004; Gan et al., 2012; Jacinto et al., 2004; Thomanetz et al., 2013). Lastly, mTORC2 phosphorylates serum and glucocorticoid-induced protein kinase 1 (SGK1) to regulate ion transport and cell survival (García-Martínez and Alessi, 2008).

1.2.3 mTOR in Cancer

Many frequently mutated oncogenic signalling pathways such as the PI3K/AKT pathway and the RAS/RAF/MAPK pathway, converge on mTORC1, leading to its hyperactivation in a range of human cancers (Saxton and Sabatini, 2017). The tumour suppressor LKB1, required for the AMPK dependent inhibition of mTORC1, is mutationally

silenced in the cancer-predisposing disorder Peutz-Jeghers Syndrome (Hemminki et al., 1998) as well as in lung adenocarcinomas (Sanchez-Cespedes et al., 2002). The negative regulators of mTORC1, TSC1 and TSC2 which function as GAPs for Rheb, are inactivated in tuberous sclerosis and lymphangioleiomyomatosis (Paul and Thiele, 2008). Similarly, the components of the tumour suppressor GATOR1 complex which acts as the GAP for the Rag GTPases, are also mutated in glioblastoma and ovarian cancer (Bar-Peled et al., 2013). On the other hand, the activating mutations of mTORC1 activators, such as RagC, are found in follicular lymphoma at a high frequency (Okosun et al., 2016), and those of Rheb are found in a wide range of tumours (Grabiner et al., 2014; Lawrence et al., 2014). In fact, mTOR itself is mutated at various amino acid residues across different types of cancer with up to 11.1% frequency, and several mutations lead to constitutive activation of mTORC1, highlighting its role in cancer progression (Grabiner et al., 2014; Sato et al., 2010).

Showing extensive physiological implications, mTORC1 has been a hot target for anti-cancer therapeutics. However, the first generation mTORC1 inhibitors, known as the rapalogs (rapamycin analogues), achieved little clinical success (Saxton and Sabatini, 2017). There are several explanations. First, rapalogs only target mTORC1 but not mTORC2, which has been shown to be essential in some PI3K/AKT-driven tumours including prostate cancer with PTEN loss as well as breast cancer cells (Guertin et al., 2009; Hietakangas and Cohen, 2008). It's also found that RICTOR levels and mTORC2 activity are elevated in gliomas which leads to hyperactivation of AKT and promotes cell growth and motility (Masri et al., 2007). Moreover, mTORC1 inhibition alone activates the IRS1 negative feedback loop, and further increases the oncogenic signalling of AKT observed in patient biopsies (Tabernero et al., 2008). Therefore, targeting both mTORC1 and mTORC2 in combination with PI3K/AKT inhibitors would be the

solution. Indeed, mTORC2 inhibition is shown to reduce metastasis and induce cell death in colorectal cancer and breast cancer (Gulhati et al., 2011; Li et al., 2012), thus showing the potential for combination therapy.

Second, although rapalogs efficiently inhibit the phophorylation of mTORC1substrates such as S6K1, the translation inhibitor 4EBP is largely insensitive to rapamycin. However, 4EBP phosphorylation-dependent translation is likely the most critical determinant in a variety of AKT- and ERK-driven tumours and the eIF4E/4EBP ratio correlates with the sensitivity to mTOR inhibition (Alain et al., 2012; Hsieh et al., 2010, 2012; She et al., 2010).

Third, mTORC1 inhibition induces autophagy, which acts as a double-edged sword for cancer. That is, autophagy suppresses cell transformation and tumour initiation, but later becomes beneficial for cancer cells to survive the nutrient poor and hypoxic microenvironment, especially in poor vascularised tumours (Shintani and Klionsky, 2004). mTORC1 inhibition may also lead to TFEB/TFE3-dependent lysosomal biogenesis to promote survival, a hallmark of pancreatic ductal adenocarcinoma (Perera et al., 2015). Unsurprisingly, mTORC1 inhibition facilitates macropinocytosis to utilise extracellular proteins and promotes cell growth in hypovascular tumours (Palm et al., 2015).

In conclusion, mTORC1 and mTORC2 both play important roles in tumorigenesis. However, treating cancer by simply targeting mTOR complexes turns out much more complicated than anticipated. Combining mTOR inhibition with inhibitors of key oncogenic pathways as well as autophagy may achieve better clinical outcome. Like 4EBP and its role in the therapeutic resistance to mTOR inhibition, other effectors downstream of mTORC1 and mTORC2 may serve as more precise and effective therapeutic targets, one of them being the MITF/TFE transcription factor family. In fact, MITF, TFE3 and TFEB are implicated in several

cancers as well as other diseases, it is therefore of great importance to further understand the regulation and the therapeutic potential of this transcription factor family.

1.3 Transcription Factor EB (TFEB)

1.3.1 The MITF/TFE family transcription factors

The microphthalmia-associated transcription factor/transcription factor E (MITF/TFE) family consists of four members, namely MITF, TFEB, TFE3 and TFEC (Steingrímsson et al., 2004). They all share a basic helix-loop-helix-leucine zipper (bHLH-LZ) region (**Figure 1.3.1**) which allows them to homodimerise or heterodimerise with one another. Like other transcription factors with a bHLH domain, MITF/TFE family members are able to bind to CANNTG E-box DNA motifs in the promoters and enhancers to initiate transcription (Levy et al., 2006). For MITF, an additional T residue to 5' end of a CATGTG E-box is required for the high affinity DNA binding ability, therefore the TCATGTG motif was termed M-box as it is highly conserved in melanocyte-specific promoters, whereas no specific flanking sequence for a CACGTG E-box was observed (Aksan and Goding, 1998). In addition, TFEB and TFE3 can bind to the GTCACGTGAC motifs expanding a canonical CACGTG E-box, in the promoter regions of many lysosomal genes, suggesting that MITF/TFE family can transcriptionally regulate lysosomal biogenesis and cellular clearance (Martina et al., 2014; Sardiello et al., 2009). The 10 base-pair motif was therefore named Coordinated Lysosomal Expression and Regulation (CLEAR) element.

MITF is a well-defined lineage-specific transcription factor crucial for melanocyte differentiation and development. After binding to M-box motifs, MITF promotes the transcription of pigmentation-related genes including TYR (Tyrosinase), TYRP1 (Tyrosinase-

related protein 1) and DCT (Dopachrome Tautomerase), as well as genes involved in melanosome biogenesis such as PMEL (Premelanosome Protein) and MLANA (Melan-A) (Cheli et al., 2010). MITF also plays key role in determining subpopulation phenotypes of melanoma cells. Cells with low levels of MITF exhibit invasive and stem cell-like properties; cells with intermediate MITF levels are proliferative and therapeutically sensitive; whereas cells with high MITF levels are differentiated and G1 arrested (Hoek and Goding, 2010).

Unlike the expression of MITF which is primarily limited to melanocyte-lineage, the retinal pigmented epithelium, mast cells and osteoclasts, TFEB and TFE3 are more widely expressed in different tissues. Emerging evidence revealed that although TFEB and TFE3 share closely related physiological functions to the melanocyte-specific isoform of MITF, the two factors have a distinct and more complicated regulation.

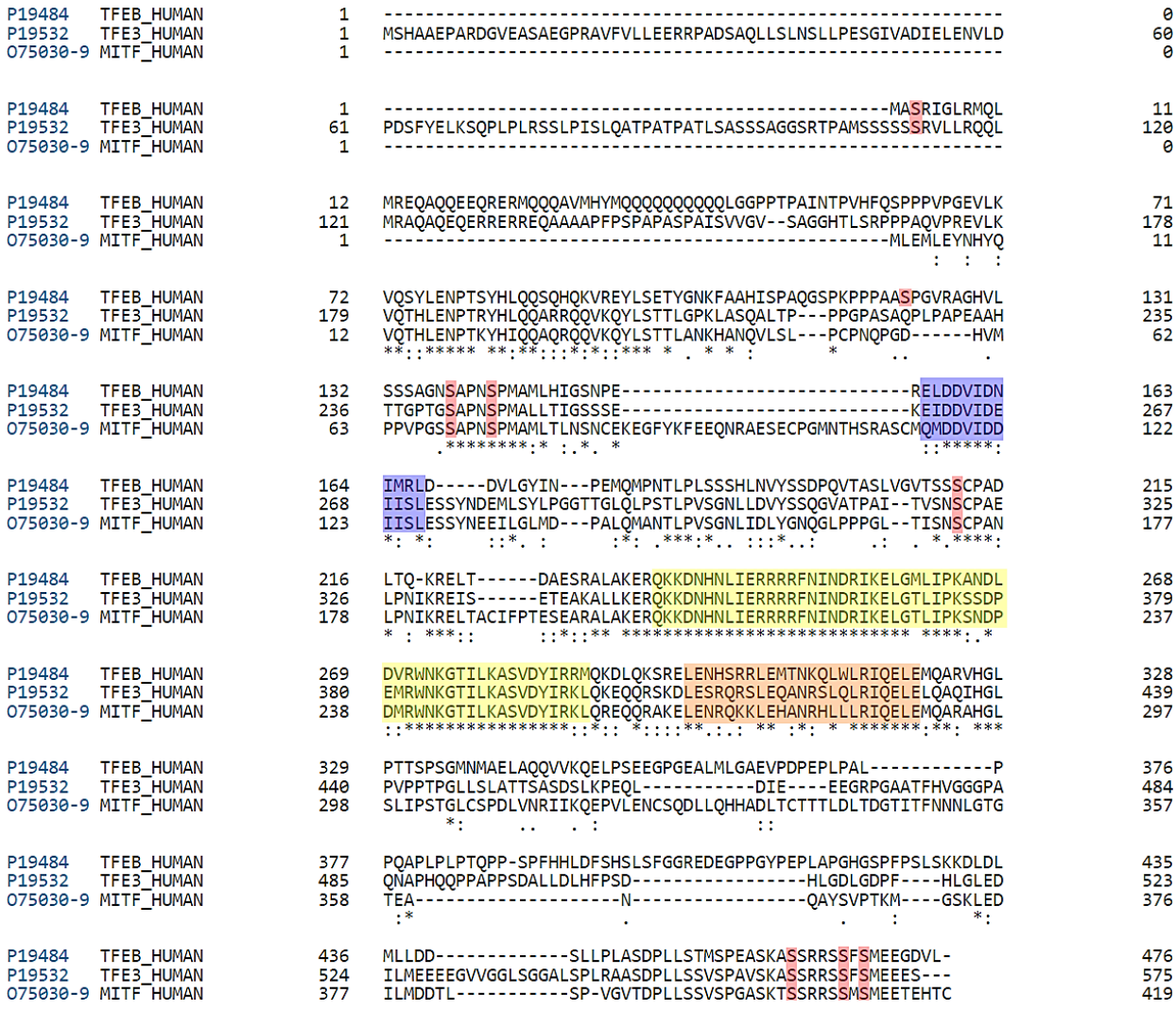


Figure 1.3.1 Protein sequence alignment of TFEB, TFE3 and MITF (melanocyte-specific isoform). The transactivation domains are highlighted in blue, while the bHLH domain and the Leucine-zipper domains are highlighted in yellow and orange, respectively. The known key phosphorylation sites of the three factors are highlighted in red. The asterisks below indicate amino acid residues conserved among the three factors.

1.3.2 Mechanisms of TFEB regulation

To ensure survival under nutrient deprivation, cells must first sense nutrient availability. The major sensor for amino acids is mTORC1, which localises on the lysosomal surface when amino acids are abundant but dissociates from the lysosomes when they are scarce. The amino

acid dependent lysosomal translocation and activation of mTORC1 is important to activate anabolic processes like protein translation and lipid synthesis while suppressing catabolic processes such as autophagy. Similarly, the subcellular localisation of TFEB and TFE3 was found to respond to nutrient levels. When cells are fully fed, TFEB and TFE3 are excluded from the nucleus and remain inactive in the cytoplasm. Conversely, when cells are starved, TFEB and TFE3 undergo rapid nuclear translocation and up-regulate a set of genes to boost autophagy and lysosomal biogenesis (Martina et al., 2014; Settembre et al., 2011). In such a manner, TFEB and TFE3 increase the chance of survival when cells are faced with nutrient stress.

It is perhaps no surprise that the synergistic effect of mTORC1 and TFEB led to the discovery of TFEB being regulated by mTORC1. In fully fed cells, TFEB and TFE3 are recruited to the lysosomal surface where they are phosphorylated by mTORC1 at multiple sites. Phosphorylation of one of these sites, serine 211 (S211), enables TFEB to bind the cytoplasmic chaperon 14-3-3 or YWHA and TFEB is consequently sequestered in the cytoplasm (Martina et al., 2012; Roczniak-Ferguson et al., 2012). In contrast, when the cells are starved, inactivation of mTORC1 and dephosphorylation of S211 result in the release of TFEB from its cytoplasmic anchor which leads to its nuclear translocation. However, S211 is not the only residue important for the nuclear entry of TFEB. S122 is also phosphorylated by mTORC1, and the phospho-mimetic serine to aspartate substitution S122D blocked the nuclear localisation of TFEB following mTORC1 inhibition irrespective of S211 phosphorylation status, but the alanine substitution S122A alone failed to induce TFEB nuclear accumulation (Vega-Rubin-de-Celis et al., 2017), suggesting a multistep regulation of TFEB nuclear entry through multiple phosphorylation events.

Since the lysosomal surface not only integrates inputs of nutrients such as amino acids, lipids and glucose, but also provides a platform for mTORC1 signalling, how TFEB is recruited to lysosomal surfaces is crucial for its phosphorylation and cytoplasmic sequestration. As previously discussed, mTORC1 is recruited by the Rag GTPases to the lysosomes where it is activated by Rheb under nutrient rich conditions. Similarly, when nutrients are abundant, the active forms of Rags, i.e. the RagA/B^{GTP}-RagC/D^{GDP} heterodimers, recruit TFEB to the lysosomal surface through the interaction with its first 30 amino acid residues, and the recruitment is independent of mTORC1 activity (Martina and Puertollano, 2013). Importantly, the mitogen-activated protein kinase kinase kinase kinase 3 (MAP4K3) phosphorylates TFEB at S3 when amino acids are abundant, and phosphorylated S3 is required for the interaction of TFEB with the Rag GTPases and further phosphorylation by mTORC1, leading to the cytoplasmic retention and inactivation of TFEB (Hsu et al., 2018). When the amino acids are scarce, TFEB is not phosphorylated at S3, nor can the inactive Rags recruit either TFEB or mTORC1, and TFEB is relieved from cytoplasmic sequestration and undergoes translocation into the nucleus.

These observations revealed a highly dynamic regulation of TFEB in response to nutrient limitation. It also suggests that TFEB, a nutrient sensor and effector, can be regulated by more than one kinase. Indeed, TFEB S467 is demonstrated to be phosphorylated by AKT and the inhibition of AKT by trehalose promotes TFEB nuclear accumulation and the activation of the CLEAR network (Palmieri et al., 2017). TFEB S142 can be phosphorylated by either mTORC1 or ERK2, and the alanine substitution mutant S142A greatly abolished the cytoplasmic retention of TFEB and enhanced autophagy (Settembre et al., 2011, 2012). In addition, TFEB S138 can be phosphorylated by GSK3β to control TFEB subcellular localisation

(Li et al., 2016). In osteoclasts, phosphorylation at S461, S466 and S468 in the carboxyl terminus of TFEB by PKCβ in response to the cytokine RANKL, stabilises TFEB protein and increases its activity (Ferron et al., 2013). Although the mechanisms underlying these phosphorylation sites being important for TFEB subcellular localisation and transcriptional activity remain to be further investigated, it is worth noting that very similar to that of mTORC1, the regulation of TFEB also involves several extracellular signalling pathways, including the PI3K/AKT, the MAPK, the PKC and likely the Wnt/β-catenin pathways.

Sequence alignment of the MITF/TFE family members shows that the residues and regions which are important for TFEB subcellular localisation are also conserved in TFE3 (**Figure 1.3.1**). Therefore TFE3 shares a highly similar regulation by mTORC1-Rag GTPases at its equivalent residues (Martina et al., 2014). The non-melanocyte MITF isoforms containing the Rag interaction motifs including MITF-A and MITF-D can be recruited to lysosomes, and their cytoplasmic retention can be disrupted through either mTORC1 inhibition or an alanine mutation at the serine residues equivalent to S3 of TFEB (Martina and Puertollano, 2013; Ngeow et al., 2018). However, the melanocyte-specific isoform of MITF which lacks the N-terminal residues required for the lysosomal recruitment does not seem to respond to starvation or mTORC1 inhibition (Martina and Puertollano, 2013). Nonetheless, S73 of MITF, equivalent to S142 of TFEB, is directly phosphorylated by ERK2 when the cells are stimulated via the c-Kit receptor tyrosine kinase, and the downstream phosphorylation mediates protein degradation of MITF (Hemesath et al., 1998; Wu et al., 2000), suggesting that MITF shares a similar yet distinct regulation with TFEB and TFE3.

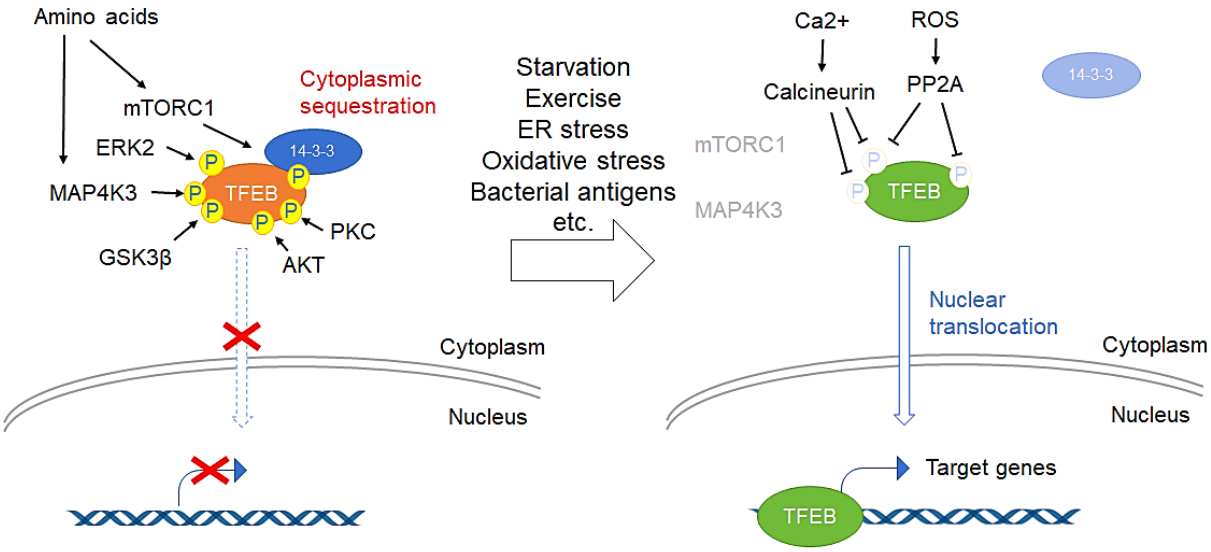


Figure 1.3.2 A model explaining current understanding of TFEB activation. Under normal nutrient rich conditions, TFEB is phosphorylated at multiple sites by different kinases and subject to cytoplasmic sequestration, therefore remains inactive. Under starvation or stressed conditions, phosphatases including calcineurin and PP2A dephosphorylate TFEB, which leads to TFEB nuclear translocation and TFEB-dependent gene transcription.

Finally, the dephosphorylation of TFEB caused by mTORC1 inactivation in response to starvation must be coupled with activation of phosphatases. Calcineurin, upon amino acid starvation, is activated by Ca^{2+} released from lysosomes and dephosphorylates TFEB, partially contributing to its nuclear translocation (Medina et al., 2015). The observation is consistent with a high-throughput screen for small-molecule agonists of TFEB, which shortlisted several compounds that elevate cytoplasmic Ca^{2+} levels (Wang et al., 2018). However, the minor effect of calcineurin inhibitors on preventing TFEB nuclear entry (Medina et al., 2015) suggests that there must be more phosphatases involved, especially considering its ability to integrate multiple inputs to monitor cellular homeostasis.

Indeed, a recent study demonstrated that under oxidative stress induced by arsenite leads to protein phosphatase 2A (PP2A) activation as well as TFEB and TFE3 nuclear translocation and activation (Martina and Puertollano, 2018). Activated PP2A dephosphorylates TFEB at several residues including S109, S114, S122 and S211, which was shown indispensable for the nuclear entry of TFEB, while mTORC1 activity remains unaffected (Martina and Puertollano, 2018). S122 and S211 are known mTORC1 phosphorylation sites. However, PP2A does not seem to affect the phosphorylation of another mTORC1 phosphorylation site S142 or the GSK3β site S138 (Martina and Puertollano, 2018), which are also shown important for TFEB subcellular localisation (Li et al., 2016; Settembre et al., 2011). Nevertheless, PP2A may cooperate with calcineurin to control TFEB activation in a wide range of scenarios.

1.3.3 Physiological roles of TFE family

1.3.3.1 Lysosomal biogenesis and autophagy

Genome-wide chromatin immunoprecipitation followed by sequencing (ChIP-seq) revealed that TFEB and TFE3 can directly bind to CLEAR elements (Martina et al., 2014; Palmieri et al., 2011), and the overexpression of TFEB and TFE3 induces transcriptional activation of lysosomal genes, including several subunits of the v-ATPase, lysosomal membrane proteins and lysosomal hydrolases, resulting in increased number of lysosomes (Martina et al., 2014; Sardiello et al., 2009). Importantly, TFEB and TFE3 activation induces the expression of genes involved in the regulation of lysosome-participated processes, such as autophagy, endocytosis and phagocytosis (Martina et al., 2014; Settembre et al., 2012). MITF, on the other hand, not only regulates biogenesis of melanosomes, a melanocyte-specific lysosome-related organelle (Cheli et al., 2010; Raposo and Marks, 2007), its expression also displays a strong correlation with that of a subset of lysosomal genes containing CLEAR

elements in their promoters (Ploper et al., 2015). Especially, MITF is a key transcriptional regulator of the v-ATPase in both fruit fly and human melanocytes (Zhang et al., 2015). Therefore, the MITF/TFE family is considered to be the master regulator of lysosomal biogenesis and autophagy.

Moreover, in addition to increasing the number of lysosomes, the expression of TFEB also leads to the redistribution of lysosomes to the proximity of plasma membrane, along with increasing the intracellular Ca^{2+} by inducing the expression of lysosomal calcium channel Mucolipin 1/MCOLN1, thus promoting lysosomal exocytosis (Medina et al., 2011). Particularly, in osteoclasts which require a high level of lysosomal exocytosis to release proteases for the bone resorption, the stabilisation of TFEB by PKCβ in response to RANKL increases lysosomal biogenesis and is required for osteoclast function in vivo (Ferron et al., 2013). This suggests that TFEB-dependent transcriptional regulation not only controls the quantity of the lysosomes, but also coordinates many lysosome-related processes to achieve maximum functionality.

1.3.3.2 Lipid metabolism

The role of TFEB in metabolism is not restricted to protein breakdown to recycle amino acids and restore nutrient balance through autophagy. It also contributes to the catabolism of lipids, another major source of energy in response to starvation. The overexpression of TFEB up-regulates the majority of genes involved in lipid uptake, β-oxidation in mitochondria and peroxisomes, while down-regulating genes involved in lipid biosynthesis (Settembre et al., 2013), thus favouring lipid catabolism while suppressing lipid anabolism to maintain energy homeostasis during fasting. Importantly, TFEB directly activates the transcription of peroxisome proliferator-activated receptor γ coactivator 1 α (PGC1-α), a key regulator of mitochondrial biogenesis and lipid metabolism (Settembre et al., 2013). Accordingly, depletion

of TFEB in mouse liver results in lipid droplet accumulation and less lipid breakdown, while overexpression of TFEB improves lipid catabolism and reduces obesity in mice fed with high-fat-diet (Settembre et al., 2013). Notably, mTORC1 senses lipid levels through lysosomal cholesterol and modulates TFEB subcellular localisation therefore presumably activity (Castellano et al., 2017). The ability of TFEB to promote lipid metabolism expands its role in both sensing and regulating nutrient levels from nitrogen sources to carbon sources.

1.3.3.3 Glucose metabolism

Similar to starvation, muscle exercise induces TFEB nuclear translocation (Mansueto et al., 2017; Medina et al., 2015). Genome wide gene array analysis following overexpression or genetic ablation of TFEB in skeletal muscle points to the notion that TFEB also regulates glucose homeostasis. In fact, TFEB directly controls the transcription of the neuronal isoform of nitric oxide synthase (nNOS), upstream of AMPK activation, to control glucose uptake through the expression of glucose transporter GLUT4 (Mansueto et al., 2017). Muscle from TFEB knockout mice shows reduced glucose uptake, glycogen consumption and insulin sensitivity, resulting in decreased glucose oxidation and accumulation of lactate (Mansueto et al., 2017). Considering that glucose is the primary energy source for muscle contraction as well as the brain, the role of TFEB in regulating glucose metabolism is particularly important for maintaining whole body energy homeostasis.

1.3.3.4 Mitochondrial biogenesis

As the major organelle where TCA cycle and β-oxidation of lipids take place, mitochondria are the power plants that produce energy for the cell. The identification of the mitochondrial regulator PGC-1α as a direct target for TFEB opens up the possibility that TFEB can also regulate mitochondrial functions. Indeed, TFEB overexpression results in increased

mitochondrial number and size, while TFEB depletion leads to abnormal mitochondria (Mansueto et al., 2017). Although the role of TFEB in mitochondrial biogenesis is independent of PGC-1α, TFEB directly promotes the expression of nuclear respiratory factors 2 (NRF2) as well as its downstream genes including the mitochondrial transcription factor A (TFAM). As a result, TFEB enhances the respiratory chain complex activities and increases ATP production (Mansueto et al., 2017). The discovery that TFEB regulates mitochondrial biogenesis and glucose metabolism positions TFEB as a nexus for the regulation of metabolic flexibility.

1.3.3.5 ER stress

Autophagy is dramatically induced by nutrient limitation to degrade damaged organelle, excessive cellular components and macromolecules, while stresses like accumulation of misfolded proteins in the endoplasmic reticulum (ER) induce other clearance pathways such as the unfolded protein response (UPR). It has been demonstrated that TFEB and TFE3 are activated in response to ER stress. Unlike starvation, TFE3 nuclear translocation is independent of mTORC1 but requires the activation of PERK, a kinase that senses misfolded protein and initiates UPR (Martina et al., 2016). Nevertheless, there is a large overlap of downstream genes induced by TFEB and TFE3 between ER stress and starvation, including not only the lysosomal and autophagic genes, but also the genes implicated in stress response, signalling and apoptosis (Martina et al., 2016). ATF4, a master regulator of integrated stress response, is induced by TFEB and TFE3 under both ER stress and starvation (Martina et al., 2016). These observations suggest that TFEB and TFE3 may play an important role in integrating multiple cellular stress pathways and modulating stress responses to promote cell survival.

1.3.3.6 Immune responses

Autophagy not only provides nutrient recycling in response to starvation, but also plays an essential role in the activation of macrophages and other cells of the innate immune system in response to pathogen exposure (Puleston and Simon, 2014). Macrophages rely on phagocytosis to internalise and kill pathogens, a process requiring the acidic and hydrolytic lysosomal lumen. Given that TFEB and TFE3 activation enhances autophagy and lysosomal biogenesis, it is not surprising that they also participate in the macrophage activation. Following liposaccharide (LPS) stimulation, TFE3 undergoes nuclear translocation and activation in an mTORC1-independent manner (Pastore et al., 2016). ChIP-seq experiment confirmed that after LPS stimulation, the binding of TFE3 to the promoters of lysosomal and autophagic genes was enriched (Pastore et al., 2016). Interestingly, TFE3 also binds to the promoters of several immune genes (Pastore et al., 2016). Double knockout of both TFEB and TFE3 severely reduces the levels of autophagy as well as cytokine secretion, while single knockout of either TFEB or TFE3 results in a similar reduction, but to a lesser extent (Pastore et al., 2016). These findings suggest that TFEB and TFE3 cooperate to mediate innate immune response. Another study found that Fcγ-receptor-mediated bacterial killing also requires the participation of TFEB, and that Fcγ-receptor activation induces TFEB nuclear translocation in a lysosomal Ca^{2+}-dependent way (Gray et al., 2016). These studies suggest that multiple modes of action converging on TFEB/3-dependent lysosomal function is important for innate immunity.

TFEB and TFE3 also play a role in adaptive immune response. TFE3 was originally identified and characterised by its binding ability to the enhancers of immunoglobulin heavy-chain and T cell receptor (TCR) (Beckmann et al., 1990). TFEB and TFE3 were later found to be essential in humoral immunity via $CD4^+$ T cell activation through controlling the expression

of CD40 ligand, thus promoting B cell-dependent production of immunoglobulin IgG and IgA (Huan et al., 2006). What's more, effective T cell function requires antigen presentation from antigen presenting cells (APC) such as dendritic cells, macrophages and B cells. Cytosolic antigens are processed by the proteasomes and presented through major histocompatibility complex (MHC) class I to $CD8^+$ T cells, while exogenous antigens are degraded by lysosomal proteases in endolysosomes and presented to $CD4^+$ T cells through MHC class II molecules. However, cross-presentation can happen and exogenous antigens can be presented through MHC class I (Blum et al., 2013; Puleston and Simon, 2014). The switch of antigen-presentation pathways from MHC class I to MHC class II in dendritic cells is also found to be regulated by TFEB (Samie and Cresswell, 2015). During dendritic cell maturation following antigen stimulation, TFEB activity is up-regulated, which results in phagosomal acidification and degradation, promoting MHC class II antigen presentation while reducing cross-presentation by MHC class I (Samie and Cresswell, 2015). Therefore, TFEB/3 affect adaptive immunity not only by regulating the expression of several immune genes, but also by modulating lymphocyte function through adjusting antigen presenting strategy according to immunological stimuli.

1.3.4 TFEB and TFE3 in cancer

Evidence accumulates that dysregulation of MITF/TFE family transcription factors leads to various types of cancers (Raben and Puertollano, 2016). As discussed above, although autophagy is demonstrated to suppress cell transformation and tumour initiation, it provides a means beneficial for cancer cells to survive often nutrient poor, hypoxic and immune intense microenvironment as well as facilitates chemotherapy resistance (Hanahan and Weinberg, 2011; Shintani and Klionsky, 2004; Wu et al, 2015a; Wu et al, 2015b). The emerging of the MITF/TFE

factors as the master regulators of autophagy and lysosomal biogenesis raises the possibility that cancer cells may exploit TFEB/TFE3 for tumorigenesis and survival.

Renal cell carcinoma (RCC) is the best known TFEB/TFE3-associated cancer type, yet TFEB/TFE3 associated RCCs resulted from chromosomal translocations are further divided into several subgroups, depending on the chromosomal breakpoint and the genes fused with MITF/TFE factors (Kauffman et al., 2014). The first documented chromosomal rearrangement in a RCC tumour was a t(X;1)(p11.2;q21.2) translocation in a paediatric patient (de Jong et al., 1986). Subsequent mapping revealed the fusion of TFE3 with a novel gene PRCC (papillary renal cell carcinoma) (Sidhar et al., 1996; Weterman et al., 1996). More gene fusions were identified in patients with RCC, namely SFPQ-TFE3 (t(X;1)(p11.2;1p34)), NONO-TFE3 (inv(X)(p11.2;q12)), ASPSCR1-TFE3 (t(X;17)(p11.2;q25) and CLTC-TFE3 (t(X;17)(p11.2;q23)), suggesting that TFE3, rather than the fusion partners, is the critical factor for the cancer incidence (Argani et al., 2001, 2003; Clark et al., 1997). These gene fusions are confirmed recurrent mutations in patients with RCC except CLTC-TFE3 (Kauffman et al., 2014). Even with the same fusion partner, the breakpoints for TFE3 vary, resulting in different isoforms. But all of chimeric proteins contain the bHLH-LZ and the transactivation domain, and they are without exception overexpressed and display strong nuclear staining (Kauffman et al., 2014).

Gene fusions for TFEB occur at a lower frequency in RCC in comparison to TFE3. The fusion of TFEB gene and the non-protein-coding gene MALAT1 (t(6;11)(p21.2;q13) has been reported in multiple cases (Davis et al., 2003; Kuiper et al., 2003), suggesting a common role of the MITF/TFE family in RCC. Interestingly, a t(6;17)(p21;q24-25) translocation was found resulting in the fusion of TFEB with ASPSCR1, at the same locus of the ASPSCR1-TFE3 fusion

(Dal Cin et al., 1991). In contrast to TFE3 fusions, the TFEB fusions often exhibit a favourable prognosis (Kauffman et al., 2014).

The mechanisms underlying the oncogenic role of TFE-fusion remain to be elucidated. However, numerous studies favour a "dysregulated activity model", wherein the fusion of the TFE genes with another gene introduces a more active promoter to up-regulate the oncogenic pathways that are already present in the wildtype cells. Consistent with this model, all the fusion partners have constitutively active promoters, and the fusions dramatically increase the expression of the TFE-fusion proteins compared to wildtype TFEs (Argani et al., 2003; Kuiper et al., 2003; Weterman et al., 1996). Particularly, the lysosomal enzymes such as Cathepsin K are highly elevated in MITF/TFE associated RCCs (Martignoni et al., 2009, 2011), confirming that the aberrant expression of TFEB/TFE3 is accompanied by up-regulated lysosomal activity. A recently identified TFEB target, Rag D, is also found up-regulated in cells derived from RCC tumour harbouring TFE-fusion, thus promoting mTORC1 signalling and cell survival (Di Malta et al., 2017). Although it remains largely a mystery why the TFE-fusion associated cancer incidence is restricted to RCC, these studies indicate that dysregulation of MITF/TFE factors and the autophagic/lysosomal pathways may lead to tumorigenesis.

In addition to chromosomal translocation, the implication of MITF/TFE in other cancers is being demonstrated. Pancreatic ductal adenocarcinoma (PDAC) is a subtype of pancreatic cancer that is characterised by its poor vascularisation and high levels of autophagy (Longo et al., 2016; Rosenfeldt et al., 2013; Yang et al., 2011). It has been shown that the high lysosomal and autophagic activity in PDAC cells compared to non-PDAC cells correlates with the expression of TFE3, and that TFE3 display a strong nuclear localisation in PDAC tumours regardless of intact mTORC1 signalling (Perera et al., 2015). Proteomic approaches revealed

that the aberrant expression of nuclear importin 7 (IPO7) and importin 8 (IPO8) overrides the negative regulation by mTORC1 signalling and forces TFEB/TFE3 into the nucleus irrespective of nutrient status or mTORC1 activity. This results in the constitutive activation of lysosomal and autophagic genes as well as increased macropinocytosis, thus promoting cell proliferation and survival (Perera et al., 2015).

Taken together, these findings support the role of TFEB and TFE3 dysregulation in tumorigenesis and provide therapeutic insights into treating cancers with abnormal lysosomal functions as well as other diseases.

1.3.5 TFE family as therapeutic targets

The study in the dysregulation of TFEB/TFE3 in pancreatic cancer provides the initial evidence of targeting TFE family to slow down cancer cell proliferation and tumour growth (Perera et al., 2015). Given that the addiction to lysosomal/autophagic activities is a common feature in many cancers, therapeutically targeting TFE family may be an effective strategy to improve anti-tumour therapies. However, cancer is not the only disease associated with lysosomes. More than 50 lysosomal storage disorders (LSDs) have been identified, characterised by defects or malfunctions in the lysosomal/autophagy pathways and the accumulation of undegraded substrates (Parenti et al., 2015). The discovery of TFE family as master regulators of lysosomal biogenesis provides new insights into understanding the pathologies as well as ameliorating the symptoms of LSDs.

Age-related Alzheimer's disease (AD) is the most prevalent neurodegenerative disorder. Patients with AD suffer an incremental memory loss and severely compromised quality of life. AD is characterised by the extracellular β-amyloid (Aβ) plaques and intracellular neurofibrillary tangles (NFT) consists of hyperphosphorylated Tau (p-Tau) protein (Hardy, 2006). The increase

of acid sphingomyelinase (ASM) in patients with AD as well as AD mice is associated with the defect of autophagy and lysosomal function to degrade the Aβ and Tau plaques (Lee et al., 2014). Inhibition of ASM by either genetic disruption or amitriptyline restored the lysosomal activity and autophagy through elevating TFEB levels (Lee et al., 2014). In astrocytes, TFEB expression reduced Aβ in the interstitial fluid by enhancing the uptake, trafficking and degradation through lysosomes (Xiao et al., 2014). Furthermore, TFEB expression promotes the degradation of p-Tau and the NFT plaques and rescues the synaptic and behavioural abnormalities in a mouse model (Polito et al., 2014). These studies provide evidence that modulating TFEB activity can be an effective way to promote clearance of Aβ and p-Tau plaques thus ameliorating AD symptoms.

Parkinson's disease (PD) is the second most common neurodegenerative disease. It mainly affects the motor system of the central nervous system, which leads to symptoms of involuntary shaking, rigidity, difficulty in movement and later dementia and depression. It is caused by the neuronal Lewy bodies composed of abnormal protein aggregates including α-synuclein, resulting in the loss of functional neurons in the brain. The inability to degrade the protein aggregates is due to impairment of lysosomes (Dehay et al., 2013). It is also noted that in dopaminergic neurons from patients with PD, nuclear activity of TFEB is reduced, presumably due to the structural homology of α-synuclein and 14-3-3 which can sequester TFEB in the cytoplasm. Accordingly, this can be reversed by TFEB overexpression or mTORC1 inhibition, which leads to activation of autophagy and clearance of α-synuclein aggregates (Decressac et al., 2013).

Huntington's disease (HD) is another neurodegenerative disease with which patients suffer involuntary movements, cognitive decline and psychiatric illness. It is caused by the

expansion of a CAG trinucleotide repeat in the huntingtin (*htt*) gene. The CAG repeat is translated into an expanded polyglutamine (polyQ) tract in the N-terminal region of the htt protein, which leads to its misfolding and pathogenesis (MacDonald et al., 1993). In both neuronal cells and HD mice, TFEB expression is significantly reduced. The overexpression of PGC-1α, a protein well-documented to be repressed in HD (Cui et al., 2006; Weydt et al., 2006), not only rescued mitochondria function, but also reduced htt protein aggregates in the hippocampus (Tsunemi et al., 2012). More importantly, the PGC-1α expression restored TFEB levels and promoted protein turnover pathways such as the autophagy-lysosome pathway (Tsunemi et al., 2012). Indeed, ectopically expressing TFEB induced cellular clearance of the pathogenic htt protein in a cell model (Sardiello et al., 2009).

Similar to HD, spinal and bulbar muscular atrophy (SBMA) is also caused by the CAG expansion in the gene encoding androgen receptor (AR) (Spada et al., 1991). The pathogenic polyQ-AR protein reduces protein turnover and autophagic flux through inhibition of TFEB transactivation. This can be explained by the notion that normal AR interacts with and acts as a coactivator of TFEB dependent gene transcription, but the polyQ-AR can still interact with TFEB although interferes with its function. The autophagy defects can be rescued by TFEB overexpression in a SBMA stem cell model (Cortes et al., 2014). This provides another example of aberrant protein hijacking TFEB leading to its abnormal cellular function, and that modulation of TFEB expression and activity may be the key to treating LSDs.

1.4 Summary and aims

Cancer cells exhibit aberrant metabolism. This is accomplished by alterations in various oncogenic pathways to ensure cells have sufficient access to glucose and amino acids, particularly glutamine.

mTORC1 and mTORC2 play important roles in promoting cell growth and survival. Importantly, mTORC1 coordinates cellular metabolism in response to nutrient availability: when nutrients are abundant, activated mTORC1 promotes anabolic processes such as protein translation, lipid and nucleotide biosynthesis etc., while suppressing the catabolic pathways such as autophagy. By contrast, when nutrients are scarce, the biosynthetic pathways promoted by mTORC1 are shut down due to mTORC1 inactivation, while the degradative autophagy machinery is activated.

As one of the major effectors downstream of mTORC1, TFEB subcellular localisation and transcription activity is regulated by mTORC1 phosphorylation in response to nutrient abundance. mTORC1 activation under nutrient rich conditions leads to phosphorylation and cytoplasmic sequestration of TFEB, whereas mTORC1 inactivation and phosphatase activation under starvation result in TFEB dephosphorylation and translocation into the nucleus. Upon nuclear translocation, TFEB binds to the E-box motifs and CLEAR elements to promote the transcription of genes involved in lysosomal biogenesis, autophagy machinery, lipid catabolism, glucose uptake and mitochondrial biogenesis etc., facilitating catabolic processes for nutrient recycling, energy production as well as cellular clearance.

The regulation of TFEB in response to levels of amino acids is fairly well-understood. When amino acids are present, MAP4K3 phosphorylates TFEB at S3 to facilitate its lysosomal recruitment by the Rag GTPases. At the lysosomal surface, TFEB is phosphorylated by mTORC1 at multiple sites including S122, S142 and S211. The phosphorylation of S211 leads to cytoplasmic sequestration of TFEB by 14-3-3 and inactivation. Upon amino acid starvation, inactivation of mTORC1 and activation of phosphatases including Calcineurin and likely PP2A, promote dephosphorylation of TFEB at S3, S122 and S211, relieving TFEB from cytoplasmic

retention. TFEB therefore undergoes nuclear translocation and activates transcription of its target genes.

Several other kinases can also phosphorylate and regulate TFEB, including AKT phosphorylating TFEB at S467 (Palmieri et al., 2017) and GSK3β at S138 (Li et al., 2016). Although the mechanisms underlying these phosphorylation events are less clear, they represent a situation where TFEB can integrate multiple inputs from different pathways, given the ability of TFEB to regulate more than amino acid metabolism. However, what other physiological stimuli regulate TFEB activity are less well-known, and how the phosphorylation of the serine residues such as S142 and S138 controls TFEB subcellular localisation is poorly understood.

Therefore, the first part of the thesis will further explore the regulation of TFEB by nutrient availability, particularly by glucose limitation, a common feature of solid tumours. This work will utilise biochemistry and cell biology approaches, attempt to link TFEB subcellular localisation to the signalling pathways in response to nutrient starvation, and dissect the molecular mechanisms by which the phosphorylation of certain serine residues controls TFEB cytoplasmic-nuclear shuttling, aimed at expanding the current understanding of TFEB regulation in maintaining cellular nutrient and energy homeostasis.

The second part of the thesis will be built upon the therapeutic implication of targeting TFEB. A high throughput image-based screen of FDA approved drugs was performed to identify small-molecule compounds that modulate TFEB nuclear translocation, followed by functional validation for lysosomal biogenesis and autophagy. The outcome of the screen may be readily useful for the clinical treatment of LSDs, and the elucidation of the mechanisms how those compounds promote TFEB activation may also provide insights into treating cancers with dysregulated lysosomal function.

Chapter 2 - Methods and materials

2.1 Bacterial methods

2.1.1 Growth conditions

Bacterial Luria-Bertani (LB) medium for culturing *E. coli* was made using 10 g/L Tryptone, 5 g/L Yeast Extract, and 5 g/L NaCl, autoclaved and cooled down to room temperature before use. The LB agar plates were made by LB agar powder (10 g/L Peptone 140, g/L Yeast Extract, and 5 g/L NaCl, 12 g Agar) from Thermo Fisher Scientific, autoclaved and poured into 10 cm petri dishes (Sterilin, Newport, UK) and cooled to room temperature before use. Liquid cultures were grown in a shaking incubator at 37 °C at 225 rpm. LB plate cultures were grown in a humidified incubator at 37 °C overnight to form colonies. In most occasions the culturing medium and LB plates were supplemented with the according antibiotics, at a concentration of 100 μg/mL for ampicillin (Thermo Fisher Scientific, Waltham, MA, USA) or 50 μg/mL for kanamycin (Fisher Scientific, Waltham, MA, USA).

2.1.2 Bacterial Strains

Subcloning efficiency DH5α competent cells purchased from Thermo Fisher Scientific, which provides a transformation efficiency of > 1 x 10^6 cfu/μg plasmid DNA, were used for general cloning. The genotype of the DH5α *E. coli* strain is F^- Φ80lacZΔM15 Δ(lacZYA-argF) U169 recA1 endA1 hsdR17(r_k^-, m_k^+) phoA supE44 thi-1 gyrA96 relA1 λ^-.

XL10-Gold ultracompetent cells purchased from Agilent, Santa Clara, CA, USA, which provides a transformation efficiency of 5 x 10^5 cfu/μg, were used for site-directed mutagenesis. The genotype of the XL10-Gold strain of *E. coli* is Tetr Δ(mcrA)183 Δ(mcrCB-hsdSMR-mrr)173 endA1 supE44 thi-1 recA1 gyrA96 relA1 lac Hte [F' proAB lacIqZ ΔM15 Tn10 (Tetr) Amy Camr].

2.1.3 Transformation of competent bacteria

Chemical competent cells were taken from -80°C and thawed on ice and aliquoted into 20 µL in pre-cooled 1.5 mL Eppendorf tubes. For plasmid DNA, less than 100 ng DNA was added to the bacteria, for ligation products, a maximum of 5 µL was used. The bacteria and DNA was mixed by gently tapping the Eppendorf tube and incubated on ice for 30 min, then heat shocked in a heat block at 42°C for 30 s, followed by chilling on ice for 2 min. Then each tube was added 250 µL of S.O.C medium (2% tryptone, 0.5% yeast extract, 10 mM NaCl, 2.5 mM KCl, 10 mM $MgCl_2$, 10 mM $MgSO_4$, and 20 mM glucose) from Thermo Fisher Scientific, and the cells were allowed to recover in a shaking incubator at 37 °C and 225 rpm for 45-60 min, before being spread on LB agar plates containing the according antibiotics.

2.2 Mammalian methods

2.2.1 Cell culture

Human colorectal cancer cell line HT29, human breast cancer cell line MCF7, human embryonic kidney cell line Phoenix and human cervical cancer cell line HeLa were grown in Dulbecco's Modified Eagle Medium (DMEM), supplemented with 10% foetal bovine serum (Biosera), and 50 units/mL penicillin, 50 units/mL streptomycin (Thermo Fisher Scientific). Human colorectal cancer cell lines COLO205, HCC2998, HCT116 and SW620 were grown in Roswell Park Memorial Institute (RPMI) 1640 media (Thermo Fisher Scientific), supplemented with 10% foetal bovine serum (Biosera), and 50 units/mL penicillin, 50 units/mL streptomycin (Thermo Fisher Scientific). For selection and maintenance, the stably inducible cell lines, the medium was supplemented with 750 µg/mL geneticin (Thermo Fisher Scientific) and 1 µg/mL puromycin (Gibco).

Unless stated otherwise, cells were grown in T75 culturing flasks (Corning) in a humidified incubator at 37 °C with 10% CO_2. Cells were grown in a monolayer until 80 % - 90 % confluency before they were passaged. For cell passaging, the medium was removed using a pump aspirator, and cells were rinsed with 3 – 5 mL of 1 x autoclaved phosphate-buffered saline (PBS) (137 mM NaCl, 2.7 mM KCl, 10 mM Na_2HPO_4, 1.8 mM KH_2PO_4, pH 7.4). Then 2 mL of 0.05% Trypsin-EDTA (Thermo Fisher Scientific) was added, allowing the cells to detach in an incubator at 37 °C. The detachment of cells was confirmed using light microscopy with a 20X magnification lens, after which the trypsin was inactivated by adding 2 mL of culture medium and mixing. The cell suspension was transferred to a 15 mL falcon tube and cells were spun down by centrifugation at 800 g for 4 min. Then the cell pellet was resuspended with culture medium and cell number was counted with an automated cell counter (Bio-rad) using 0.4 % trypan-blue (Sigma-Aldrich) to indicated live cells. An appropriate number of cells was then inoculated into a fresh culture vessel.

For storage, cell pellets after centrifugation were resuspended in foetal bovine serum containing 10 % dimethyl sulfoxide (DMSO) (Sigma-Aldrich) and aliquoted into cryo tubes (Thermo Fisher Scientific), then placed into a Mr Frosty freezing container (Thermo Fisher Scientific) and stored in a freezer at -80°C. For long term storage, frozen cells were transferred from -80°C to liquid nitrogen. To recover frozen cells, the cryo tubes were taken out of -80°C freezer or liquid nitrogen and quickly placed in a water bath at 37°C. The thawed cells were then spun down at 800 g for 4 min in a centrifuge, resuspended in fresh culture medium and inoculated into appropriate culture vessel.

2.2.2 Transient transfection of Plasmids

1 X 10^5 cells were seeded in each well of a 6-well plate the day before transfection and allowed to grow in culture medium. FuGENE 6 (Promega) was used according to manufacturer's instructions. Briefly, 0.5 – 2 µg plasmid DNA was mixed with FuGENE 6 at a 1:3 ratio, in 100 µL Opti-MEM (Thermo Fisher), and incubated at room temperature for 15 min. Then 100 µL of transfection mixture was added drop-wise to each well and mixed by gently swirling the 6-well plate. The cells were incubated for 24 – 48 hours before further analysis. The transfection mixture can be scaled up or down depending on the number of cells and size of the culture vessel.

2.2.3 Generation of stable cell lines

To generate stably inducible cell lines, three plasmids were used: a Piggybac vector containing the gene of interest driven by a tetracycline-responsive promoter, a vector containing the Piggybac transposase, and a vector containing the trans-activator for the transposase. The three plasmids were transfected at a 10:1:1 ratio using the method described in transient transfection of plasmids. After 48 hours of transfection, the cells were detached using 0.05% Trypsin-EDTA, reattached in the medium containing 750 µg/mL geneticin and 1 µg/mL puromycin, and incubated for another 48 hours. The detaching-reattaching process was repeated every 48 hours until all control cells (with no plasmid transfected) died. Then the stably transfected cells after antibiotic selection were inoculated in larger culture vessels and expanded for storage and further analysis.

2.2.4 Transient transfection of siRNA

1 X 10^5 cells were seeded in each well of a 6-well plate the day before transfection and allowed to grow in culture medium without antibiotics. Lipofectamine RNAiMAX was used for

the transfection of siRNA according to manufacturer's protocol. Briefly, 6 µL of Lipofectamine RNAiMAX was mixed with 150 µL Opti-MEM, and incubated at room temperature for 5 min. In a separate tube, 9 pmol of siRNA was diluted in 150 µL of Opti-MEM. The diluted siRNA was then mixed with diluted Lipofectamine RNAiMAX to form a transfection complex, and incubated at room temperature for another 15 min. After the incubation, 250 µL of the transfection complex was added drop-wise to a single well. The amount of the transfection complex can be scaled up or down depending on the cell number and the size of the culture vessels. Cells were incubated for 48 to 72 hours before further analysis.

2.2.5 Virus-mediated transduction of shRNA or DNA

1 X 10^5 cells were seeded in each well of a 6-well plate the day before the transduction. Appropriated amount of lentivirus containing shRNA or retrovirus harbouring genes of interest was added to the wells. After incubation in the quarantine incubator at 37 °C overnight, the medium containing viruses was replaced with medium containing appropriate antibiotics. The cells were selected for 48 hours before further analysis.

2.3 Nucleic acid methods

2.3.1 Agarose gel electrophoresis

Agarose gel electrophoresis was used to resolve DNA fragments by their sizes. Agarose (Web Scientific) was dissolved and heated in TBE buffer (100 mM Tris, 90 mM boric acid, 1 mM EDTA) in the microwave. After the agarose gel solution was cooled to room temperature, peqGREEN (PEGLAB) was added to the gel at a concentration of 1:10,000 before the gel was cast into a mold and to allow solidification. DNA samples were mixed with 0.2 volumes of 6X purple gel loading dye (New England Biolabs) before loaded into the wells of the agarose gel.

HyperLadder 50bp and HyperLadder 1 kb (Bioline) were used to indicate molecular sizes. Electrophoresis was performed at 120 V in TBE buffer for approximately 25 min. The DNA was visualized under ultraviolet (UV) light in an UVIdoc (UVItec).

2.3.2 Plasmid purification

For small scale plasmid purification, individual bacterial colonies from LB agar plates were inoculated into 3 to 6 mL LB medium containing the corresponding antibiotics in a 14 mL polypropylene round-bottom tube (Falcon). The bacteria were grown at 37 °C at 225 rpm overnight. The next day, the bacteria were spun down at 5000 g and the pellets were proceeded to purification with QIAprep Spin Miniprep Kit (QIAGEN) following manufacturer's protocol. Purified plasmid DNA was eluted in deionized water and the concentration was measured with a NanoDrop 2000 spectrophotometer (Thermo Fisher Scientific).

For middle- or large-scale plasmid purification, 50 µL of bacteria from 3 mL culture was inoculated into 50-100 mL LB medium containing the appropriate antibiotics and grown at 37 °C at 225 rpm overnight. The next day the bacteria were pelleted at 5000 g for 10 min at room temperature and proceeded to purification with Plasmid Midiprep Kit (QIAGEN) following manufacturer's protocol. Purified plasmid DNA was dissolved in deionized water and the concentration was measured with a NanoDrop 2000 spectrophotometer.

2.3.3 Polymerase chain reaction

Polymerase chain reaction (PCR) was performed with AccuPrime Taq DNA polymerase (Thermo Fisher Scientific) to amplify DNA fragments with high fidelity. 100 ng of DNA template and 0.1 nmol of each forward and reverse primers were used in a 50 µL reaction, in which the polymerase and other components were mixed according to manufacturer's protocol. The reaction was carried out in a Veriti Thermal Cycler (Applied Biosystems, Thermo Fisher).

An initial step of 94 °C for 2 min was used to denature the DNA template and 32 cycles of the following steps were performed: denaturation at 94 °C for 30 s, annealing at 55 °C – 60 °C for 30 s and extension at 68 °C for 1 min per kb. The final step at 68 °C was set for 5 min to allow complete extension of DNA amplification, after which the samples were cooled to room temperature for visualization by agarose gel electrophoresis and/or purification.

For PCR of the bacterial colonies on LB agar plates following DNA transformation, 2X MyTaq Red Mix (Bioline) was used instead to obtain of 10 µL mixture of 1X MyTaq Red, 50 pmol of each primer and a touch of bacteria by a pipette tip. Reactions were performed with an initial denaturation step at 95 °C for 3 min, followed by 30 cycles of denaturation at 95 °C for 15 s, annealing at 60 °C for 15 s and extension at 72 °C for 30 s. A final extension step at 72 °C for 5 min was performed, after which the PCR products were visualized on an agarose gel.

2.3.4 Restriction enzyme digestion

Restriction enzyme digestion was performed using the appropriate restriction enzymes from New England Biolabs. 2 µg of DNA was mixed with 20 units of enzyme, 2 µL of the appropriate 10X reaction buffer (determined using the online NEB Double Digest Finder tool https://international.neb.com/tools-and-resources/interactive-tools/double-digest-finder) and deionized water to obtain a total volume of 20 µL. The reaction was incubated at 37 °C for 2 h. To prevent self-ligation of the vector DNA after restriction enzyme digestion, the vector DNA was dephosphorylated with 2 units of calf intestinal alkaline phosphatase (CIP) directly added into the digestion reaction and incubate at 37 °C for 20 min. The digestion products were then purified with the QIA quick PCR Purification Kit (QIANGEN) following manufacturer's protocol.

2.3.5 Ligation

Following the purification of the digestion products, the insert DNA was mixed with vector DNA at a molar ratio of 10:1, in a 10 µL reaction in which 400 units of T4 DNA ligase and 1 µL of 10X T4 DNA ligase buffer (New England Biolabs) were mixed with deionized water. The ligation was performed at 16 °C for 1 h, after which it was transformed into DH5α competent cells.

2.3.5 Site-directed mutagenesis

The site-directed mutagenesis was performed using a PCR based method with the QuickChange Lightning Site-Directed Mutagensis Kit (Agilent) to introduce point mutations or cause deletions of amino acid residues at specific loci in genes of interest. The primers used for site-directed mutagenesis were designed using an online tool from Agilent available at https://www.genomics.agilent.com/primerDesignProgram.jsp.

For each reaction, 100 ng of plasmid DNA template and 125 ng of each primer were mixed with 1 µL 10X reaction buffer, 0.2 µL dNTP mix, 0.3 µL Quick Solution and 1 µL QuickChange Lightning Enzyme in deionized water to obtain a volume of 50 µL. The PCR was performed in a Veritis Thermal Cycler with an initial denaturation step at 95 °C for 2 min, followed by 25 cycles of denaturation at 95 °C for 20 s, annealing at 60 °C for 10 s and extension at 68 °C for 30 s per kb. A final extension step at 68 °C was performed for 5 min. The methylated plasmid template was then digested by adding 1 µL DpnI to the reaction mix and incubating at 37 °C for 5 min. Finally, the PCR products were transformed into XL10-Gold ultracompetent cells, and colonies were screen for mutations by sequencing.

2.3.6 Quantitative real time PCR

RNA was isolated using RNeasy Mini Kit (QIAGEN) following manufacturer's protocol. At the final step, Nuclease-free water was used to elute RNA and the concentration was measured using a Nanodrop 2000 spectrophotometer. The cDNA synthesis was performed using the QuantiTect Reverse Transcription Kit (QIAGEN) following manufacturer's protocol. 1 µg RNA was used for each condition. The quantitative real-time PCR (qRT-PCR) was performed with Brillian III Ultra-Fast SYBR Green QPCR Master Mix (Agilent) in a Rotor-Gene 6000 or Rotor-Gene Q real-time thermal cycler (Corbett). 1 µL of the cDNA synthesized from 1µg RNA was added to 15 µL reaction volume containing 7.5 µL of 2X SYBR Green Master Mix and 3 pmol of each primer. The reactions were performed with an initial step at 95 °C for 10 min, followed by 50 cycles of denaturation at 95 °C for 5 s, annealing at 60 °C for 10 s and extension at 72 °C for 5s. At the end the reaction, the temperature was increased from 72 °C to 95 °C with an interval of 1 °C every 5 s to generate melt-curves. The quantification was performed using the ΔΔCT method, in which the expression of gene of interest was normalized to that of a housekeeping gene, ΔCT=CT[gene of interest]-CT[housekeeping gene], ΔΔCT= ΔCT[treated]- ΔCT[untreated], and that the relative fold change of the gene of interest compared to untreated control is $2^{-\Delta\Delta CT}$.

2.4 Protein methods

2.4.1 Whole cell lysate

The whole cell lysate was prepared by directly adding 1X Laemmli sample buffer (62.5 mM Tris-HCl pH 6.8, 2% Sodium dodecyl sulfate (SDS), 0.01% bromophenol blue, 10% glycerol) to the culture vessel. The cells were detached by a 200 µL pipette tip and transferred

to an Eppendorf tube, after which the lysate was boiled at 95 °C for 10 min and cooled to room temperature for further analysis. For storage, the lysates were kept in a freezer at -20 °C.

2.4.2 Subcellular fractionation

The nuclear-cytoplasmic fractionation was performed using the Rapid, Efficient And Practical (REAP) method (Suzuki et al., 2010). Briefly, the cells were grown to around 80% confluence and treated in a single well of a 6-well plate for each condition. Then the cells were harvested using a cell scraper, washed in 1 mL ice-cold 1X PBS and spun down with a centrifuge at 500 g for 3 min at 4 °C. 500 µL ice-cold PBS containing 0.1% Nonidet P-40 (Sigma-Aldrich) was used to resuspend the cell pellets. After incubation on ice for 5 min, 100 µL of the lysate was removed as whole cell lysate. The rest of the lysate was spun down at 500 g for 3 min at 4°C, and the supernatant was removed as the cytoplasmic fraction. The pellet was washed with 1mL ice-cold PBS containing 0.1% NP40 and spun down in a centrifuge. After the supernatant was discarded, the pellet was resuspended in 400 µL of 1X Triton lysis buffer and sonicated for 5 min at 4 °C. 100 µL of the sonicated extract was kept as nuclear fraction. Finally, the whole cell lysate, the cytoplasmic fraction and the nuclear fraction each were added 100 µL of 2X protein loading buffer to denature the proteins on a heat block at 95 °C for 5 min before further analysis using Immunoblotting.

2.4.3 Immunoprecipitation

Cells grown in a 10 cm petri dish (Corning) for each condition were washed once with cold 1X PBS, detached using a cell scrapper (TPP) in 1 mL cold IP lysis buffer (50 mM Tris-HCl pH 7.5, 150 mM NaCl, 1 mM EDTA, 1% Triton X-100, with 1X Complete Protease Inhibitor and 1X PhosSTOP Phosphatase Inhibitor (Roche) and lysed on ice for 20 min. After sonication for 3 min, the cell lysate was spun at 16000X g at 4 °C for 15 min using a centrifuge,

and 50 µL was stored as input. The rest of the supernatant was transferred to a pre-chilled 1.5 mL Eppendorf tube and incubated with 1 µg antibody on a rotator at 4 °C overnight. The next day, if using a rabbit antibody, 20 µL of resuspended Protein A Dynabeads (Thermo Fisher Scientific) was added to the samples, or Protein G Dynabeads (Thermo Fisher Scientific) if using a mouse antibody. After incubation on a rotator at 4 °C for another 2 h, the beads were washed 3 times with cold IP lysis buffer for 10 min each time, with the assistance of the magnetic separator (Thermo Fisher Scientific), resuspend in 100 µL 1X Laemmli sample buffer and boiled at 95 °C for 6 min with occasional agitation. The samples were then cooled to room temperature for further analysis or stored at -20 °C.

In cases where HA- tag was expressed, the cell lysate was incubated with 20 µL Pierce Anti-HA Magnetic Beads (Thermo Fisher Scientific) instead on a rotator at 4 °C overnight before being washed and boiled, and no additional Protein G or Protein A Dynabeads were needed.

2.4.4 SDS-PAGE

Proteins were separated by sodium dodecyl sulphate polyacrylamide gel electrophoresis (SDS-PAGE). The resolving gel that resolves proteins with their according molecular sizes, consists of 12 % acrylamide (made from 30 % acrylamide solution, 37.5 acrylamide : 1 bis-acrylamide (Severn Biotech)), 375 mM Tris, 0.1 % SDS, pH 8.8. Ammonium persulhate (APS) and tetramethylethylenediamine (TEMED) were added to a final concentration of 0.1 % to the acrylamide solution to allow acrylamide polymerisation. To resolve TFEB, 12 % resolving gel was made from 45 % acrylamide solution (200 acrylamide:1 bis-acryladmide) (Severn Biotech) to obtain better separation of TFEB phospho-variants. After filling around 70 % volume of the

gel casting apparatus with acrylamide solution, appropriate amount of isopropanol was added on top to create a smooth edge for resolving gel to solidify.

After polymerization of the resolving gel, the isopropanol was decanted. The resolving gel was then overlaid with stacking gel comprising of 3.75 % acrylamide, 125 mM Tris, 0.1 % SDS, pH 6.8, containing 0.17 % APS and 0.083% TEMED to allow polymerization.

Protein samples were denatured by adding 1 volume of 2X Laemmli sample buffer (125 mM Tris-HCl pH 6.8, 4 % SDS, 0.02 % bromophenol blue, 20 % glycerol) and boiled at 95 °C for 5 min before being cooled to room temperature. Denatured samples were loaded to the gel and separated at 100 V for 20 min and 140 V for approximately 50 min in 1X running buffer (25 mM Tris, 192 mM glycine, 0.1 % SDS) until the bromophenol blue dye reached the bottom of the gel. Precision Plus Dual Colour Protein Standards (Bio-Rad) was used as an indicator of molecular size.

2.4.5 Immunoblotting

After SDS-PAGE, the proteins from the gel were transferred to a nitrocellulose membrane (Amersham, GE) in 1X transfer buffer (25 mM Tris, 192 mM glycine, 20 % methanol) in a semi-dry transfer tank (Thermo Fisher Scientific) at a constant current of 0.1 A per gel for 75 to 105 min, depending on the molecular size of the protein of interest. The membrane was blocked in 5 % milk in PBS containing 0.1 % Tween-20 (PBST) at room temperature for 60 min before incubation with primary antibodies diluted accordingly in 5 % milk in PBST at 4 °C on a shaker overnight. In cases where phospho-specific antibodies were used, the blocking solution was replaced with 5 % BSA in Tris-buffered saline containing 0.1 % Tween-20 (TBST) and the primary antibodies were diluted also in 5% BSA in TBST. The following day, the membrane was washed 3 time in PBST for 10 min each. Then the membrane

was incubated with species-specific HRP-conjugated secondary antibodies (Bio-Rad) diluted 1:5000 in 5 % milk in PBST (or 5 % BSA in TBST for phospho-specific antibodies) at room temperature for 2 to 3 h before the washed 3 times in PBST (or TBST) for 10 min each. At last, enhanced chemiluminescence (ECL) reagent (Amersham, GE) was applied to the membrane before the fluorescence was detected using X-ray film (Fujifilm) with a film developer in a dark room.

2.5 Cell biology methods

2.5.1 Immunofluorescent microscopy

Cells were grown to 70% to 80% confluency on a round glass coverslip (VWR) for each treatment, and were fixed with 4% paraformaldehyde (PFA, pH 7.4, in PBS) (Sigma-Aldrich) at room temperature for 15 min and washed 3 times with 1X PBS. Then cells were permeabilised with 0.2% Trition-X in PBS at room temperature for 7 min and washed 3 times with 1X PBS. This was followed by blocking in 5% BSA in PBS at room temperature for 30 min. Then the coverslips were placed (the side with cells up) on top of moisturized Whatman filter paper in a foil wrapped container and were added 30 µL of blocking solution containing appropriate dilution of primary antibodies and incubated at 4 °C overnight. The next day the coverslips were washed 3 times with 1X PBS and incubated with appropriated Alexa Fluor-conjugated secondary antibodies (Life Technologies) in 1:1000 dilution in PBS containing 5% BSA and 300 nM 4', 6-diamidino-2-phenylindole (DAPI) (Thermo Fisher Scientific) at room temperature for 1 h in the dark. After 3 times washed in 1X PBS, the coverslips were mounted (the side with cells down) on microscope glass slides (VWR) with Vectashield H-1000 mounting medium (Vector Laboratories) in between, and sealed with nail polish around the edges. Fluorescent

images were acquired using a LSM710 confocal microscope (Carl-Zeiss). In cases where cells express fluorescent proteins, the cells were fixed, permeabilized and stained with DAPI. The antibody staining was omitted unless non-fluorescent protein detection was also required.

2.5.2 Fluorescent live cell imaging

The cells were grown to 70%-80% confluency on a 35 mm-diameter glass-bottom µ-Dish (Ibidi) for each condition. The medium was replaced with FluoroBrite DMEM containing no phenol red (Thermo Fisher Scientific) before imaging using the LSM710 microscope.

2.5.3 Flow cytometry

1 X 10^5 cells were seeded in a single well of a 12-well plate for each condition and incubated overnight. LysoTracker Deep Red 647 (Thermo Fisher Scientific) was added to a working concentration of 50 nM, 30 min before the end of treatments. In cases where cells express fluorescent proteins, no additional staining was required. Then the cells were washed with 1 mL 1X PBS, trypsinised with 400 µL 0.05% Trypsin-EDTA, neutralized with 400 µL DMEM and spun down with a centrifuge at 600 g for 4 min. The cells pellets were resuspended in 400 µL 1X PBS before transferred to flow cytometry tubes (BD Biosciences) for analysis. The flow cytometry data was acquired using FACS Canto flow cytometer (BD Biosciences) with BD FACSDiva software. Briefly, the single live cells were gated using forward scatter (FSC) and side scatter (SSC), then appropriated channels were selected for detection of fluorescent dyes or proteins, namely APC channel for LysoTracker Deep Red 647, FITC channel for EGFP, and PE channel for mCherry. The flow cytometry data was then analysed using FlowJo software (FlowJo, LLC).

2.6 Reagents

2.6.1 Chemicals

Glycerol, Tris, glycine, sodium dodecyl sulphate (SDS), Tween, ampicillin and kanamycin were purchased from Thermal Fisher Scientific (Waltham, USA). Dimethyl sulfoxide (DMSO), methanol, ethanol, isopropanol, butanol, Nonidet-P40 (NP-40) were purchased from Sigma-Aldrich. Chemical salts such as NaCl were obtained from Sigma-Aldrich unless otherwise specified. Triton X-100 was obtained from Merck (Darmstadt, Germany). Paraformaldehyde (PFA) was obtained from Electron Microscopy Science (Hatfield, USA).

Torin 1 was from Tocris (Bristol, UK). Leptomycin B, Triciribine, BIO and Cycloheximide were from Sigma-Aldrich. U0126 and Bafilomycin A were from Cell Signaling Technology (Danvers, USA). LY333531 was from Cayman Chemical (Michigan, USA). Compound C was from Merck (Darmstadt, Germany).

The Pharmakon 1,600 small compound library was kindly provided by Dr. Daniel Ebner laboratory. The information of the compounds used in the validation of the screen hits are listed in table below.

Compound	Source	Catalogue
ESCITALOPRAM OXALATE	Sigma-Aldrich Co Ltd	E4786
BENAZEPRIL HYDROCHLORIDE	Abcam	ab141166-50mg
NAFTOPIDIL	Abcam	ab120756-10mg
DOXEPIN HYDROCHLORIDE	Insight Biotechnology Ltd	sc-203930
ETICLOPRIDE HYDROCHLORIDE	Abcam	ab120602-10mg
FAMOTIDINE	Abcam	ab120760-500mg
AMLODIPINE BESYLATE	Abcam	ab141777-10mg
FLUPHENAZINE HYDROCHLORIDE	Cambridge Bioscience Ltd	F4584-1 g

ABAMECTIN	Cambridge Bioscience Ltd	19201-100 mg-CAY
PIZOTYLINE MALATE	Cambridge Bioscience Ltd	P3597-1 g
DIGOXIN	Bio-Techne (R&D Systems	4583/50
CARVEDILOL PHOSPHATE	Cambridge Bioscience Ltd	C0366-1 g
NORTRIPTYLINE HYDROCHLORIDE	Cambridge Bioscience Ltd	15904-10 mg-CAY
PIMOZIDE	Cambridge Bioscience Ltd	16222-50 mg-CAY
PRAZOSIN HYDROCHLORIDE	Cambridge Bioscience Ltd	15023-50 mg-CAY
TRIFLUOPERAZINE HYDROCHLORIDE	Cambridge Bioscience Ltd	15068-1 g-CAY
PERHEXILINE MALEATE	Cambridge Bioscience Ltd	16982-5 mg-CAY
QUINACRINE HYDROCHLORIDE	Cambridge Bioscience Ltd	15041-100 mg-CAY
PAROXETINE HYDROCHLORIDE	Cambridge Bioscience Ltd	14998-10 mg-CAY
THIORIDAZINE HYDROCHLORIDE	Cambridge Bioscience Ltd	14400-1 g-CAY
DESLORATIDINE	Cambridge Bioscience Ltd	21847-1 mg-CAY
ALEXIDINE HYDROCHLORIDE	Cambridge Bioscience Ltd	13876-10 mg-CAY
CEPHARANTHINE	Cambridge Bioscience Ltd	19648-50 mg-CAY
TOREMIPHENE CITRATE	Cambridge Bioscience Ltd	20854-50 mg-CAY
MAPROTILINE HYDROCHLORIDE	Cambridge Bioscience Ltd	15892-50 mg-CAY
METERGOLINE	Cambridge Bioscience Ltd	21336-10 mg-CAY
DOXORUBICIN	Cambridge Bioscience Ltd	15007-5 mg-CAY
LOPERAMIDE HYDROCHLORIDE	Cambridge Bioscience Ltd	L5660-5 g
SERTRALINE HYDROCHLORIDE	Cambridge Bioscience Ltd	14839-5 mg-CAY
RALOXIFENE HYDROCHLORIDE	Cambridge Bioscience Ltd	10011620-50 mg-CAY
AMOXAPINE	Cambridge Bioscience Ltd	17347-100 mg-CAY

DOXAZOSIN MESYLATE	Cambridge Bioscience Ltd	18633-100 mg-CAY
CARVEDILOL	Cambridge Bioscience Ltd	15418-50 mg-CAY
FLORFENICOL	Cambridge Bioscience Ltd	19458-500 mg-CAY
AZELASTINE HYDROCHLORIDE	Cambridge Bioscience Ltd	CAY20873-10 mg
TRIMIPRAMINE MALEATE	Cambridge Bioscience Ltd	15921-1g-CAY
Tilorone (hydrochloride)	Cambridge Bioscience Ltd	17868-50 mg-CAY
ARIPIPRAZOLE	Cambridge Bioscience Ltd	19989-5 mg-CAY
TERFENADINE	Cambridge Bioscience Ltd	20305-500 mg-CAY
PRIMAQUINE PHOSPHATE	Cambridge Bioscience Ltd	18223-1 g-CAY
DAUNORUBICIN	Cambridge Bioscience Ltd	14159-5 mg-CAY
MITOXANTRONE HYDROCHLORIDE	Cambridge Bioscience Ltd	14842-10 mg-CAY
ETODOLAC	Cambridge Bioscience Ltd	20833-1 g-CAY
TOLAZOLINE HYDROCHLORIDE	Cambridge Bioscience Ltd	18865-5 g-CAY
ASTEMIZOLE	Cambridge Bioscience Ltd	16967-25 mg-CAY
MITOMYCIN	Cambridge Bioscience Ltd	11435-1 mg-CAY
NISOLDIPINE	Cambridge Bioscience Ltd	20998-100 mg-CAY
PERHENAZINE	Cambridge Bioscience Ltd	20735-1 g-CAY
CHLORAMPHENICOL SODIUM SUCCINATE	Fisher Scientific UK Ltd	15529483
AMITRIPTYLINE HYDROCHLORIDE	Fluorochem Ltd	463103-5g
ACRIFLAVINIUM HYDROCHLORIDE	Insight Biotechnology Ltd	sc-214490
SULOCTIDIL	Insight Biotechnology Ltd	sc-236957
BENZETHONIUM CHLORIDE	Insight Biotechnology Ltd	sc-239299
HEXETIDINE	Insight Biotechnology Ltd	sc-228301
PYRONARIDINE TETRAPHOSPHATE	Insight Biotechnology Ltd	sc-205828
MEBHYDROLIN NAPHTHALENESULFONATE	Insight Biotechnology Ltd	sc-263459

PROCHLORPERAZINE EDISYLATE	Insight Biotechnology Ltd	sc-296136B
CHLOROPYRAMINE HYDROCHLORIDE	Insight Biotechnology Ltd	sc-234345
OXYCLOZANIDE	Insight Biotechnology Ltd	sc-236264
TRIFLUPROMAZINE HYDROCHLORIDE	Insight Biotechnology Ltd	sc-251335
LOBELINE HYDROCHLORIDE	Insight Biotechnology Ltd	sc-203114A
THONZONIUM BROMIDE	Insight Biotechnology Ltd	sc-396750
CLOPERASTINE HYDROCHLORIDE	Insight Biotechnology Ltd	sc-234405
CHLORHEXIDINE DIHYDROCHLORIDE	Insight Biotechnology Ltd	sc-203886
SODIUM PHENYLBUTYRATE	Insight Biotechnology Ltd	sc-200652
RESERPINE	Cambridge Bioscience Ltd	16474-1 g-CAY
METHYLENE BLUE	Scientific Laboratory Supplies Limited	CHE2584
IVERMECTIN	Sigma-Aldrich Co Ltd	I8898-250MG
THIOTHIXENE	Sigma-Aldrich Co Ltd	1665003-250MG
TRIMEPRAZINE TARTRATE	Sigma-Aldrich Co Ltd	1689001-200MG
CITALOPRAM HYDROBROMIDE	Sigma-Aldrich Co Ltd	PHR1640-1G
PENBUTOLOL SULFATE	Sigma-Aldrich Co Ltd	P0307000
FLUOXETINE	Sigma-Aldrich Co Ltd	F-918-1ML
BENZYL ISOTHIOCYANATE	Sigma-Aldrich Co Ltd	252492-5G
PROFLAVINE HEMISULFATE	Sigma-Aldrich Co Ltd	P2508-10G
THIRAM	Sigma-Aldrich Co Ltd	T24201-5G
AMSACRINE	Sigma-Aldrich Co Ltd	A9809-10MG
PERPHENAZINE	Sigma-Aldrich Co Ltd	P6402-1G
GENTIAN VIOLET	Sigma-Aldrich Co Ltd	48770-25G
EMETINE DIHYDROCHLORIDE	Sigma-Aldrich Co Ltd	E2375-500MG
THIMEROSAL	Sigma-Aldrich Co Ltd	30376-100MG
MERBROMIN (Mercury dibromofluorescin disodium)	Sigma-Aldrich Co Ltd	M7011-10G
METHYLBENZETHONIUM CHLORIDE	Sigma-Aldrich Co Ltd	M7379-10G
OUABAIN	Sigma-Aldrich Co Ltd	O3125-250MG
HEXACHLOROPHENE	Sigma-Aldrich Co Ltd	40323
PROGESTERONE	Sigma-Aldrich Co Ltd	P8783-1G
ARSENIC TRIOXIDE	Sigma-Aldrich Co Ltd	202673-5G
DESIPRAMINE HYDROCHLORIDE	Sigma-Aldrich Co Ltd	D3900-1G
DICHLOROPHEN	Sigma-Aldrich Co Ltd	133221-50G
MENADIONE	Sigma-Aldrich Co Ltd	M5750-25G
DIBUCAINE HYDROCHLORIDE	Sigma-Aldrich Co Ltd	D0638-1G

PRIDINOL METHANESULFONATE	Sigma-Aldrich Co Ltd	P4419-5G
BENZALKONIUM CHLORIDE	Sigma-Aldrich Co Ltd	12060-5G
CROTAMITON	Sigma-Aldrich Co Ltd	128201-5G
PYRIDOSTIGMINE BROMIDE	Sigma-Aldrich Co Ltd	P9797-1G
PENFLURIDOL	Stratech Scientific Ltd	S4151-SEL-50mg
SIROLIMUS	Stratech Scientific Ltd	S1039-SEL-5mg
CHLOROXYLENOL	Stratech Scientific Ltd	S4518-SEL-100mg

All buffers were made and all reactions were performed using autoclaved type 1+ 18.2 MΩ-cm deionised water from a PURELAB Ultra system (ELGA LabWater, Albania) unless otherwise specified.

2.6.2 Oligonucleotides

All oligonucleotides were synthesised by Integrated DNA Technologies (Leuven, Belgium) and are listed in the table below.

Application	**Description**	**Sequence 5' → 3'**
Cloning	Cloning TFEB-GFP into pPB-iCMV-MCS, SacII, forward	CTAGCCGCGGGCCACCATGGCGTCACGC
Cloning	Cloning TFEB-GFP into pPB-iCMV-MCS, NotI, reverse	CTAGGCGGCCGCTCACAGCACATCGCCC
Cloning	Cloing 3xHA-TFEB into pPB-iCMV-MCS, BglII, forward	AAAAAGATCGGCCACCATGTATCCTTATGATGTACCAG
Cloning	Cloing 3xHA-TFEB into pPB-iCMV-MCS, NotI, reverse	AAAAGCGGCCGCTCACAGCACATCGCCCTC
Cloning	Cloning 3xHA-GSK3β into pPB-iCMV-MCS, EcoRI, forward	GCTAGAATTCGCCACCATGTCAGGGCGGCCCAG
Cloning	Cloning 3xHA-GSK3β into pPB-iCMV-MCS, NotI, reverse	GCTAGCGGCCGCCTAGTTGGGACCACCCAAGCT
Cloning	Cloning human TFEB residues 1-159 into NLS-CARGO, AgeI, forward	CTAGACCGGTGCCACCATGGCGTCACGCATAGGGTTGCG
Cloning	Cloning human TFEB residues 1-159 into NLS-CARGO, AgeI, reverse	CTAGACCGGTATATCATCCAACTCCCTCTCAGGGTTGG
Site-directed mutagenesis	TFEB S138A mutagenesis forward	CCTCCGCTGGCAACGCTGCTCCCAATAGCC

Site-directed mutagenesis	TFEB S138A mutagenesis reverse	GGCTATTGGGAGCAGCGTTGCCAGCGGAGG
Site-directed mutagenesis	TFEB S142A mutagenesis forward	TGGCAACAGTGCTCCCAATGCCCCCATG
Site-directed mutagenesis	TFEB S142A mutagenesis reverse	GGCCATGGGGGCATTGGGAGCACTGTTG
Site-directed mutagenesis	TFEB M144A mutagenesis forward	GCTCCCAATAGCCCCGCGGCCATGCTGCACAT
Site-directed mutagenesis	TFEB M144A mutagenesis reverse	ATGTGCAGCATGGCCGCGGGGCTATTGGGAGC
Site-directed mutagenesis	TFEB M146A mutagenesis forward	CAATAGCCCCATGGCCGCGCTGCACATTGGCTCC
Site-directed mutagenesis	TFEB M146A mutagenesis reverse	GGAGCCAATGTGCAGCGCGGCCATGGGGCTATTG
Site-directed mutagenesis	TFEB L147A mutagenesis forward	GCCCCATGGCCATGGCGCACATTGGCTCCA
Site-directed mutagenesis	TFEB L147A mutagenesis reverse	TGGAGCCAATGTGCGCCATGGCCATGGGGC
Site-directed mutagenesis	TFEB I149A mutagenesis forward	CATGGCCATGCTGCACGCTGGCTCCAACCCTGAG
Site-directed mutagenesis	TFEB I149A mutagenesis reverse	CTCAGGGTTGGAGCCAGCGTGCAGCATGGCCATG
Site-directed mutagenesis	TFEB S211A mutagenesis forward	GTCACCAGCAGCGCCTGCCCTGCGG
Site-directed mutagenesis	TFEB S211A mutagenesis reverse	CCGCAGGGCAGGCGCTGCTGGTGAC
Site-directed mutagenesis	TFEB basic region (235-248) deletion, forward	GGCCAAGGAGCGGCAGTTCAACATCAATGACC
Site-directed mutagenesis	TFEB basic region (235-248) deletion, reverse	GGTCATTGATGTTGAACTGCCGCTCCTTGGCC
Site-directed mutagenesis	GSK3β S9A mutagenesis forward	GCCCAGAACCACCGCCTTTGCGGAGAG
Site-directed mutagenesis	GSK3β S9A mutagenesis forward	CTCTCCGCAAAGGCGGTGGTTCTGGC
qRT-PCR analysis	Human *TFEB* gene, forward	CAAGGCCAATGACCTGGAC
qRT-PCR analysis	Human *TFEB* gene, reverse	AGCTCCCTGGACTTTTGCAG
qRT-PCR analysis	Human *GAPDH* gene, forward	TGCACCACCAACTGCTTAGC
qRT-PCR analysis	Human *GAPDH* gene, reverse	TCTTCTGGGTGGCAGTGATG
qRT-PCR analysis	Human *CDKN1A* gene, forward	GGCAGACCAGCATGACAGATT
qRT-PCR analysis	Human *CDKN1A* gene, reverse	GCGGATTAGGGCTTCCTCTT

qRT-PCR analysis	Human *RRAGD* gene, forward	GTGACCAGGGCCTACAAAG
qRT-PCR analysis	Human *RRAGD* gene, reverse	TTTGCCCTCTGGTGAATATCT

2.6.3 Plasmids

The plasmids used in this study are listed in the table below.

Construct	**Notes**
pEGFP-C1-TFEB	From Addgene; GFP-tagged human TFEB
pEGFP-C1-TFEB(S211A)	Available in the laboratory; TFEB(S211A)-GFP
pEGFP-C1-TFEB(S142A)	Available in the laboratory; TFEB(S142A)-GFP
pEGFP-C1-NLS-GST	Available in the laboratory; GFP-NLS-GST cargo (NLS-CARGO)
pEGFP-C1-NLS-GST-NES	Available in the laboratory; NLS-CARGO with PKI NES (nlsCARGO-NES)
pEGFP-C1-NLS-GST-TFEB (1-159)	Available in the laboratory; NLS-CARGO with TFEB residues 1-159
pEGFP-C1-NLS-GST-TFEB (1-159) (S142A)	Available in the laboratory; TFEB (1-159) (S142A)-NLS-CARGO
pPB-iCMV-MCS	Available in the laboratory; PiggyBac vector with Tet-On inducible system
pPB-iCMV-3xHA	Prepared by the candidate; 3xHA in Tet-On with piggyBac transposon elements
pPB-iCMV-3xHA-TFEB	Prepared by the candidate; 3xHA-tagged TFEB in Tet-On with piggyBac transposon elements
pPB-iCMV-TFEB-GFP	Available in the laboratory; TFEB-GFP in Tet-On with piggyBac transposon elements
pPB-iCMV-TFEB(S138A) -GFP	Prepared by the candidate; TFEB (S138A)-GFP in Tet-On with PiggyBac transposon elements
pPB-iCMV-TFEB(S142A) -GFP	Prepared by the candidate; TFEB (S142A)-GFP in Tet-On with PiggyBac transposon elements
pPB-iCMV-TFEB(M144A) -GFP	Available in the laboratory; TFEB (M144A)-GFP in Tet-On with PiggyBac transposon elements
pPB-iCMV-TFEB(M146A) -GFP	Available in the laboratory; TFEB (M146A)-GFP in Tet-On with PiggyBac transposon elements
pPB-iCMV-TFEB(L147A) -GFP	Available in the laboratory; TFEB (L147A)-GFP in Tet-On with PiggyBac transposon elements
pPB-iCMV-TFEB(I149A) -GFP	Available in the laboratory; TFEB (I149A)-GFP in Tet-On with PiggyBac transposon elements
pPB-iCMV-TFEB(S211A) -GFP	Prepared by the candidate; TFEB (S211A)-GFP in Tet-On with PiggyBac transposon elements

pPB-iCMV-3xHA-GSK3β (S9A)	Prepared by the candidate; 3xHA-GSK3β (S9A) in Tet-On with PiggyBac transposon elements
pPB-iCMV-3xHA-GSK3β (K85A)	Prepared by the candidate; 3xHA-GSK3β (K85A) in Tet-On with PiggyBac transposon elements
pmCherry-C1-RanQ69L	Addgene plasmid #30309, a gift from Jay Brenman; mCherry-tagged Ran Q69L
pmCherry-LacR-NLS	Available in the laboratory, a gift from Nico Dantuma; mCherry-tagged LacR
pBABE-puro mCherry-EGFP-LC3B	Addgene plasmid #22418, a gift from Jayanta Debnath; Retroviral expression of mCherry, EGFP-tagged LC3B
pTRIP-shCN puro	Available in the laboratory; vector for lentiviral expression of control shRNA, puromycin selection
pTRIP-shTFEB2 puro	Available in the laboratory; vector for lentiviral expression of shRNA for TFEB, puromycin selection

2.6.4 Antibodies

The information of the antibodies used in this study are listed in the table below.

Antibody	**Immunogen**	**Source (Catalogue)**	**Dilution (Application)**
α-TFEB rabbit polyclonal	Region surrounding G412 of human TFEBd	Cell Signaling 4240	1:1000 (WB) 1:250 (IF)
α-TFE3 rabbit polyclonal	Transcription factor binding to ighm enhancer 3 recombinant protein epitope signature tag (PrEST)	Sigma-Aldrich HPA023881	1:5000 (WB)
α-actin (AC-40) mouse monoclonal	Synthetic actin C-terminal peptide Ser-Gly-Pro-Ser-Ile -Val-His-Arg-Lys-Cys-Phe, attached to a Multiple Antigen Peptide (MAP) backbone	Sigma-Aldrich A4700	1:1000 (WB)
α-HA (HA-7) mouse monoclonal	Residues 98-106 (YPYDVPDYA) of human Influenza virus hemagglutinin	Sigma-Aldrich H3663	1:500 (IF)
α-ERK (C-14) rabbit polyclonal	C-terminus of ERK2 of rat origin	Santa Cruz sc-154	1:10000 (WB)
α-GAPDH rabbit polyclonal	Residues 314-333	Sigma-Aldrich G9545	1:20000 (WB)
α-H3 rabbit polyclonal	Residue 100 to C-terminus	Abcam ab1791	1:2,000 (WB)
α-p70 S6 Kinase (C-18) rabbit polyclonal	C-terminus of p70 S6 kinase α of rat origin	Santa Cruz sc-230	1:1000 (WB)

α-S6 Ribosomal Protein (5G10) rabbit monoclonal	Residues of human S6 ribosomal protein	Cell Signaling 2217	1:1000 (WB)
α-phospho ERK1/2 (T202/Y204) rabbit polyclonal	Region surrounding T202/Y204	Cell Signaling 4377	1:1000 (WB)
α-phospho p70 S6 Kinase (T389) rabbit polyclonal	Region surrounding T389	Cell Signaling 9205	1:1000 (WB)
α-phospho-S6 Ribosomal Protein (Ser235/236) rabbit polyclonal	Residues surrounding Ser235 and Ser236 of human ribosomal protein S6	Cell Signaling 2211	1:1000 (WB)
α-phospho-AKT (Ser473) rabbit polyclonal	Residues surrounding Ser473 of mouse AKT	Cell Signaling 9271	1:2000 (WB)
α-Akt rabbit polyclonal	C-terminus of mouse AKT	Cell Signaling 9272	1:2000 (WB)
α-phospho-GSK3β (S9) rabbit polyclonal	Residues surrounding S9 of human GSK3β	Cell Signaling 9336	1:2000 (WB)
α-GSK3α/β (21A) mouse monoclonal	Full length *Xenopus laevis* GSK3	Life Technologies 44-610	1:2000 (WB)
α-phospho-β-Catenin (Ser33/37/Thr41) Rabbit Polyclonal	Synthetic phosphopeptide corresponding to residues surrounding Ser33, Ser37 and Thr41 of human β-catenin	Cell Signaling 9561	1:1000 (WB)
α-β-Catenin Clone 14 Mouse monoclonal	Mouse β-Catenin amino acids 571-781	BD Biosciences 610153	1:5000 (WB) 1:100 (IF)
α-RICTOR (7B3) mouse monoclonal	Full length RICTOR	Abnova MAB10313	1:1000(WB) 1:100 (IF)
α-phospho-IRS-1 (S302) rabbit polyclonal	Residues surrounding Ser302 of mouse IRS-1	Cell Signaling 2384	1:1000 (WB)
α-phospho-IRS-1 (S1101) rabbit polyclonal	Residues surrounding Ser1101 of human IRS-1	Cell Signaling 2385	1:1000 (WB)
α-IRS-1 rabbit polyclonal	C-terminal sequence of human IRS-1	Cell Signaling 2382	1:1000 (WB)
α-phospho-ULK1 (S757) rabbit polyclonal	Residues surrounding Ser757 of mouse ULK1	Cell Signaling 6888	1:1000 (WB)
α-ULK1 (D8H5) rabbit monoclonal	Residues surrounding Arg600 of human ULK1	Cell Signaling 8054	1:1000 (WB)
α-SGK1 rabbit polyclonal	Residues surrounding Gly420 of human SGK1	Cell Signaling 12103	1:1000 (WB)

α-LC3B rabbit polyclonal	Residues near the amino terminus of LC3B	Cell Signaling 2775	1:1000 (WB)
α-phospho-MITF (pSer130/73)/ phospho-TFEB (Ser142) Rabbit polyclonal	Synthesized peptide derived from human MITF around the phosphorylation site of Ser180/73	Sigma-Aldrich SAB4503940	1:5000 (WB)
Donkey anti-Rabbit IgG (H+L) Highly Cross-Adsorbed Secondary Antibody, Alexa Fluor 488	Rabbit gamma Immunoglobins Heavy and Light chains	Thermo Fisher Scientific A-21206	1:5000 (IF)
Donkey anti-Mouse IgG (H+L) Highly Cross-Adsorbed Secondary Antibody, Alexa Fluor 546	Mouse Gamma Immunoglobin	Thermo Fisher Scientific A10036	1:5000 (IF)

2.6.5 siRNA

The information of the siRNAs used in this study are listed in the table below.

siRNA	**Sequence 5' → 3'**	**Source (Catalogue)**
TFEB siRNA pool	CUACAUCAAUCCUGAAAUG; AGACGAAGGUUCAACAUCA; CAAGUUUGCUGCCCACAUC; CGGGAGUACCUGUCCGAGA.	Dharmacon M-009798-02-0005
Hs_TFEB siRNA	GGUUCAACAUCAAUGACCGtt	Thermal Fisher Scientific AM16708, 6616
Hs_TFE3 siRNA #1	TCGCAGGCGATTCAACATTAA	QIAGEN, SI00089285
Hs_TFE3 siRNA #2	TCCGGGATTGTTGCTGACATA	QIAGEN, SI00089292
Hs_TFE3 siRNA #3	CAGCTCCGAATTCAGGAACTA	QIAGEN, SI00089299
Hs_TFE3 siRNA #4	AAGGAGATTGATGATGTCATT	QIAGEN, SI00089306
Hs_RICTOR siRNA #1	GUAGUUCAGUUUCAACUAAtt	Thermal Fisher Scientific 4392420, s226000
Hs_RICTOR siRNA #2	GCACUUACUACUUACCGGAtt	Thermal Fisher Scientific 4392420, s48408
Hs_RICTOR siRNA #3	GGAGUACUUUGCAUACCAAtt	Thermal Fisher 4392420, s48410
Negative Control siRNA	Scrambled	QIAGEN SI03650318

Chapter 3 – TFEB subcellular localisation is regulated by nutrient availability through nuclear export

3.1 Introduction

In the last decade, TFEB has emerged as the master regulator of lysosomal biogenesis and autophagy (Sardiello et al., 2009; Settembre et al., 2011). It is also involved in lipid metabolism (Settembre et al., 2013), glucose metabolism, mitochondrial biogenesis (Mansueto et al., 2017), integrated stress response (Martina et al., 2016) as well as the immune response (Pastore et al., 2016; Samie and Cresswell, 2015). Studies on the regulation of TFEB established that under normal nutrient rich conditions, TFEB undergoes phosphorylation by kinases such as MAP4K3 and mTORC1 on the lysosomal surface followed by cytoplasmic sequestration, thus remains inactive in the cytoplasm (Hsu et al., 2018; Martina et al., 2012; Roczniak-Ferguson et al., 2012; Settembre et al., 2012). In contrast, conditions such as amino acid starvation, oxidative stress, ER stress, muscle exercise or the presence of the bacterial antigen LPS lead to TFEB nuclear translocation and transcriptional activation after its dephosphorylation mediated by phosphatases including Calcineurin and PP2A (Martina and Puertollano, 2018; Medina et al., 2015).

Although most studies used overexpression to investigate the regulation and functions of TFEB in cultured cell lines, endogenous TFEB or its related factor TFE3 in vivo was not thoroughly examined with the exception being in PDAC and osteoclasts (Ferron et al., 2013; Perera et al., 2015). Amino acid limitation has been intensively used to study the mechanism of starvation induced TFEB nuclear translocation. However, the effect of limitation of other nutrients such as glucose was rarely noted. A previous study used small-molecule drugs to demonstrate that the phosphorylation of TFEB at S138 by GSK3β is important for nuclear translocation and activation of TFEB (Li et al., 2016), but the proposed model had several

discrepancies to the data generated in our laboratory. How TFEB phosphorylation by GSK3β is regulated under physiological conditions is another issue.

This chapter will firstly address the physiological relevance of TFEB by examining its expression in cancers using data acquired from multiple platforms. Then TFEB nuclear translocation by nutrient limitation will be closely examined using various conditions, particularly glucose starvation. We will attempt to dissect the cellular signalling events under glucose limitation and try to establish the connection to TFEB regulation. Finally, a new mechanism will be proposed with regard to the highly dynamic spatial distribution of TFEB and how glucose plays a part.

3.2 Results

3.2.1 TFEB/3 expression in different cancer origins and cell types

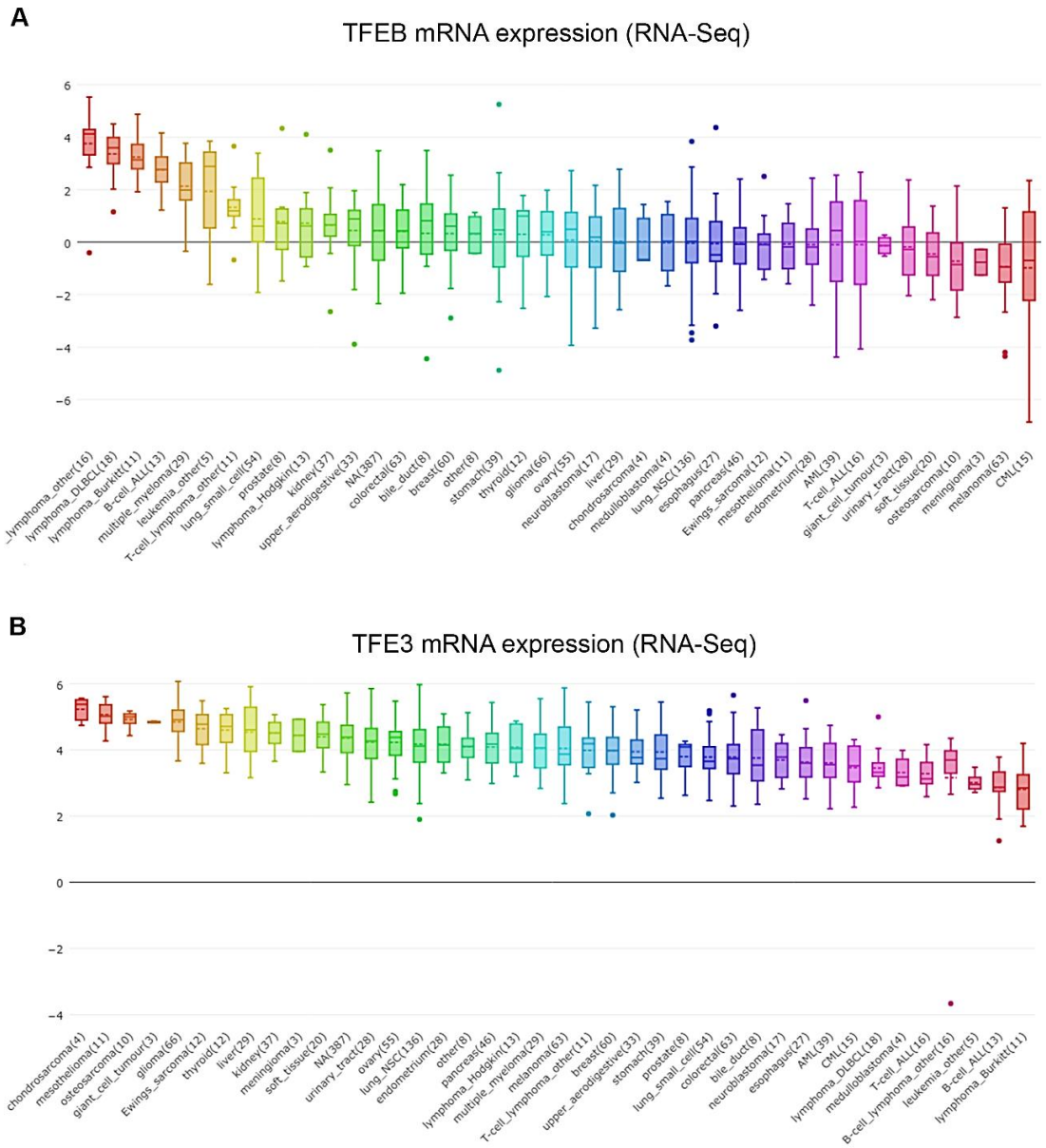


Figure 3.2.1.1 mRNA expression profile of TFEB (A) and TFE3 (B) in different cancer cell lines generated using RNA-Seq data from CCLE. The box plot is sorted and coloured by average distribution of a gene's expression (displayed as Transcripts Per Kilobase per Million (TPM) in log2 scale) in a lineage. Lineages are composed of a number of cell lines from the same area or system of the body. The number next to the lineage name indicates how many cell lines are in the lineage. The highest average distribution is on the left and is colored red. The dashed line within a box is the mean.

Previous studies on TFEB regulation either relied on ectopic overexpression of TFEB or focused on endogenous TFEB only in limited cell lines. However, the expression of TFEB or TFE3 across different tissue types or cell lineages was not addressed. Using the online database Cancer Cell Line Encyclopedia (CCLE, https://portals.broadinstitute.org/ccle), the relative mRNA expression profile generated from RNA-seq data for TFEB and TFE3 genes was visualised. For TFEB, the lymphoma and myeloid leukemia cell lines displayed the highest expression, followed by small-cell lung, prostate, kidney cancer cell lines and the ones originated from the upper aerodigestive tract. The tissue origins that exhibit intermediate levels of TFEB expression include breast, ovary, liver, and the digestive tract such as colorectal, bile duct and stomach, as well as brain tumours such as neuroblastoma, glioma and medulloblastoma. Chronic myeloid leukemia, melanoma, meningioma and osteosarcoma are among the cancer cell types with the lowest TFEB mRNA expression (**Figure 3.2.1.1 A**). In contrast, the mRNA expression of TFE3 is more evenly distributed across all cancer cell types, and the relative levels are high with no exception. Interestingly, cell lines with the highest TFEB mRNA expression display the lowest TFE3 mRNA levels, including Burkitt lymphoma, T-cell, B-cell lymphomas and leukemia (**Figure 3.2.1.1 B**).

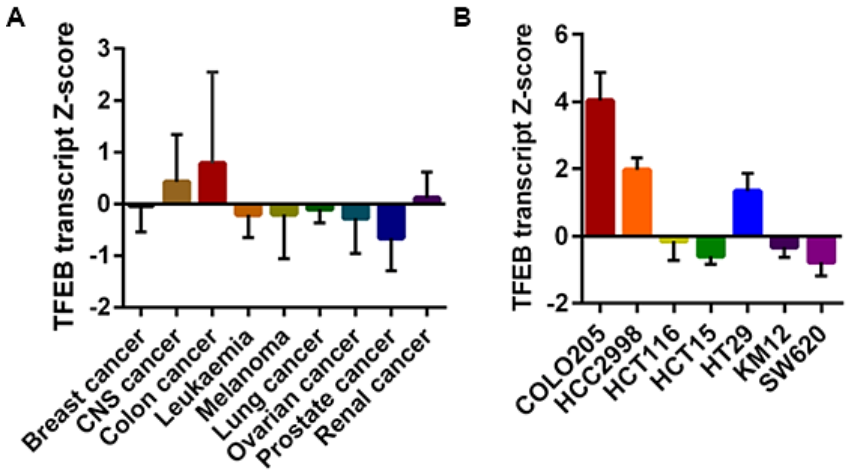


Figure 3.2.1.2 mRNA expression of TFEB in NCI-60 cancer cell lines. (**A)** Transcript Z-score of TFEB in different cancer cell types, graph generated using microarray data of NCI-60 cancer cell lines. (**B)** Transcript Z-score of TFEB in colorectal cancer cell lines, graph generated using microarray data of NCI-60 cancer cell lines.

To gain further information on TFEB expression in readily accessible NCI-60 cancer cell lines, another online database, CellMiner (https://discover.nci.nih.gov/cellminer/), was used to obtain mRNA transcript probe data from five microarray platforms. The relative expression of TFEB was determined by gene transcript Z-score averages for TFEB probe measurements in microarray datasets in different cancer types. Z-score is a mathematical transformation that subtracts the mean and divides by the standard deviation for each probe measurement of a certain microarray dataset. Colon cancer displayed the highest average TFEB mRNA expression, followed by central nervous system (CNS) cancer, while prostate cancer showed the lowest (**Figure 3.2.1.2 A**). Among the colon cancer cell lines, TFEB mRNA expression was the highest in COLO205, possibly due to a copy number variation that resulted in 12 copies of TFEB gene in this cell line. HCC2998 and HT29 cell lines displayed similarly high TFEB transcript Z scores compared to the other colon cell lines. SW620, HCT115, KM12 and HCT116 cell lines displayed negative transcript Z scores, indicating that TFEB mRNA levels of these cell lines are below the average among all samples assessed (**Figure 3.2.1.2 B**).

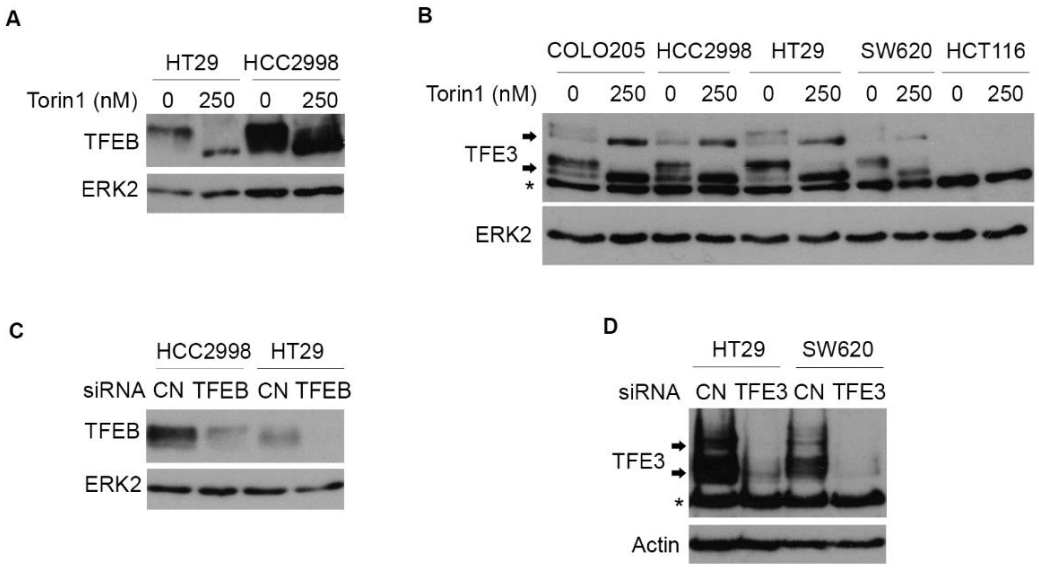


Figure 3.2.1.3 Protein expression of TFEB and TFE3 in colorectal cancer cell lines. (**A**) Immunoblotting of whole cell lysates of HT29 and HCC2998 cell lines with or without Torin 1 (250 nM, 1 h) treatment using an antibody against TFEB and an antibody against ERK2. (**B**) Immunoblotting of whole cell lysates of COLO205, HCC2998, HT29, SW620 and HCT116 cell lines with or without Torin 1 (250 nM, 1 h) treatment using an antibody against TFE3 and an antibody against ERK2. (**C**) Immunoblotting of whole cell lysates of HCC2998 and HT29 cell lines transiently transfected with control siRNA or a siRNA against TFEB, using an antibody against TFEB and an antibody against ERK2. (**D**) Immunoblotting of whole cell lysates of HCC2998 and HT29 cell lines transiently transfected with control siRNA or a siRNA against TFE3, using an antibody against TFE3 and an antibody against ACTIN. ERK2 and ACTIN were used as loading controls. Arrows indicate TFE3 protein variants, asterisks indicate nonspecific bands.

Colorectal cancer cell lines HT29 and HCC2998 which have relatively high levels of TFEB mRNA expression were used for detection of TFEB protein levels by immunoblotting. Consistent with transcript Z score (**Figure 3.2.1.3 B**), HCC2998 cells displayed higher level of TFEB protein than HT29 cells. Since TFEB is phosphorylated by mTORC1 at multiple sites, the treatment of Torin 1, a selective mTOR inhibitor, resulted in a faster migration species of bands detected in both HT29 and HCC2998 cell lines (**Figure 3.2.1.3 A**). Using a small

interfering RNA (siRNA) pool specifically targeting endogenous TFEB gene transcript, TFEB protein was partially reduced in HCC2998 cells and strongly diminished in HT29 cells (**Figure 3.2.1.3 C**), confirming that the antibody was specific for endogenous TFEB. By contrast, immunoblotting using TFE3 antibody revealed similar expression levels of TFE3 protein in colorectal cancer cell lines COLO205, HCC2998, HT29 and SW620, and that TFE3 bands comprised of four species: the top bands, the upper middle bands, the lower middle bands and the bottom band (**Figure 3.2.1.3 B**). Since the HCT116 cell line harbours a TFE3 null mutation, the presence of the bottom band indicates that it can only be a non-specific band recognised by the TFE3 antibody, which was confirmed by a knockdown experiment using a siRNA pool against TFE3 gene in HT29 and SW620 cells that silenced the top three species but retained the bottom band (**Figure 3.2.1.3 D**). Similarly, Torin 1 treatment resulted in a mobility shift of the upper middle bands of TFE3 toward the lower middle bands, as well as a condensed top band, presumably due to post translational modifications such as ubiquitylation or SUMOylation (**Figure 3.2.1.3 B**).

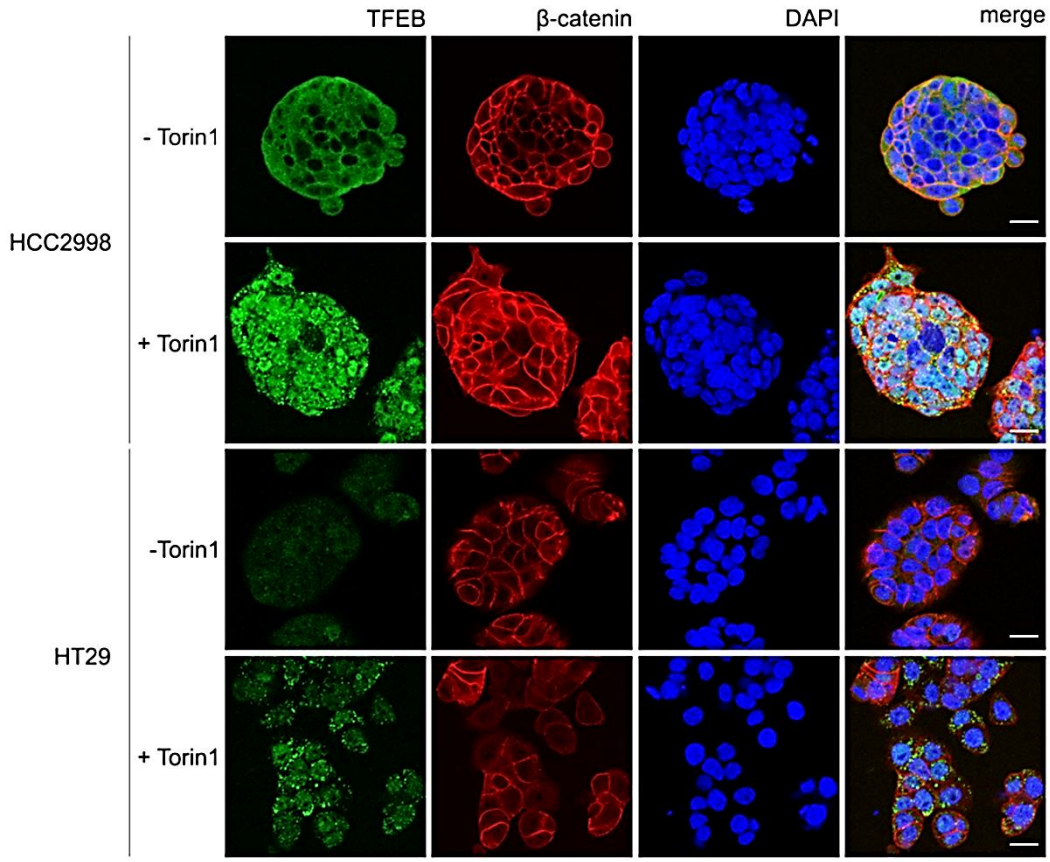


Figure 3.2.1.4 Endogenous TFEB in HCC2998 and HT29 cell lines. HCC2998 and HT29 cells were treated with or without Torin 1 (250 nM, 1 h) and subject to immunofluorescent microscopy using an antibody against TFEB. β-Catenin antibody was used to stain the cell periphery, DAPI was used to stain the nuclei of the cells. Scale bars = 20 μm.

Since the TFEB antibody exhibited fairly good specificity by immunoblotting, an immunofluorescent microscopy experiment was performed to observe the subcellular localisation of TFEB. In HCC2998 cells, TFEB staining was mainly observed in the cytoplasm but became rapidly accumulated in the nuclei when treated with Torin 1 (**Figure 3.2.1.4** upper panels). In HT29 cells, TFEB staining was fainter as its protein levels were lower compared to HCC2998 cells. Nevertheless, Torin 1 treatment also resulted in TFEB nuclear accumulation in

HT29 cells, although to a lesser extent of HCC2998 (**Figure 3.2.1.4** lower panels), confirming that mTOR inhibition indeed causes TFEB nuclear translocation. Notably, Torin 1 treatment not only increased the nuclear localisation of TFEB, but also increased its lysosomal localisation as described in literature (Martina and Puertollano, 2013) and confirmed later by co-staining with the lysosomal marker LAMP2 (**Figure 3.2.9.2**). Unfortunately, due to the incomplete specificity of the TFE3 antibody, immunofluorescent staining for TFE3 was not successful in the colorectal cancer cell lines tested above.

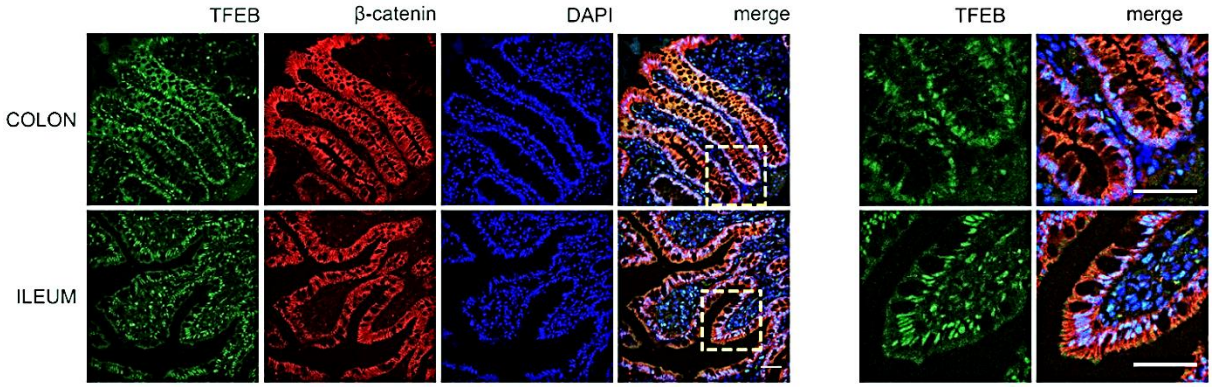


Figure 3.2.1.5 TFEB expression in normal human colon and ileum. Normal human colon and ileum frozen sections were immuno-stained using anti-TFEB antibody. β-Catenin was stained for cell periphery and DAPI was used to stain the nuclei of the cells. Scale bars = 50 µm.

Normal human colon and ileum frozen sections derived from patients were immuno-stained to check for the subcellular localisation of TFEB. TFEB staining was observed throughout the crypts of the colon and the epithelium of the ileum. In contrast to immunofluorescent staining in cell lines, TFEB exhibited exclusively nuclear localisation as co-stained with DAPI in both colon and ileum (**Figure 3.2.1.5**), suggesting that either

physiologically TFEB constantly undergoes nuclear translocation in response to the fluctuation of nutrients or the tissue processing may have introduced artificial conditions.

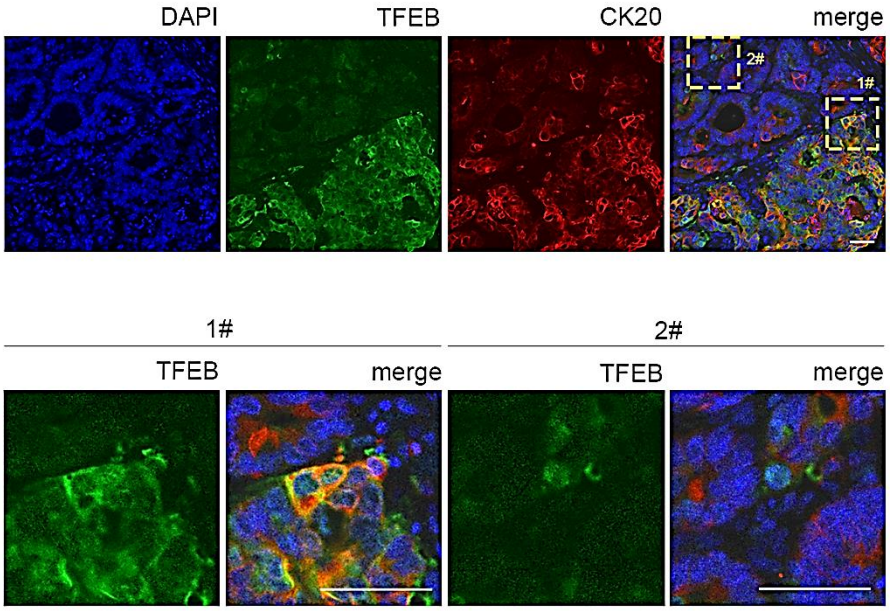


Figure 3.2.1.6 TFEB expression in colorectal adenocarcinoma. Paraffin-embedded human colorectal adenocarcinoma section was immuno-stained for endogenous TFEB using an antibody against TFEB. An antibody against CK20 was used to stain the colorectal tumour cells. DAPI was used to stain the nuclei of the cells. Scale bars = 50 μm.

In order to check whether TFEB subcellular localisation in cultured colorectal cancer cell lines was in consistency with that under physiological conditions, paraffin embedded human colorectal adenocarcinoma samples were co-stained for TFEB and the colorectal tumour marker cytokeratin 20 (CK20). Unexpectedly, in an area where the tumour cells intensively marked by CK20 confronted the normal cells which formed the glandular structures as indicated by their nuclei, TFEB was expressed at much higher levels in the tumour than in the normal region (**Figure 3.2.1.6** upper panel). Unlike the normal colon or ileum frozen sections, the tumour sample exhibited mostly cytoplasmic TFEB staining in the tumour but less clearly in the normal region (**Figure 3.2.1.6** lower panel). Despite the limited accessible samples, this

result suggests that TFEB subcellular localisation in physiological conditions may be similar to that of cultured cell lines. However, the sample processing may bring in variations such as starvation and difficulty in antigen retrieval, and without additional controls the interpretation of the staining patterns should be tentative.

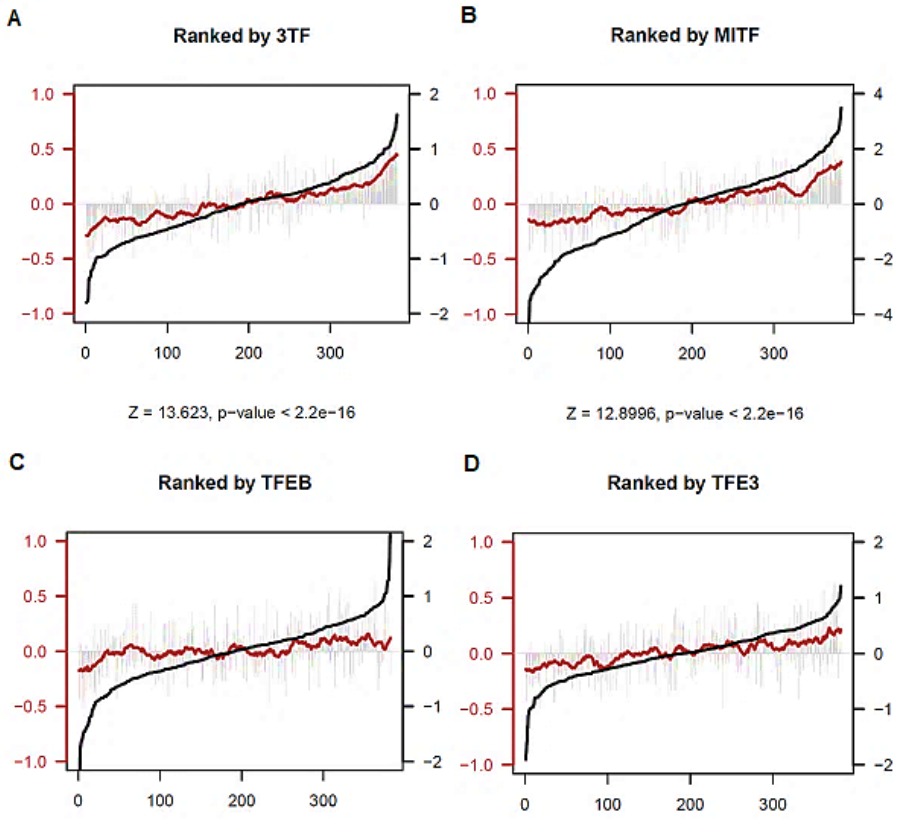


Figure 3.2.1.7 Gene signature analysis of TCGA human colorectal tumours. Tumour samples were analysed for the correlation between the expression of MITF (**B**), TFEB (**C**), TFE3 (**D**) or all the three transcription factors (**A**) and the lysosomal and autophagic gene expression signatures. The black line indicates TCGA colorectal tumour samples ranked by the expression of indicated factors. Vertical grey lines indicate the average lysosomal/autophagic gene expression signatures in each sample. The red line indicates the moving average of lysosomal/autophagic gene expression signatures across colorectal tumour samples analysed. (Analysed by Jagat Chauhan)

The observation that TFEB expression was elevated in colorectal adenocarcinoma led us to perform a gene expression signature analysis. Using mRNA expression data of colorectal

tumours from TCGA (The Cancer Genome Atlas), the samples were analysed for the expression of TFEB, TFE3, the related family member MITF, or the combination of the three transcription factors (3TF). The analysis demonstrated a highly significant correlation between the lysosomal/autophagic gene signature and the expression of the three transcription factors together or each alone (**Figure 3.2.1.7**). This analysis supported the role of the MITF/TFE family in lysosomal biogenesis and autophagy in the context of colorectal cancer. Although the elevation of TFEB expression may not necessarily be a feature of all the colorectal tumours, the enhanced lysosomal and autophagic functions could be beneficial for cancer cell survival, similar to that in pancreatic adenocarcinoma cells (Perera et al., 2015).

3.2.2 TFEB nuclear translocation is regulated by amino acid and glucose levels

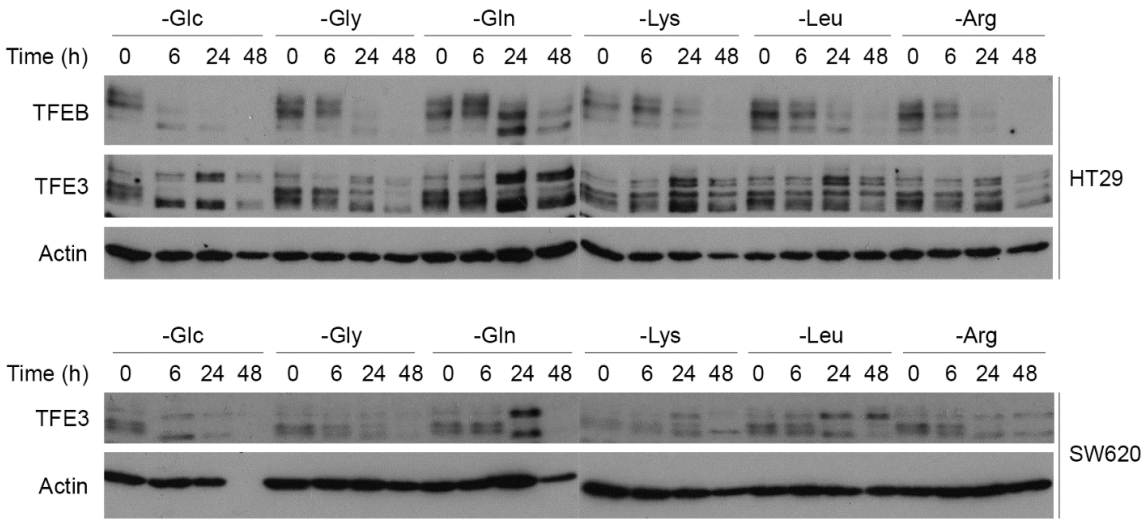


Figure 3.2.2.1 TFEB and TFE3 protein mobility shift was regulated by glucose and single amino acid levels. Endogenous TFEB and TFE3 were detected by immunoblotting of the whole cell lysates of HT29 (top) and SW620 (bottom) cell lines treated with indicated conditions using anti-TFEB, anti-TFE3 and anti-ACTIN antibodies.

Previous studies on the regulation of TFEB subcellular localisation used conditions as harsh as complete amino acid depletion, serum starvation or mTORC1 inhibition. To assess the

effects of single amino acid limitation or glucose depletion, the culture medium was customised by supplementing appropriate amino acids to Minimum Essential Medium (MEM, Thermo Fisher Scientific) lacking glutamine, glycine and serine, DMEM lacking glucose or DMEM lacking lysine, leucine and arginine (Sigma-Aldrich). HT29 cells or SW620 cells were incubated in glucose- or single amino acid-depleted medium for a duration of 48 hours. In HT29 cells, TFEB and TFE3 protein underwent a mobility shift on immunoblotting from 6 hours when the medium was deprived of glucose, indicating dephosphorylation of the two proteins and likely nuclear translocation. TFEB levels were dramatically decreased after 24 hours of glucose starvation, but TFE3 levels were slightly increased at 24 hours (**Figure 3.2.2.1** upper panel). Glycine depletion resulted in decreased levels of TFEB at 24 hours and 48 hours and that of TFE3 at 48 hours, while this condition did not induce an obvious mobility shift or dephosphorylation of either protein (**Figure 3.2.2.1** upper panel). Glutamine starvation had no effect on either protein at 6 hours, but induced a mobility shift of both TFEB and TFE3 at 24 hours and 48 hours and caused decreased TFEB levels at 48 hours (**Figure 3.2.2.1** upper panel). Lysine, leucine or arginine deprivation, on the other hand, had little effect on mobility shift of the two proteins, while these conditions similarly decreased TFEB protein levels from 6 hours until it almost disappeared at 48 hours (**Figure 3.2.2.1** upper panel).

In SW620 cells, TFEB was not detectable, but TFE3 immunoblotting displayed a similar pattern to that in HT29 cells. Glucose starvation induced TFE3 mobility shift at 6 hours and 24 hours and killed all the cells by 48 hours (**Figure 3.2.2.1** lower panel). Glycine depletion resulted in no noticeable change on TFE3 immunoblotting except for a minor decrease of levels at 48 hours (**Figure 3.2.2.1** lower panel). Glutamine deprivation had no effect on TFE3 at 6 hours but induced its mobility shift, but a relatively stronger upper band appeared at 24 hours,

while most of the cells died by 48 hours as indicated by the decreased Actin level (**Figure 3.2.2.1** lower panel). Since the Actin protein levels at 24 hours and 48 hours differ from those at 0 h and 6 hours (**Figure 3.2.2.1** lower panel), the relative protein levels of TFE3 under glutamine starvation remain to be thoroughly assessed. In contrast to HT29 cells, lysine, leucine or arginine depletion caused a mobility shift of TFE3 protein at 24 hours and 48 hours, with the upper band being more pronounced in leucine-deprived condition (**Figure 3.2.2.1** lower panel). Interestingly, glutamine starvation in both HT29 and SW620 cells induced a strong top band similar to that observed under leucine starvation in SW620 cells, possibly due to a high molecular weight post-translational modification that has yet to be determined.

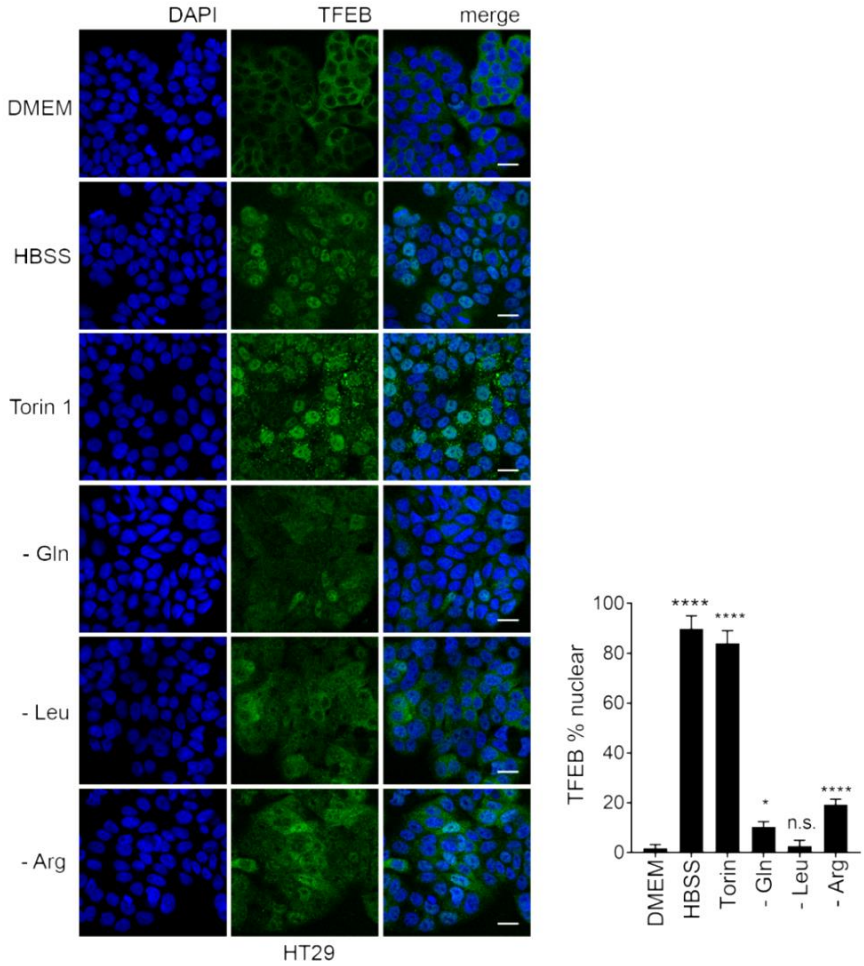


Figure 3.2.2.2 TFEB subcellular localisation is regulated by amino acid levels. *Legend continues at the bottom of next page.*

Glutamine, leucine and arginine are the three known amino acids that stimulate mTORC1 kinase activity, and the phosphorylation by mTORC1 is important for TFEB subcellular localisation and activity. If the withdrawal of these amino acids was sufficient to inactivate mTORC1, it should also promote TFEB nuclear translocation. However, the immunoblotting result suggests that TFEB did not undergo dephosphorylation under leucine or arginine depletion, except for glutamine starvation. Therefore, an immunofluorescent microscopy experiment was performed to investigate TFEB subcellular localisation under these conditions. In fully fed culture medium, DMEM, TFEB protein was exclusively localised in the cytoplasm. Whereas in HBSS (Hank's Balanced Salt Solution, Thermo Fisher Scientific), a medium that contains glucose but lacks any amino acid, or when treated with the mTOR inhibitor Torin 1, 80 % to 90 % cells displayed nuclear TFEB staining by 1 hour. This suggests that TFEB nuclear translocation happens rapidly following complete amino acid starvation or mTOR inhibition.

Even though on immunoblotting glutamine starvation induced a considerable mobility shift of TFEB at 24 hours (**Figure 3.2.2.1**), by immunofluorescent imaging only 10 % cells underwent TFEB nuclear translocation (**Figure 3.2.2.2**). The effect of arginine starvation was slightly higher (**Figure 3.2.2.2**), but around 20 % cells with TFEB nuclear staining at 24 hours was not comparable to HBSS or Torin 1 treatment at 1 hour, nor did it cause detectable TFEB

Figure 3.2.2.2 TFEB subcellular localisation is regulated by amino acid levels. Endogenous TFEB was immuno-stained with an antibody and imaged by fluorescent microscopy using HT29 cells in normal DMEM, treated with complete amino acid starvation using HBSS, Torin (250 nM, 1 h), or treated with medium lacking glutamine (-Gln), leucine (-Leu) or arginine (-Arg) for 24 h. DAPI was used to stain the nuclei of the cells (left). The percentage of cells with TFEB nuclear localisation was quantified (right). $n > 40$ cells per condition. Scale bars = 20 μm. Student's *t*-test: ****$P < 0.0001$, *$P < 0.05$, n.s.: not significant. Error bars represent standard deviation (SD).

dephosphorylation shown by immunoblotting (**Figure 3.2.2.1**). Leucine starvation did not induce either dephosphorylation or nuclear translocation of TFEB by 24 hours (**Figure 3.2.2.1** and **Figure 3.2.2.2**). Overall, depletion of single amino acid was very inefficient in inducing TFEB nuclear entry, even though they are reported to contribute to mTORC1 activation. This result suggests that regulation of TFEB by amino acids and mTORC1 is more complicated than the field might have expected.

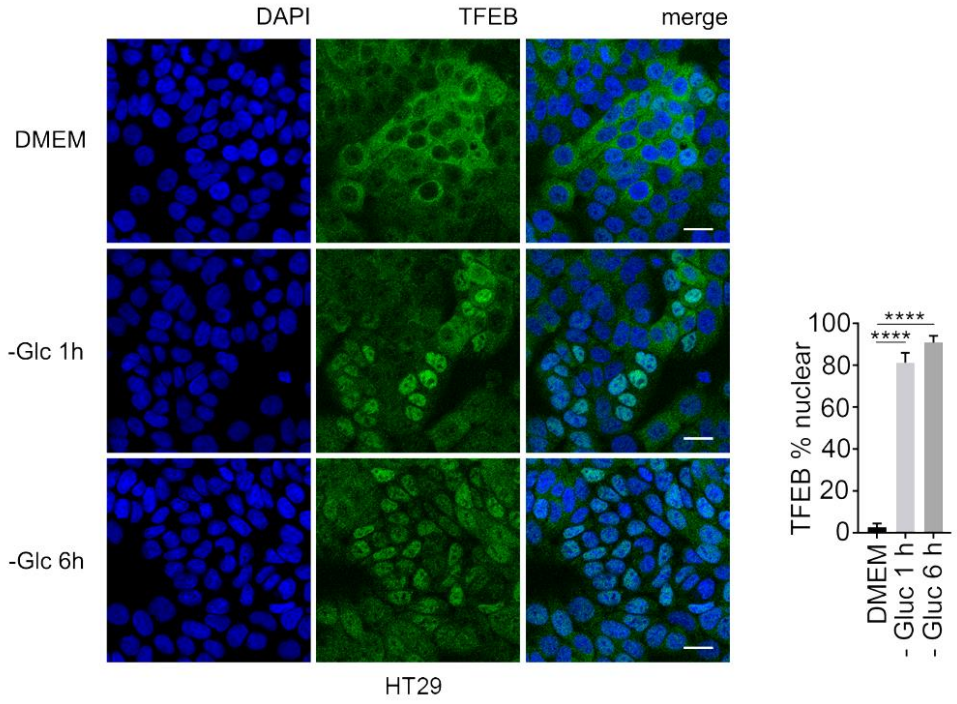


Figure 3.2.2.3 TFEB subcellular localisation is regulated by glucose levels. Endogenous TFEB was immuno-stained and imaged by fluorescent microscopy using HT29 cells in normal DMEM or glucose depleted medium (-Glc) for 1 h or 6 h (left). DAPI was used to stain the nuclei of the cells. $n > 100$ cells per condition. Scale bars = 20 µm. Student's *t*-test: ****$P < 0.0001$. Error bars = SD. (Re-use of published data from Li et al., 2018)

One interesting observation was that glucose starvation alone induced the mobility shift and presumably dephosphorylation of both TFEB and TFE3 (**Figure 3.2.2.1**). Although a

similar result was observed in MEF cells (Peña-Llopis et al., 2011), no further study on TFEB regulation by glucose has been published. Using the same immunofluorescent imaging approach, HT29 cells displayed strong cytoplasmic staining of TFEB in nutrient rich DMEM. When incubated in DMEM lacking glucose, around 80 % cells showed nuclear staining of TFEB at 1 hour, and around 90 % cells at 6 hours (**Figure 3.2.2.3**), indicating that glucose starvation indeed induces TFEB nuclear translocation. Note that this effect was much more pronounced than the depletion of single amino acids which are stimulators of mTORC1.

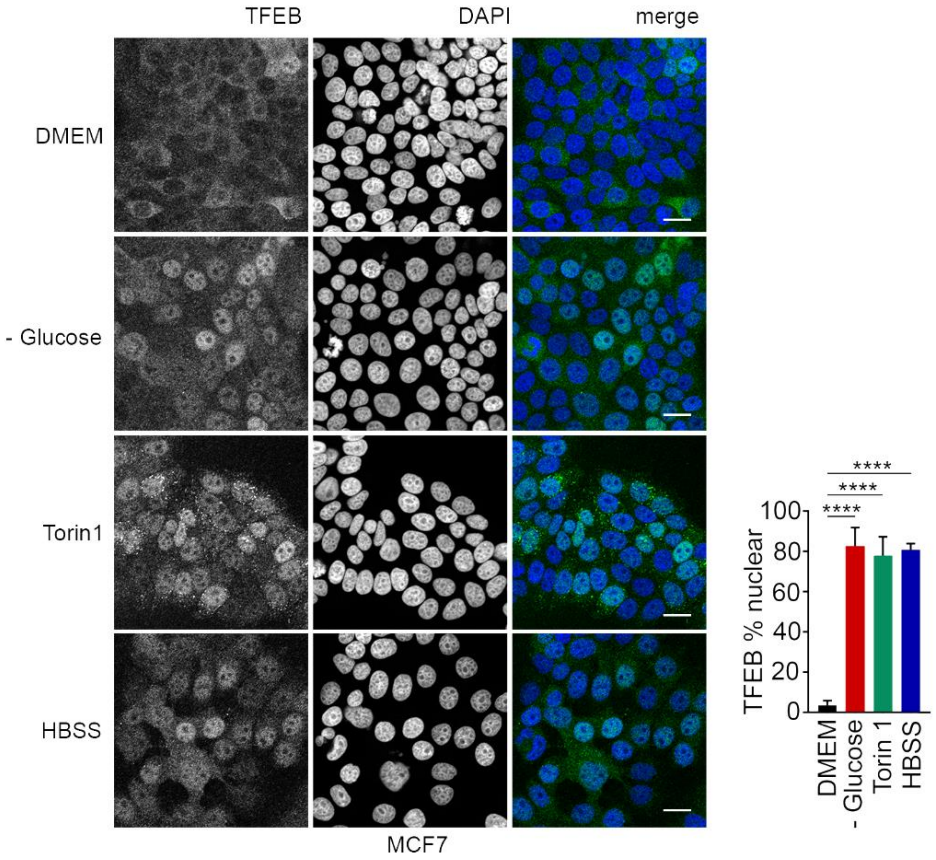


Figure 3.2.2.4 TFEB nuclear translocation is regulated by both glucose and amino acid levels. Endogenous TFEB was immuno-stained and imaged by fluorescent microscopy using MCF7 cells grown in normal DMEM, glucose depleted medium for 1 h, treated with Torin 1 (250 nM, 1 h) or HBSS for 1 h. DAPI was used to stain the nuclei of the cells. $n > 30$ cells per condition. Scale bars = 20 µm. Student's *t*-test: ****$P < 0.0001$. Error bars = SD. (Re-use of published data from Li et al., 2018)

To assess whether the effect of glucose on TFEB nuclear localisation was cell line- or tissue-specific, a human breast cancer cell line MCF7 was used for the immunofluorescent microscopy experiment. Similarly, TFEB was mainly localised in the cytoplasm in complete medium and accumulated quickly in the nucleus when treated with glucose-depleted medium (**Figure 3.2.2.4**). Torin 1 treatment and HBSS incubation resulted in similar nuclear translocation of TFEB (**Figure 3.2.2.4**), suggesting that TFEB localisation is indeed regulated by both amino acids and glucose in more than one cell line or tissue type.

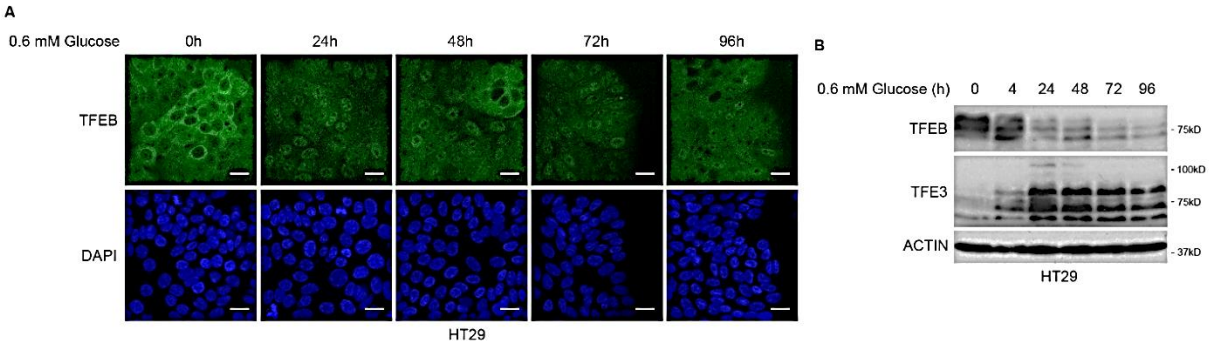


Figure 3.2.2.5 TFEB nuclear translocation is induced by low glucose levels. (**A**) Endogenous TFEB was immuno-stained and imaged by fluorescent microscopy using HT29 cells grown in normal DMEM or medium containing 0.6 mM glucose for indicated duration. DAPI was used to stain the nuclei of the cells. Scale bars = 20 μm. (**B**) Immunoblotting of HT29 cells grown in medium containing 0.6 mM glucose for indicated duration using anti-TFEB, anti-TFE3 and anti-ACTIN antibodies.

The glucose concentration in human blood stream is normally around 5 mM (compared to 25 mM in DMEM), while in solid tumours it is often much less due to its consumption by proliferating cancer cells and sometimes poor vascularisation. To examine the effect of glucose limitation on TFEB subcellular localisation under conditions mimicking the tumour microenvironment, D-glucose was added to DMEM with no glucose to obtain a concentration of 0.6 mM, as it is the concentration measured in solid tumours (Gullino et al., 1964; Ho et al.,

2015). Immunofluorescent imaging demonstrated increased TFEB nuclear localisation from 24 hours to 96 hours in the medium containing 0.6 mM glucose (**Figure 3.2.2.5 A**), despite that less of a mobility shift in TFEB was induced compared to complete glucose deprivation (**Figure 3.2.2.5 B**). 0.6 mM glucose also decreased TFEB protein levels, shown both by the decrease in its fluorescent intensity and by immunoblotting from 24 hours to 96 hours (**Figure 3.2.2.5 A**). Interestingly, TFE3 protein levels displayed a pattern which inversely correlated with that of TFEB for the duration of the incubation (**Figure 3.2.2.5 B**). Although it remains to be investigated why TFEB levels decrease while TFE3 levels increase under glucose limitation, the result suggests that TFEB subcellular localisation, and presumably transcriptional activity, is sensitive to physiological glucose levels. This is particularly important, as in tumours where glucose is often limited, TFEB may be responsive to the fluctuation of glucose availability and may activate the transcription of a wide range of genes to promote cancer cell survival.

3.2.3 TFEB transcriptional activity is induced by glucose deprivation

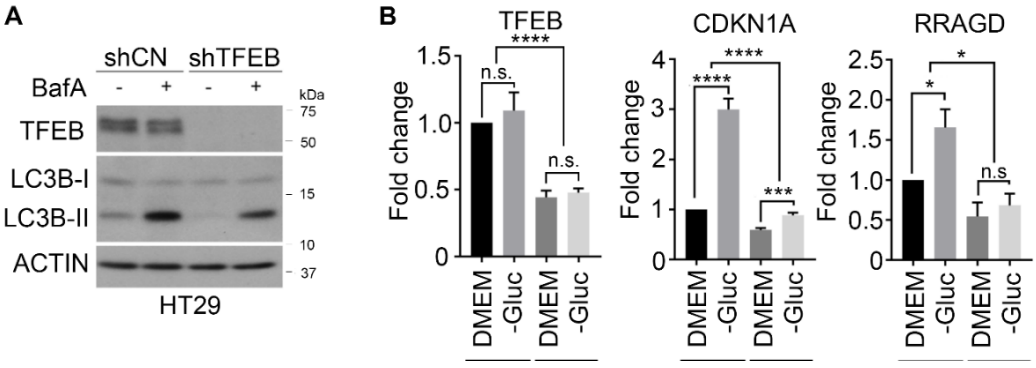


Figure 3.2.3 Glucose deprivation activates TFEB-dependent gene transcription of CDKN1A and RRAGD. (**A**) Immunoblotting of HT29 cells expressing control shRNA or shTFEB in the absence or presence of Bafilomycin A (10 nM, 2 h) using anti-TFEB, anti-LC3B and anti-ACTIN antibodies. (**B**) Quantitative real time PCR of *TFEB*, *CDKN1A* and *RRAGD* mRNAs from control or shTFEB cells grown in normal DMEM or glucose depleted medium for 3 h. Two-way ANOVA: ****$P < 0.0001$, ***$P < 0.001$, *$P < 0.05$, n.s. not significant. Error bars = SD. (Re-use of published data from Li et al., 2018)

As a transcription factor, the nuclear translocation of TFEB in response to starvation is the prerequisite to its transcriptional activity. To examine the effect of glucose limitation on TFEB-dependent gene transcription, a polyclonal TFEB knockdown cell line was generated using lentiviral transduction of short hairpin RNA targeting TFEB gene (shTFEB). In addition, another shRNA containing a scrambled targeting sequence was used as a control for the infection and the stable knockdown (shCN). Shown by immunoblotting, shTFEB effectively reduced endogenous TFEB protein levels compared to shCN in HT29 cells. The introduction of shTFEB also decreased LC3B-II levels, an autophagy marker which is known to controlled by TFEB, in the absence and presence of bafilomycin A (BafA) which blocks the turnover of autophagosomes by the lysosomes, indicating a reduced autophagic flux in shTFEB cells (**Figure 3.2.3 A**). In order to assess the mRNA expression of TFEB target genes under glucose starvation, a quantitative real time PCR (qRT-PCR) experiment was performed. shTFEB reduced *TFEB* mRNA levels by 50% under both nutrient rich and glucose depleted conditions, confirmed by using primers against *TFEB* gene transcript (**Figure 3.2.3 B**).

Given that glucose starvation may differ from amino acid starvation in terms of the target selectivity of TFEB, a well-characterised MITF target gene, *CDKN1A*, which encodes the cell cycle inhibitor p21 and has two canonical E-box elements in its promoter (Carreira et al., 2005), was used in this experiment. In control cells expressing control shRNA, glucose starvation led to a 3-fold increase of *CDKN1A* mRNA levels, and this increase was blocked by the expression of shTFEB, despite that the shTFEB cells also exhibiting a significant ($P < 0.001$) but relatively minor increase of *CDKN1A* transcription possibly due to an effect of TFE3. The mRNA expression of another recently identified TFEB target, *RRAGD* (Di Malta et al., 2017), which encodes RagD GTPase that is essential for mTORC1 activation, was also elevated under glucose

deprivation in shCN cells but not in shTFEB cells (**Figure 3.2.3 B**). Although a wider range of target genes need analysing, these results suggest the activation of TFEB transcriptional activity concomitant with its nuclear translocation under glucose limited conditions. Interestingly also, the effects of shTFEB on *CDKN1A* and *RRAGD* in DMEM in which TFEB is mainly cytoplasmic suggest that either there is a steady state basal level of TFEB nuclear translocation and activation under nutrient rich conditions, or that TFEB has cytoplasmic functions which have not yet been uncovered.

3.2.4 Cellular signalling events under glucose starvation

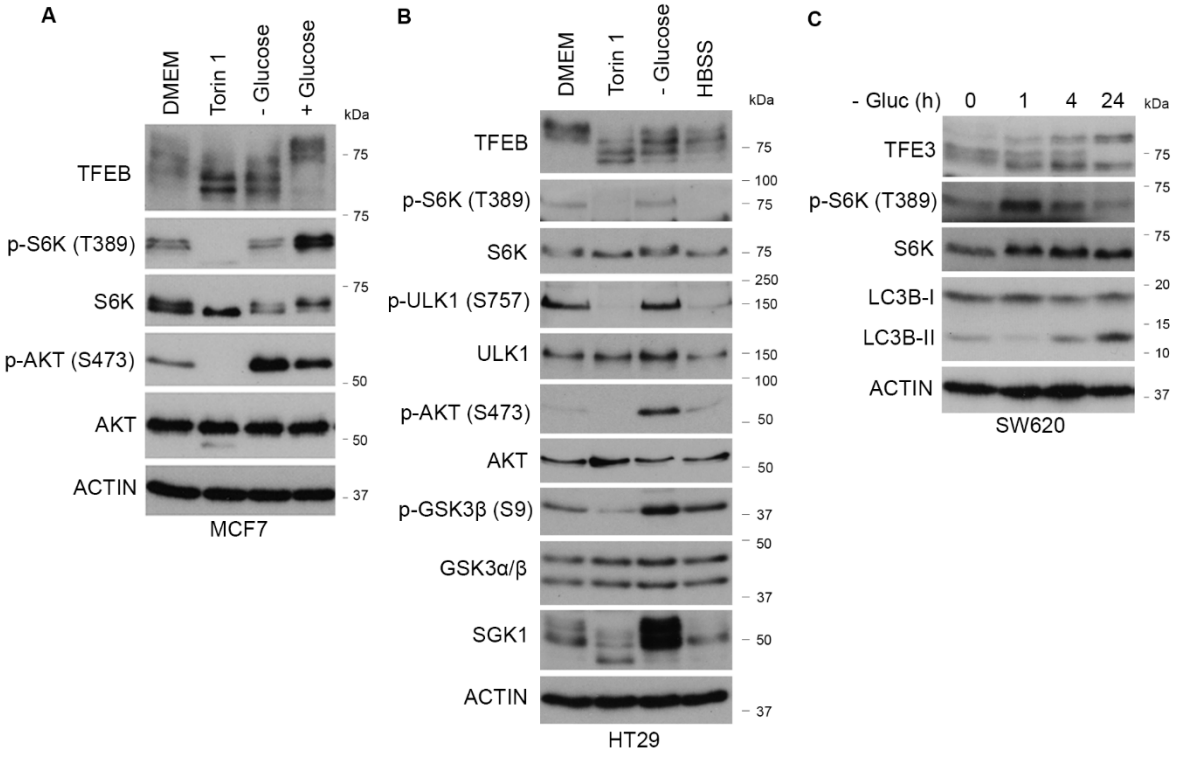


Figure 3.2.4.1 Signalling pathways under glucose or amino acid starvation. (**A**) Immunoblotting of MCF7 cells grown in normal DMEM, medium containing Torin 1 (250 nM, 1 h), glucose-depleted medium or glucose re-added medium for 2 h using indicated antibodies. (**B**) Immunoblotting of HT29 cells grown in normal DMEM, medium containing Torin 1 (250 nM, 1 h), glucose depleted medium or HBSS for 2 h using indicated antibodies. (**C**) Immunoblotting of SW620 cells grown in glucose depleted medium for indicated duration using indicated antibodies. ((**A**), (**B**) are published data in Li et al., 2018)

Deciphering the signalling events under glucose starvation is the key to understanding how TFEB is regulated by glucose. In MCF7 cells, as shown by immunoblotting (**Figure 3.2.4.1 A**), the mobility shift of TFEB which normally indicates its dephosphorylation was observed under Torin 1 treatment as well as glucose starvation, but was restored with re-addition of glucose. Torin 1 treatment greatly reduced the phosphorylation of S6K at T389, consistent with the mobility shift of S6K protein (**Figure 3.2.4.1 A**), indicating the loss of mTORC1 activity. However, S6K phosphorylation remained unaltered under glucose deprivation and was significantly enhanced when glucose was re-added (**Figure 3.2.4.1 A**). Furthermore, the activating phosphorylation of AKT at S473 was decreased by Torin 1 but was substantially increased by glucose depletion, and the increase was blunted by glucose re-addition (**Figure 3.2.4.1 A**).

Similarly, in HT29 cells TFEB dephosphorylation indicated by the protein mobility shift was induced by Torin 1 and, to a lesser extent, by glucose deprivation and amino acid starvation using HBSS (**Figure 3.2.4.1 B**). The phosphorylation of S6K which reflects mTORC1 activity was inhibited by Torin 1 and HBSS, but not by glucose starvation (**Figure 3.2.4.1 B**). In addition, the phosphorylation of another direct mTORC1 target ULK1 at S757 was lost under Torin 1 treatment and HBSS incubation, but was retained in the absence of glucose (**Figure 3.2.4.1 B**). The phosphorylation of AKT at S473, on the other hand, was reduced by Torin 1, and very similar to that in MCF7 cells, was strongly induced by glucose deprivation but not by HBSS (**Figure 3.2.4.1 B**). Accordingly, the inactivating phosphorylation of GSK3β at S9 was reduced by Torin 1, induced by glucose starvation, and relatively unaltered by HBSS (**Figure 3.2.4.1 B**). To our surprise, the protein levels of the mTORC2 target SGK1, was strongly elevated under

glucose starvation, whereas HBSS had little effect and Torin 1 reduced its mobility (phosphorylation) (**Figure 3.2.4.1 B**).

In another colorectal cancer cell line SW620, although TFEB protein was not detectable, TFE3 protein mobility shift was induced during a time course of glucose starvation and a strong upper band was observed possibly due to an uncharacterised modification such as ubiquitination or SUMOylation (**Figure 3.2.4.1 C**). S6K phosphorylation was transiently increased at 1 hour but reduced to levels at steady state from 4 hours to 24 hours (**Figure 3.2.4.1 C**). Levels of LC3B-II which is an essential component of the autophagosome membrane was reduced at 1 hour, consistent with higher mTORC1 activity indicated by S6K phosphorylation, but was increased after 4 hours until 24 hours (**Figure 3.2.4.1 C**), suggesting an accumulation of autophagic flux by glucose starvation despite a repression at early times.

These results revealed that although TFEB dephosphorylation arises as a consequence of glucose starvation, low glucose did not cause mTORC1 inactivation like Torin 1 or HBSS. Instead low glucose induced AKT activation and GSK3β inactivation. By contrast, both Torin 1 and HBSS led to inactivation of mTORC1 evidenced by decreased S6K phosphorylation. Since Torin 1 acts as an ATP-competitor specifically for the mTOR kinase, it not only inhibits mTORC1 but also mTORC2. The reduction of AKT phosphorylation by Torin 1 but not HBSS in HT29 cells can be explained by the inhibition of mTORC2; amino acid starvation only affects mTORC1 but not mTORC2, therefore AKT phosphorylation in HT29 cells was not changed by HBSS. Intriguingly, glucose starvation induced stabilised SGK1, again suggesting the activation of mTORC2, with the mobility shift of SGK1 protein caused by Torin 1 treatment mostly likely due to mTORC2 inhibition.

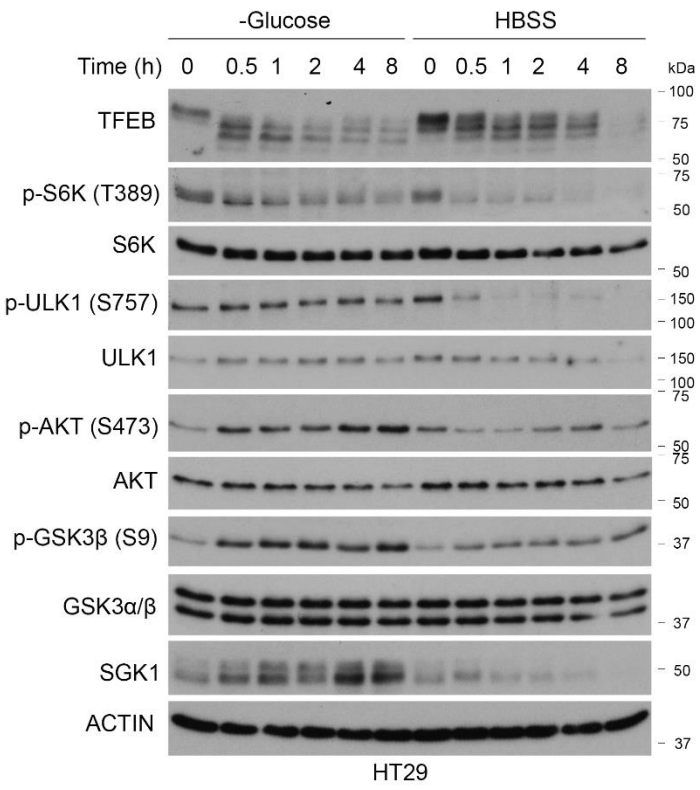


Figure 3.2.4.2 Glucose starvation affects different signalling pathways from amino acid starvation. Immunoblotting of HT29 cells grown in glucose depleted medium or HBSS for indicated duration using indicated antibodies. (Re-use of published data from Li et al., 2018)

To further understand the difference between glucose and amino acid starvation, a time course experiment was performed for each condition. Both glucose and amino acid starvation induced TFEB dephosphorylation shown by the mobility shift soon after the starvation started until later time points (**Figure 3.2.4.2**). As expected, S6K phosphorylation was reduced by amino acid starvation using HBSS from 0.5 hour and almost disappeared from 4 hours, while the reduction was relatively moderate during glucose starvation in comparison to amino acid starvation (**Figure 3.2.4.2**). The phosphorylation of ULK1 was quickly reduced by HBSS at 0.5 hour and diminished from 1 hour until the endpoint, whereas it remained at the same level for the duration of glucose starvation (**Figure 3.2.4.2**). Together with S6K, this observation

suggests that mTORC1 activity remains largely unaffected by glucose limitation. On the other hand, activation of AKT indicated by the phosphorylation at S473 was induced shortly after the initiation of glucose starvation and stayed until later time points, while S473 phosphorylation remained at a low level during HBSS incubation (**Figure 3.2.4.2**). The inactivating phosphorylation of GSK3β at S9 correlated well with the AKT phosphorylation pattern under glucose deprivation, but was relatively unaltered by HBSS (**Figure 3.2.4.2**). Strikingly, SGK1 protein started to accumulate shortly after glucose depletion and reached a high point after 4 hours and 8 hours, while it remained at low levels during HBSS incubation (**Figure 3.2.4.2**). Taken together, unlike amino acid starvation, glucose limitation had very little effect on mTORC1 downstream signalling but induced the activation of AKT, inactivation of GSK3β, and the stabilisation of SGK1, which is another indication of mTORC2 activation.

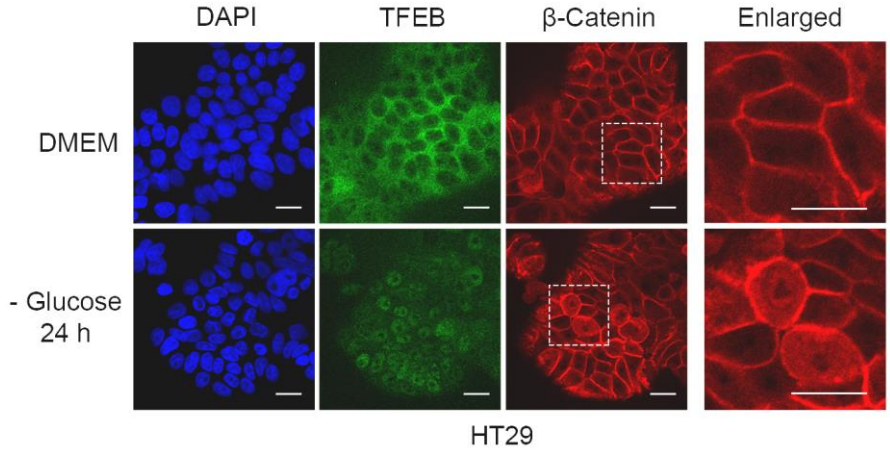


Figure 3.2.4.3 Glucose starvation induces nuclear translocation of TFEB and β-Catenin. Immunofluorescence of HT29 cells grown in normal DMEM or glucose depleted medium for 24 h using anti-TFEB and anti-β-Catenin antibodies. Scale bars = 20 µm.

One of the GSK3β substrates is the transcription co-factor β-Catenin, which is mainly localised at the plasma membrane in the absence of Wnt signalling. When phosphorylated by GSK3β, β-Catenin undergoes proteasomal degradation. Therefore, inactivation of GSK3β leads to accumulation and nuclear translocation of β-Catenin. As shown by immunofluorescent staining, a long-term glucose starvation (24 hours) which led to TFEB nuclear accumulation also resulted in relatively higher fluorescence intensity as well as stronger nuclear staining of β-Catenin in contrast to that in DMEM, in a number of HT29 cells (**Figure 3.2.4.3**), consistent with the inactivation of GSK3β by glucose limitation. However, the effect was very minor compared to that of TFEB possibly due to different phosphatase selectivity of TFEB and β-Catenin under these conditions.

3.2.5 Low glucose activates mTORC2-AKT-GSK3β axis

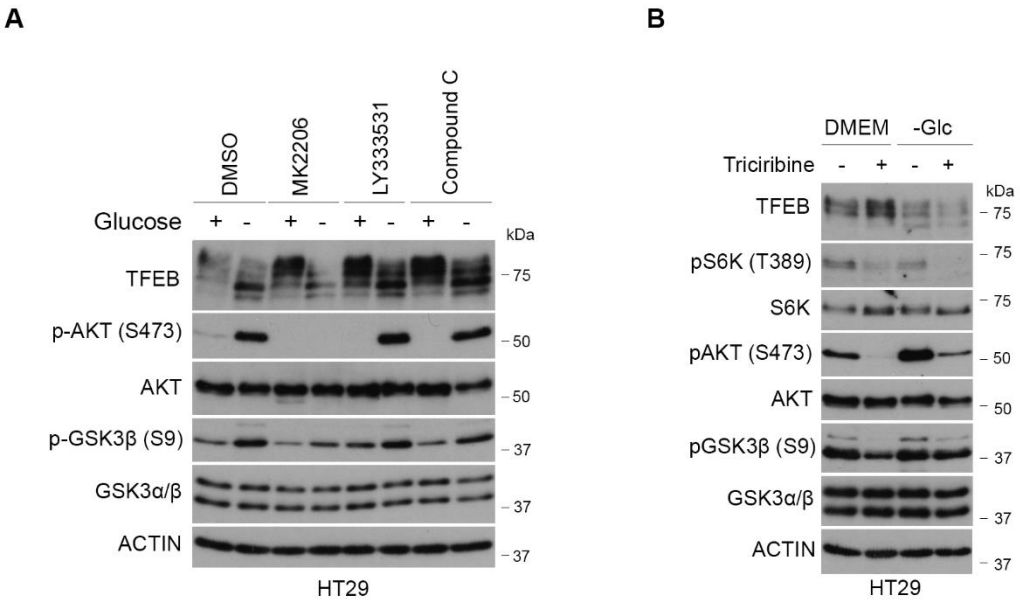


Figure 3.2.5.1 Glucose limitation inactivates GSK3β through AKT. (**A**) Immunoblotting of HT29 cells grown in medium with or without glucose containing DMSO, MK2206 (3 μM), LY333531 (5 μM) or Compound C (5 μM) for 4 h using indicated antibodies. (**B**) Immunoblotting of HT29 cells grown in medium with or without glucose in the absence or presence of triciribine (5 μM) for 4 h using indicated antibodies. ((**A**) is published data from Li et al., 2018)

Phosphorylation of GSK3β S9 can be by affected by a number of kinases including AKT, PKC and S6K (Cross et al., 1995; Li et al., 2016; Zhang et al., 2006). To dissect the signalling pathways that contribute to GSK3β inactivation, the effect of its phosphorylation under glucose starvation using pharmacological inhibitors of several kinases was assessed. With DMSO as a control, the absence of glucose induced the phosphorylation of AKT as well as GSK3β. The AKT inhibitor MK2206 not only blocked the phosphorylation of AKT at S473 caused by glucose starvation, but also prevented the phosphorylation of GSK3β at S9 (**Figure 3.2.5.1 A**). In comparison, neither the selective PKC inhibitor LY333531 nor the selective AMPK inhibitor Compound C blocked the inactivating phosphorylation of GSK3β (**Figure 3.2.5.1 A**). To confirm the effect of AKT on GSK3β inactivation, a second AKT inhibitor triciribine was used. In DMEM, triciribine slightly reduced S6K phosphorylation, and also strongly decreased the basal levels of AKT phosphorylation and GSK3β phosphorylation. Under glucose starvation, S6K phosphorylation did not change in the absence of triciribine but was abolished in its presence. AKT phosphorylation induced by glucose limitation was efficiently blocked by triciribine, and a similar effect was observed with GSK3β phosphorylation (**Figure 3.2.5.1 B**). These results suggest that GSK3β inactivation under glucose limitation was largely attributed to AKT activation, but not PKC or the supposedly activated AMPK under these conditions, and it is unlikely that S6K plays a significant role in regulating GSK3β activity under glucose deprivation because the phosphorylation of S6K did not increase correspondingly (**Figure 3.2.5.1 B**).

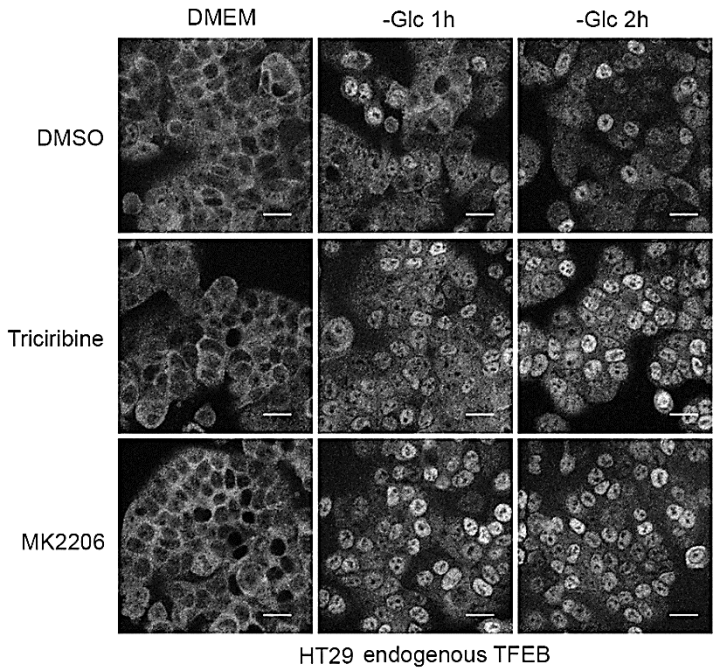


Figure 3.2.5.2 AKT inhibitors do not prevent TFEB nuclear accumulation under glucose starvation. Endogenous TFEB was immuno-stained using anti-TFEB antibody in HT29 cells grown in normal DMEM or glucose depleted medium containing DMSO, Triciribine (5 μM) or MK2206 (3 μM) for indicated duration. Scale bars = 20 μm.

Immunofluorescent imaging of endogenous TFEB in HT29 cells revealed that the administration of triciribine or MK2206 did not cause TFEB nuclear accumulation in DMEM nor prevent its nuclear translocation under glucose starvation (**Figure 3.2.5.2**). Note that triciribine alone decreased S6K phosphorylation (**Figure 3.2.5.1 B**), which can be explained by AKT acting upstream of mTORC1 signalling (**Figure 1.2.1**). But the failure to induce TFEB nuclear translocation by AKT inhibitors at steady state suggests that TFEB nuclear translocation by mTORC1 inhibition needs the concomitant activation of phosphatases, and the inability of the AKT inhibitors to prevent TFEB nuclear accumulation in the absence of glucose invigorated the notion that phosphatases must be involved.

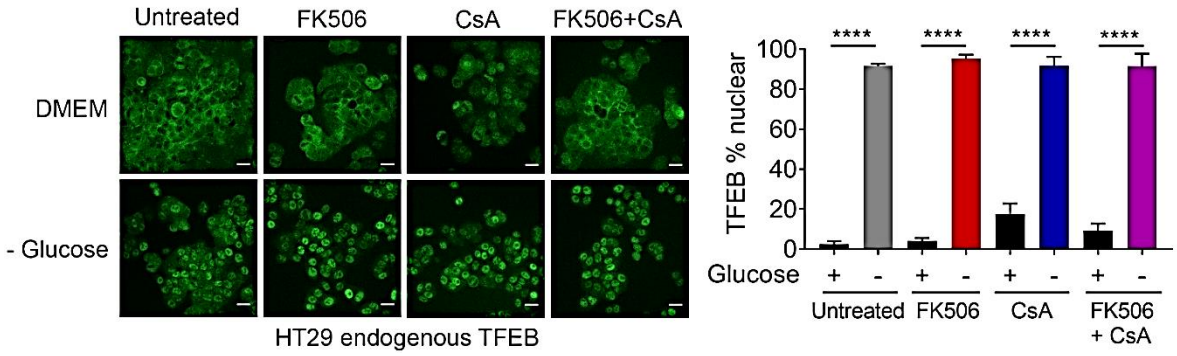


Figure 3.2.5.3 Calcineurin inhibitors do not prevent TFEB nuclear accumulation under glucose starvation. Endogenous TFEB was immuno-stained using anti-TFEB antibody in HT29 cells grown in normal DMEM or glucose depleted medium and treated with FK506 (5 μM), cyclosporine A (CsA, 10 μM) or both for 1 h. $n > 50$ cells per condition. Scale bars = 20 μm. Student's *t*-test: ****P < 0.0001. Error bars = SD.

To examine the potential involvement of Calcineurin, a reported phosphatase for TFEB (Medina et al., 2015), under glucose starvation, two Calcineurin inhibitors were used in an immunofluorescent microscopy experiment. In nutrient rich DMEM, FK506 did not make any difference from the untreated samples, while Cyclosporine A (CsA) induced a minor increase of TFEB nuclear localisation, and the effect was smaller when FK506 and CsA were combined (**Figure 3.2.5.3**). In the absence of glucose, FK506 and CsA either alone or in combination failed to prevent the nuclear translocation of TFEB (**Figure 3.2.5.3**). Despite the need for more genetic and biochemical analyses, the inability of the two well characterised phosphatase inhibitors to block TFEB nuclear accumulation hinted that Calcineurin was unlikely to be involved in the regulation of TFEB by glucose. Nevertheless, the dephosphorylation of TFEB under glucose starvation supports the idea that activated phosphatases promote TFEB nuclear

translocation regardless of mTORC1 activity. More phosphatases, including the recently identified PP2A (Martina and Puertollano, 2018), remain to be analysed.

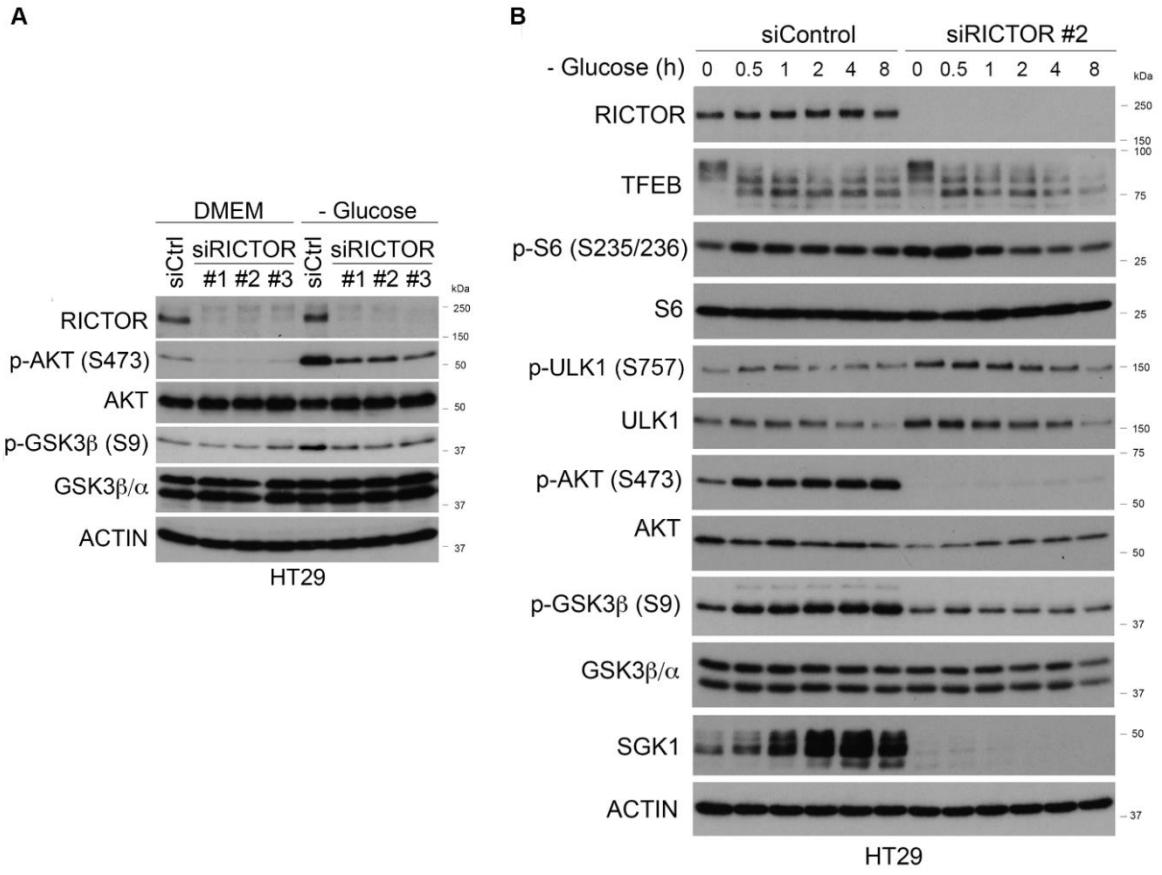


Figure 3.2.5.4 mTORC2 regulates GSK3β in response to glucose deprivation. (**A**) Immunoblotting of HT29 cells using indicated antibodies. 48 h after transient transfection of control siRNA or 3 individual siRNA targeting RICTOR, cells were grown in normal DMEM or glucose starved for 2 h. (**B**) Immunoblotting of HT29 cells transfected with control siRNA or siRICTOR #2 for 48 h and placed in glucose depleted medium for indicated duration. (Re-use of published data from Li et al., 2018)

Since the results showed that glucose starvation induced phosphorylation of AKT and accumulation of SGK1 protein, two hallmarks of mTORC2 activation, we sought to understand whether the inactivating phosphorylation of GSK3β mediated by AKT was caused by the effect of mTORC2. Using 3 individual siRNAs targeting RICTOR (siRICTOR), one of the essential

components of mTORC2, RICTOR protein levels were efficiently reduced in HT29 cells. Under nutrient rich conditions, basal level of AKT phosphorylation was decreased by all three siRICTOR compared to the control siRNA (siCtrl), while the effect of siRICTOR on GSK3β phosphorylation was minor (**Figure 3.2.5.4 A**). In the absence of glucose, the AKT phosphorylation as well as GSK3β phosphorylation was increased with siCtrl, but all the siRICTOR severely blocked the increase of AKT phosphorylation and maintained GSK3β phosphorylation at a similar level to that in DMEM (**Figure 3.2.5.4 A**).

A time course experiment was performed using siRICTOR #2 to analyse the signalling during glucose starvation in detail. RICTOR protein was efficiently knocked down for the duration of 8 hours (**Figure 3.2.5.4 B**). Glucose depletion resulted in a mobility shift of TFEB protein with both siCtrl and siRICTOR #2 (**Figure 3.2.5.4 B**), indicating that compromised mTORC2 did not affect TFEB dephosphorylation caused by glucose starvation, further supporting the potential involvement of phosphatases. The phosphorylation of ribosomal protein S6, a downstream effector of mTORC1 signalling, remained unaffected for the duration of glucose starvation with both siCtrl and siRICTOR #2 (**Figure 3.2.5.4 B**). The direct substrate of mTORC1, ULK1, maintained a similar level of phosphorylation at S757 during glucose deprivation with siCtrl. The same was observed with siRICTOR #2 until a minor decrease at a later time point 8 hours, and the levels of ULK1 phosphorylation with siRICTOR #2 were slightly higher compared to the control (**Figure 3.2.5.4 B**), suggesting an interesting compensating mechanism between the two mTOR complexes. On the other hand, AKT phosphorylation was increased shortly after glucose depletion and maintained at a high level with siCtrl but was abolished by the introduction of siRICTOR #2 (**Figure 3.2.5.4 B**). GSK3β phosphorylation displayed a similar pattern to that of AKT with siCtrl, but in siRICTOR #2

transfected cells glucose starvation failed to up-regulate the phosphorylation at S9 as it did with siCtrl (**Figure 3.2.5.4 B**). SGK1 protein started to accumulate 1 hour after glucose depletion and kept rising until 8 hours with siCtrl, while siRICTOR #2 completely diminished SGK1 protein during the time course of glucose starvation (**Figure 3.2.5.4 B**), confirming the accumulation of SGK1 by glucose deprivation resulted from mTORC2 activation. The maintained phosphorylation of S6 and ULK1 supported the conclusion that mTORC1 signalling was largely unaffected by acute glucose withdrawal. Instead, these results strongly suggest that mTORC2 was activated by glucose limitation, in line with the observations from a previous study using MEF and HeLa cell lines (Moloughney et al., 2016). Activated mTORC2 leads to AKT phosphorylation and activation, which subsequently phosphorylates GSK3β at S9 to inactivate its kinase activity.

3.2.6 The IRS1 feedback loop does not participate in GSK3β regulation under glucose starvation

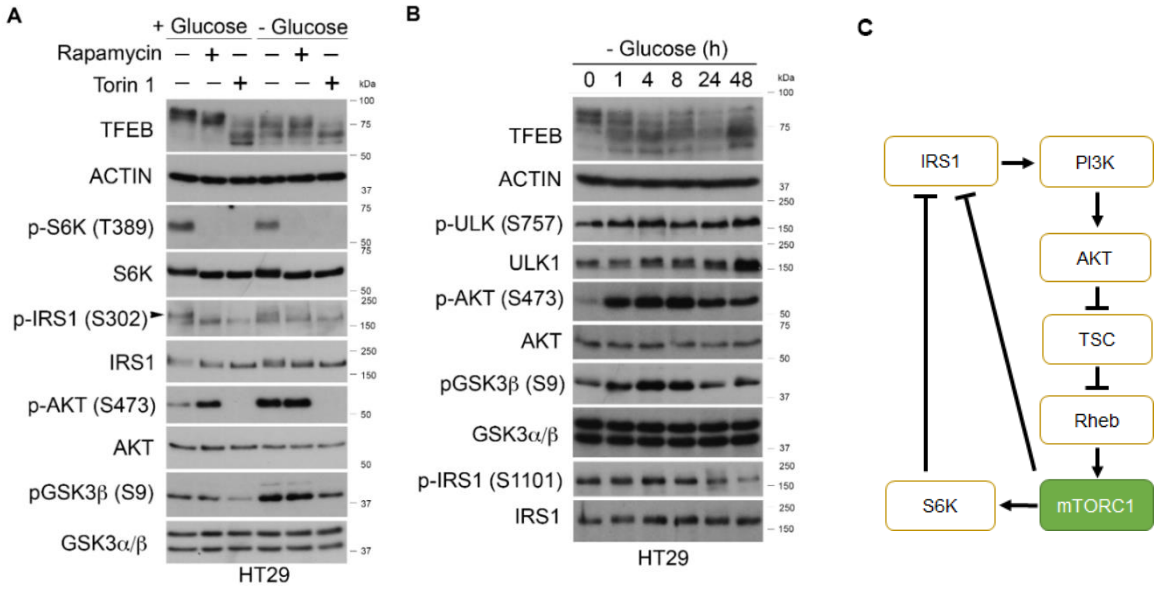


Figure 3.2.6 The IRS1 feedback loop does not affect AKT-GSK3β signalling under glucose starvation. *Legend continues at the bottom of next page.*

Previous studies established that mTORC1 can modulate AKT activity through the IRS1 negative feedback loop. Through phosphorylation of IRS1 by mTORC1 and S6K at multiple sites, insulin signalling was attenuated by proteasomal degradation of IRS1. When mTORC1 is inhibited, IRS1 is relieved from degradation mediated by mTORC1 and S6K phosphorylation, and its stabilisation allows PI3K docking and activation which further leads to AKT phosphorylation and activation (Gual et al., 2005 and **Figure 3.2.6 C**). To assess the contribution of the IRS1 feedback loop to glucose limitation induced AKT activation, the mTORC1-specific inhibitor rapamycin and the ATP-competitive inhibitor of both mTORC1 and mTORC2 Torin 1 were used in the presence and absence of glucose. Both rapamycin and Torin 1 efficiently reduced S6K phosphorylation in the presence of glucose (**Figure 3.2.6 A**), indicating an inhibition of mTORC1. Rapamycin and Torin 1 also decreased of the phosphorylation of IRS1 at S302, as a result of mTORC1 and S6K inhibition. Rapamycin alone induced AKT phosphorylation at S473 in the presence of glucose (**Figure 3.2.6 A**), in consistence with IRS1 feedback loop mediated AKT activation, while Torin 1 led to decreased AKT phosphorylation (**Figure 3.2.6 A**) since it also inhibits mTORC2. Strikingly, although rapamycin resulted in AKT activation as did glucose depletion, it failed to induce GSK3β phosphorylation at S9 in the presence of glucose (**Figure 3.2.6 A**). Moreover, the absence of glucose did not decrease S6K phosphorylation or IRS1 phosphorylation, while it consistently caused AKT activation and the subsequent inactivating phosphorylation of GSK3β (**Figure**

Figure 3.2.6 The IRS1 feedback loop does not affect AKT-GSK3β signalling under glucose starvation. (**A**) Immunoblotting of HT29 cells using indicated antibodies. Cells were grown in the presence or absence of glucose and treated with Rapamycin (1 μM) or Torin 1 (250 nM) for 4 h. (**B**) Immunoblotting of HT29 cells grown in glucose depleted medium for indicated duration using indicated antibodies. (**C**) Schematic depicting the signalling of the IRS1 feedback loop. (Re-use of published data from Li et al., 2018)

3.2.6 A). In addition, rapamycin reduced the phosphorylation of S6K and IRS1 in the absence of glucose, but it did not cause further phosphorylation of AKT or GSK3β (**Figure 3.2.6 A**). Torin 1 treatment reduced phosphorylation of S6K, IRS1, AKT and GSK3β irrespective of glucose availability (**Figure 3.2.6 A**), which is most likely due to a mixed effect of inhibition of both mTORC1 and mTORC2. The inability of rapamycin to induce GSK3β phosphorylation as opposed to glucose limitation addresses the importance of AKT substrate selectivity under different conditions. It also suggests that the IRS1 feedback loop did not participate in the inactivation of GSK3β despite a similar AKT activation.

A 48 hour-time course of glucose starvation was performed to examine the possible IRS1 feedback loop in a long term. Consistent with the previous results, glucose starvation led to dephosphorylation of TFEB without affecting mTORC1 activity indicated by ULK1 phosphorylation (**Figure 3.2.6 B**). The phosphorylation of AKT and GSK3β increased from 1 hour and started to decline after 24 hours, the patterns of which correlated well with each other. The phosphorylation of another IRS1 site S1101 which is also involved in the feedback loop did not change until 48 hours, much later than the increased phosphorylation of AKT and GSK3β (**Figure 3.2.6 B**). Therefore, it is unlikely that the IRS1 feedback loop participates in glucose limitation-induced AKT activation and subsequent GSK3β inactivation.

3.2.7 GSK3β kinase activity is required for TFEB cytoplasmic localisation

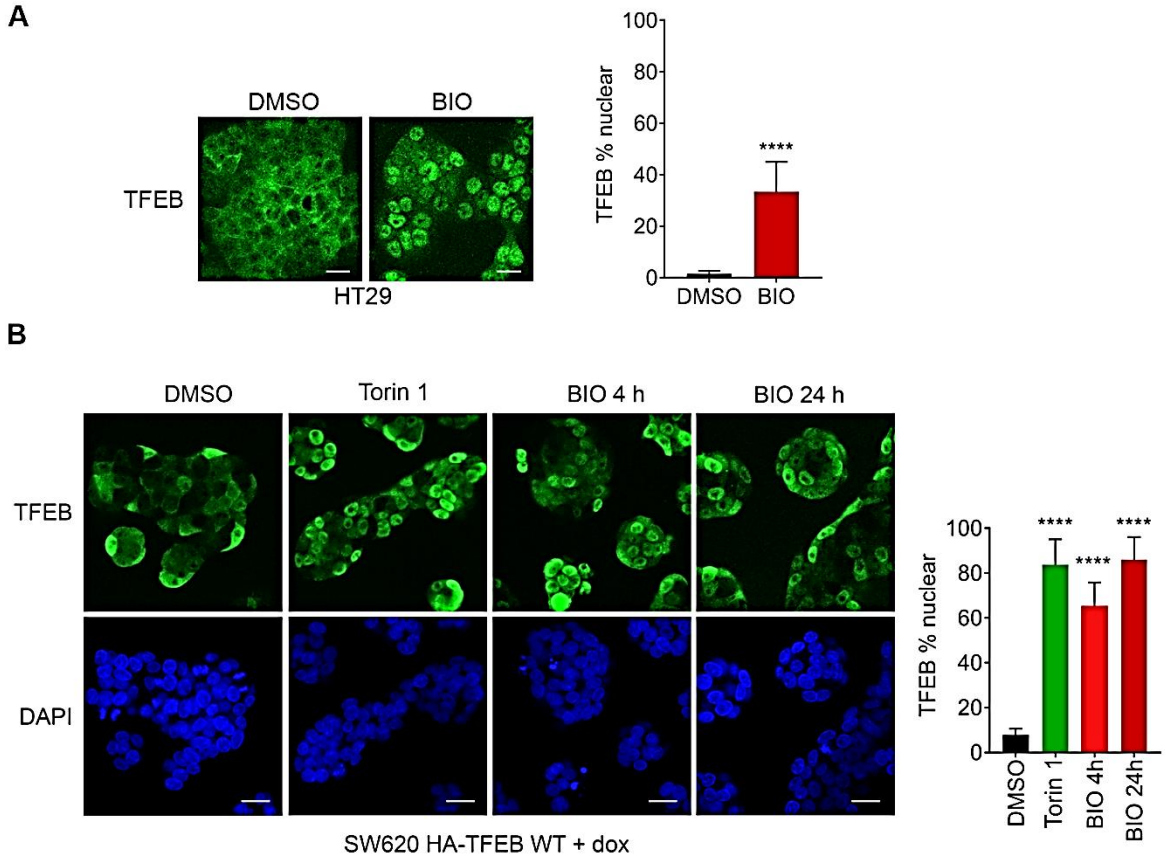


Figure 3.2.7.1 Pharmacological inhibition of GSK3 leads to TFEB nuclear accumulation. (**A**) Immunofluorescent imaging of HT29 cells using anti-TFEB antibody. Cells were treated with DMSO or BIO (5 µM) for 4 h. $n > 100$ cells per condition. (**B**) Immunofluorescent imaging of SW620 cells expressing HA-TFEB when induced with doxycycline (50 ng/mL, 20 h) using anti-HA antibody. Cells were treated with Torin 1 (250 nM, 1 h) or BIO (5 µM, 4 h or 24 h). $n > 50$ cells per condition. DAPI was used to stain the nuclei of the cells. Scale bars = 20 µm. Student's *t*-test: ****$P < 0.0001$. Error bars = SD.

A number of studies have shown that GSK3 inhibition leads to higher levels of lysosomal biogenesis and autophagy (Marchand et al., 2015; Parr et al., 2012; Weikel et al., 2016), and one study demonstrated that GSK3β can phosphorylate TFEB directly (Li et al., 2016). Our data suggests that glucose limitation induces GSK3β inactivation as well as TFEB nuclear translocation. It is therefore necessary to understand the connection between GSK3β

and TFEB and the mechanism by which GSK3β can potentially regulate TFEB under physiological conditions.

A previous study used HEP14 (5β-O-angelate-20-deoxyingenol) and HEP15 (3β-O-angelate-20-deoxyingenol) to induce PKC mediated GSK3β inactivation and TFEB nuclear translocation (Li et al., 2016). However, our data suggested that glucose starvation induced GSK3β was independent of PKC (**Figure 3.2.5.1 A**). To test the direct effect of GSK3β inhibition, a selective GSK3 inhibitor, BIO, was used in an immunofluorescent imaging experiment. As shown by antibody staining, BIO significantly induced nuclear translocation of TFEB in HT29 cells, but the translocation was only seen in around 30 % cells (**Figure 3.2.7.1 A**), which can be possibly explained by the predominant inhibitory effect of mTORC1. Using SW620 cells which have low levels of endogenous TFEB protein, a monoclonal inducible HA-tagged TFEB-expressing cell line was generated. Ectopic TFEB was induced by addition of doxycycline. The exogenous TFEB was mainly localised in the cytoplasm with DMSO control but accumulated rapidly in nuclei when the cells were treated with Torin 1 (**Figure 3.2.7.1 B**), the same as endogenous TFEB. 4 hours of BIO treatment led to around 60 % cells with nuclear TFEB, and this effect was increased to a similar extent to that with Torin 1 by longer incubation (**Figure 3.2.7.1 B**). This confirms that TFEB nuclear accumulation can be induced by direct pharmacological inhibition of GSK3 kinases, and long-term GSK3 inhibition can indeed override the effect of mTORC1 on TFEB subcellular localisation.

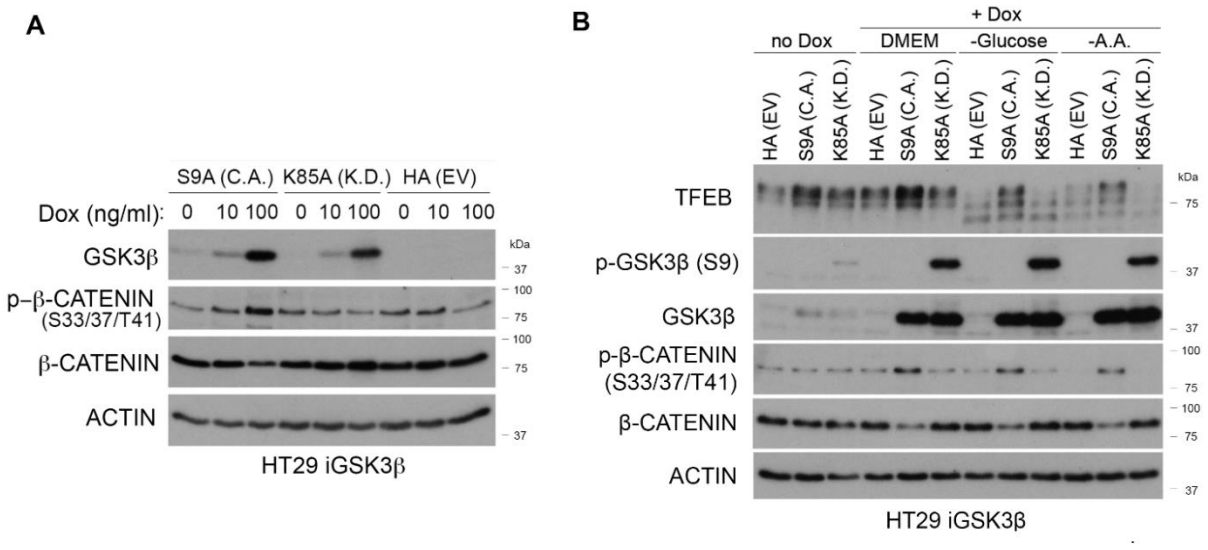


Figure 3.2.7.2 GSK3β kinase activity partially retains TFEB phosphorylation under glucose starvation. (**A**) Immunoblotting of HT29 cells stably expressing doxycycline-inducible constitutively active (C.A.) S9A or kinase dead (K.D.) K85A HA-GSK3β or HA empty vector control using indicated antibodies. HA-GSK3β expression was induced by 10 ng/mL or 100 ng/mL doxycycline for 20 h. (**B**) Immunoblotting of HT29 cells stably expressing constitutively active (C.A.) S9A or kinase dead (K.D.) K85A HA-GSK3β or HA empty control using indicated antibodies. HA-GSK3β expression was induced by 100 ng/mL doxycycline for 20 h. Then the cells were grown in normal DMEM, medium without glucose or HBSS for 1 h. ((**A**) is published data from Li et al., 2018)

To investigate whether the kinase activity of GSK3β regulates TFEB subcellular localisation, HT29 cells were engineered to express either HA-GSK3β S9A mutant which is constitutively active (C.A.) or HA-GSK3β K85A mutant which is kinase dead (K.D.). The empty vector containing the HA-tag was used as a control. Driven by a Tet-on promoter, the expression of both S9A and K85A mutants can be titrated by the incremental addition of doxycycline (**Figure 3.2.7.2 A**). The induction of the S9A mutant caused increased phosphorylation of the well-known GSK3 substrate β-Catenin at S33/37/T41, sites which are involved in the turnover of β-Catenin protein. The function of these phosphorylation sites by constitutively active GSK3β was confirmed by the decreased β-Catenin levels following

doxycycline titration. On the contrary, the K85A mutant did not cause any change in β-Catenin phosphorylation while β-Catenin protein levels slightly went up with 100 ng/mL doxycycline (**Figure 3.2.7.2 A**), suggesting that this mutant has no kinase activity but rather partially acts as a dominant negative form of GSK3β. The empty vector control had little effect on β-Catenin.

By carefully titrating doxycycline concentrations, the S9A and K85A mutants were expressed at similar levels. The lack of an inactivating phosphorylation site in S9A mutant was confirmed by the immunoblotting with phospho-specific antibody, but S9 can still be phosphorylated in the kinase dead mutant K85A (**Figure 3.2.7.2 B**). In addition, the presence of S9A mutant caused increased phosphorylation and decreased protein levels of β-Catenin in DMEM, under glucose starvation and amino acid starvation, whereas the K85A mutant or empty vector control had no such effects (**Figure 3.2.7.2 B**). Interestingly, while glucose and amino acid starvation both led to dephosphorylation of TFEB in the presence or absence of GSK3β, the constitutively active mutant S9A partially retained the mobility shift of TFEB under both conditions (**Figure 3.2.7.2 B**). This result suggests that the kinase activity of GSK3β may contribute to TFEB phosphorylation.

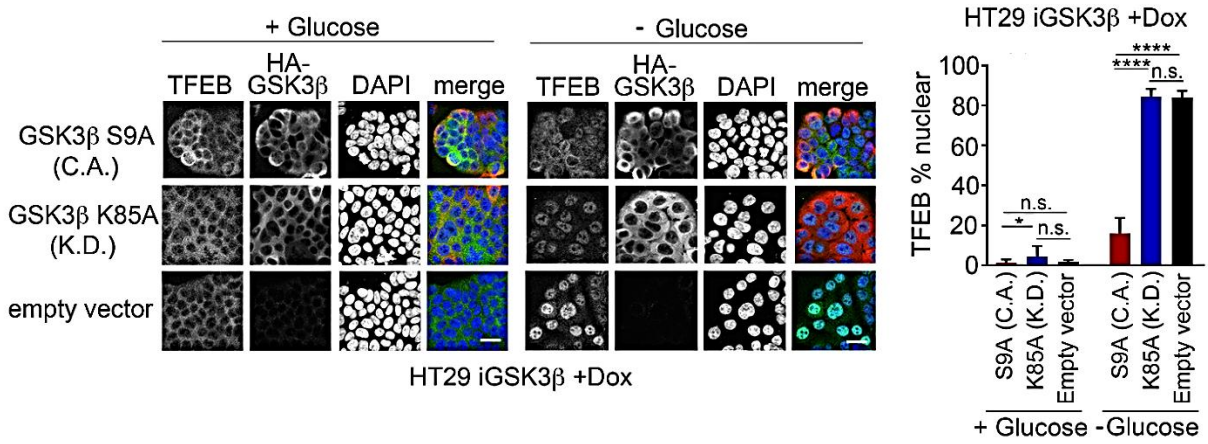


Figure 3.2.7.3 GSK3β activity is required for TFEB cytoplasmic localisation under glucose starvation. Immunofluorescent microscopy was performed using anti-TFEB and anti-HA antibodies with HT29 cells stably expressing constitutively active (C.A.) S9A or kinase dead (K.D.) K85A HA-GSK3β or HA empty control. HA-GSK3β expression was induced with 100 ng/mL doxycycline for 20 h. Then the cells were grown with or without glucose for 1 h. $n > 200$ cells per condition. Scale bars = 20 μm. Student's *t*-test: ****$P < 0.0001$, *$P < 0.05$, n.s. not significant. Error bars = SD. (Re-use of published data from Li et al., 2018)

The partially retained mobility shift of TFEB protein by constitutively active GSK3β indicates a lesser dephosphorylation under glucose starvation. Since numerous studies established that the dephosphorylation is often a concomitant event of TFEB nuclear translocation, an immunofluorescent imaging experiment was performed to examine the effect of GSK3β kinase activity on TFEB nuclear localisation. In the presence of glucose, TFEB was predominantly localised in the cytoplasm regardless of GSK3β mutants or empty vector, with the K85A mutant causing a significant but negligibly higher TFEB nuclear distribution (**Figure 3.2.7.3**). In the absence of glucose, more than 80 % cells exhibited TFEB nuclear accumulation with both K85A mutant and empty vector, but the percentage was substantially reduced by the S9A mutant. Consistent with the mobility shift under glucose starvation, TFEB nuclear accumulation was substantially prevented by GSK3β kinase activity (**Figure 3.2.7.3**), which in turn suggests the latter being required for TFEB cytoplasmic localisation.

3.2.8 TFEB S138 phosphorylation by GSK3β is primed by S142 phosphorylation

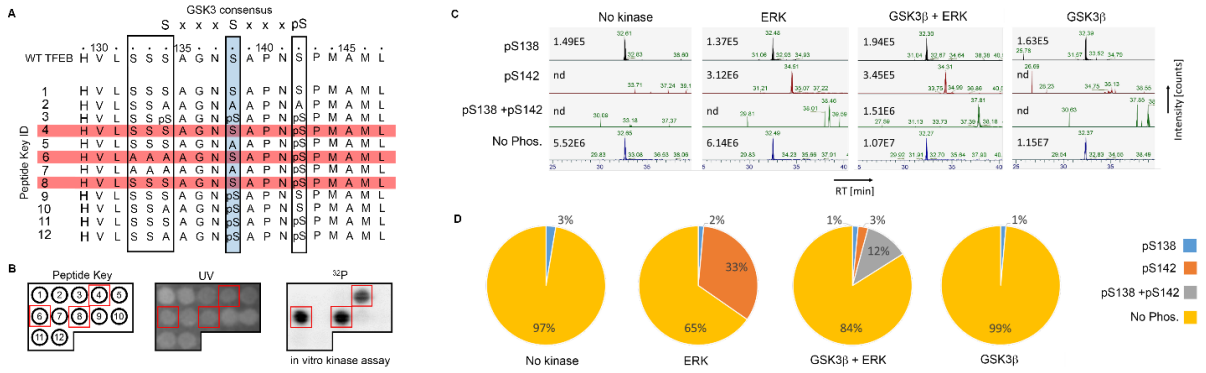


Figure 3.2.8 TFEB phosphorylation at S138 by GSK3β is primed by phosphorylation at S142. (**A**) TFEB amino acids 129–152 showing the GSK3β consensus sequence. The S138 GSK3β site is highlighted in blue, the ERK/mTOR phosphorylation site S142 is boxed, as are three additional potential GSK3β sites that could be primed by phosphorylation at S138. Peptides 1–12 were spotted onto a membrane and subject to GSK3β phosphorylation in vitro. Peptides highlighted in red were phosphorylated by GSK3β. (**B**) Peptide key corresponding to peptides above spotted onto a membrane (left) and visualized by UV (middle). The result of the GSK3β kinase assay is shown in the right panel and the red boxes correspond to phosphorylated peptides highlighted in red above. (**C**) Extracted ion chromatograms of tryptic peptides covering S138 and S142 in their differential phosphorylation states after indicated kinase treatment. A peptide with a single phosphorylation on S138 was detected at low intensity in all samples, including those not treated with GSK3β, while a peptide with a phosphorylation event on S142 was only detected in the ERK and GSKβ + ERK treated samples. Peptides dually phosphorylated on both S138 and on S142 were detected only after GSKβ + ERK treatment. Numbers represent maximum ion count for each peptide/phospho-peptide. (**D**) Quantification of TFEB in vitro kinase/Mass Spec data. The pie-charts illustrate the signal contribution of each (phospho-) peptide variant to total signal intensity covering the analysed phosphorylation locus after kinase treatments. Assuming that each peptide variant has identical ionization characteristics, the charts reflect the stoichiometry of the different phospho-proteoforms of TFEB after kinase treatment). ((**A**), (**B**) are published data from Li et al., 2018 produced by Hans Friedrichsen, and (**C**), (**D**) by Sarah Andrews.)

A previous study using bacterially expressed and purified TFEB protein showed that S134 and S138 can be phosphorylated by GSK3β (Li et al., 2016). However, since GSK3 favours a consensus sequence of S/T-X-X-X-pS/pT (S: serine, T: threonine, pS: phospho-serine, pT: phospho-threonine, X: any amino acid) (Wu and Pan, 2010), the priming potential of

phosphorylation at S134 and S138 by phospho-S142 was not addressed. We therefore undertook a kinase assay making use of a peptide array technique. TFEB 129-152 peptides were designed with the key serine residues (S132, S133, S134, S138 and S142) unmodified, mutated to alanine or phosphorylated, and the peptides were synthesised on cellular membranes to form peptide arrays using the SPOT technology (Hilpert et al., 2007). The peptide array was incubated with GSK3β kinase (purchased from NEB), 1x NEBuffer for protein kinases (NEB) and [γ-^{32}P]-ATP at 30°C for 30 min before thoroughly rinsed and exposed to a phosphor imager to detect incorporated radioactivity. There was no detectable ^{32}P incorporation above background with the WT peptide, whereas strong radiolabelling was observed when S142 was phosphorylated and S138 intact (**Figure 3.2.8 A, B**). The mutation of S138 to alanine completely diminished the signal facilitated by phospho-S142, suggesting that the S138 was phosphorylated by GSK3β only when S142 was phosphorylated. The potential phosphorylation at S134 was also examined but the results revealed no detectable signal even when S138 and S142 were either or both phosphorylated (**Figure 3.2.8 A, B**).

Complementarily, we also performed a quantitative mass spectrometry experiment using bacterially expressed and purified recombinant TFEB protein containing the first 200 amino acids. Commercial ERK2 or GSK3β kinase alone or in combination were used for the in vitro kinase assay prior to mass spectrometry analysis. Quantification of the phosphorylation events confirmed that ERK2 phosphorylated S142 but not S138, GSK3β alone did not phosphorylate either S142 or S138 (**Figure 3.2.8 C, D**). In agreement with the peptide array kinase assay, S138 phosphorylation only occurred when S142 was phosphorylated by ERK2 (**Figure 3.2.8 C, D**). These results again suggested that phosphorylation of S138 is dependent on prior phosphorylation of S142. Indeed, previous high throughput phospho-proteomic

analyses revealed that TFEB phosphorylation at S138 was only detected in the presence of phospho-S142 whereas phosphorylation at S142 could occur regardless of S138 phosphorylation status (Beausoleil et al., 2006; Dephoure et al., 2008).

3.2.9 Phosphorylation of S138 and S142 is required for TFEB nuclear export

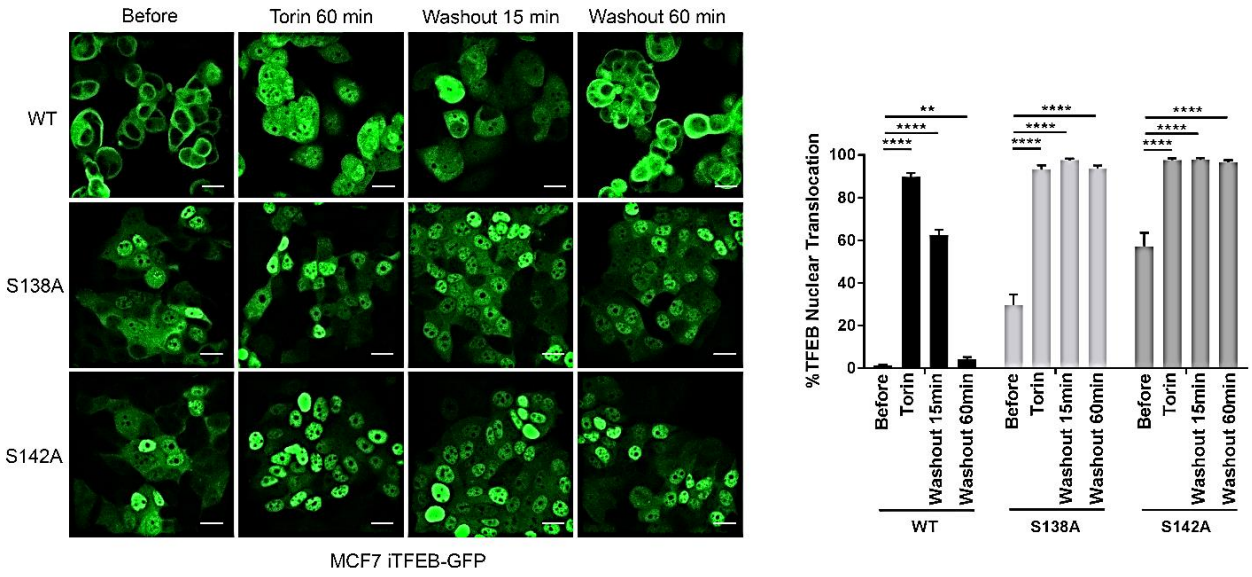


Figure 3.2.9.1 Phosphorylation of S138 and S142 is required for TFEB nuclear export. Live cell imaging of MCF7 cell lines stably expressing WT, S138A or S142A TFEB when induced with 10 ng/mL doxycycline for 20 h. Cells were treated with Torin (20 nM, 1 h) before the medium was replaced with normal DMEM for 15 min or 60 min. $n > 100$ cells per condition. Scale bars = 20 μm. Student's *t*-test: ****$P < 0.0001$, **$P < 0.01$. Error bars = SD. (Re-use of published data from Li et al., 2018)

Although the phosphorylation of TFEB at S142 has been shown to be important for TFEB cytoplasmic localisation, the mechanism had yet to be elucidated. Our data demonstrated that the phosphorylation of S142 primes for the phosphorylation at S138 by GSK3β, which prompted us to consider that these two phosphorylation events may cooperate in controlling TFEB subcellular localisation. Unlike many other studies using transient or adenovirus mediated overexpression of TFEB, GFP-tagged wild-type (WT), S138A or S142A mutant

TFEB constructs driven by a doxycycline-inducible promoter were stably introduced into MCF7 cells. By titrating doxycycline concentrations, these fusion proteins were expressed at a low level. Shown by fluorescent imaging, the WT TFEB-GFP was cytoplasmic in almost 100 % cells under normal nutrient rich conditions, while the S138A mutant was in the nucleus in around 30 % cells and S142A close to 60 % (**Figure 3.2.9.1**). If these two phosphorylation sites served a role in cytoplasmic sequestration, the mutation of the two serine residues to alanine should result in much higher nuclear portion of TFEB at steady state. Another possibility is that the serine to alanine mutation disrupts the nuclear export process and consequently TFEB was retained in the nucleus. To test this hypothesis, a fluorescent imaging experiment was set out to induce TFEB nuclear translocation using Torin 1 which was then washed out using normal DMEM. 60 min of Torin 1 treatment efficiently increased the nuclear localisation of WT TFEB and both S138A and S142A mutants. 15 min after Torin 1 was washed out, WT TFEB started

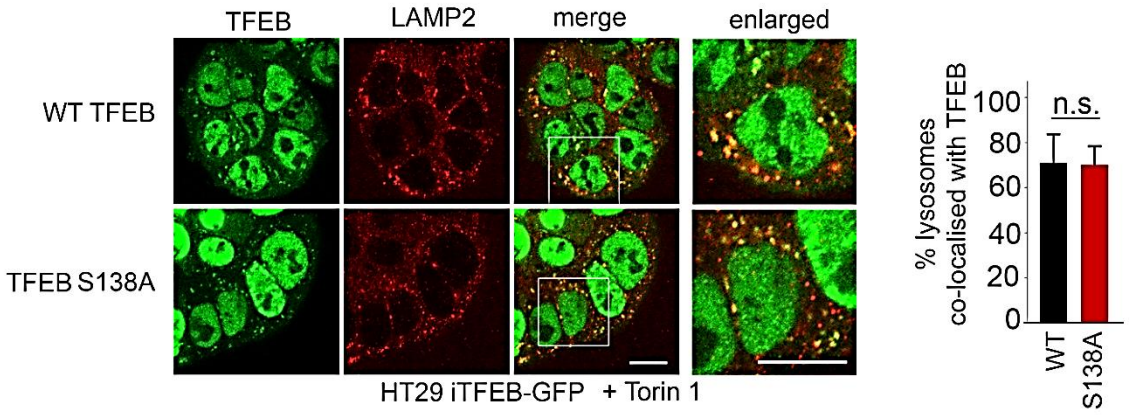


Figure 3.2.9.2 Phosphorylation of S138 is not required for TFEB lysosomal localisation. Immunofluorescent imaging of HT29 cell lines stably expressing WT or S138A TFEB-GFP when induced with 10 ng/mL doxycycline for 20 h and treated with Torin 1 (250 nM, 1 h). Co-localisation of TFEB and lysosomes were shown using anti-LAMP2 antibody. For lysosome co-localisation quantification, lysosomes were stained by anti-LAMP2 antibody and their total numbers were counted. The percentage of TFEB lysosome co-localisation was defined by the percentage of lysosomes with positive TFEB-GFP co-localisation. $n > 50$ cells per condition. Scale bars = μm. Student's *t*-test: n.s. not significant. Error bars = SD. (Re-use of published data from Li et al., 2018)

to relocate into the cytoplasm in a portion of cells and the relocalisation was almost complete by 60 min, In comparison, the nuclear accumulation of either the S138A or S142A mutant TFEB induced by Torin 1 was not reduced by washout for the duration of 60 min (**Figure 3.2.9.1**), confirming a severely impaired nuclear export capability of these mutants.

Previous work suggested a role of S134/S138 phosphorylation in the association of TFEB to lysosomes (Li et al., 2016). A similar experiment was performed under conditions where TFEB was drastically recruited to the lysosomes (Martina and Puertollano, 2013). Precisely, Torin 1, an ATP-competitive inhibitor of mTOR, only inhibits the catalytic subunit of mTOR but not the Rag GTPases. TFEB can still be recruited to the surface of the lysosomes by the Rags in the presence of Torin 1 but cannot be further phosphorylated and sequestered, whereas cytosolic TFEB molecules undergo dephosphorylation and nuclear translocation, resulting in a nuclear pool and a lysosomal pool of TFEB. Lysosomes were visualised by immuno-staining of the lysosome marker LAMP2 in HT29 cells stably expressing inducible WT or mutant TFEB-GFP. Under Torin 1 treatment, WT TFEB was co-localised with around 70 % lysosomes and a similar percentage was seen with the S138A mutant (**Figure 3.2.9.2**). Therefore, this result suggests that S138 is unlikely to play a role in the ability of TFEB to bind lysosomes.

3.2.10 TFEB contains a NES adjacent to S138 and S142

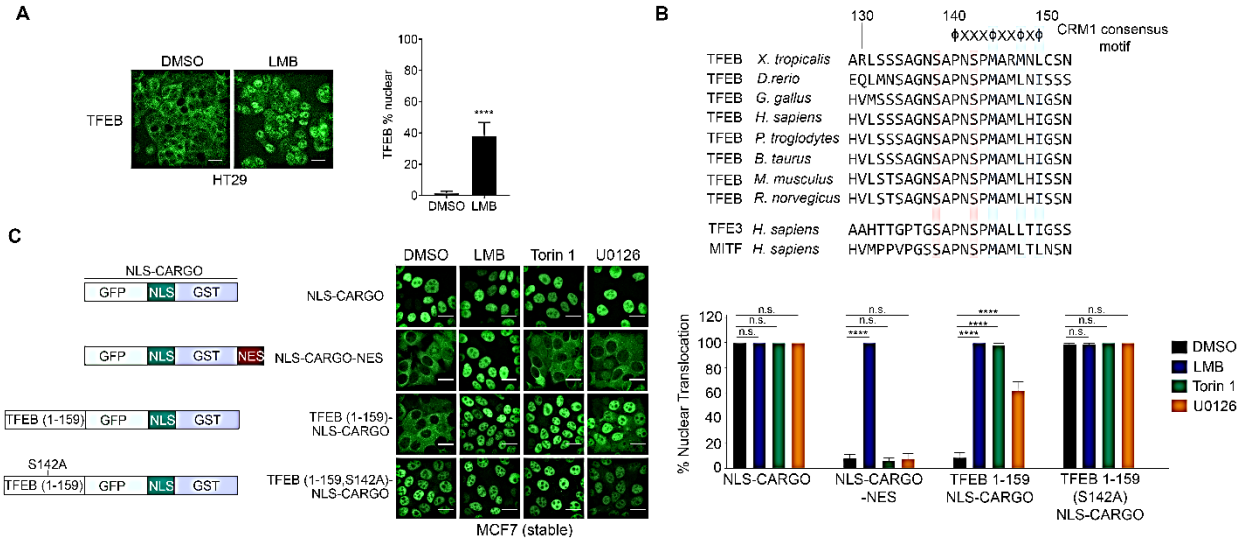


Figure 3.2.10.1 TFEB contains a nuclear export signal. (**A**) immunofluorescent imaging of HT29 cells treated with DMSO or Leptomycin B (LMB, 20 nM, 1 h) using anti-TFEB antibody. $n > 100$ cells per condition. (**B**) Sequence alignment of TFEB amino acids 129-152 in different species as well as related factors TFE3 and MITF. S138 and S142 residues were highlighted in red. Hydrophobic residues highlighted in blue conform to the consensus for an NES. (**C**) Fluorescent imaging of MCF7 cell lines stably expressing indicated chimeric proteins. Cells were treated with DMSO, LMB (20 nM, 2 h), Torin 1 (250 nM, 1 h) or U0126 (20 µM, 3 h) before the cells were fixed and imaged. $n > 50$ cells per condition. Scale bars = 20 µm. Student's *t*-test: ****$P < 0.0001$, n.s not significant. Error bars = SD. ((**C**) is published data from Li et al., 2018)

The effect of S138A and S142A on TFEB nuclear export after Torin treatment and wash out suggested the existence of a nuclear export signal (NES). In fact, when treated with leptomycin B (LMB), a natural compound specifically blocking the interaction between Chromosomal Region Maintenance 1(CRM1)/ nuclear exportin 1 (XPO1) and NES-containing cargo proteins, TFEB was significantly retained in the nucleus (**Figure 3.2.10.1 A**). By closely examining the amino acid sequence adjacent to S138 and S142, an evolutionarily conserved hydrophobic residue-rich region was identified that possesses the consensus CRM1 binding

motif: ϕXXXϕXXϕXϕ (ϕ: a hydrophobic amino acid, X: any amino acid). This motif is also conserved in other family members TFE3 and MITF (**Figure 3.2.10.1 B**).

To test whether this motif functions as a NES, a chimeric protein was designed utilising the fusion of GST and GFP to a canonical PKKKRKV nuclear localisation signal (NLS) from the SV40 large T-antigen (Kalderon et al., 1984). This NLS-cargo protein which has a size sufficient so as to be excluded from passive diffusion through nuclear pores, was constitutively nuclear and unaffected by the treatment of LMB, Torin 1 or MEK/ERK2 inhibitor U0126 (**Figure 3.2.10.1 C**). When further fused with an LALKLAGLDI NES from the cAMP-dependent protein kinase inhibitor (PKI) (Wen et al., 1995), this GST-NLS-GFP-NES cargo protein re-localised to the cytoplasm. Cytoplasmic localisation was prevented by the nuclear export inhibitor LMB but not by Torin 1 or U0126 (**Figure 3.2.10.1 C**).

When the NES of PKI was replaced by the N-terminal region of TFEB (1-159) containing the putative NES but not the S211 site known to modulate cytoplasmic sequestration through interaction with 14-3-3, the TFEB (1-159)-GST-NLS-GFP cargo also localised to the cytoplasm (**Figure 3.2.10.1 C**). LMB completely blocked the cytoplasmic localisation of the TFEB cargo, as well as Torin 1. U0126 reduced the cytoplasmic localisation to a lesser extent (**Figure 3.2.10.1 C**). As expected, the mutation of S142 to alanine abolished the cytoplasmic relocalisation of the TFEB (1-159)-GST-NLS-GFP cargo protein (**Figure 3.2.10.1 C**).

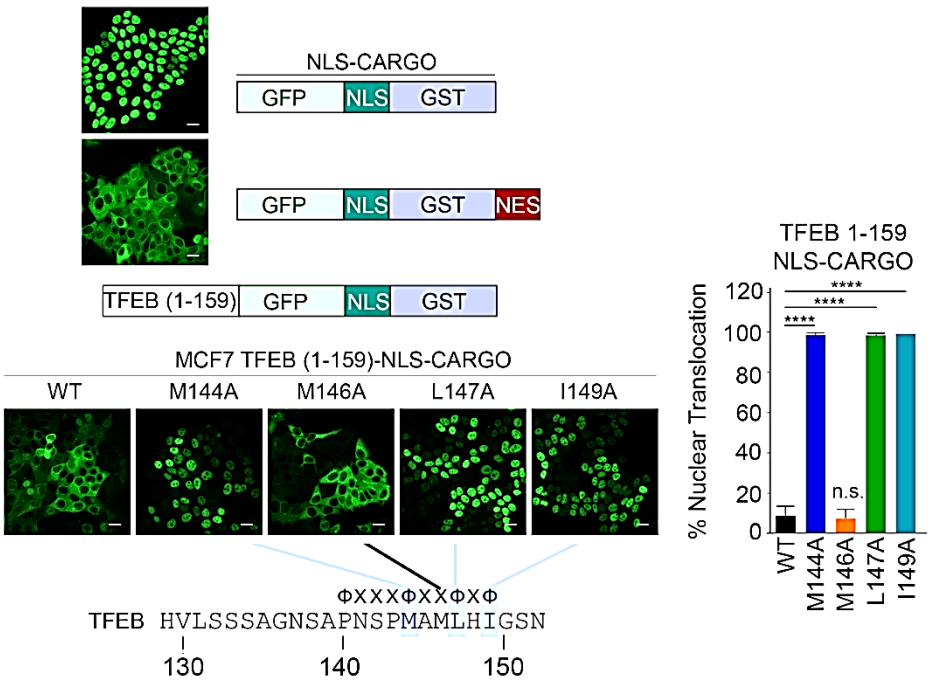


Figure 3.2.10.2 The hydrophobic residues are indispensable for the NES. Fluorescent imaging of MCF7 cell lines stably expressing the NLS-CARGO, NLS-CARGO-NES (top) or WT or hydrophobic residue-mutated TFEB (1-159)-NLS-CARGO proteins (bottom). *n* >120 cells per condition. Scale bars = 20 μm. Student's *t*-test: ****$P < 0.0001$. Error bars = SD.

The cytoplasmic localisation by the addition of a NES sequence strongly suggested that the re-location of the GST-NLS-GFP cargo was due to nuclear export. We sought to answer whether the cytoplasmic re-location of the cargo by adding the N-terminal region of TFEB was achieved via the same mechanism. Therefore, the hydrophobic residues of the putative CRM1 consensus sequence in the TFEB (1-159)-GST-NLS-GFP cargo were mutated to alanine. Promisingly, the M144A, L147A and I149A substitutions completely disabled the re-localisation of the cargo protein, while the mutation of an irrelevant hydrophobic residue M146

to alanine behaved just as WT (**Figure 3.2.10.2**), highlighting the indispensable roles of the consensus motif in functioning as an NES.

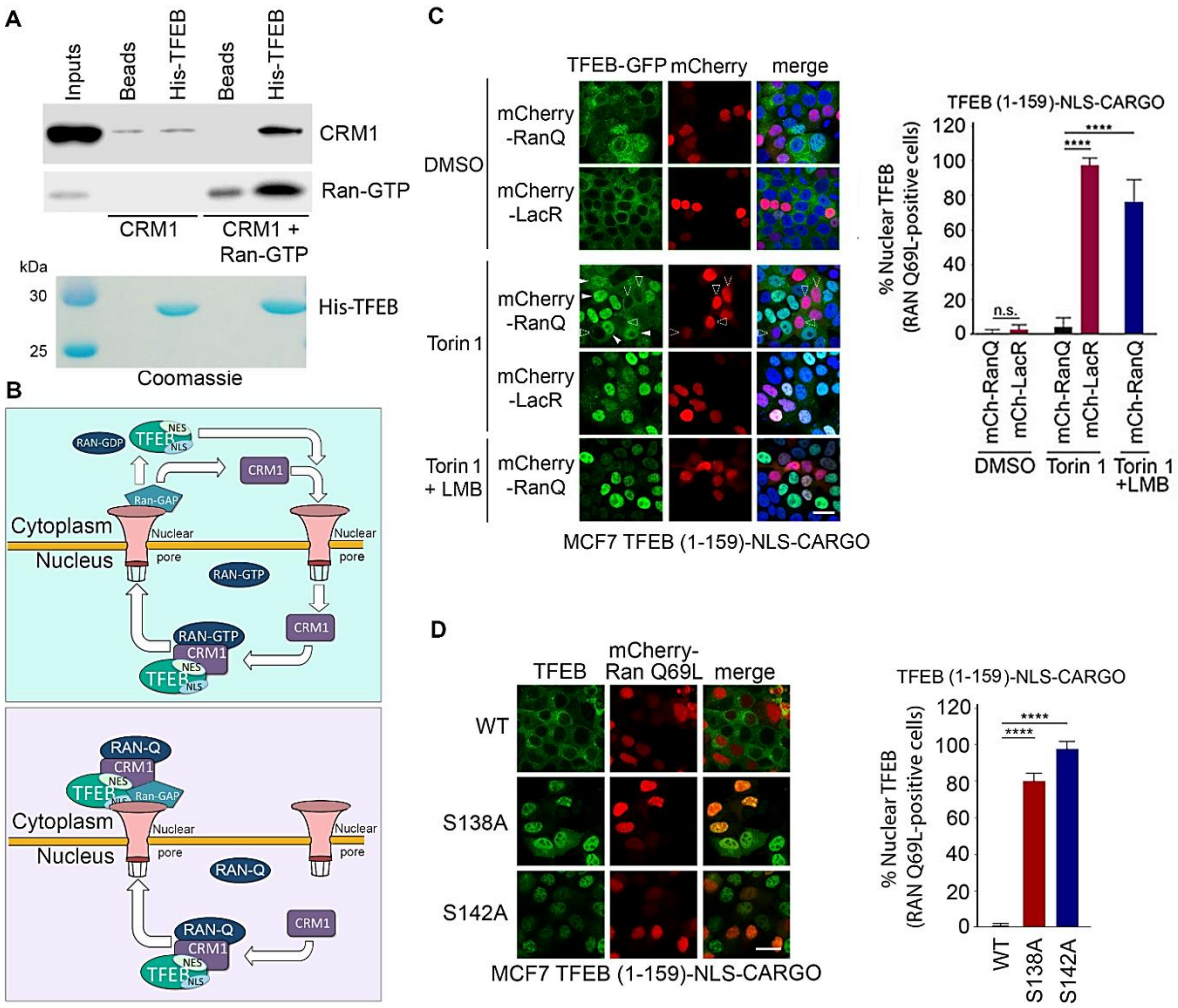


Figure 3.2.10.3 TFEB nuclear export is CRM1- and Ran-dependent. *Legend continues at the bottom of next page.*

A previous study of the CRM1 interactome revealed that among its over 4,400 binding partners, TFEB ranked as the 2nd in the interaction score, TFE3 the 59th and MITF the 762nd (Kırlı et al., 2015). In collaboration with Dr Katherine Borden's group from University of Montreal, Canada, we were able to show that recombinant TFEB amino acids 1-200 can indeed interact with CRM1 in vitro, but only in the presence of Ran-GTP, a Ras-related small GTP binding protein (**Figure 3.2.10.3 A**) since the binding of CRM1 to its cargos requires Ran-GTP. When the CRM1-Ran-cargo complex is transported from the nucleus to the cytoplasm through the nuclear pore, the GTPase activity of Ran is activated. The hydrolysis of GTP to GDP by Ran releases the cargo from the association with CRM1, the latter can therefore re-shuttle into the nucleus for the next export cycle (**Figure 3.2.10.3 B**, upper panel). The GTPase activity of Ran can be prevented by a Q69L mutation (Hughes et al., 1998; Inoue and Zhang, 2014; Dumont

Figure 3.2.10.3 TFEB nuclear export is CRM1- and Ran-dependent. (**A**) Immunoblotting using indicated antibodies to detect CRM1 and RAN after pull down of immobilized HIS-tagged TFEB (aa 1–200). All proteins were bacterially expressed and purified. Purified TFEB was visualized by Coomassie staining (lower panel). (**B**) Schematic showing the working model of TFEB nuclear export mediated by CRM1-RAN complex. CRM1 binds to the NES of TFEB in the presence of RAN-GTP and exports out of the nucleus through the nuclear pore, after which RAN-GTPase is activated, and TFEB is released from the complex upon GTP hydrolysis. The free TFEB and CRM1 can therefore enter the nucleus again (top). The GTPase-deficient RAN-Q69L mutant prevents the CRM1-TFEB-RAN complex from dissembling after export through the nuclear pore, and the trapped TFEB cannot enter the nucleus again (bottom). (**C**) Fluorescent imaging of MCF7 cells stably expressing the TFEB 1-159-NLS-cargo together with either mCherry-LacR or mCherry RAN-Q69L. Cells were treated with DMSO, Torin 1 (250 nM) alone or with LMB (20 nM) as indicated. Subcellular localisation of TFEB-GFP was quantified for cells expressing mCherry. $n > 100$ cells per condition. (**D**) Fluorescent imaging of MCF7 cells stably expressing WT, S138A or S142A TFEB-NLS-CARGO transfected with mCherry RAN-Q69L. Quantification is for mCherry-RAN Q69L-expressing cells only. $n > 40$ cells per condition. Scale bars = 20 μm. Student's *t*-test: ****$P < 0.0001$, n.s. not significant. Error bars = SD. The solid arrows indicate RAN-negative cells, and the empty arrows indicate RAN-positive cells. ((**A**)(**B**)(**C**)(**D**) are published data from Li et al., 2018. (**A**) was produced by Laurent Volpon.)

et al., 2007), which permits nuclear export but keeps the CRM1-Ran-cargo complex from dissociation. If TFEB interacts with CRM1 in vivo, the expression of Ran Q69L should trap TFEB in the cytoplasm because TFEB will be unable to dissociate from CRM1 or re-enter the nucleus after export (**Figure 3.2.10.3 B**, lower panel).

To test this model, mCherry-tagged Ran Q69L mutant (mCherry-RanQ) was transfected into MCF7 cells stably expressing inducible TFEB (1-159)-GST-NLS-GFP cargo, with mCherry-LacR as a negative control. The expression of mCherry-RanQ and mCherry-LacR made no difference in the cytoplasmic localisation of TFEB (1-159)-NLS-CARGO at steady state (**Figure 3.2.10.3 C**). Torin 1 treatment greatly increased the nuclear accumulation of TFEB-NLS-CARGO in the presence or absence of mCherry-LacR (**Figure 3.2.10.3 C**). By contrast, the expression of mCherry-RanQ blocked the effect of Torin 1 in promoting nuclear localisation of TFEB-NLS-CARGO (**Figure 3.2.10.3 C**). Since nuclear import also requires the participation of Ran GTPase, LMB was used to uncouple the effect of RanQ between nuclear import and export. Indeed, LMB reversed the effect of RanQ in the presence of Torin 1 (**Figure 3.2.10.3 C**), indicating nuclear export being required prior to TFEB cytoplasmic retention by Ran Q69L mutant. These results are consistent with the model in which TFEB nuclear export mediated by CRM1 is Ran-dependent. The GTPase-incapable Ran mutant drastically facilitated the nuclear export process following TFEB nuclear translocation induced by conditions such as nutrient limitation or mTORC1 inhibition, and the incapability to disassemble the CRM1-Ran-cargo complex prevented TFEB nuclear re-entry after its nuclear export.

Using the same assay, the roles of S138 and S142 phosphorylation in nuclear export were reassured by co-expressing TFEB (1-159)-NLS-CARGO containing either S138A or S142A mutation with mCherry-Ran Q69L. Although the WT cargo protein displayed only

cytoplasmic localisation, S138A and S142A mutants were mainly distributed in the nucleus even in the presence of Ran Q69L (**Figure 3.2.10.3**). This is consistent with the observations described earlier in which full-length TFEB with either S138A or S142A was incapable of being exported from the nucleus.

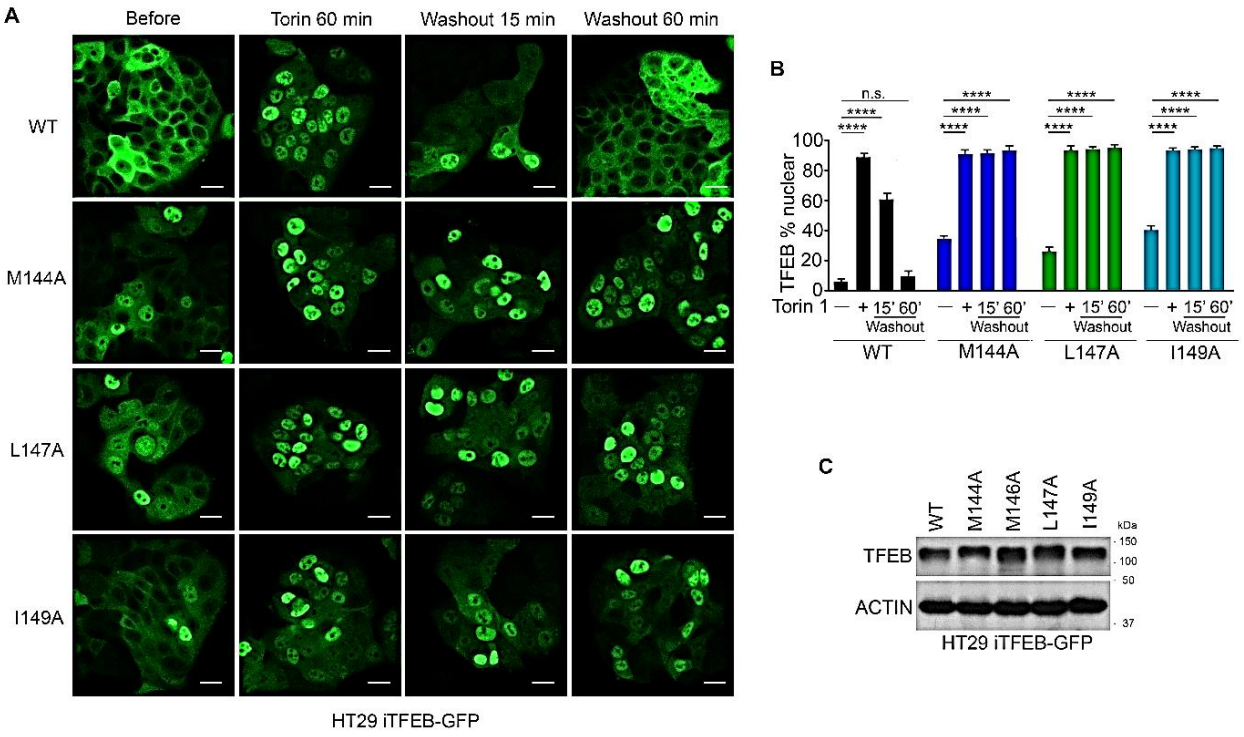


Figure 3.2.10.4 The NES controls the nuclear export of full length TFEB. (**A**) Fluorescent imaging of HT29 cell lines stably expressing WT or NES-mutated TFEB. The cells were treated with Torin (250 nM) for 60 min before the medium was replaced with normal DMEM for 15 min or 60 min. $n > 80$ cells per condition. Scale bar = 20 µm. (**B**) Quantification of the percentage of cells with TFEB nuclear localisation under conditions specified in (**A**). Student's *t*-test: ****$P < 0.0001$, n.s. not significant. Error bars = SD. ((**C**) is published data from Li et al., 2018.)

To assess the effect of the NES in full-length TFEB protein, the hydrophobic residues in the CRM1 binding motif were mutated to alanine in TFEB-GFP constructs. Under the control of a doxycycline-inducible promoter, the NES mutated TFEB-GFP proteins were carefully

titrated to similar expression levels (**Figure 3.2.10.4 C**). In contrast to that in TFEB (1-159)-GST-NLS-GFP cargo proteins, the mutation of M144, L147 and I149 displayed TFEB nuclear localisation in only 30 % to 40 % cells, very likely due to the effect of residues such as S211 in regulating cytoplasmic sequestration. Nevertheless, Torin 1 treatment resulted in a strong nuclear localisation of WT, M144A, L147A and I149A TFEB proteins. While WT TFEB re-localised to the cytoplasm after washing out Torin 1, M144A, L147 or I149A mutant TFEB remained in the nuclei by 60 min of the washout (**Figure 3.2.10.4 A, B**). These results suggest that the hydrophobic-rich motif indeed functions as an NES that controls TFEB nuclear export.

3.2.11 TFEB nuclear export is regulated by glucose

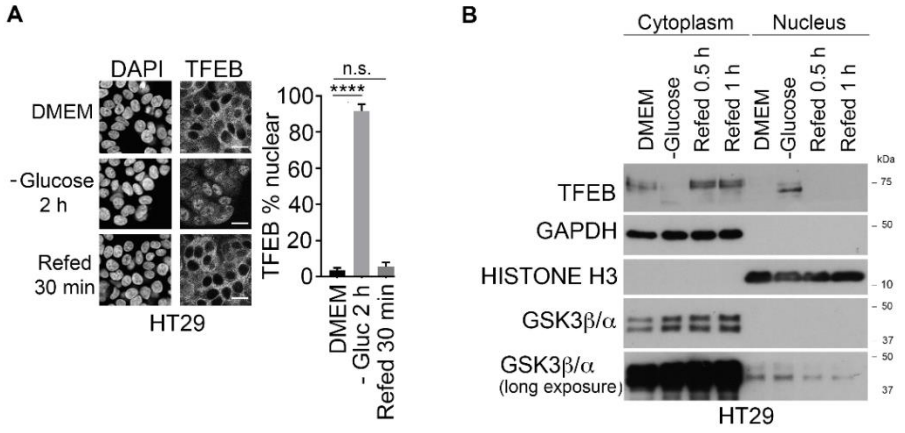


Figure 3.2.11.1 TFEB nuclear export is regulated by glucose. (**A**) Immunofluorescent imaging of HT29 cells using anti-TFEB antibody. The cells were grown in normal DMEM, glucose starved for 2 h or refed with 25 mM D-glucose. DAPI was used to stain the nuclei of the cells. $n > 100$ cells per condition. Scale bar = 20 µm. Student's *t*-test: ****$P < 0.0001$, n.s. not significant. Error bars = SD. (**B**) Immunoblotting of fractionated HT29 cells under indicated conditions using indicated antibodies. (Re-use of published data from Li et al., 2018)

The discovery of an NES in TFEB and the observations that the phosphorylation of S138 by GSK3β primed by phospho-S142 is required for TFEB nuclear export led us to re-examine the effect of glucose limitation which inactivates GSK3β mediated by AKT activation via mTORC2. Glucose starvation efficiently caused the nuclear accumulation of endogenous TFEB in HT29 cells, but glucose refeeding reversed the effect within 30 min (**Figure 3.2.11.1 A**). The immunoblotting of a cytoplasmic-nuclear fractionation experiment showed that at steady state TFEB only appeared in the cytoplasm but translocated completely into the nucleus upon glucose depletion (**Figure 3.2.11.1 B**). Consistent with fluorescent staining results, glucose refeeding redistributed TFEB back into the cytoplasm within 30 min. The blotting also revealed a small portion of GSK3β protein in the nucleus, together with the reports showing nuclear localisation of GSKβ (Meares and Jope, 2007; Zmijewski and Jope, 2004), providing the potential of GSK3β phosphorylating TFEB within the nucleus (**Figure 3.2.11.1 B**).

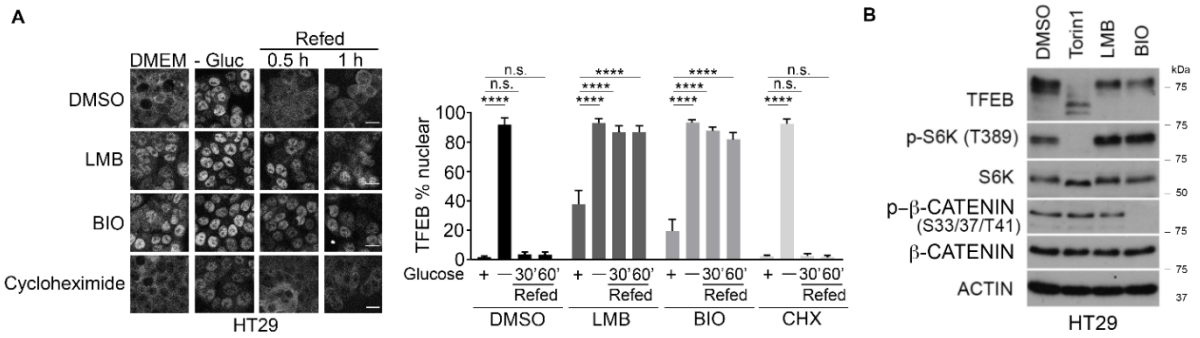


Figure 3.2.11.2 TFEB cytoplasmic relocation following glucose refeeding is subject to GSK3β-dependent nuclear export. (A) Immunofluorescent imaging of HT29 cells grown in DMEM, or starved of glucose 1 h before refeeding with glucose with DMSO, LMB (20 nM), BIO (10 μM) or cycloheximide (50 μg/ml). $n > 500$ cells per condition. Scale bars = 20 μm. Student's *t*-test; ****$P < 0.0001$, n.s. not significant. Error bars = SD. (**B**) Immunoblotting of HT29 cells treated with DMSO, Torin 1 (250 nM), LMB (20 nM) or BIO (10 μM) using indicated antibodies. (Re-use of published data from Li et al., 2018)

Endogenous TFEB accumulated in the nucleus following glucose deprivation and relocalised into the cytoplasm after glucose refeeding (**Figure 3.2.11.2 A**). The cytoplasmic relocalisation upon refeeding can be blocked by LMB as well as BIO (**Figure 3.2.11.2 A**), suggesting that it was indeed due to nuclear export and GSK3-dependent. The protein translation inhibitor cycloheximide did not affect TFEB nuclear translocation or cytoplasmic relocalisation, indicating that this apparent rapid TFEB cytoplasmic-nuclear -cytoplasmic shuttling in response to glucose availability did not arise from de novo protein synthesis (**Figure 3.2.11.2 A**). Importantly, LMB or BIO did not decrease mTORC1 activity indicated by S6K phosphorylation as opposed to Torin 1 (**Figure 3.2.11.2 B**). On the contrary, LMB and BIO slightly increased S6K phosphorylation thus mTORC1 signalling, which could be possibly explained by the transcriptional activation of *RRAGD* gene by nuclear TFEB (described in Di Malta et al. 2017 and in **Figure 3.2.3B**) under these conditions. BIO decreased the phosphorylation of β-Catenin as an indication of GSK3 inhibition, while Torin 1 or LMB did not. These data confirmed the function of LMB as a nuclear export inhibitor without affecting mTORC1 or GSK3β activity, and that BIO specifically inhibits GSK3 but not mTORC1. Pharmacological inhibition of GSK3β using other inhibitors was shown not to affect mTORC1 activity either (Marchand et al., 2015). This is also consistent with the data in **Figure 3.2.7.3** in which ectopically expressed constitutively active GSK3β substantially promoted TFEB relocalisation to the cytoplasm under glucose starvation.

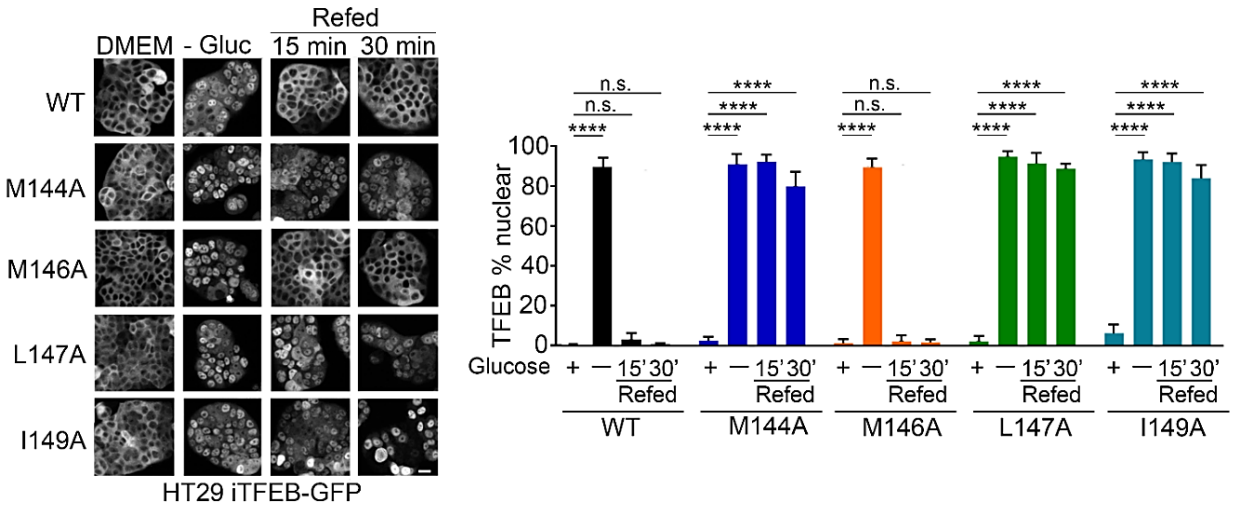


Figure 3.2.11.3 The NES controls TFEB cytoplasmic relocation following glucose refeeding. Immunofluorescent imaging of HT29 cell lines stably expressing WT, NES mutated, or M146A TFEB. The cells were glucose starved for 60 min, then were refed with 25 mM D-glucose for 15 min or 30 min. $n > 60$ cells per condition. Scale bars = 20 μm. Student's *t*-test; ****$P < 0.0001$, n.s. not significant. Error bars = SD. (Re-use of published data from Li et al., 2018)

To test whether TFEB nuclear export following glucose refeeding is mediated by the same NES, WT or hydrophobic residue-mutated TFEB-GFP was stably expressed in HT29 cells. When induced by doxycycline to express at low levels, the WT or mutant TFEB-GFP proteins all displayed strong cytoplasmic localisation in DMEM (**Figure 3.2.11.3**). Although glucose deprivation resulted in the nuclear translocation of WT and all mutants, the nuclear export of TFEB-GFP protein upon glucose refeeding only occurred with WT and the negative control M146A mutant within 15 min (**Figure 3.2.11.3**). The mutation of M144, L147 or I149 to alanine severely impaired the relocalisation of TFEB-GFP from the nucleus to the cytoplasm (**Figure 3.2.11.3**). These observations highlighted the importance of the newly identified NES not only in conditions with mTORC1 inactivation such as amino acid starvation, but also in response to

glucose limitation. Notably, even though the hydrophobic residue mutants severely blocked TFEB cytoplasmic relocalisation, there was a decrease in the percentage of cells with nuclear TFEB (**Figure 3.2.11.3**), suggesting that either the effect of single mutation of the NES consensus residues does not completely abolish nuclear export, or that there are additional nuclear export signals within TFEB protein.

3.2.12 TFEB NES mutants exhibit higher levels of autophagy

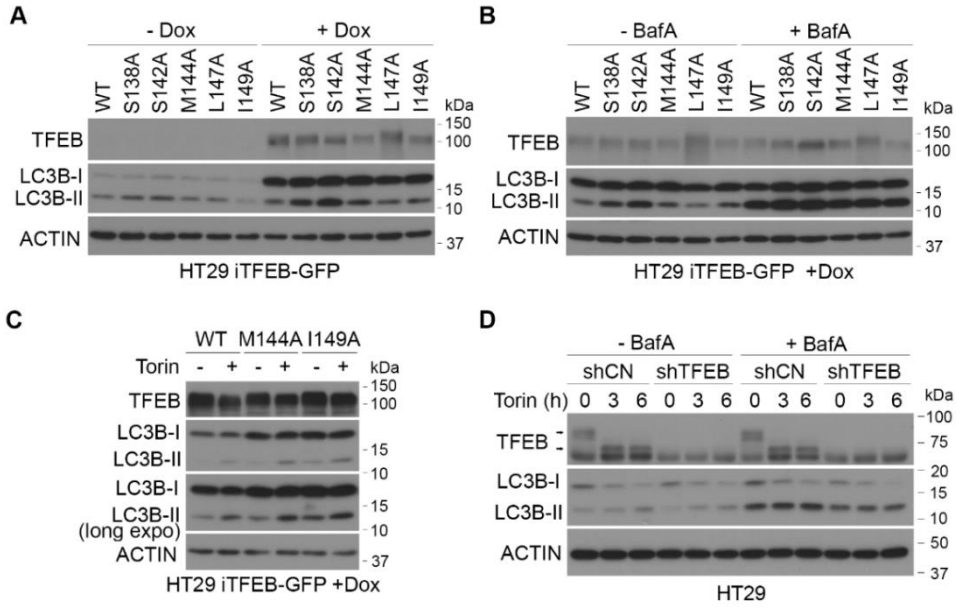


Figure 3.2.12 TFEB NES mutants exhibit higher levels of autophagy. (**A**) Immunoblotting of HT29 cell lines stably expressing WT, S138A, S142A or NES mutated TFEB-GFP in the absence or presence of doxycycline, using indicated antibodies. (**B**) Immunoblotting of HT29 cell lines stably expressing WT, S138A, S142A or NES mutated TFEB-GFP when induced with appropriate amount of doxycycline, in the absence or presence of Bafilomycin A (10 nM, 2 h). (**C**) Immunoblotting of HT29 cell lines stably expressing WT, S138A, S142A or NES mutated TFEB-GFP when induced with appropriate amount of doxycycline, in the absence or presence of Torin (250 nM, 3 h). (**D**) Immunoblotting of HT29 cells stably expressing control shRNA or shTFEB and treated with Torin (250 nM) for indicated duration, in the absence or presence of Bafilomycin A (10 nM, 2 h), using indicated antibodies. The arrows indicate TFEB protein variants.

The role of TFEB in promoting autophagy has been underscored by its transcriptional activation of a range of lysosomal and autophagic genes. Particularly TFEB regulates the

expression of LC3B that is an essential component of autophagosomes to enhance the autophagic flux (Settembre et al., 2011). As shown by immunoblotting, the expression of WT, S138A, S142A, M144A, L147A and I149A TFEB-GFP induced by doxycycline all increased the levels of unmodified LC3B-I (**Figure 3.2.12 A**). Compared to that in the uninduced cells, the phosphatidylethanolamine (PE)-conjugated LC3B-II which marks the formation of autophagosomes, was also slightly increased with WT, M144A and I149A TFEB but not L147A (**Figure 3.2.12 A**) since they displayed mostly cytoplasmic localisation at steady state. The increase in LC3B-II levels was higher with the S138A mutant which was already partially nuclear, and even higher with S142A (**Figure 3.2.12 A**), proportional to its higher nuclear localisation. Since autophagy is in constant flux, the increase in LC3B-II levels could either result from increased autophagic flux or impaired lysosomal degradation. Using BafA that blocks the lysosomal v-ATPase therefore the turnover of autophagosomes, LC3B-II levels were further increased in WT and all mutant TFEB-expressing cells, confirming that the autophagic flux was indeed boosted by the expression of WT TFEB, the GSK3β phosphorylation site mutant S138A, the ERK2/mTORC1 phosphorylation site mutant S142A and all the NES mutants M144A, L147A and I149A (**Figure 3.2.12 B**).

Since our data indicated that the difference between WT TFEB and the NES mutants lies in the ability to be exported under starvation conditions, Torin that inactivates mTORC1 to mimic amino acid starvation was used to study the effects of NES mutants in promoting autophagy. The expression of WT, M144A and I149A mutant TFEB was titrated to similar levels. In the absence of Torin, M144A and I149A mutants already exhibited slightly higher levels of LC3B-I which is the precursor of LC3B-II (**Figure 3.2.12 C**). When treated with Torin, M144A and I149A mutants resulted in noticeably higher LC3B-II levels (**Figure 3.2.12 C**),

indicating relatively higher levels of autophagy compared to that with WT TFEB. The experiment with Ran Q69L suggested that nuclear export of TFEB could still happen even when mTORC1 was inhibited (**Figure 3.2.10.3 C**). This may explain why the NES mutants did not differ from WT TFEB at steady state but exhibited higher autophagy levels under Torin treatment. Besides, it may take a longer time to maximise the difference in transcriptional activity between WT and NES mutant TFEB.

Finally, shRNA mediated knockdown of endogenous TFEB protein reduced the increase in LC3B-II levels during Torin treatment. Blocking the turnover of autophagosomes by BafA revealed that less LC3B-II formation with shTFEB was indeed due to lower autophagic flux (**Figure 3.2.12 D**). However, the effect of TFEB knockdown on LC3B was relatively mild, probably due to the redundant roles of other MITF/TFE family factors including TFE3. Double knockout of TFEB and TFE3 is therefore anticipated to cause stronger effects in reducing autophagic flux. Nevertheless, these results suggest that the effect of TFEB in promoting autophagy can be enhanced either by blocking the phosphorylation of S138 or S142, which are required for TFEB nuclear export, or by directly disrupting the NES motif.

3.3 Discussion

Using colorectal cancer and breast cancer cell lines, our data for the first time demonstrated that TFEB subcellular localisation is regulated by not only amino acid levels, but also glucose availability, highlighting the ability of TFEB to integrate inputs from both nitrogen and carbon sources. It is not surprising, since TFEB is shown to activate the genes involved in lipid catabolism as well as glucose uptake and utilisation (Mansueto et al., 2017; Settembre et al., 2013). TFEB as part of the nutrient sensing machinery is at the same time a direct effector.

Although sensing amino acids, lipids and glucose by mTORC1 is well established, our data revealed that mTORC1 activity was largely unaffected by acute glucose withdrawal, instead mTORC2 activity was dramatically elevated, consistent with the observations of a previous study (Moloughney et al., 2016). Although the mechanism underlying mTORC2 activation by low glucose remains to be elucidated, one of the consequences is that the activation of AKT leads to the inhibition of GSK3β, which is shown to phosphorylate TFEB at S138 to control its nuclear localisation. It is worth mentioning that a similar AKT activation by IRS1 feedback loop did not affect GSK3β phosphorylation, suggesting that the inactivation of GSK3β by AKT is specific at least for glucose limitation.

A number of studies have shown that GSK3β disruption by either pharmacological inhibition or RNAi-mediated knockdown increased TFEB nuclear translocation as well as lysosomal biogenesis and autophagy (Marchand et al., 2015; Parr et al., 2012; Weikel et al., 2016). The study which demonstrated direct phosphorylation of TFEB by GSK3β (Li et al., 2016) posited that the phosphorylation of TFEB S134/S138 is S142 or mTOR independent, and that GSK3β inhibition dissociates TFEB from the lysosomes and reduces its interaction with 14-3-3. However, our data making use of kinase assays on a peptide array and phospho-mapping by quantitative mass spectrometry, proved that in principle the phosphorylation of S138 by GSK3β only occurs when primed by S142 phosphorylation. High-throughput phospho-proteomics studies further supported our in vitro results (Beausoleil et al., 2006; Dephoure et al., 2008). Furthermore, the serine to alanine substitution of the GSK3β phosphorylation site S138A did not affect TFEB lysosomal recruitment or the interaction with 14-3-3 as shown in our peer reviewed publication (**Fig.5b** in Li et al., 2018). Therefore, the mechanism by which

the phosphorylation of S142 and S138 coordinate to control TFEB subcellular localisation must be more than simply cytoplasmic anchoring and sequestration at this point.

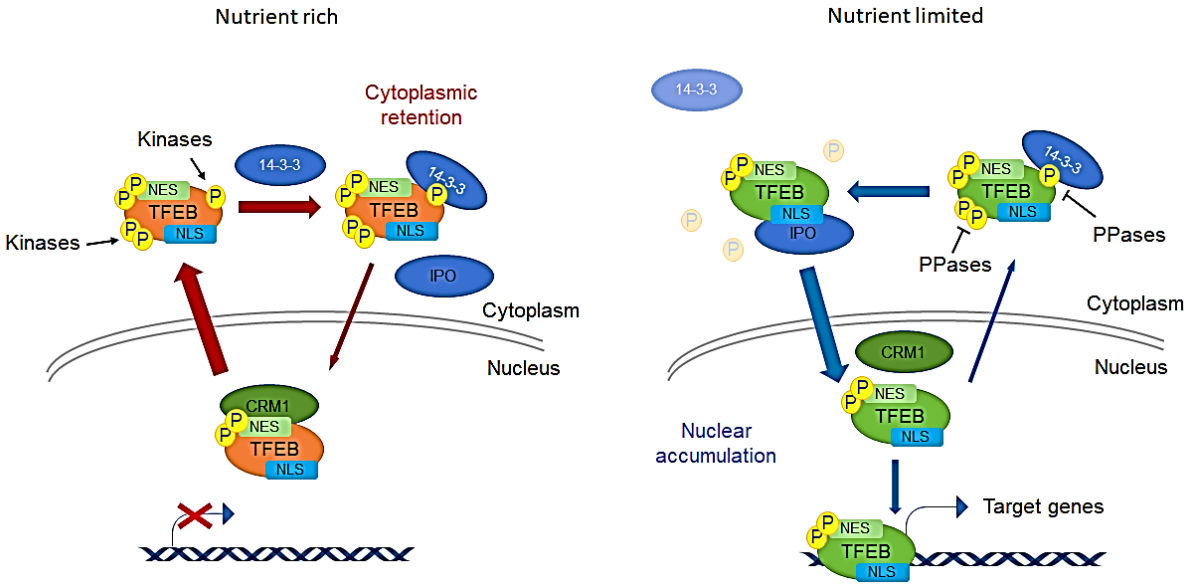


Figure 3.3.1 Model explaining the nuclear import-export equilibrium of TFEB. Left: under nutrient rich conditions, more nuclear export and less nuclear import resulting from phosphorylation and cytoplasmic sequestration lead to TFEB inactivation in the cytoplasm. Right: under nutrient limited conditions, the activation of protein phosphatases (PPases) lead to dephosphorylation and subsequently more nuclear import of TFEB than nuclear export, resulting in its nuclear accumulation and transcriptional activation. Note that TFEB may not be completed dephosphorylated in the nucleus.

In fact, our data suggested that instead of controlling nuclear import, phosphorylation of S142 and S138 together, but not either alone, activate the nuclear export of TFEB. The identification of a highly evolutionarily conserved nuclear export signal in the vicinity of S142 and S138 is the key to understanding the cytoplasmic relocalisation of TFEB upon nutrient replenishment. This NES acts through the interaction with the nuclear exportin CRM1 in a Ran-dependent manner. Our live cell imaging results (**Fig. 1b** in Li et al., 2018) and the effect of LMB (**Figure 3.2.10.1 A** and **Fig. 1e** in Li et al., 2018) indicate that even under nutrient rich conditions, there is a constant shuttling of TFEB in and out of the nucleus. On the other hand,

TFEB cytoplasmic re-localisation could be facilitated by the dominant negative Ran Q69L mutant under conditions where mTORC1 was inhibited, suggesting that TFEB retains its nuclear export potential even under nutrient starvation. Rather than a black-or-white situation, the highly dynamic TFEB nuclear-cytoplasmic trafficking is more of an equilibrium which shifts toward rebalancing cellular metabolism in accordance with the physiological nutrient fluctuation. When nutrients are abundant, more nuclear export and less import of TFEB lead to its cytoplasmic inactivation. When nutrients are scarce, more nuclear import and less export physically positions TFEB at a working state, which activates the transcription of genes involved in catabolic processes such as lysosomal biogenesis, autophagy, lipid breakdown and glucose utilisation, in order to maintain nutrient and energy homeostasis (**Figure 3.3.1**).

Although we have not definitively shown how the phosphorylation of S138 and S142 activates TFEB nuclear export, we hypothesise that intra-molecular folding of TFEB may bury the NES beneath the molecular interface required for CRM1 interaction, and the phosphorylation at S138 and S142 which introduces more local polarisation may help open up the closed conformation to expose the hydrophobic interface of the NES. Alternatively, the NES may be masked by other proteins when S138 and S142 are not phosphorylated, with phosphorylation disrupting this interaction and unmasking the NES, a mechanism seen with the tumour repressor BRCA2 (Jeyasekharan et al., 2013). However, testing these hypotheses requires intensive structural studies. Despite the fact that nuclear export promoted by single residue phosphorylation is commonly seen with e.g. p53, Cyclin D1, MAPKAP and PHAX (Alt et al., 2000; Engel et al., 1998; Ohno et al., 2000; Zhang and Xiong, 2001), TFEB nuclear export regulated by two sequential phosphorylation events appears to be rare. And it is particularly interesting that the NES in TFEB receives inputs from multiple signalling pathways, including

mTORC1 or ERK2 for S142 and mTORC2-AKT-GSK3β for S138, to orchestrate cellular responses to amino acid and glucose availability as well as other stimuli such as growth factors (**Figure 3.3.2**).

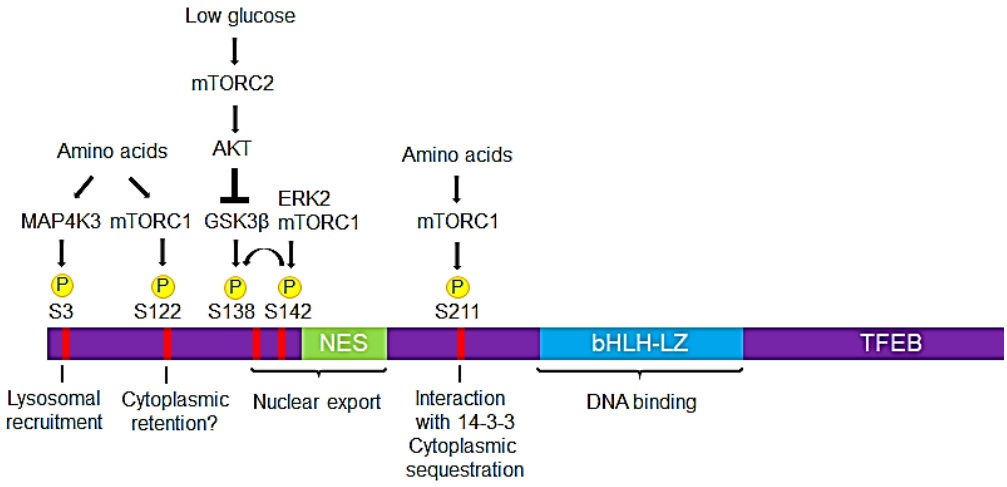


Figure 3.3.2 Model explaining the role of phosphorylation in regulating TFEB subcellular localisation. An illustration of key phosphorylation events that control TFEB subcellular localisation and their corresponding kinases in response to nutrient levels.

The dephosphorylation of TFEB under glucose deprivation suggested the participation of the phosphatases. However, our data do not support Calcineurin as being involved in low glucose-induced TFEB nuclear accumulation. PP2A was recently shown to dephosphorylate TFEB under oxidative stress (Martina and Puertollano, 2018). Considering that disruption of glycolytic flux may also cause perturbation in the respiratory chain complexes in the mitochondria, it is likely that PP2A has a similar effect under glucose starvation. Interestingly, in that study, PP2A dephosphorylates TFEB at several residues including S109, S114, S122 and S211 (Martina and Puertollano, 2018), but not S138 or S142. Although S211 has already been shown as an important cytoplasmic anchoring site of TFEB, the role of S122 is less clear but

has a similar function. Losing cytoplasmic anchoring is sufficient to promote TFEB nuclear entry. The phospho-proteomic data supports a model in which the dephosphorylation of S138 or S142 are not required for TFEB nuclear import (Martina and Puertollano, 2018), while another model argues that S138 and S142 are dephosphorylated before entering the nucleus and re-phosphorylated upon nutrient refeeding. In fact, the nuclear pool of TFEB is at least partially phosphorylated (Peña-Llopis et al., 2011). It is therefore likely that the retained phosphorylation at S138 and S142 may be important for the rapid attenuation of TFEB transcriptional activity soon after nutrient replenishment through its nuclear export (**Figure 3.3.1**). Although the phosphorylation status of S138 under glucose starvation remains to be determined using phospho-specific antibodies or mass spectrometry, our data using loss-of-function and gain-of-function approaches suggested that GSK3β activity is equally, if not more, as important as the phosphatases.

Lastly, S138A and S142A mutant TFEB exhibited higher levels of autophagy compared to WT due to the defect in nuclear export. A similar effect was seen with the NES mutants under conditions where mTORC1 was inhibited. These results link the spatial restraints of TFEB to its function. Consistent with our data, a recent study reported that inhibition of protein nuclear export enhanced autophagy and extended life span in *C. elegans* through the nuclear accumulation of HLH-30 (the *C. elegans* ortholog of TFEB) and DAF-16/FOXO (Silvestrini et al., 2018). This in vivo evidence consolidates the physiological role of TFEB nuclear export. It also provides a potential new therapeutic strategy for treating neurodegenerative diseases or cancer by modulating TFEB activity through adjusting nuclear import-export equilibrium.

Chapter 4 – A high-throughput small compound screen to identify TFEB/3 modulators

4.1 Introduction

In recent years, the role of MITF/TFE family transcription factors as master regulators of lysosomal biogenesis and autophagy has been unveiled. The potential of manipulating TFEB was immediately put on the table as a therapeutic strategy to treat lysosomal storage disorders (LSDs) such as neurodegenerative diseases as well as cancer. A growing number of studies provided promising pre-clinical data in a wide range of disease models including Alzheimer's disease, Parkinson's disease, Huntington's disease, spinal-bulbar muscular atrophy as well as Pompe disease (Cortes et al., 2014; Decressac et al., 2013; Martina et al., 2014; Polito et al., 2014; Spampanato et al., 2013; Tsunemi et al., 2012). The growth of pancreatic ductal adenocarcinoma (PDAC) cell lines can also be prevented by reducing aberrant TFE3 and MITF activity (Perera et al., 2015).

However, the majority of the studies have been restricted to using transient transfection or virus-mediated overexpression or shRNA-mediated stable knockdown of TFEB or TFE3, which is not ideal for clinical purposes. Pharmacological inhibition of mTORC1 is an efficient way to up-regulate TFEB activity, but has many complications as discussed in section 1.2.3 Nevertheless, the idea of modulating TFEB/TFE3 subcellular localisation and transcriptional activity by small molecule compounds is appealing.

We therefore performed a high-throughput screen using 1,600 FDA-approved drugs, aimed at identifying small-molecule modulators of TFEB. Agonists of TFEB, defined as compounds that promote TFEB nuclear localisation and transcriptional activity, can be used in treating neurodegenerative diseases with defects in lysosomal functions. Antagonists of TFEB which decrease TFEB levels or its activity, on the other hand, can be used to improve therapeutic treatment of cancers such as PDAC which exhibits abnormally high lysosomal and autophagic

activity. The unbiased approach chosen may repurpose the drugs that are already approved for certain clinical use toward novel therapeutic implications, and the existing FDA approval may also speed up the clinical trial process.

This project comprises three major steps. The first is the high content imaging-based initial screen. Given that TFEB is the key to balancing lysosomal homeostasis and that its subcellular localisation determines its transcriptional activity, this step attempted to use TFEB localisation as well as protein level as a phenotypic readout to indicate the potentially effective compounds. The second step is to validate the hits from the initial screen for their function in lysosomal biogenesis and autophagy using various cell-based assays. The third step will be testing the effectiveness in a number of disease models.

The benefit from this project is not limited to the potential clinical value of the compounds. Deciphering the mechanisms through which the drugs activate or repress TFEB may also potentially reveal its novel regulation, providing new insights into understanding the nature of nutrient and energy homeostasis of the cell. In return, more precise and effective medication can be designed and developed based on the knowledge acquired.

4.2 Screen Procedure

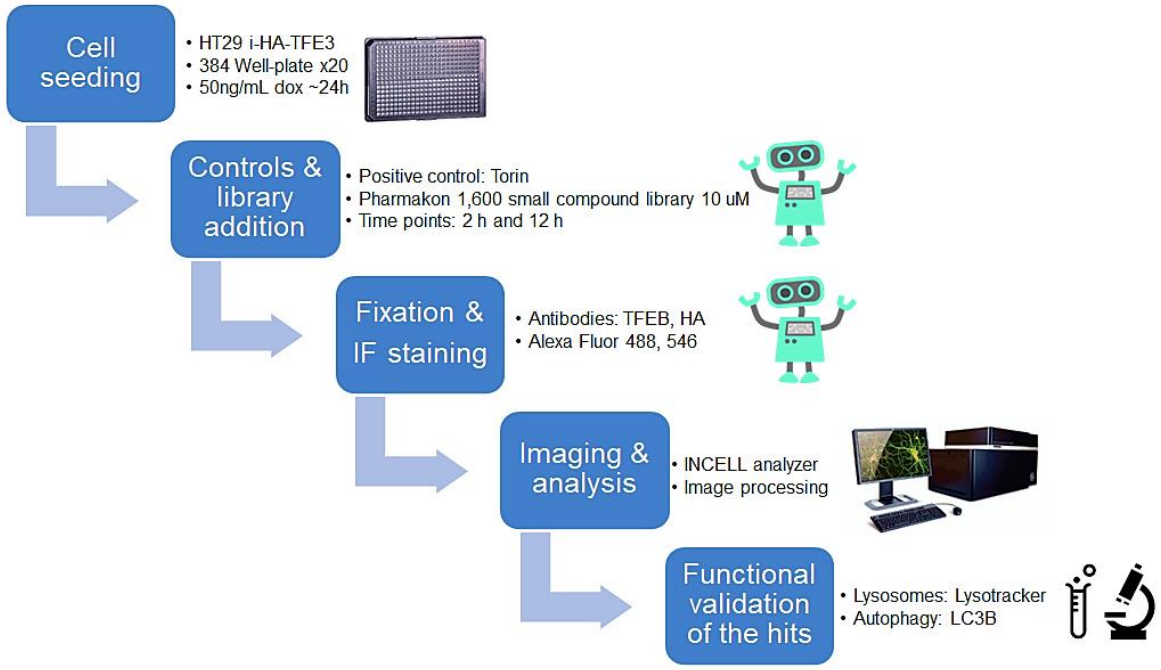


Figure 4.2.1 A flow chart of the screen procedure. The details of cell seeding, the addition of controls and compound library, immunofluorescent staining, high-content imaging, image processing and functional validation are described in the text.

Since studies in the last decade revealed that TFEB and TFE3 are the master regulators of lysosomal biogenesis and autophagy, the key to treating cancer and LSDs such as neurodegenerative diseases is to identify compounds that can modulate the nuclear translocation of TFEB and TFE3. To fulfil such purpose, the high-throughput screen was performed making use of the colorectal cancer cell line HT29 which expresses endogenous TFEB and exogenous HA-tagged TFE3 when induced with doxycycline (**Figure 4.2.1**). The screen was performed in a 384-well plate format in duplicates, where in addition to a cells alone control, the negative control DMSO and positive control Torin were added to individual wells, as well as the Pharmakon 1,600 small compound library which constitute 5 experimental plates. 2 hours and

12 hours of incubation was carried out for each treatment considering that different compounds may have different effective kinetics to the cells. After the incubation with the controls and the library compounds, the cells were fixed, permeabilised and immuno-stained for endogenous TFEB (Alexa Fluor 488 as secondary staining) and exogenous HA-TFE3 using an anti-HA antibody (Alexa Fluor 546 as secondary staining). The cell seeding, doxycycline addition, control and compound library treatment and immunofluorescent staining procedures were automated utilising the robotics of the BioStar liquid handling system. The high-content imaging of the screen was performed using IN Cell Analyzer 6000 (GE Healthcare), and image processing was performed using a protocol customised in GE Developer Toolbox software. The hits from the imaged-based screen were then subject to validation with functional assays to measure their effects in lysosomal biogenesis and autophagy.

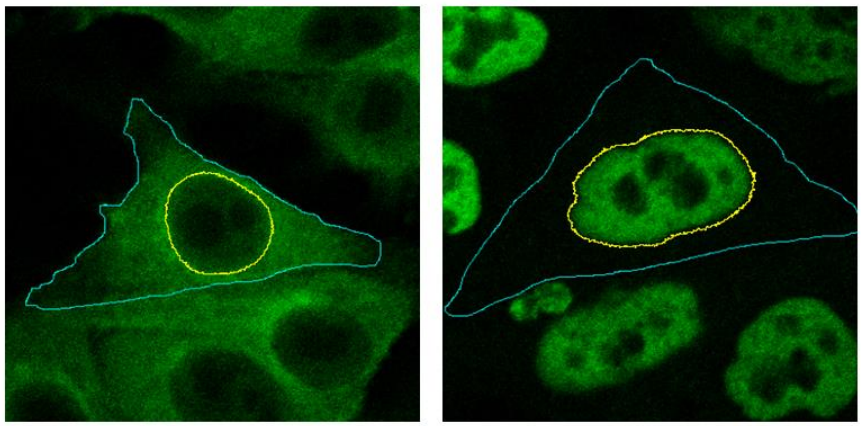


Figure 4.2.2 Ratio Nuc/Cyto is used as a metric to determine the subcellular localisation of TFEB. Left: TFEB is more cytoplasmic if the ratio of nuclear intensity to cytoplasmic intensity is below 1. Right: TFEB is more nuclear if the ratio is above 1.

As an automated process, the image analysis used the ratio of the nuclear fluorescent intensity to cytoplasmic fluorescent intensity (Ratio Nuc/Cyto) as a readout to determine the predominant localisation of TFEB and TFE3 (**Figure 4.2.2**). If the ratio is below 1, the proteins is more localised in the cytoplasm, whereas a ratio of above 1 indicates a more nuclear localisation.

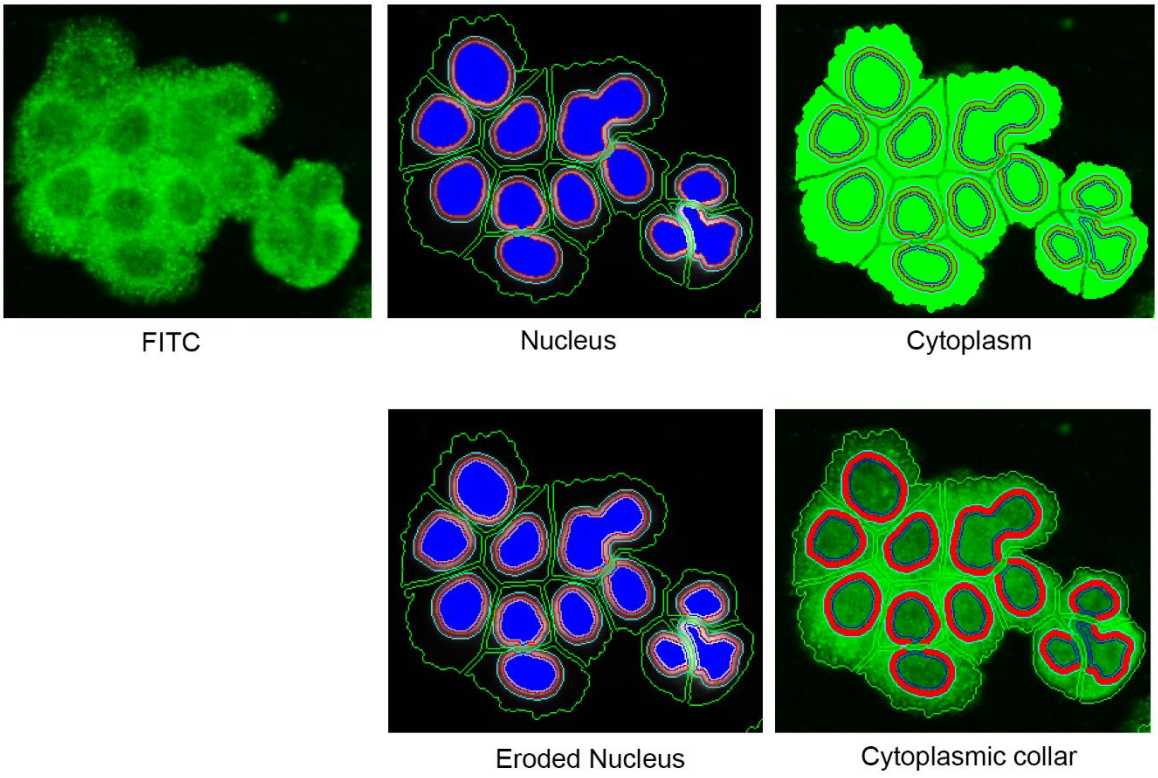


Figure 4.2.3 The two masking methods to isolate cytoplasmic area and nuclear area. The nuclear area was determined by DAPI staining and cytoplasm by TFEB staining using the FITC channel (top). Alternatively, the eroded nucleus was created to represent nuclear area and a cytoplasmic collar around the nucleus was selected to represent the cytoplasmic area (bottom). (Image processing protocol is developed by Val Millar)

The key to separating the nucleus and the cytoplasm is to create corresponding masks using the fluorescent images. With the assistance of the software, DAPI staining was used to demarcate the nuclear area, and the cytoplasmic area of each cell was determined by the fluorescent intensity in FITC or DsRed channel for TFEB or HA-TFE3, respectively. Since the

boundaries between the nucleus and the cytoplasm are often vague and the fluorescent intensity in the cytoplasm is not evenly distributed (higher around the nucleus while lower closed to cell membrane), to reduce the noise-signal ratio, the nuclear area and the cytoplasmic area were trimmed using an eroded nucleus mask and a cytoplasmic collar mask when calculating the Ratio Nuc/Cyto for the purpose of comparison (**Figure 4.2.3**).

4.3 Screen Results

4.3.1 Image based screen results

Plate_Time	QC criteria	Ratio Nuc/Cyto FITC (Cytoplasm)	Ratio Nuc/Cyto FITC (Cytplasmic Collar)	Ratio Nuc/Cyto DsRed (Cytoplasm)	Ratio Nuc/Cyto DsRed (Cytoplasmic Collar)
P1_2h	Z-factor	0.67	0.72	0.73	0.84
P1_12h	Z-factor	0.19	0.24	0.79	0.88
P2_2h	Z-factor	0.65	0.64	0.82	0.87
P2_12h	Z-factor	-1.48	-1.36	0.83	0.87
P3_2h	Z-factor	0.62	0.63	0.61	0.72
P3_12h	Z-factor	-1.29	-2.00	0.78	0.83
P4_2h	Z-factor	0.43	0.46	0.71	0.76
P4_12h	Z-factor	10.08	4.98	0.79	0.84
P5_2h	Z-factor	0.62	0.57	0.64	0.76
P5_12h	Z-factor	2.19	2.28	0.81	0.86
P1_2h	SSMD	12.75	14.99	14.27	23.10
P1_12h	SSMD	5.18	5.58	18.08	31.90
P2_2h	SSMD	12.00	11.75	21.30	30.62
P2_12h	SSMD	1.70	1.79	20.73	28.76
P3_2h	SSMD	10.98	11.36	10.84	14.74
P3_12h	SSMD	1.82	1.38	18.06	23.53
P4_2h	SSMD	6.62	7.20	14.80	17.56
P4_12h	SSMD	-0.47	-1.06	20.04	27.07
P5_2h	SSMD	9.60	9.62	11.71	17.81
P5_12h	SSMD	-3.45	-3.30	22.26	30.55

Table 4.3.1.1 Quality control for the high-throughput image-based screen results. *Legend continues at the bottom of next page.*

The analysis of the high-content imaging results was automated with the customised protocol. For the purpose of quality control of the controls used in the screen, Z-factor and Strictly Standardised Mean Difference (SSMD) were calculated from the duplicates of each 384-well plate. Z-factor, defined as $\mathrm{Z-factor} = 1 - \frac{3(\sigma_P + \sigma_N)}{|\mu_P - \mu_N|}$, where σ_P and σ_N are the standard deviation of the positive (P) and negative (N) controls, μ_P and μ_N are the means of the positive and negative controls, was used to assess the robustness of the assay. If Z-factor is between 0.5 and 1.0, the assay is robust with good controls. As shown in Table 4.3.1.1, the assay readout using Ratio Nuc/Cyto in the FITC channel (TFEB) was robust for 2 hours of compound treatment for all the 5 experimental plates, but not for 12 hours (**Table 4.3.1.1**). This was most likely due to the use of Torin as a positive control, the effect of which on endogenous TFEB nuclear localisation peaks at about 1 hour but fades after around 3 hours, consistent with a previous study (Zapata et al., 2016). By contrast, Torin as a positive control was robust for both 2 hours and 12 hours using DsRed channel (HA-TFE3), indicating that TFE3 may exhibit slightly different regulation from TFEB or the difference was simply due to the ectopic expression.

As a second criteria of quality control, SSMD takes the size of the effect of the controls into account. It is defined as $\mathrm{SSMD} = \frac{\mu_P - \mu_N}{\sqrt{{\sigma_P}^2 + {\sigma_N}^2}}$, where μ_P and μ_N are the means of the positive (P) and negative (N) controls, and σ_P and σ_N are the standard deviation of the positive and negative controls. The controls are excellent if SSMD is larger than 5. Similar to the Z-factor,

Table 4.3.1.1 Quality control for the high-throughput image-based screen results. Each experimental plate at each time point was assessed for its individual Z-factor and SSMD using Ratio Nuc/Cyto derived using two masking methods for both TFEB in the FITC channel and HA-TFE3 in the DsRed Channel. The cells highlighted in blue indicate that the corresponding experimental settings meet the quality control standards for robustness.

SSMD derived from Ratio Nuc/Cyto suggested robustness of all experimental plates and time points using DsRed channel, whereas the controls were only robust for 2 hours of all plates and 12 hours of only plate 1 (**Table 4.3.1.1**). Notably, the ratio Nuc/Cyto calculated using whole cytoplasm mask displayed no difference from cytoplasmic collar method in terms of robustness.

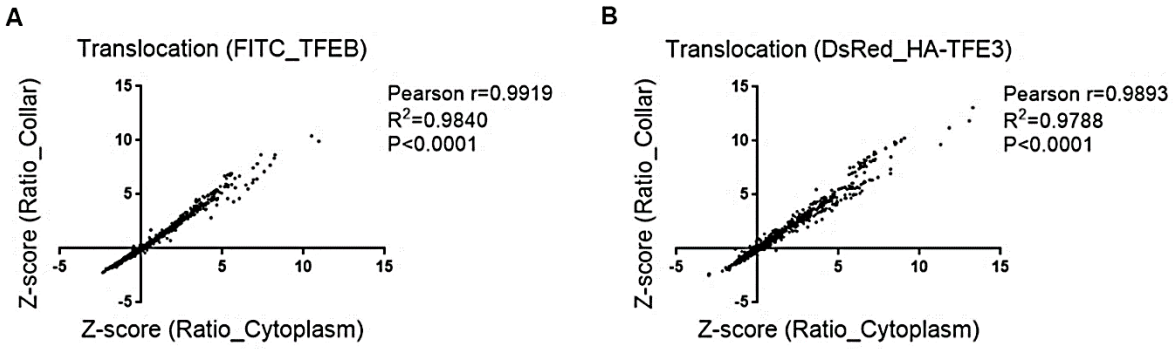


Figure 4.3.1.2 The two masking methods display no difference in generating the Z-score. (**A**) The analysis for linear correlation between the Z-scores derived from Ratio Nuc/Cyto using whole cytoplasm method (Ratio_Cytoplasm) and cytoplasmic collar method (Ratio_Collar) for TFEB in the FITC channel. (**B**) The analysis for linear correlation between Z-scores derived from Ratio Nuc/Cyto using whole cytoplasm method (Ratio_Cytoplasm) and cytoplasmic collar method (Ratio_Collar) for HA-TFE3 in the DsRed channel.

The nuclear translocation metrics using ratio Nuc/Cyto were normalised within each experimental plate into Z-score, defined as $Z = \frac{x-\mu}{\sigma}$, where x is the raw value, μ is the mean of the whole plate and σ is the standard deviation of the whole plate. A compound with a higher Z-score suggests that it promotes stronger TFEB nuclear translocation. The raw value of ratio Nuc/Cyto was calculated using the total cytoplasmic mask or the cytoplasmic collar mask as described above. The difference in Z-scores calculated between the two methods of each compound was evaluated using the Pearson correlation coefficient, which showed nearly perfect linear correlation for both FITC and DsRed channels (**Figure 4.3.1.2 A, B**), indicating that there

was no difference between the two masking methods. For this reason, Z-score derived from individual ratio Nuc/Cyto calculated using total cytoplasmic mask was used as the main parameter for the following studies.

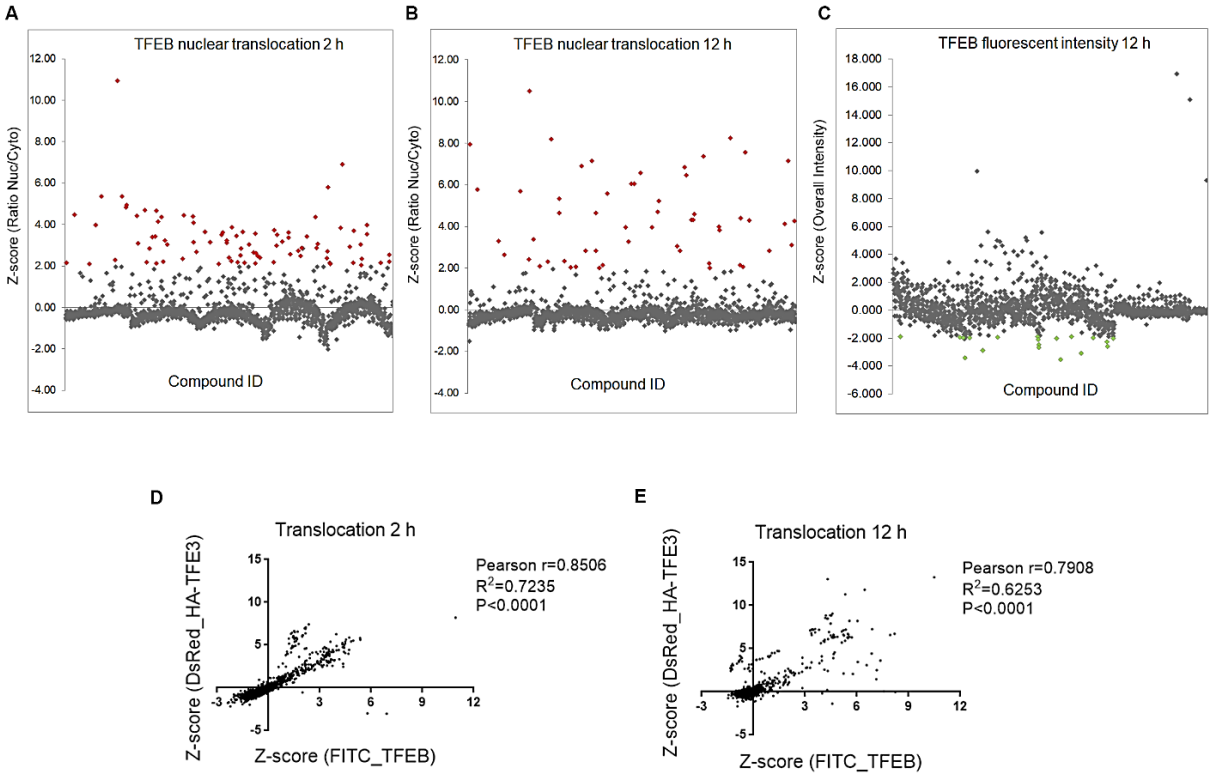


Figure 4.3.1.3 Image-based screen results indicated by the Z-scores of the small compounds. (**A**) Scatter dot plot showing the Z-scores of all the compounds for TFEB nuclear translocation at 2 h. Red indicates that the individual compound has a Z-score above 2.0. (**B**) Scatter dot plot showing the Z-scores of all the compounds for TFEB nuclear translocation at 12 h. Red indicates that the individual compound has a Z-score above 2.0. (**C**) Scatter dot plot showing the Z-scores of all the compounds for TFEB fluorescent intensity at 12 h. Red indicates that the individual compound has a Z-score below -2.0. (**D**) Analysis for linear correlation of the Z-scores of all the compounds for nuclear translocation at 2 h between TFEB and HA-TFE3. (**E**) Analysis for linear correlation of the Z-scores of all the compounds for nuclear translocation at 12 h between TFEB and HA-TFE3.

The Z-score allows us to compare the effect of the compounds on nuclear localisation of TFEB or HA-TFE3 among different plates. A threshold of 2.0 was set to narrow down the compounds that had the strongest effects. A compound with a Z-score of above 2.0 was counted as a hit. For TFEB nuclear translocation, there were 86 initial hits for 2 hours and 54 hits for 12 hours (**Figure 4.3.1.3 A, B**), including the ones picked up at both time points. The Z-score for overall fluorescent intensity of TFEB was also calculated. Since the nuclear translocation of TFEB also dramatically increased its overall intensity, the increase in fluorescent intensity was not considered as a valid observation but an artefact from image processing. On the other hand, the decrease in fluorescent intensity is less likely to result from effects other than an actual protein level decrease. Therefore, a threshold of -2.0 was set as the cut-off to filter the compounds that down-regulate endogenous TFEB protein levels at 12 hours. In this case, a total number of 24 compounds were included as hits (**Figure 4.3.1.3 C**).

Although the majority of the compounds had the same effect on both TFEB and TFE3 shown by the high degree of correlation at both 2 hours and 12 hours, interestingly, a small cluster of compounds which diverged from the mainstream preferentially enhanced TFE3 nuclear translocation over TFEB at 2 hours, and a similar subset was observed at 12 hours as well as a handful of compounds which preferentially affected TFEB translocation (**Figure 4.3.1.3 D, E**). Examining the differential effect of those compounds may reveal the potential differential regulation between the two factors. However, the possible effect of ectopic expression of HA-TFE3 remains to be thoroughly assessed, thus this study will momentarily focus on endogenous TFEB.

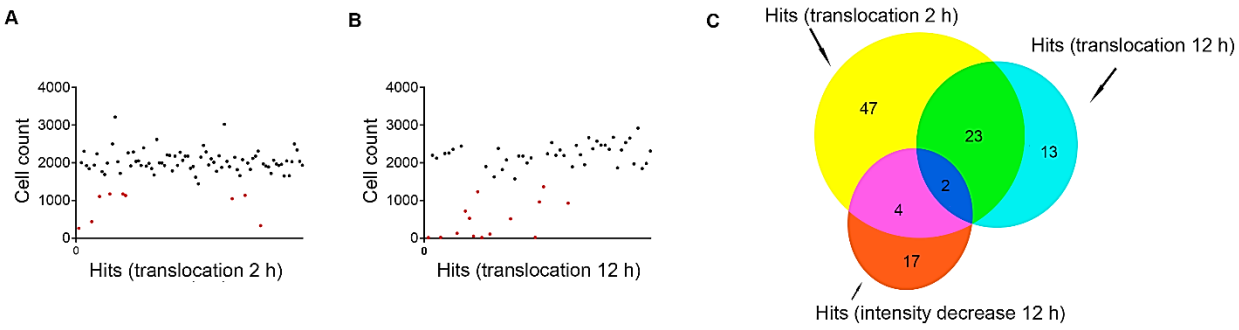


Figure 4.3.1.4 Screen hits are filtered for cytotoxicity. (**A**) Dot plot of the cell counts of the hits for TFEB nuclear translocation at 2 h. Red dots indicate the potential cytotoxicity of the hits. (**B**) Dot plot of the cell counts of the hits for TFEB nuclear translocation at 12 h. Red dots indicate the potential cytotoxicity of the hits. (**C**) The Venn diagram depicting the relations of the non-cytotoxic hits for TFEB nuclear translocation at 2 h, 12 h and TFEB fluorescent intensity decrease at 12h.

The cytotoxicity of the compounds was determined by the number of living cells compared to the average cell count of each well. From the initial hits, there were 9 compounds that severely decreased the viability of the cells at 2 hours, and 13 compounds at 12 hours (**Figure 4.3.1.4 A, B**). After excluding the toxic compounds, an overlap of 23 hits was seen both at 2 hour and 12 hour-time points. Two hits were found to cause both nuclear translocation at 2 hours and 12 hours translocation and intensity decrease at 12 hours. From the hits in the 2 hour translocation subset, 4 compounds were able to decrease TFEB intensity at 12 hours. The remaining 47 hits in the 2 hour translocation, 13 hits in 12 hour translocation and 17 hits in 12 hour intensity decrease, together with the hits shared by two or three of these groups, constitute a total of 106 hits from the initial image-based screen (**Figure 4.3.1.4 C**).

4.3.2 Functional validation of the hits

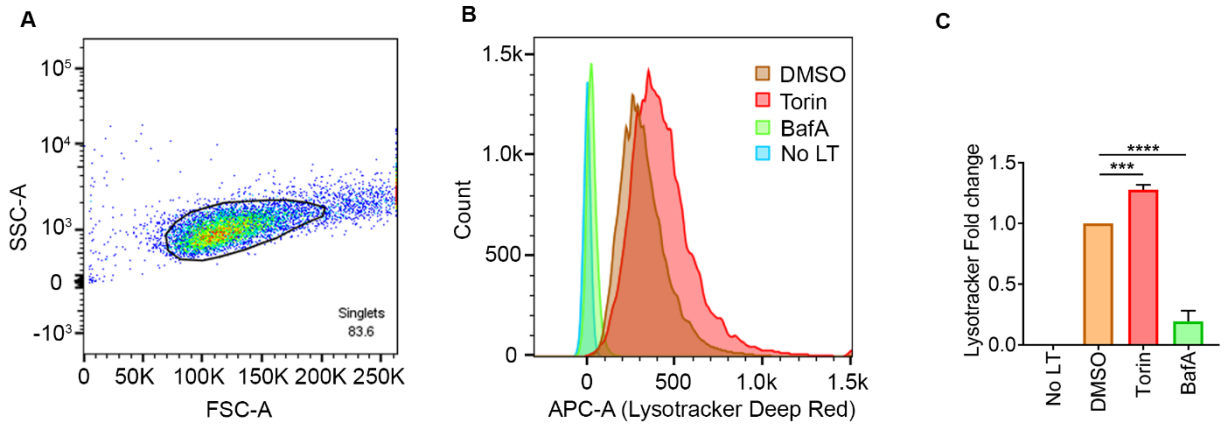


Figure 4.3.2.1 LysoTracker staining is a suitable indicator for functional lysosomes by flow cytometry. (**A**) Scatter plot showing the gating of the single HeLa cells using forward scatter (FSC-A) and side scatter (SSC-A). (**B**) The spectra of the LysoTracker staining of the HeLa cells treated with DMSO, Torin (1 µM, 3 h) or BafA (10 µM, 3 h), or without LysoTracker Deep Red dye (No LT). n > 8,000 cells per condition. (**C**) Quantification of LysoTracker mean intensity of each condition in (**A**) normalised to DMSO. Student's t-test: ****P < 0.0001, ***P < 0.001. Error bars = SD.

To evaluate the effect of the initial hits on lysosomal biogenesis, LysoTracker Deep Red was used to measure the quantity of functional lysosomes in the flow cytometry experiment. LysoTracker is a fluorescent dye that has a high selectivity for acidic organelles such as lysosomes. The fluorophore is linked to a weak base that is partially protonated at neutral pH, which allows the dye to freely permeate the membrane and accumulate in the acid particles with low pH. Therefore, the accumulated fluorescent intensity is an indicator of the quantity of functional lysosomes. Single cells were gated in the flow cytometry experiment and the LysoTracker intensity was quantified using the APC channel (**Figure 4.3.2.1 A**). When normalised to a negative control, DMSO, the positive control Torin 1 which is a known mTOR inhibitor and TFEB activator, induced a spectral shift and a significant 1.3-fold change in LysoTracker staining mean intensity, suggesting a mild increase in the numbers of lysosomes within the cells (**Figure 4.3.2.1 B, C**). On the other hand, the treatment with BafA, an antibiotic

known to inhibit the v-ATPase thus blocking lysosomal acidification, severely reduced LysoTracker staining. The no LysoTracker control (no LT) resulted in no fluorescent signal (**Figure 4.3.2.1 B, C**), suggesting that background of this dye is negligible.

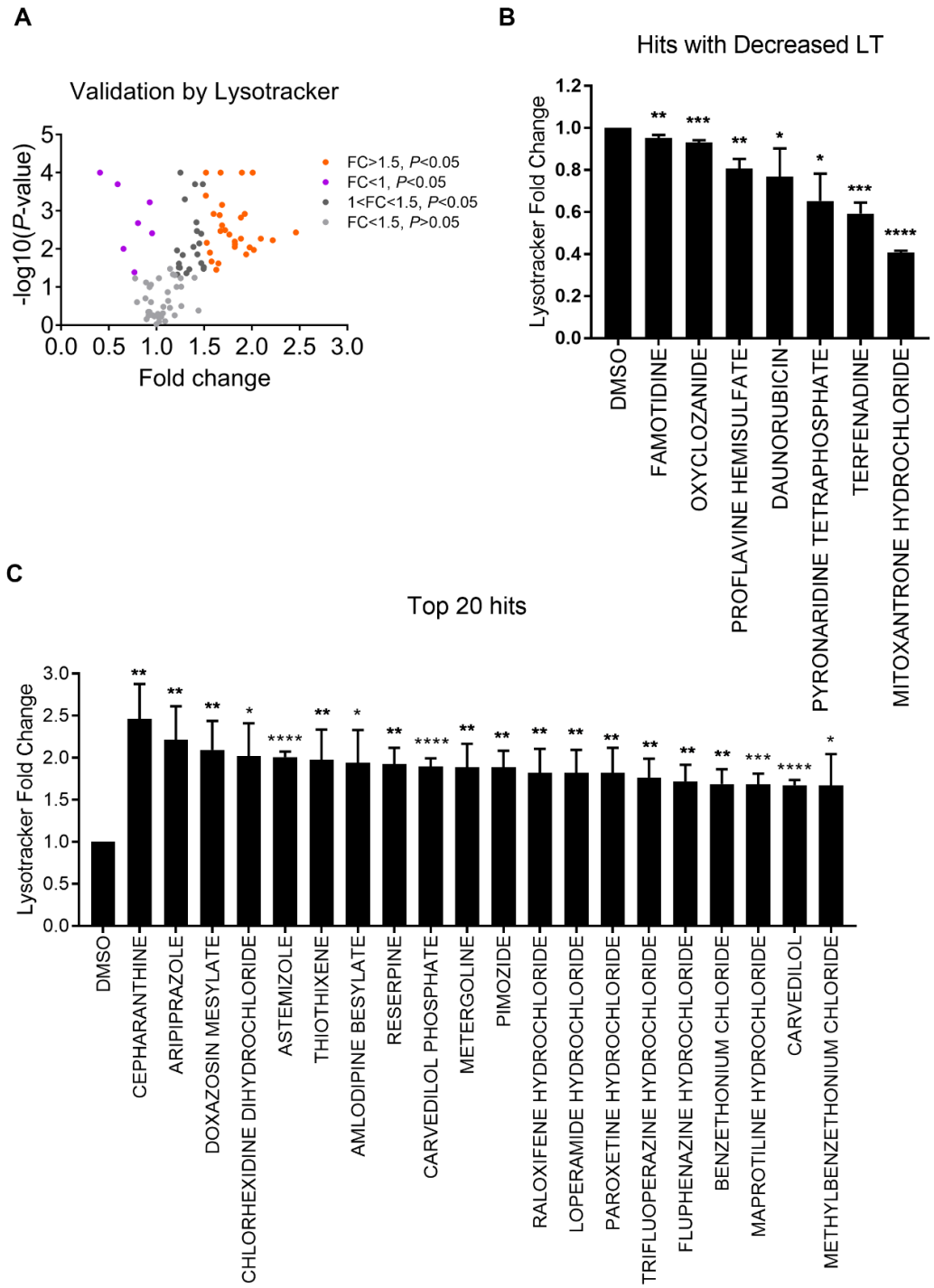


Figure 4.3.2.2 Functional validation of the hits using LysoTracker. *Legend continues at the bottom of next page.*

Using this assay, 94 available hits from the initial screen were assessed for their function in lysosomal biogenesis. 29 hits exhibited significantly ($P < 0.05$) high potential (fold change > 1.5), while 21 hits moderately (1 < fold change < 1.5) yet significantly ($P < 0.05$) increased LysoTracker staining (**Figure 4.3.2.2 A**). Among the 7 hits which decreased LysoTracker staining, mitoxantrone hydrochloride had the strongest effect and was the top hit to decrease TFEB fluorescent intensity from the initial screen (**Figure 4.3.2.2 B, Table 4.3.2.3**). Mitoxantrone is a Topoisomerase inhibitor that is approved as a chemotherapeutic drug to treat acute myeloid leukemia and prostate cancer (https://www.cancer.gov/). Although a previous study argued that mitoxantrone induced TFEB nuclear localisation and lysosomal biogenesis (Zhitomirsky and Assaraf, 2015), our unbiased screen data indicated the opposite (**Table 4.3.2.3**). Nevertheless, the ability to decrease TFEB protein levels as well lysosomal function may help to explain its cancer suppressing role in clinical use. To our surprise, although terfenadine, daunorubicin, proflavine hemisulfate and oxyclozanide appeared to increase TFEB nuclear localisation at both 2 hours and 12 hours in the initial screen, they had a negative effect on lysosomal function (**Figure 4.3.2.2 B, Table 4.3.2.3**). This is potentially attributed to the weak-base lipophilic nature of the compounds such as terfenadine and daunorubicin, which are proposed as the lysosomotropic agents that can be protonated and trapped within the lysosomes (Dielschneider et al., 2017), resulting in disrupted lysosomal function and potentially abolished lysosomal recruitment and subsequent phosphorylation of TFEB. The unphosphorylated TFEB therefore loses its cytoplasmic anchor and undergoes nuclear translocation. However, the effect

Figure 4.3.2.2 Functional validation of the hits using LysoTracker. (**A**) Volcano plot of the hits tested for LysoTracker staining. The $-\log_{10}$ (*P*-value) of each hit was plotted against its fold change in LysoTracker staining normalised to DMSO. (**B**) The bar graph showing the fold change of the hits that decreased LysoTracker staining. (**C**) Bar graph showing the fold change of the top 20 hits that increased LysoTracker staining. $n > 8{,}000$ cells per condition. All experiments were performed in triplicates. Student's *t*-test: $^{****}P < 0.0001$, $^{***}P < 0.001$, $^{**}P < 0.01$, $^{*}P < 0.05$. Error bars = SD.

of lysosomal gene expression following TFEB activation may be deteriorated by the lysosome-deteriorating drugs. The proposed working mechanism necessitates the functional validation of the hits from the imaged based screen, as TFEB nuclear translocation may not always have a functional outcome. Indeed, the validation experiment using LysoTracker confirmed only around 50 % hits from the nuclear translocation screen exhibited lysosomal biogenesis potential (**Figure 4.3.2.2**).

Drug name	Z-score_2h Translocation	Z-score_12h Translocation	Z-score_12h Intensity	LysoTracker Fold change	LysoTracker *P*-value
Torin 1	2.114	1.110	0.088	1.354	<0.0001
Mitoxantrone hydrochloride	-0.991	-0.783	-3.520	0.408	<0.0001
Terfeneadine	2.18	6.566	1.472	0.593	0.0002
Daunorubicin	2.12	5.33	5.048	0.769	0.0413
Proflavine hemisulfate	6.91	7.57	-0.069	0.806	0.0021
Oxyclozanide	2.92	0.025	-0.095	0.917	0.0006
Cephranthine	2.54	3.11	-0.157	2.462	0.0037
Astemizole	3.62	3.97	-1.906	2.009	<0.0001
Carvedilol	3.15	1.755	-0.147	1.895	<0.0001
Amlodipine	2.41	6.05	1.776	1.941	0.0139
Trifluoperazine	4.41	2.10	-0.126	1.764	0.0042
Pimozide	4.83	2.41	-1.090	1.886	0.0015
Loperamide	5.37	1.782	-1.741	1.821	0.0064

Table 4.3.2.3 Selected hits from the high throughput screen and the functional validation and their effects on TFEB nuclear translocation, protein levels and LysoTracker staining. The Z-scores for TFEB nuclear translocation at 2 h and 12 h were calculated from the Nuc/Cyto ratios generated using the whole nuclear and cytoplasmic masks. The Z-scores for TFEB intensity at 12 h were calculated using the whole cell mask. LysoTracker fold changes of the hits at 3h were normalised to DMSO control, and the *P*-values were generated using two tailed t-test. The LysoTracker experiments were performed in 3 biological replicates. Z-scores higher than 2.0 are highlighted in blue, and lower than -1.0 in red. LysoTracker fold changes higher than 1.0 are highlighted in green, and lower than 1.0 in orange.

Among the top hits that increased LysoTracker staining, cepharanthine induced the highest fold change (**Figure 4.3.2.2 C**). This is consistent with another study showing cepharanthine being able to enhance autophagy and autophagic cell death through the AMPK-

mTORC1 cascade (Law et al., 2015), therefore its ability to induce TFEB nuclear translocation and lysosomal biogenesis by inhibiting the mTORC1 pathway is not surprising. The histamine H1 receptor antagonist astemizole which was approved as an anti-allergic drug, ranked the 5th highest to induce lysosomal biogenesis in our functional validation (**Table 4.3.2.3**). It was reported to cause ER stress-induced autophagy and cell death independently of Beclin 1 but through p53 phosphorylation (Jakhar et al., 2016). The calcium channel blocker amlodipine was shown to restore the abnormal lysosomal hydrolase activity and preserve lysosomal integrity in a mouse model (Sathish et al., 2003), and it both induced TFEB nuclear translocation and increased LysoTracker staining (**Table 4.3.2.3**). Carvedilol, a non-selective α- and β-adrenoceptor blocker used to treat hypertension as well as moderate congestive heart failure, which caused TFEB nuclear translocation at 2 hours but not 12 hours in the initial screen, also increased lysosomal staining in the functional validation (**Table 4.3.2.3**). In an acute myocardial infarction rat model, the administration of carvedilol increased the formation of autophagic vacuoles and protected cardiac myocytes from cell death (Zhang et al., 2009). The examples above validated our unbiased screen. Despite that the connection between the hits and TFEB needs to be established, treating disease by modulating TFEB activity and lysosomal/autophagic functions using small-molecule compounds is plausible.

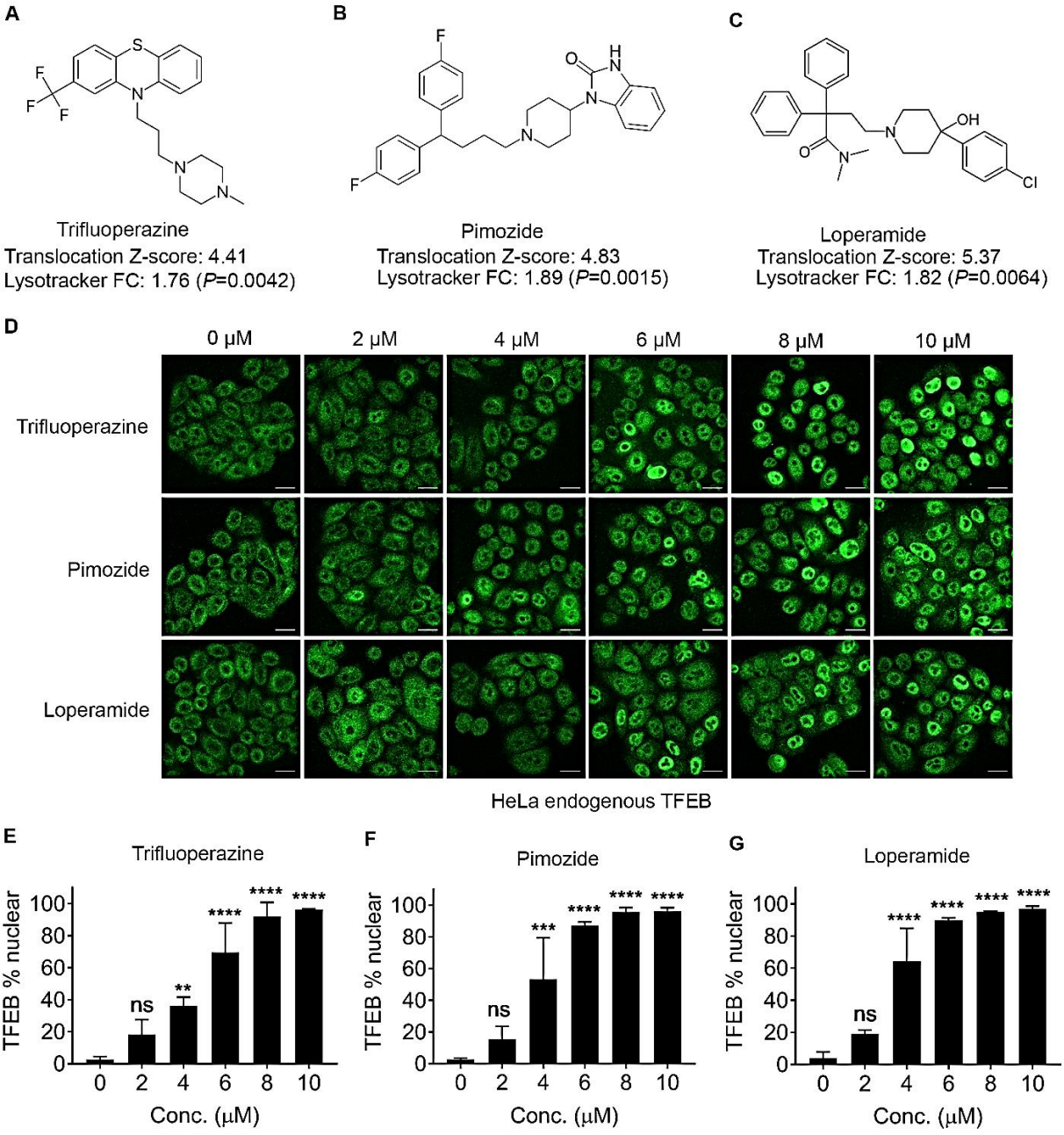


Figure 4.3.2.4 Trifluoperazine, pimozide and loperamide promote TFEB nuclear translocation. (**A**)(**B**)(**C**) Structural formulas of trifluoperazine, pimozide and loperamide with their corresponding translocation Z-score in the image-based screen and LysoTracker fold change in the functional validation. (**D**) Immunofluorescent imaging of TFEB in HeLa cells treated with trifluoperazine, pimozide or loperamide with indicated concentrations for 3 h. Scale bars = 20 µm. (**E**)(**F**)(**G**) Quantification of the percentage of cells with TFEB nuclear localisation under each condition in (**D**). $n > 50$ cells per condition. Student's *t*-test: ****$P < 0.0001$, ***$P < 0.001$, **$P < 0.01$, ns not significant. Error bars = SD.

Among the top hits from both the image-based screen and functional validation, trifluoperazine, pimozide and loperamide are particularly interesting (**Figure 4.3.2.3 A, B, C**). Not only they were identified as autophagy inducers from another high throughput screen, their effects were also shown to be mTORC1-independent (Zhang et al., 2007). Functioning as a dopamine D1, D2 receptor antagonist, trifluoperazine is primarily used to treat schizophrenia. Pimozide is also clinically used for schizophrenia and chronic psychosis for its antagonistic effect on dopamine receptors as well as 5-HT receptors. Loperamide, on the other hand, is an opioid receptor agonist that is effective for the treatment of diarrhoea. Although how trifluoperazine activates autophagy at the cellular level is not clear, pimozide and loperamide are believed to function as calcium channel blockers which reduce intra-cytosolic Ca^{2+} levels (Fleming et al., 2011), as opposed to other compounds that increase intracellular Ca^{2+} levels (Wang et al., 2018), indicating a distinct mechanism to modulate TFEB activity and autophagy. In the image-based screen, trifluoperazine, pimozide and loperamide all exhibited relatively high Z-scores for TFEB nuclear translocation (**Table 4.3.2.3**). They also resulted in bigger fold changes in lysosomal staining than Torin 1 (1.4 fold) in the functional validation using LysoTracker (**Figure 4.3.2.4 A, B, C**).

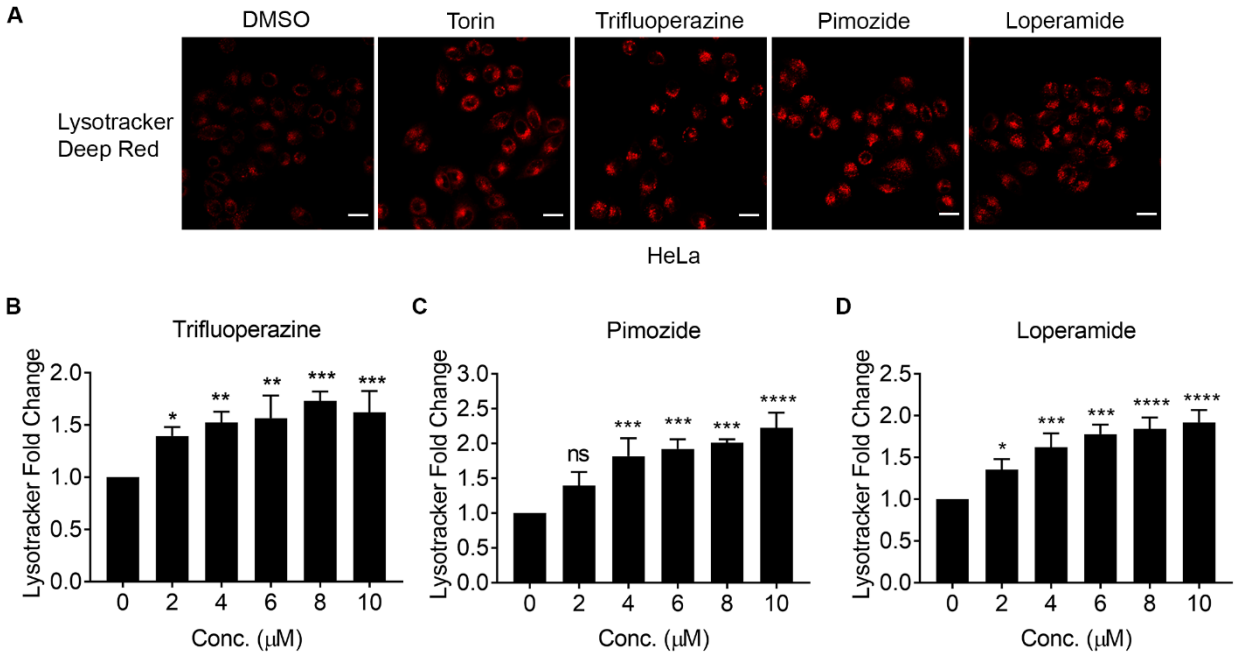


Figure 4.3.2.5 Trifluoperazine, pimozide and loperamide promote lysosomal biogenesis. (**A**) Live cell imaging of HeLa cells stained with LysoTracker Deep Red (50 nM, 30 min) after the cells were treated with DMSO, Torin (1 μM), trifluoperazine (8 μM), pimozide (6 μM) or loperamide (6 μM) for 3 h. Scale bars = 20 μm. (**B**)(**C**)(**D**) Bar graphs showing the fold change in LysoTracker staining of HeLa cells treated with trifluoperazine, pimozide or loperamide at indicated concentration for 3 h. The LysoTracker mean intensity of each condition was normalised to that of DMSO control. n > 8,000 cells per condition. Student's t-test: ****P < 0.0001, ***P < 0.001, **P < 0.01, *P < 0.05, ns not significant. Error bars = SD.

In HeLa cells, validation of these three drugs by immunofluorescent imaging revealed a dose-dependent increase of the nuclear accumulation of endogenous TFEB. Treatment of these compounds at the concentration of 2 μM had no significant effect. 4 μM of trifluoperazine caused TFEB nuclear localisation in around 40 % cells, while the percentage was slightly higher (50 %) with pimozide and loperamide at 4 μM. Trifluoperazine reached nearly maximum effect at the concentration of 8 μM, whereas 6 μM was sufficient for pimozide and loperamide (**Figure 4.3.2.4 D, E, F, G**). These results confirmed that trifluoperazine, pimozide and loperamide were able to induce TFEB nuclear translocation in a different cell line from the initial screen. To

reduce the potential off-target or cytotoxic effect of the drugs, 8 µM of trifluoperazine, 6 µM of pimozide and loperamide were used for the following experiments.

The effect of trifluoperazine, pimozide and loperamide on lysosomal function can be visualised by LysoTracker staining using live cell imaging. In HeLa cells, Torin 1 treatment increased the fluorescent intensity of LysoTracker Deep Red over the negative control DMSO, in line with the notion that mTORC1 inhibition promotes lysosomal biogenesis. Similarly, the increased LysoTracker staining was also seen with trifluoperazine, pimozide and loperamide (**Figure 4.3.2.5 A**), indicating increased numbers of functional lysosomes by these drugs. A quantitative flow cytometry experiment using LysoTracker was also performed. Consistent with the results showing dose-dependent TFEB nuclear translocation, the compounds had small or no significant effect on LysoTracker staining at the concentration of 2 µM, and the fold change continued to increase with their concentration (**Figure 4.3.2.5 B, C, D**). Therefore, all the three compounds exhibited dose-dependent effect on lysosomal biogenesis.

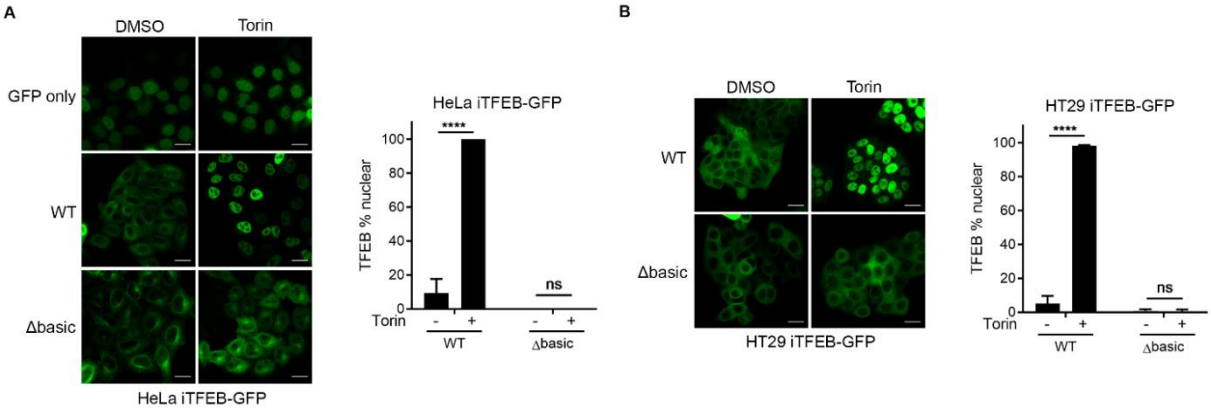


Figure 4.3.2.6 TFEB nuclear import is impaired by deletion of the basic region. (A) Fluorescent imaging of HeLa cell lines stably expressing GFP only, WT or Δbasic TFEB-GFP treated with DMSO or Torin (250 nM, 1 h). $n > 70$ cells per condition. (B) Fluorescent imaging of HT29 cell lines stably expressing WT or Δbasic TFEB-GFP treated with DMSO or Torin (250 nM, 1 h). $n > 60$ cells per condition. Scale bars = 20 µm. Student's *t*-test: ****$P < 0.0001$, ns not significant. Error bars = SD.

In attempt to investigate the TFEB-dependence in the lysosomal biogenesis induced by the three compounds, we made use of a gain-of-function assay in which WT or the basic region deleted (Δbasic) TFEB were expressed and tested with the drugs. The basic region (235-248) of TFEB contains a putative NLS that is required for the nuclear import and transcriptional activity of TFEB, similar to that of MITF (Fock et al., 2018), its absence should prevent TFEB from entering the nucleus and activating gene transcription. Fluorescent microscopy revealed that WT TFEB-GFP was localised in the cytoplasm in the absence of Torin in both HeLa and HT29 cells, while Torin treatment induced its nuclear translocation in the majority of cells as expected (**Figure 4.3.2.6 A, B**). However, the Δbasic TFEB-GFP exhibited exclusively cytoplasmic localisation irrespective of the presence of Torin. The GFP only control was used to rule out the potential artefact introduced by fusing TFEB to a fluorescent tag. Thus, the results confirmed that nuclear import of Δbasic TFEB was disabled.

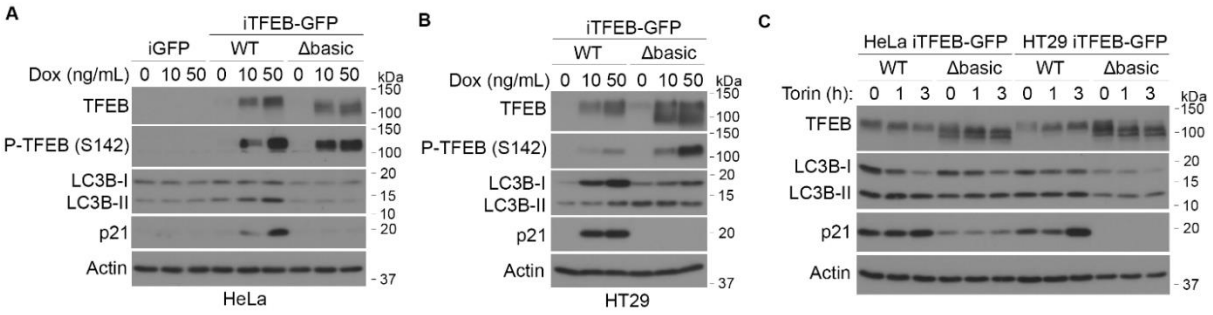


Figure 4.3.2.7 TFEB transcriptional activity is impaired by deletion of the basic region. (**A**) Immunoblotting of HeLa cell lines stably expressing GFP only, WT or Δbasic TFEB-GFP using indicated antibodies. The expression of the TFEB-GFP variants was induced by 10 ng/mL or 50 ng/mL doxycycline for 20 h. (**B**) Immunoblotting of HT29 cell lines stably expressing WT or Δbasic TFEB-GFP using indicated antibodies. The expression of the TFEB-GFP variants was induced by 10 ng/mL or 50 ng/mL doxycycline for 20 h. (C) Immunoblotting of HeLa or HT29 cell lines stably expressing WT or Δbasic TFEB-GFP using indicated antibodies. The expression of the TFEB-GFP variants was induced by 50 ng/mL doxycycline for 20 h.

To test whether the nuclear import-incapable Δbasic TFEB is also transcriptionally inert, it was expressed at similar levels to that of WT TFEB by titrating the doxycycline concentration. In HeLa cells, increasing expression of WT TFEB resulted in elevated levels of LC3B-II as well as p21 within 20 hours, two transcriptional targets of TFEB (**Figure 4.3.2.7 A**). However, the increase of LC3B or p21 was not seen with Δbasic TFEB or the GFP only control, indicating that TFEB dependent expression of LC3B or p21 could not be induced by Δbasic TFEB. A similar result was observed in HT29 cells, except that instead of the autophagosome-associated LC3B-II, it was the precursor LC3B-I that was substantially up-regulated by WT TFEB, possibly due to the difference in basal levels of autophagy induction between the two cell lines. A minor increase of LC3B-I level was seen with Δbasic TFEB, but was inconsequential compared to that obtained with WT TFEB, even though the protein level of Δbasic TFEB was higher than WT (**Figure 4.3.2.7 B**). Worth mentioning, both in HeLa and HT29 cells, the phosphorylation of S142 in both WT and Δbasic TFEB correlated well with the total protein levels, indicating that the deletion of the basic region did not affect TFEB phosphorylation by ERK2 or mTORC1 (**Figure 4.3.2.7 A, B**).

The effect of WT expression at steady state can be enhanced by conditions that induce its nuclear localisation. Indeed, in HeLa cells, Torin treatment which increased WT TFEB nuclear translocation decreased LC3B-I levels, possibly due to enhanced autophagic flux that converted LC3B-I into LC3B-II and the subsequent lysosomal degradation of autophagosomes (**Figure 4.3.2.7 C**). But the change in LC3B-I levels was relatively small with Δbasic TFEB (**Figure 4.3.2.7 C**). In HT29 cells, the effect of Torin on LC3B was minor, but it dramatically increased the protein levels of p21 at 3 hours with WT TFEB but not Δbasic (**Figure 4.3.2.7 C**). Even though the up-regulation of p21 protein levels was not as striking in HeLa cells, the

expression of WT TFEB induced much higher p21 protein levels than Δbasic. Overall, acute Torin treatment that pushed TFEB into the nucleus amplified the effect of WT, but not Δbasic TFEB.

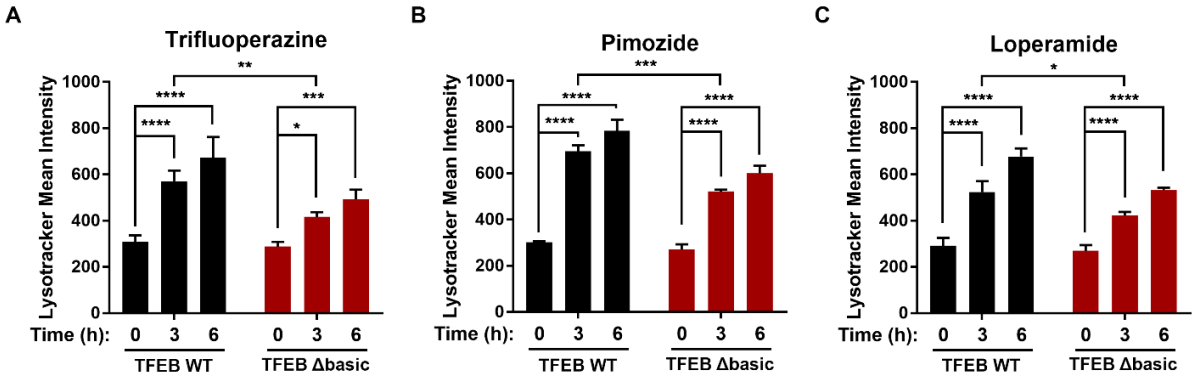


Figure 4.3.2.8 TFEB is implicated in trifluoperazine, pimozide and loperamide induced lysosomal biogenesis. (**A**)(**B**)(**C**) Bar graphs showing LysoTracker mean intensity of HeLa cell lines stably expressing WT or Δbasic TFEB after treated with trifluoperazine (8 μM), pimozide (6 μM) or loperamide (6 μM) for 3 h or 6 h. Statistical analysis between WT and Δbasic TFEB was performed using Two-way ANOVA: ****$P < 0.0001$, *** $P < 0.001$, ** $P < 0.01$, * $P < 0.05$. Error bars = SD.

Like Torin 1, if trifluoperazine, pimozide and loperamide on lysosomal biogenesis work through a TFEB-dependent mechanism, the effects induced by the compounds should be enhanced by the expression of WT TFEB, but not Δbasic TFEB. A flow cytometry analysis for LysoTracker staining was performed to test this hypothesis. The expression of WT TFEB made little difference from Δbasic TFEB in LysoTracker staining before drug treatment, most likely due to the cytoplasmic sequestration at steady state. When treated with the three compounds individually, both WT and Δbasic TFEB-expressing cells exhibited a time-dependent increase in LysoTracker mean intensity (**Figure 4.3.2.8 A-C**). Since the Δbasic can in principle dimerise with both TFEB and TFE3, the increase observed with Δbasic was most likely due to the effect

of residual endogenous TFEB and TFE3. The dynamics of TFEB/3 dimerisation and dissociation have not yet been assessed, but the potentially dominant negative effect of Δbasic TFEB was not seen. Nevertheless, the increased lysosomal staining was statistically higher with WT TFEB than Δbasic TFEB, when treated with the three compounds individually (**Figure 4.3.2.8 A-C**). Thus lysosomal biogenesis and TFEB nuclear translocation promoted by trifluoperazine, pimozide and loperamide were unlikely to be unrelated events. Nonetheless, loss-of-function analysis such as knockout of TFEB/TFE3 and genetic rescue experiments need to be performed to fully claim that these drugs function to regulate lysosomal biogenesis through TFEB or TFE3.

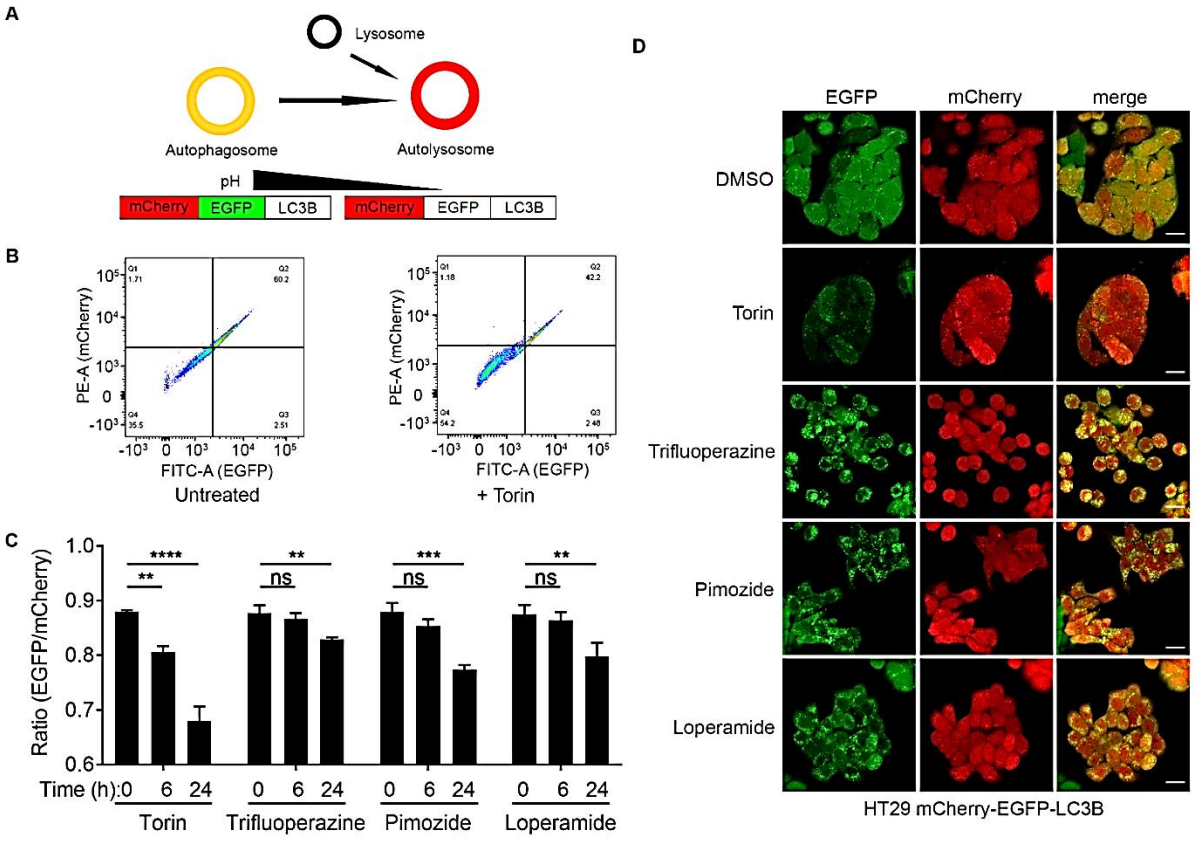


Figure 4.3.2.9 Trifluoperazine, pimozide and loperamide promote autophagy. *Legend continues at the bottom of next page.*

One of the most important events during autophagy is the fusion of the autophagosomes to the lysosomes to form autolysosomes where the autophagic cargo is degraded by lysosomal hydrolases at low pH. To capture and quantify this dynamic event, we introduced a mCherry-EGFP-LC3B tandem vector into HT29 cells through retrovirus-mediated stable transduction. When cells are fully fed and the autophagy level is low, the dual coloured LC3B exhibits a diffuse localisation within the cell and gives both green and red fluorescence. Upon autophagy induction, LC3B is recruited to the autophagosomes and forms puncta where the neutral pH does not affect the fluorescent intensity of either mCherry or EGFP. However, when autophagosomes fuse with lysosomes, the easily quenched nature of EGFP at low pH leads to a decrease in green fluorescence but the red fluorescence is preserved (Kimura et al., 2007; N'Diaye et al., 2009; Pankiv et al., 2007). Autophagic flux is therefore reflected in the ratio of green/red fluorescent intensity (**Figure 4.3.2.9 A**). Using flow cytometry, HT29 cells stably expressing mCherry-EGFP-LC3B exhibited a linear correlation between green and red fluorescence under normal conditions. But the green fluorescent spectrum shifted toward lower readings in the presence of Torin, and the ratio of EGFP/mCherry fluorescent intensity was

Figure 4.3.2.9 Trifluoperazine, pimozide and loperamide promote autophagy. (**A**) Schematic depicting the working mechanism of the mCherry-EGFP-LC3B tandem vector. The dual fluorescence-tagged LC3B is recruited to autophagosome where pH is neutral and emits both green and red fluorescence. When the autophagosomes fuse with the lysosomes where pH is low, the fluorescence of EGFP is quenched and LC3B only emits red fluorescence. (**B**) Scatter plots of fluorescent intensities of EGFP (FITC-A) and mCherry (PE-A) of single HT29 cells treated with or without Torin (1 μM, 6 h) by flow cytometry. (**C**) Quantification of the ratio of fluorescent intensity between EGFP and mCherry in HT29 cells treated with Torin (1 μM), trifluoperazine (8 μM), pimozide (6 μM) or loperamide (6 μM) for indicated duration. Student's *t*-test: ****$P < 0.0001$, ***$P < 0.001$, **$P < 0.01$, ns not significant. Error bars = SD. (**D**) Live cell imaging of HT29 cells constitutively expressing mCherry-EGFP-LC3B tandem protein. The cells were treated with DMSO, Torin (1 μM), trifluoperazine (8 μM), pimozide (6 μM) or loperamide (6 μM) for 24 h before. Scale bars = 20 μm.

dramatically decreased at 6 hours and 24 hours, indicating an increased autophagic flux induced by mTOR inhibition (**Figure 4.3.2.9 B, C**).

Using this assay, trifluoperazine, pimozide and loperamide were tested for their ability to induce autophagy. Unlike Torin, 6 hours treatment of these drugs did not cause significantly decreased EGFP/mCherry ratio, but at 24 hours the decrease was significant and robust for all the three compounds, although not as strong as Torin (**Figure 4.3.2.9 C**). The reduced EGFP fluorescence can be visualised using fluorescent microscopy, which demonstrated not only decreased overall EGFP intensity and preserved mCherry intensity, but also the formation of LC3B puncta with Torin 1 as well as the three compounds (**Figure 4.3.2.9 D**). These results suggest that trifluoperazine, pimozide and loperamide enhance autophagic flux.

Autophagic flux can also be reflected by the quantity of LC3B puncta. Using the HT29 cell line expressing the dual coloured LC3B, the number of autophagosomes and autolysosomes under the treatment of these compounds were quantified. The EGFP and mCherry double-positive puncta were counted as autophagosomes, whereas the mCherry positive, EGFP negative puncta were counted as autolysosomes due to the fluorescent quenching of EGFP at low pH. The treatment with Torin, trifluoperazine, pimozide and loperamide not only decreased the basal fluorescence of EGFP within the cells, but also significantly increased average numbers of both autophagosomes and autolysosomes (**Figure 4.3.2.10**), further confirming their autophagy promoting function. Interestingly, although the patterns of LC3B puncta were similar with pimozide and loperamide, the autophagosomes induced by trifluoperazine appeared to be relatively larger in size (**Figure 4.3.2.10**), suggesting that these compounds possibly promote autophagy induction through different mechanisms.

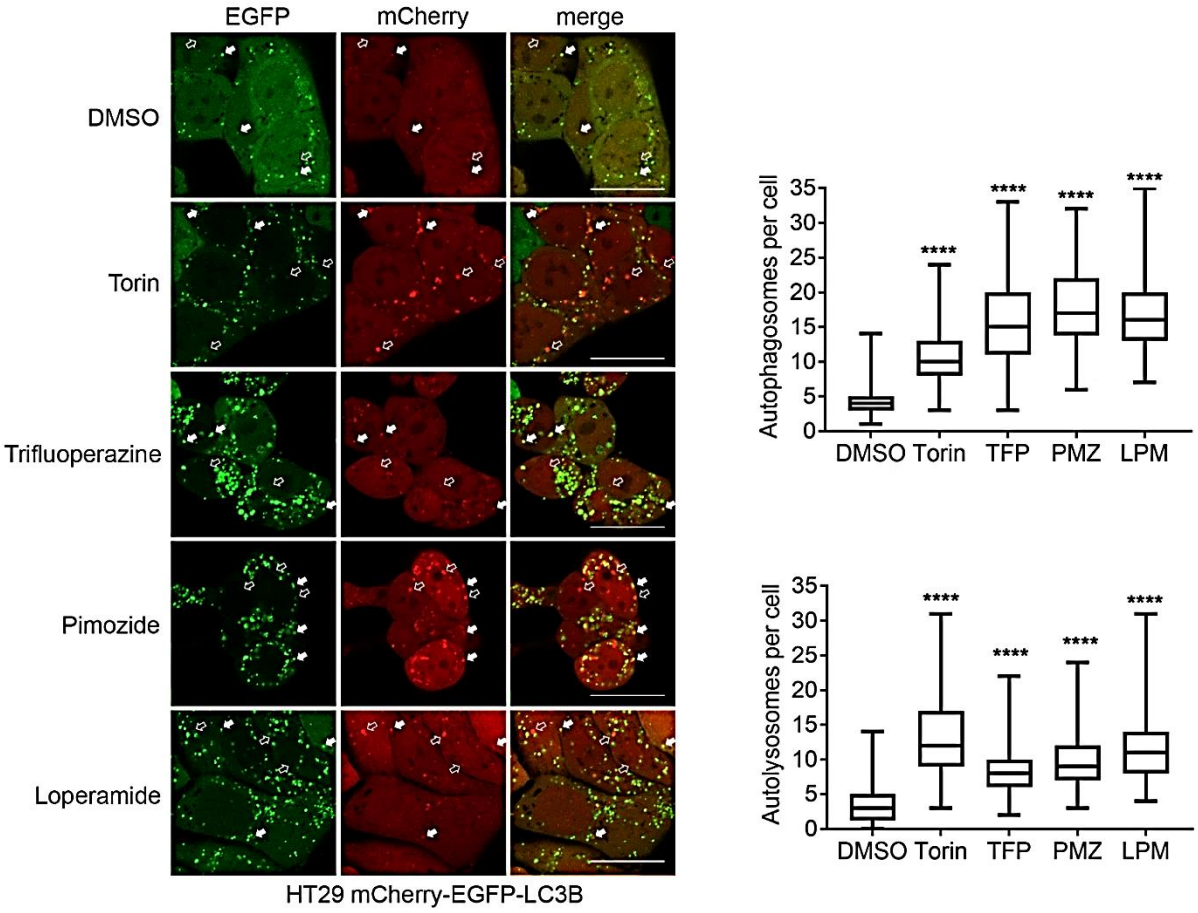


Figure 4.3.2.10 Trifluoperazine, pimozide and loperamide promote autophagy. Live cell imaging of HT29 cells constitutively expressing mCherry-EGFP-LC3B tandem protein. The cells were treated with DMSO, Torin (1 µM), trifluoperazine (8 µM), pimozide (6 µM) or loperamide (6 µM) for 24 h before imaging. Scale bars = 20 µm. The double fluorescence positive puncta were identified as autophagosomes (indicated by solid arrows), and the mCherry positive, EGFP negative puncta were identified as autolysosomes (indicated by empty arrows). The numbers of autophagosomes and autolysosomes were quantified for each condition. $n > 30$ cells per condition. Student's *t*-test: ****$P < 0.0001$. Error bars represent the min to max range. The boxes represent the standard deviation. The middle lines represent the mean.

4.3.3 Cellular signalling events induced by the hits

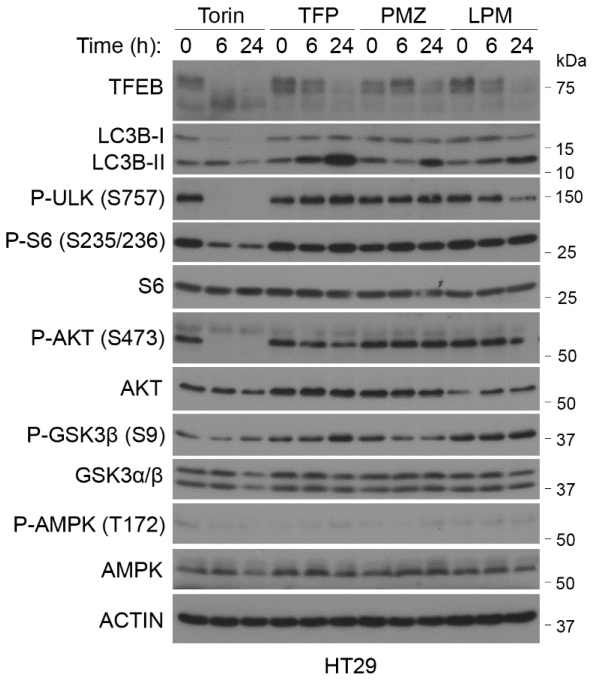


Figure 4.3.3 Trifluoperazine, pimozide and loperamide do not affect mTORC1 or AMPK signalling. Immunoblotting of HT29 cells treated with Torin (1 μM), trifluoperazine (8 μM), pimozide (6 μM) or loperamide (6 μM) for 6 h or 24 h, using indicated antibodies.

In order to understand the mechanism through which these compounds promote TFEB nuclear translocation, lysosomal function and autophagy, trifluoperazine (TFP), pimozide (PMZ) and loperamide (LPM) were compared to Torin for their effects on cellular signalling pathways. Unlike Torin 1 which drastically caused TFEB dephosphorylation, these three compounds did not affect protein mobility shift of TFEB (**Figure 4.3.3**). However, all three drugs markedly decreased TFEB protein levels at 24 hours, while the decrease was relatively mild at 6 hours except for pimozide (**Figure 4.3.3**). Torin 1 did not appear to increase LC3B-II levels, it reduced the levels of its precursor LC3B-I, possibly due to the inhibition of protein translation, or increased turnover rate of autophagosomes which indicated enhanced autophagic flux. By contrast, LC3B-II levels were dramatically elevated with trifluoperazine from 6 hours

to 24 hours. Loperamide had a similar effect, but to a lesser extent. Although the level of LC3B-II seemed to mildly decrease with 6 hours of pimozide treatment, it went up at 24 hours to a similar extent of loperamide (**Figure 4.3.3**). The elevated endogenous LC3B-II levels confirmed the fluorescent imaging results which indicated the potency of these three drugs in promoting autophagy induction. As an mTOR inhibitor, Torin 1 abolished the phosphorylation of ULK1 at S757 and substantially reduced the phosphorylation of ribosomal protein S6 (**Figure 4.3.3**), confirming its function to inhibit mTORC1 downstream signalling. On the other hand, trifluoperazine and pimozide had little effect on the phosphorylation of either ULK1 or S6. While loperamide did not affect S6 phosphorylation, it only decreased ULK1 phosphorylation at 24 hours (**Figure 4.3.3**). But TFEB translocation induced by loperamide happened at much earlier time points, which suggests that the ability of the three compounds to promote TFEB nuclear translocation and autophagy is mTORC1-independent, consistent with the data from a previous study (Zhang et al., 2007). Furthermore, all the three compounds did not affect AKT phosphorylation as Torin 1 did (**Figure 4.3.3**), which suggests that mTORC2 or PI3K signalling pathway is not likely affected by the drugs. Trifluoperazine increased the inactivating phosphorylation of GSK3β at 24 hours but not at 6 hours, while pimozide slightly decreased this phosphorylation, whereas loperamide did not seem to affect GSK3β phosphorylation (**Figure 4.3.3**). Despite that the kinase activity of GSK3β remains to be assessed, this result suggests that the inhibition of GSK3β-dependent TFEB nuclear export was less likely to be the main cause of TFEB nuclear accumulation induced by the three compounds. Lastly, neither Torin nor any of these three drugs caused phosphorylation of AMPK T172 (**Figure 4.3.3**), ruling out the potential participation of AMPK activation in TFEB nuclear translocation or autophagy. Taken together, TFEB nuclear translocation, lysosomal biogenesis and autophagy

induced by trifluoperazine, pimozide and loperamide is most likely mTORC1-, mTORC2- and AMPK-independent. Nevertheless, how these compounds function as TFEB agonists is intriguing, and the underlying mechanisms require further investigation.

4.4 Discussion

Numerous studies have established the great potential of TFEB in treating LSD. How to pharmacologically target TFEB has yet to be tackled. Here, we undertook an unbiased high-throughput screen using 1,600 FDA-approved small-molecule compounds, identified around 100 compounds that affected TFEB subcellular localisation or protein level, of which around 50 compounds showed lysosomal biogenesis potential while 7 exhibited lysosome-dampening features indicated by LysoTracker staining. This two-step screen-validation approach excluded the ones that potentially promote lysosomal biogenesis in a TFEB-independent way, but it would be slightly more difficult to understand the mechanisms, even though the UPR transcription factor XBP1 and the forkhead family transcription factor FOXO3 are attractive candidates (Mammucari et al., 2007; Shaffer et al., 2004; Vidal et al., 2012; Zhao et al., 2007). Therefore, this project only focused on TFEB-and CLEAR element-dependent lysosomal biogenesis, which was reasoned as the predominant mechanism.

The fact that not all hits that caused TFEB nuclear translocation resulted in more functional lysosomes necessitates the consideration of chemical properties of the compounds. As previous studies (Moruno-Manchon et al., 2016; Zhitomirsky and Assaraf, 2015) suggested, the weakly base lipophilic lysosomotropic agents such as doxorubicin, daunorubicin and terfenadine which can penetrate the lysosomes prevent lysosomal acidification, but cause TFEB nuclear translocation as a consequence. Those compounds may induce TFEB-dependent

transcription of lysosomal genes, but block lysosomal functions, which makes them unfavourable for treating neurodegenerative diseases. For this reason, we used LysoTracker staining to measure the effect of the compounds at the endpoint instead of qRT-PCR to check for gene transcription of the CLEAR network. Nonetheless, interestingly, this lysosomotropic feature may explain why doxorubicin and daunorubicin are effective in treating various cancers on top of their senescence-inducing function (Gewirtz, 1999).

Among the validated hits which both caused TFEB nuclear translocation and increased lysosomal biogenesis, several were already reported to enhance lysosomal or autophagic functions through unknown mechanisms. Especially, trifluoperazine, pimozide and loperamide were identified in an independent high-throughput screen to promote autophagy in an mTORC1-independent way (Zhang et al., 2007). The three compounds were also among the top 20 hits which enhanced lysosomal biogenesis in our unbiased validation (**Figure 4.3.2.2 C**). Our screen for the first time provided clues that TFEB may be implicated in the mechanisms of action of these compounds. Worth noting, the top hit in the functional validation acts as an mTORC1 antagonist, confirming the negative role of mTORC1 signalling in TFEB regulation.

Even though the working mechanisms of most of the hits at cellular levels are not clear, a subset of hits which function as calcium channel blockers, such as amlodipine, pimozide and loperamide, are particularly interesting. In contrast to the hits identified in another screen (Wang et al., 2018) which increase intracellular Ca^{2+} levels, these calcium channel blockers instead decrease Ca^{2+} influx, and are therefore unlikely to activate Calcineurin-dependent dephosphorylation of TFEB. Indeed, immunoblotting results suggested pimozide or loperamide did not change TFEB phosphorylation as do Torin or starvation (**Figure 4.3.3**). This is striking, as it suggests that global dephosphorylation is not necessary for TFEB nuclear entry.

Although further analysis is required to examine the phosphorylation status of specific sites of TFEB, we hypothesise that these compounds may affect TFEB localisation through disrupting its nuclear import-export equilibrium in a way similar to the nuclear export inhibitor LMB, as well as the curcumin analogue C1 which promotes TFEB nuclear translocation by directly binding to it, and the binding disrupts 14-3-3/YWHA interaction without altering TFEB's phosphorylation (Song et al., 2016). Either boosting nuclear import or impairing nuclear export would result in nuclear accumulation. This could potentially be achieved via various interacting partners of TFEB, such as Rag GTPases, 14-3-3, nuclear importins IPO7, IPO8 as well as the nuclear exportin CRM1 without affecting the majority of the phosphorylation events. Moreover, the overlapping function of these compounds as calcium channel blockers is intriguing, and the role of calcium channels in the regulation of TFEB localisation and activity needs to be examined through measuring the Ca^{2+} influx in the presence of the blockers as well as silencing the expression of calcium channels.

Our data demonstrated that trifluoperazine, pimozide and loperamide can further enhance functional lysosomal staining with the ectopic overexpression of WT TFEB, but not the nuclear import-deficient Δbasic mutant, suggesting the implication of TFEB as a mediator of these compounds inducing lysosomal biogenesis and autophagy. However, the evidence is not yet adequate. Analysis using loss-of-function of TFEB needs to be carried out. Given the potentially redundant functions of TFEB and TFE3, siRNA- or shRNA-mediated knockdown of either protein will not be favourable. Instead, TFEB and TFE3 double knockout cell lines are being generated in the laboratory using the CRISPR-Cas9 technique. With the double knockout cell lines and genetic re-introduction of TFEB or TFE3, we will be able to confirm whether these compounds affect gene expression of the CLEAR network as well as lysosomal function

through the two factors, and dissect the potential differential role of each protein. Nonetheless, the concomitant TFEB nuclear translocation, lysosomal biogenesis and induction of autophagy in the presence of these compounds are unlikely to be independent events, although the possibility cannot be ruled out that some of the compounds promote lysosomal and autophagic functions through multiple mechanisms.

In summary, we performed a high-throughput screen using 1,600 FDA-approved small compounds and identified close to 100 chemical modulators for TFEB/3, of which around 50 % exhibited lysosomal biogenesis promoting potential. Further analysis revealed that trifluoperazine, pimozide and loperamide induced TFEB nuclear accumulation as well as lysosomal biogenesis and autophagy in an mTORC1- and AMPK- independent manner. Therefore, our screen provided a reservoir not only for seeking the therapeutic potential of manipulating TFEB/TFE3 in lysosomal storage-related disorders such as neurodegenerative diseases and cancer, but also for acquiring knowledge to further understand the nature of cellular nutrient and energy homeostasis controlled by the TFE family transcription factors.

Chapter 5 – Discussion

5.1 TFEB in nutrient and energy homeostasis

Cells must maintain nutrient and energy homeostasis in order to grow, proliferate, differentiate and function. Especially, it is important for cancer cells to take advantage of various mechanisms to circumvent nutrient limitation and stress that occur within the tumour microenvironment. Many oncogenic pathways involved in glucose and amino acid metabolism, including c-Myc, PI3K and MAPK pathways, are often aberrantly hyperactivated in cancer cells to increase the uptake and utilisation of nutrients from the environment (reviewed in Pavlova and Thompson, 2016). In poorly vascularised tumours such as pancreatic ductal adenocarcinoma, cancer cells also increase the internal nutrient recycling through high levels of autophagy (Perera et al., 2015). When faced with nutrient limitation or energy stress, cancer cells not only increase external and internal nutrient supply, but also decrease their demand. For instance, melanoma cells become less proliferative and more invasive under low glutamine conditions through eIF2α-dependent translational reprogramming and ATF4 expression (Falletta et al., 2017). In other words, they require less nutrients for growth, but become more mobile in order to migrate to distant tissues where nutrients are abundant. Therefore, understanding how nutrient supply and demand is regulated through nutrient and energy homeostasis is the key to improving therapeutic treatments against cancer progression as well as metastasis.

The two mTOR complexes, mTORC1 and mTORC2, play a central role in coordinating cellular metabolism and controlling cell growth and survival. mTORC1 regulates cellular homeostasis in response to nutrient and energy status. When nutrients are abundant, mTORC1 promotes anabolic pathways including protein synthesis, lipid and nucleotide biosynthesis while suppressing the catabolic pathways such as autophagy and other lysosome-related degradation

processes. On the other hand, when nutrients are limited, mTORC1-controlled anabolism is suppressed while catabolism is activated. In such a way, the biosynthesis-degradation balance of the cell is maintained. Although mTORC2 does not directly sense nutrient availability, it is a major component of the insulin-PI3K signalling pathway to transduce whole body energy status down to cellular level. The observations that mTORC2 is activated by low levels of glutamine catabolites as well as glucose (Moloughney et al., 2016) highlight the implication of mTORC2 in regulating both amino acid and glucose metabolism through the PI3K-AKT axis.

TFEB, being one of the key downstream effectors of mTORC1, controls the transcription of genes involved in lysosomal biogenesis and autophagy, lipid catabolism, glucose utilisation, mitochondrial biogenesis, integrated stress response as well as immune responses. TFEB protein per se displays an interesting regulation: under nutrient rich conditions, TFEB is retained in the cytoplasm and remains inactive; under nutrient limitation or other stressed conditions, TFEB undergoes nuclear translocation and activates its target genes as a transcription factor. The low nutrient-induced activation fits well with its catabolism-promoting role.

The transcriptional activity of TFEB determined by its subcellular localisation in response to nutrient levels is similar to that of SREBP, a key regulator in lipid biosynthesis (Li et al., 2011; Wang et al., 1994). In contrast to proteolytic cleavage of SREBP, the subcellular localisation of TFEB is predominantly controlled by phosphorylation. TFEB is phosphorylated at multiple sites by a number of kinases, including S3 by MAP4K3 (Hsu et al., 2018), S122, S142 and S211 by mTORC1 (Martina et al., 2012; Roczniak-Ferguson et al., 2012; Settembre et al., 2012; Vega-Rubin-de-Celis et al., 2017), S138 by GSK3β (Li et al., 2016; Li et al., 2018), S142 by ERK2 (Settembre et al., 2011), S467 by AKT (Palmieri et al., 2017), and S461, S466

and S468 by PKC (Ferron et al., 2013). Therefore, regulation of TFEB subcellular localisation and transcriptional activity by phosphorylation is complex.

Generally, the mechanisms underlying TFEB activation via phosphorylation include: 1. Cytoplasmic retention, for instance, S3 phosphorylation enables TFEB to be recruited to the lysosomal surface through the interaction with Rag GTPases (Hsu et al., 2018; Martina and Puertollano, 2013), where TFEB can be further phosphorylated by mTORC1 at residues such as S122 and S211. The phosphorylation at S211 leads to interaction with 14-3-3 which sequesters TFEB in the cytoplasm (Martina et al., 2012; Roczniak-Ferguson et al., 2012). The role of S122 phosphorylation is less clear, but it was shown to have a similar cytoplasmic retaining function (Vega-Rubin-de-Celis et al., 2017). 2. Protein turnover, particularly the phosphorylation of C-terminal serine residues by PKCβ stabilises TFEB and enhances its activity in osteoclasts (Ferron et al., 2013). 3. Nuclear export, specifically, S142 phosphorylation by either ERK2 or mTORC1 primes for S138 phosphorylation by GSK3β, the dual phosphorylation in turn facilitates nuclear export of TFEB mediated by the CRM1-RAN complex, as our data demonstrated (Li et al., 2018). This mechanism appears to be evolutionarily conserved (**Figure 3.2.10.1 B** and Silvestrini et al., 2018), and it is also found by our laboratory to operate for the related factor MITF, despite that S73 of the melanocyte isoform of MITF (equivalent to S142 of TFEB) is only phosphorylated by ERK2 (Ngeow et al., 2018). Importantly, the S138A mutation of TFEB did not affect its association with lysosomes or interaction with 14-3-3 (Li et al., 2018), indicating a different role of the dual phosphorylation sites from others.

Regulation of mTORC1 activity by amino acid levels is well established. Therefore, TFEB nuclear translocation under amino acid starvation or mTOR inhibition is mainly due to

the loss of cytoplasmic anchoring phosphorylation by MAP4K3 and mTORC1 (Hsu et al., 2018; Martina et al., 2012; Roczniak-Ferguson et al., 2012). Our data showed that TFEB nuclear translocation and transcriptional activity are also regulated by glucose levels, in a way different from amino acid starvation. While mTORC1 activity is largely unaffected, mTORC2 signalling is activated by glucose limitation. Elevated mTORC2 further activates AKT, subsequently leading to inactivation of GSK3β, of which the kinase activity is required for the nuclear export of TFEB. In this sense, the nuclear export signal of TFEB serves as a nexus for both mTORC1 and mTORC2 signalling.

The implication of GSK3β in lysosomal biogenesis and autophagy has been described by several studies, but the mechanism was previously unclear (Marchand et al., 2015; Parr et al., 2012; Weikel et al., 2016). Our work fills the gap with evidence supporting that GSK3β phosphorylation at S138 of TFEB is required for the nuclear export of the latter. GSK3β is known to phosphorylate a range of transcription factors including β-Catenin, CREB and SREBP to inhibit their function (Ding et al., 2000; Kim et al., 2004; Tullai et al., 2007). Similarly, the suppressive role of GSK3β on lysosomal biogenesis and autophagy can be explained by its function to promote TFEB nuclear export. However, GSK3β activity can be inhibited by the often aberrantly up-regulated PI3K/AKT pathway in many cancers (reviewed in Martini et al., 2014), which may lead to disrupted TFEB nuclear export and activation of autophagy to promote cancer cell survival. By contrast, GSK3β is often hyperactivated by Aβ plaques in Alzheimer's disease, resulting in hyperphosphorylation of Tau and disrupted synaptic function (Kremer, 2011; Takashima, 2006). Up-regulation of active GSK3β is also frequently found in Parkinson's disease (Golpich et al., 2015). Dysregulation of GSK3β will supposedly decrease TFEB activity through its constant nuclear export, resulting in deficient lysosomal and

autophagic function, which is a hallmark of neurodegenerative diseases. Therefore, the elucidation of TFEB nuclear export regulated by phosphorylation also sheds light on the role of GSK3β in energy homeostasis and its physiological relevance in human diseases.

Although the phosphorylation status of TFEB S138 under glucose or amino acid starvation remains to be determined, it is likely that S138 and S142 are partially exempt from starvation-induced dephosphorylation by phosphatases such as Calcineurin and PP2A, as a study suggested (Martina and Puertollano, 2018). The partially retained S138 and S142 phosphorylation may be critical for the rapid relocalisation of TFEB into the cytoplasm upon nutrient replenishment. Thus, our discovery of a dual phosphorylation-regulated nuclear export signal provides the missing link in the regulation of TFEB nuclear import-export equilibrium through multiple cellular signalling inputs, highlighting the dynamic nature of TFEB in nutrient signalling and energy homeostasis. It is also intriguing whether and how TFEB's potentially differential phosphorylation statuses under amino acid starvation, glucose starvation and other stress conditions would impact its transcriptional activity as well as target gene selectivity.

Beyond the role of integrating amino acid levels and glucose availability, how TFEB coordinates nutrient supply and demand of the cell is an interesting topic. Firstly, TFEB directly regulates a wide range of catabolic genes to promote lysosome-related degrative pathways, lipid breakdown as well as glucose transport, to increase intracellular nutrient recycling as well as extracellular nutrient uptake and scavenging when nutrient levels are low. Secondly, our data for the first time demonstrated that TFEB regulates the expression of p21 (encoded by *CDKN1A*) at both mRNA and protein levels (**Figure 3.2.3 B**, **Figure 4.3.2.7 A, B, C**). Although the effect of TFEB on the cell cycle remains to be assessed, it is anticipated that the enrichment of *CDKN1A* mRNA pool may contribute to cell cycle arrest under long-term starvation. In that

sense, cells reduce nutrient demand via TFEB in order to survive undesirable conditions such as nutrient limitation and stress. Thirdly, TFEB-dependent transcriptional activation of the RagD GTPase (**Figure 3.2.3 B** and described in Di Malta et al., 2017) up-regulates mTORC1 activity upon nutrient refeeding, which not only helps to compensate the paused protein synthesis and other anabolic processes, but also quickly attenuates the highly activated autophagy and cellular clearance during starvation, allowing cells to adapt to physiological nutrient fluctuation. As it can be posited, all of these points need to be accomplished through the dynamic nuclear import-export cycle of TFEB.

This mechanism may be especially beneficial for tumour cells which require a high nutrient supply, as aberrant TFE3/MITF nuclear import is seen in PDAC (Perera et al., 2015). Besides, a recent study described that aberrant nuclear pore composition promotes prostate cancer aggressiveness and lethality through enhancing the nuclear import of several oncogenic transcription factors including Myc, E2F1 and androgen receptor (AR) (Rodriguez-Bravo et al., 2018), suggesting that dysregulated nuclear transport may be a more prevalent feature in cancer than previously considered. Despite the fact that glucose or amino acid limitation often occurs in tumour microenvironment, whether cancer cells in general exploit or unbalance TFEB nuclear trafficking equilibrium to satiate their altered metabolism needs further examination. It will also be important to investigate the status of TFEB nuclear import and export in LSDs such as neurodegenerative diseases that frequently exhibit defects in lysosomal clearance of misfolded protein aggregates.

5.2 TFEB as a therapeutic target

Genetic alterations of TFE family transcription factors through chromosomal rearrangement often leads to renal cell carcinoma (Kauffman et al., 2014). Aberrant nuclear import of TFE3 and MITF is commonly seen in PDAC (Perera et al., 2015). Most TFE-related cancers exhibited elevated lysosomal and autophagic activity (Martignoni et al., 2009, 2011). On the other hand, many neurodegenerative diseases are characterised by the misfolded protein aggregate plaques that cannot be cleared through the lysosomal degradative pathways. Although overexpression of TFEB ameliorated the symptoms in various disease models including Alzheimer's disease, Parkinson's disease, Huntington's disease, spinal-bulbar muscular atrophy and Pompe disease (Cortes et al., 2014; Decressac et al., 2013; Martina et al., 2014; Polito et al., 2014; Spampanato et al., 2013; Tsunemi et al., 2012), effective TFEB-targeting drugs are still being discovered.

Existing drugs that affect TFEB activity include mTOR inhibitors which mimic cellular effects of starvation and induce autophagy and lysosomal biogenesis. While some mTOR inhibitors such as Torin 1 are potent in promoting TFEB nuclear translocation, other mTORC1 specific inhibitors such as rapamycin fail to do so, even though rapamycin is efficient in promoting autophagy and effective in reducing neurotoxicity in Alzheimer's, Parkinson's and Huntington's diseases (reviewed in Vidal et al., 2014). Trehalose also promotes autophagy in neurodegenerative disease models (reviewed in Vidal et al., 2014) mostly likely through AKT inhibition which prevents TFEB phosphorylation at S467, therefore increasing TFEB nuclear localisation and transcriptional activity (Palmieri et al., 2017). Tunicamycin protects dopaminergic neuron in a Parkinson's model, and also promotes TFEB activation through induction of ER stress (Martina et al., 2016; Vidal et al., 2014). The elucidation of the role of

GSK3β in promoting TFEB nuclear export makes it another potential targeting point. Indeed, inhibition of GSK3β by HEP14 or HEP15 induces autophagy and clearance of Aβ plaques in a cell model (Li et al., 2016).

However, targeting TFEB by inhibiting its upstream regulators may not always be ideal as most are involved in a broad range of cellular pathways. For instance, mTORC1 inhibition will result in less protein synthesis which is important for neuronal function. AKT inhibition may affect metabolic pathways of glucose, which is the sole energy source of the brain. GSK3 inhibition may affect other transcription factors such as β-Catenin and CREB. ER stress induces TFEB activation and autophagy, but also may lead to neuronal cell death. In order to be recognised as an effective TFEB-targeting drug, the potential side effects must be minimised. Besides, much is to be explored about the regulation of TFEB, since evidence accumulates that TFEB can be regulated through many mTORC1-independent mechanisms.

We therefore undertook an unbiased phenotypic screen for small-molecule modulators that activate TFEB nuclear translocation as well as lysosomal/autophagic functions. We addressed TFEB implication in the 1st round screen to deliberately exclude the compounds acting via TFEB-independent mechanisms. Shortlisted compounds were then tested for their effects on lysosomes. The two-step approach ensures our purpose of seeking effective TFEB-targeting drugs while leaving room for studying the modes of action.

Another high-throughput screen identified three chemical agonists of TFEB and autophagy, digoxin, ikarugamycin and alexidine dihydrochloride (Wang et al., 2018). Although digoxin acts through lysosomal Ca^{2+} release, alexidine dihydrochloride through mitochondrial perturbation induced calcineurin activation and ikarugamycin through ER Ca^{2+} release, they all elevated cytosolic Ca^{2+} levels to promote dephosphorylation of TFEB by Calcineurin (Wang et

al., 2018). Interestingly, our screen identified a subset of calcium channel blockers, including amlodipine, pimozide, loperamide and verapamil, which promoted TFEB nuclear accumulation and autophagy. The calcium channel blockers per se are recognised as a category of chemical inducers of autophagy through reducing cytosolic Ca^{2+} influx (reviewed in Fleming et al., 2011). Furthermore, we showed that pimozide and loperamide induced TFEB nuclear translocation appears to be mTORC1- and AMPK-independent (**Figure 4.3.3**). The calcium channel blockers are unlikely to cause Ca^{2+}-dependent activation of Calcineurin or other Ca^{2+} sensors such as Calmodulin-dependent kinases. Nevertheless, reduced Ca^{2+} influx may dampen the function of Calpain, a calcium-dependent protease, resulting in a shift from apoptosis toward autophagy of the cells through modulating an essential component of the autophagy machinery, ATG5 (Xia et al., 2010; Yousefi et al., 2006). But the potential participation of Calpain in TFEB nuclear shuttling and activation have not been investigated. Overall, the counterintuitive data hint at an undiscovered regulation of TFEB by intracellular Ca^{2+} homeostasis, through which TFEB may serve as a mediator for cellular Ca^{2+} oscillations. Global dephosphorylation of TFEB was not observed with these drugs as seen with Torin 1 treatment or glucose deprivation (**Figure 4.3.3** and **Figure 3.2.4.1**), suggesting that TFEB nuclear translocation accompanied by supposed low cytosolic Ca^{2+} levels is regulated via a very different mechanism from nutrient starvation.

At this stage, we have shown that trifluoperazine, pimozide and loperamide are efficient in promoting TFEB nuclear accumulation and lysosomal/autophagic function in HeLa and HT29 cell lines. The mTORC1- and AMPK- independent modes of action may render these compounds advantages over kinase inhibitors. The mechanisms of action will be examined, and once deciphered, more effective and specific compounds can be designed and developed. Antagonists of the unveiled pathways can be potentially used to treat cancers that have

aberrantly high lysosomal/autophagic activity. In the near future we will also test the effectiveness of the compounds in disease models, aiming to provide an effective therapeutic strategy for lysosome-implicated disorders.

5.3 Conclusion

In conclusion, using HT29 and MCF7 cell lines, this study demonstrated that TFEB subcellular localisation and transcriptional activation are regulated by not only amino acids, but also glucose levels. While mTORC1 activity is largely unaffected, glucose starvation activates mTORC2, leading to the activation of AKT. The mTORC2 to AKT signalling subsequently inactivates GSK3β. We also showed that GSK3β kinase activity is required for TFEB cytoplasmic localisation under glucose limitation. Furthermore, TFEB phosphorylation at S138 by GSK3β is primed by phosphorylation of S142 by ERK2 or mTORC1. The hierarchical phosphorylation facilitates CRM1-RAN-mediated nuclear export of TFEB via a newly identified NES consisting of S138, S142, M144, L147 and I149. This mechanism is important for TFEB cytoplasmic relocalisation and inactivation upon nutrient replenishment.

Additionally, we performed a high-throughput screen using FDA-approved small compounds and identified around 100 chemical modulators of TFEB and TFE3 in HeLa and HT29 cell lines. A further 50 % of the hits enhanced lysosomal biogenesis. Particularly, trifluoperazine, pimozide and loperamide induce TFEB nuclear accumulation and promote lysosomal biogenesis and autophagy with minimum perturbation in mTORC1 or AMPK signalling. Our screen therefore provides a useful resource, from which therapeutic treatments for neurodegenerative diseases and cancer can be sought, and potential novel mechanisms of TFEB regulation unveiled.

References

Aguirre-Ghiso, J.A., Estrada, Y., Liu, D., and Ossowski, L. (2003). ERKMAPKactivity as a determinant of tumor growth and dormancy; regulation by p38SAPK. Cancer Res. *63*, 1684–1695.

Aksan, I., and Goding, C.R. (1998). Targeting the microphthalmia basic helix-loop-helix-leucine zipper transcription factor to a subset of E-box elements in vitro and in vivo. Mol. Cell. Biol. *18*, 6930–6938.

Alain, T., Morita, M., Fonseca, B.D., Yanagiya, A., Siddiqui, N., Bhat, M., Zammit, D., Marcus, V., Metrakos, P., Voyer, L.-A., et al. (2012). eIF4E/4E-BP ratio predicts the efficacy of mTOR targeted therapies. Cancer Res. *72*, 6468–6476.

Alt, J.R., Cleveland, J.L., Hannink, M., and Diehl, J.A. (2000). Phosphorylation-dependent regulation of cyclin D1 nuclear export and cyclin D1-dependent cellular transformation. Genes Dev. *14*, 3102–3114.

Argani, P., Antonescu, C.R., Illei, P.B., Lui, M.Y., Timmons, C.F., Newbury, R., Reuter, V.E., Garvin, A.J., Perez-Atayde, A.R., Fletcher, J.A., et al. (2001). Primary Renal Neoplasms with the ASPL-TFE3 Gene Fusion of Alveolar Soft Part Sarcoma: A Distinctive Tumor Entity Previously Included among Renal Cell Carcinomas of Children and Adolescents. Am. J. Pathol. *159*, 179–192.

Argani, P., Lui, M.Y., Couturier, J., Bouvier, R., Fournet, J.-C., and Ladanyi, M. (2003). A novel CLTC-TFE3 gene fusion in pediatric renal adenocarcinoma with t(X;17)(p11.2;q23). Oncogene *22*, 5374–5378.

Baenke, F., Chaneton, B., Smith, M., Van Den Broek, N., Hogan, K., Tang, H., Viros, A., Martin,

M., Galbraith, L., Girotti, M.R., et al. (2016). Resistance to BRAF inhibitors induces glutamine dependency in melanoma cells. Mol. Oncol. *10*, 73–84.

Bar-Peled, L., Schweitzer, L.D., Zoncu, R., and Sabatini, D.M. (2012). Ragulator is a GEF for the rag GTPases that signal amino acid levels to mTORC1. Cell *150*, 1196–1208.

Bar-Peled, L., Chantranupong, L., Cherniack, A.D., Chen, W.W., Ottina, K.A., Grabiner, B.C., Spear, E.D., Carter, S.L., Meyerson, M., and Sabatini, D.M. (2013). A Tumor suppressor complex with GAP activity for the Rag GTPases that signal amino acid sufficiency to mTORC1. Science *340*, 1100–1106.

Barthel, A., Okino, S.T., Liao, J., Nakatani, K., Li, J., Whitlock, J.P., and Roth, R.A. (1999). Regulation of GLUT1 gene transcription by the serine/threonine kinase Akt1. J. Biol. Chem. *274*, 20281–20286.

Beausoleil, S.A., Villén, J., Gerber, S.A., Rush, J., and Gygi, S.P. (2006). A probability-based approach for high-throughput protein phosphorylation analysis and site localization. Nat. Biotechnol. *24*, 1285–1292.

Beckmann, H., Su, L.K., and Kadesch, T. (1990). TFE3: a helix-loop-helix protein that activates transcription through the immunoglobulin enhancer muE3 motif. Genes Dev. *4*, 167–179.

Ben-Sahra, I., Howell, J.J., Asara, J.M., and Manning, B.D. (2013). Stimulation of de novo pyrimidine synthesis by growth signaling through mTOR and S6K1. Science *339*, 1323–1328.

Ben-Sahra, I., Hoxhaj, G., Ricoult, S.J.H., Asara, J.M., and Manning, B.D. (2016). mTORC1 induces purine synthesis through control of the mitochondrial tetrahydrofolate cycle. Science *351*, 728–733.

Blum, J.S., Wearsch, P.A., and Cresswell, P. (2013). Pathways of Antigen Processing. Annu. Rev. Immunol. *31*, 443–473.

Brown, E.J., Albers, M.W., Bum Shin, T., ichikawa, K., Keith, C.T., Lane, W.S., and Schreiber, S.L. (1994). A mammalian protein targeted by G1-arresting rapamycin–receptor complex. Nature *369*, 756–758.

Brunet, A., Bonni, A., Zigmond, M.J., Lin, M.Z., Juo, P., Hu, L.S., Anderson, M.J., Arden, K.C., Blenis, J., and Greenberg, M.E. (1999). Akt Promotes Cell Survival by Phosphorylating and Inhibiting a Forkhead Transcription Factor. Cell *96*, 857–868.

Brunn, G.J., Hudson, C.C., Sekulić, A., Williams, J.M., Hosoi, H., Houghton, P.J., Lawrence, J.C., and Abraham, R.T. (1997). Phosphorylation of the translational repressor PHAS-I by the mammalian target of rapamycin. Science *277*, 99–101.

Burnett, P.E., Barrow, R.K., Cohen, N.A., Snyder, S.H., and Sabatini, D.M. (1998). RAFT1 phosphorylation of the translational regulators p70 S6 kinase and 4E-BP1. Proc. Natl. Acad. Sci. *95*, 1432–1437.

Carreira, S., Goodall, J., Aksan, I., La Rocca, S.A., Galibert, M.-D., Denat, L., Larue, L., and Goding, C.R. (2005). Mitf cooperates with Rb1 and activates p21 Cip1 expression to regulate cell cycle progression. Nature *433*, 764–769.

Castellano, B.M., Thelen, A.M., Moldavski, O., Feltes, M., van der Welle, R.E.N., Mydock-McGrane, L., Jiang, X., van Eijkeren, R.J., Davis, O.B., Louie, S.M., et al. (2017). Lysosomal cholesterol activates mTORC1 via an SLC38A9-Niemann-Pick C1 signaling complex. Science *355*, 1306–1311.

Cavalli, L.R., Varella-Garcia, M., chang Liang, B., Liang, B.C., V-g, M., C L, P.B., Auritiba, P., and R C, B.L. (1997). Diminished tumorigenic phenotype after depletion of mitochondrial DNA Narrowing Gaps in Breast Adjuvant Therapy View project Clinical and cytogenetic features of a Brazilian sample of patients with phenotype of oculo-auriculo-vertebral spectrum: A cross-sectional study View project Diminished Tumorigenic Phenotype after Depletion of Mitochondrial DNA1. Cell Growth Differ. *8*, 189–191.

Chantranupong, L., Wolfson, R.L., Orozco, J.M., Saxton, R.A., Scaria, S.M., Bar-Peled, L., Spooner, E., Isasa, M., Gygi, S.P., and Sabatini, D.M. (2014). The Sestrins interact with GATOR2 to negatively regulate the amino-acid-sensing pathway upstream of mTORC1. Cell Rep. *9*, 1–8.

Chantranupong, L., Scaria, S.M., Saxton, R.A., Gygi, M.P., Shen, K., Wyant, G.A., Wang, T., Harper, J.W., Gygi, S.P., and Sabatini, D.M. (2016). The CASTOR Proteins Are Arginine Sensors for the mTORC1 Pathway. Cell *165*, 153–164.

Cheli, Y., Ohanna, M., Ballotti, R., and Bertolotto, C. (2010). Fifteen-year quest for microphthalmia-associated transcription factor target genes. Pigment Cell Melanoma Res. *23*, 27–40.

Chung, J., Kuo, C.J., Crabtree, G.R., and Blenis, J. (1992). Rapamycin-FKBP specifically blocks growth-dependent activation of and signaling by the 70 kd S6 protein kinases. Cell *69*, 1227–1236.

Clark, J., Lu, Y.-J., Sidhar, S.K., Parker, C., Gill, S., Smedley, D., Hamoudi, R., Linehan, W.M., Shipley, J., and Cooper, C.S. (1997). Fusion of splicing factor genes PSF and NonO (p54nrb) to the TFE3 gene in papillary renal cell carcinoma. Oncogene *15*, 2233–2239.

Cortes, C.J., Miranda, H.C., Frankowski, H., Batlevi, Y., Young, J.E., Le, A., Ivanov, N., Sopher, B.L., Carromeu, C., Muotri, A.R., et al. (2014). Polyglutamine-expanded androgen receptor interferes with TFEB to elicit autophagy defects in SBMA. Nat. Neurosci. *17*, 1180–1189.

Cross, D.A.E., Alessi, D.R., Cohen, P., Andjelkovich, M., and Hemmings, B.A. (1995). Inhibition of glycogen synthase kinase-3 by insulin mediated by protein kinase B. Nature *378*, 785–789.

Cui, L., Jeong, H., Borovecki, F., Parkhurst, C.N., Tanese, N., and Krainc, D. (2006). Transcriptional Repression of PGC-1α by Mutant Huntingtin Leads to Mitochondrial Dysfunction and Neurodegeneration. Cell *127*, 59–69.

Dal Cin, P., van Gool, S., Brock, P., Proesmans, W., Casteels-van Daele, M., de Wever, I., Baert, L., van Damme, B., and van den Berghe, H. (1991). Renal cell carcinoma in a child. Cancer Genet. Cytogenet. *57*, 137–138.

Davis, I.J., Hsi, B.-L., Arroyo, J.D., Vargas, S.O., Yeh, Y.A., Motyckova, G., Valencia, P., Perez-Atayde, A.R., Argani, P., Ladanyi, M., et al. (2003). Cloning of an Alpha-TFEB fusion in renal tumors harboring the t(6;11)(p21;q13) chromosome translocation. Proc. Natl. Acad. Sci. U. S. A. *100*, 6051–6056.

DeBerardinis, R.J., and Cheng, T. (2010). Q's next: the diverse functions of glutamine in metabolism, cell biology and cancer. Oncogene *29*, 313–324.

Decressac, M., Mattsson, B., Weikop, P., Lundblad, M., Jakobsson, J., and Björklund, A. (2013). TFEB-mediated autophagy rescues midbrain dopamine neurons from α-synuclein toxicity. Proc. Natl. Acad. Sci. U. S. A. *110*, E1817-26.

Dehay, B., Martinez-Vicente, M., Caldwell, G.A., Caldwell, K.A., Yue, Z., Cookson, M.R., Klein, C., Vila, M., and Bezard, E. (2013). Lysosomal impairment in Parkinson's disease. Mov. Disord. *28*, 725–732.

Dephoure, N., Zhou, C., Villen, J., Beausoleil, S.A., Bakalarski, C.E., Elledge, S.J., and Gygi, S.P. (2008). A quantitative atlas of mitotic phosphorylation. Proc. Natl. Acad. Sci. *105*, 10762–10767.

Deprez, J., Vertommen, D., Alessi, D.R., Hue, L., and Rider, M.H. (1997). Phosphorylation and activation of heart 6-phosphofructo-2-kinase by protein kinase B and other protein kinases of the insulin signaling cascades. J. Biol. Chem. *272*, 17269–17275.

Dibble, C.C., Elis, W., Menon, S., Qin, W., Klekota, J., Asara, J.M., Finan, P.M., Kwiatkowski, D.J., Murphy, L.O., and Manning, B.D. (2012). TBC1D7 Is a Third Subunit of the TSC1-TSC2 Complex Upstream of mTORC1. Mol. Cell *47*, 535–546.

Dielschneider, R.F., Henson, E.S., and Gibson, S.B. (2017). Lysosomes as Oxidative Targets for Cancer Therapy. Oxid. Med. Cell. Longev. *2017*, 1–8.

Ding, V.W., Chen, R.H., and McCormick, F. (2000). Differential regulation of glycogen synthase kinase 3beta by insulin and Wnt signaling. J. Biol. Chem. *275*, 32475–32481.

Dos, D.S., Ali, S.M., Kim, D.H., Guertin, D.A., Latek, R.R., Erdjument-Bromage, H., Tempst, P., and Sabatini, D.M. (2004). Rictor, a novel binding partner of mTOR, defines a rapamycin-insensitive and raptor-independent pathway that regulates the cytoskeleton. Curr. Biol. *14*, 1296–1302.

Dumont, J., Petri, S., Pellegrin, F., Terret, M.-E., Bohnsack, M.T., Rassinier, P., Georget, V.,

Kalab, P., Gruss, O.J., and Verlhac, M.-H. (2007). A centriole- and RanGTP-independent spindle assembly pathway in meiosis I of vertebrate oocytes. J. Cell Biol. *176*, 295–305.

Düvel, K., Yecies, J.L., Menon, S., Raman, P., Lipovsky, A.I., Souza, A.L., Triantafellow, E., Ma, Q., Gorski, R., Cleaver, S., et al. (2010). Activation of a metabolic gene regulatory network downstream of mTOR complex 1. Mol. Cell *39*, 171–183.

Eagle, H. (1955). The minimum vitamin requirements of the L and I~a cells in tissue culture, the production of specific vitamin deficiencies, and their cure. J. Exp. Med. *102*, 595–600.

Eberhardy, S.R., and Farnham, P.J. (2001). c-Myc mediates activation of the cad promoter via a post-RNA polymerase II recruitment mechanism. J. Biol. Chem. *276*, 48562–48571.

Eberlé, D., Hegarty, B., Bossard, P., Ferré, P., and Foufelle, F. (2004). SREBP transcription factors: master regulators of lipid homeostasis. Biochimie *86*, 839–848.

Efeyan, A., Zoncu, R., Chang, S., Gumper, I., Snitkin, H., Wolfson, R.L., Kirak, O., Sabatini, D.D., and Sabatini, D.M. (2012). Regulation of mTORC1 by the Rag GTPases is necessary for neonatal autophagy and survival. Nature *493*, 679–683.

Eng, C.P., Sehgal, S.N., and Vézina, C. (1984). Activity of rapamycin (AY-22,989) against transplanted tumors. J. Antibiot. (Tokyo). *37*, 1231–1237.

Engel, K., Kotlyarov, A., Gaestel, M., Attwood, P., Morrice, N., Marshall, C.J., and Cohen, P. (1998). Leptomycin B-sensitive nuclear export of MAPKAP kinase 2 is regulated by phosphorylation. EMBO J. *17*, 3363–3371.

Falletta, P., Sanchez-Del-Campo, L., Chauhan, J., Effern, M., Kenyon, A., Kershaw, C.J.,

Siddaway, R., Lisle, R., Freter, R., Daniels, M.J., et al. (2017). Translation reprogramming is an evolutionarily conserved driver of phenotypic plasticity and therapeutic resistance in melanoma. Genes Dev. *31*, 18–33.

Fan, J., Kamphorst, J.J., Mathew, R., Chung, M.K., White, E., Shlomi, T., and Rabinowitz, J.D. (2013). Glutamine-driven oxidative phosphorylation is a major ATP source in transformed mammalian cells in both normoxia and hypoxia. Mol. Syst. Biol. *9*. 712. doi: 10.1038/msb.2013.65

Ferron, M., Settembre, C., Shimazu, J., Lacombe, J., Kato, S., Rawlings, D.J., Ballabio, A., and Karsenty, G. (2013). A RANKL-PKCβ-TFEB signaling cascade is necessary for lysosomal biogenesis in osteoclasts. Genes Dev. *27*, 955–969.

Fleming, A., Noda, T., Yoshimori, T., and Rubinsztein, D.C. (2011). Chemical modulators of autophagy as biological probes and potential therapeutics. Nat. Chem. Biol. *7*, 9–17.

Fock, V., Gudmundsson, S.R., Gunnlaugsson, H.O., Stefansson, J.A., Ionasz, V., Schepsky, A., Viarigi, J., Reynisson, I.E., Pogenberg, V., Wilmanns, M., et al. (2018). Subcellular localization and stability of MITF are modulated by the bHLH-Zip domain. Pigment Cell Melanoma Res. doi: 10.1111/pcmr.12721

Frias, M.A., Thoreen, C.C., Jaffe, J.D., Schroder, W., Sculley, T., Carr, S.A., and Sabatini, D.M. (2006). mSin1 Is Necessary for Akt/PKB Phosphorylation, and Its Isoforms Define Three Distinct mTORC2s. Curr. Biol. *16*, 1865–1870.

Gaglio, D., Metallo, C.M., Gameiro, P.A., Hiller, K., Sala Danna, L., Balestrieri, C., Alberghina, L., Stephanopoulos, G., and Chiaradonna, F. (2011). Oncogenic K-Ras decouples glucose and glutamine metabolism to support cancer cell growth. Mol. Syst. Biol. *7*. 523. doi:

10.1038/msb.2011.56

Gan, X., Wang, J., Wang, C., Sommer, E., Kozasa, T., Srinivasula, S., Alessi, D., Offermanns, S., Simon, M.I., and Wu, D. (2012). PRR5L degradation promotes mTORC2-mediated PKC-δ phosphorylation and cell migration downstream of Gα12. Nat. Cell Biol. *14*, 686–696.

Gao, P., Tchernyshyov, I., Chang, T.-C., Lee, Y.-S., Kita, K., Ochi, T., Zeller, K.I., De Marzo, A.M., Van Eyk, J.E., Mendell, J.T., et al. (2009). c-Myc suppression of miR-23a/b enhances mitochondrial glutaminase expression and glutamine metabolism. Nature *458*, 762–765.

Garami, A., Zwartkruis, F.J.., Nobukuni, T., Joaquin, M., Roccio, M., Stocker, H., Kozma, S.C., Hafen, E., Bos, J.L., and Thomas, G. (2003). Insulin activation of Rheb, a mediator of mTOR/S6K/4E-BP signaling, is inhibited by TSC1 and 2. Mol. Cell *11*, 1457–1466.

García-Martínez, J.M., and Alessi, D.R. (2008). mTOR complex 2 (mTORC2) controls hydrophobic motif phosphorylation and activation of serum- and glucocorticoid-induced protein kinase 1 (SGK1). Biochem. J. *416*, 375–385.

Gewirtz, D.A. (1999). A critical evaluation of the mechanisms of action proposed for the antitumor effects of the anthracycline antibiotics adriamycin and daunorubicin. Biochem. Pharmacol. *57*, 727–741.

Golpich, M., Amini, E., Hemmati, F., Ibrahim, N.M., Rahmani, B., Mohamed, Z., Raymond, A.A., Dargahi, L., Ghasemi, R., and Ahmadiani, A. (2015). Glycogen synthase kinase-3 beta (GSK-3β) signaling: Implications for Parkinson's disease. Pharmacol. Res. *97*, 16–26.

Gottlob, K., Majewski, N., Kennedy, S., Kandel, E., Robey, R.B., and Hay, N. (2001). Inhibition of early apoptotic events by Akt/PKB is dependent on the first committed step of glycolysis and

mitochondrial hexokinase. Genes Dev. *15*, 1406–1418.

Grabiner, B.C., Nardi, V., Birsoy, K., Possemato, R., Shen, K., Sinha, S., Jordan, A., Beck, A.H., and Sabatini, D.M. (2014). A diverse array of cancer-associated MTOR mutations are hyperactivating and can predict rapamycin sensitivity. Cancer Discov. *4*, 554–563.

Grassian, A.R., Coloff, J.L., and Brugge, J.S. (2011). Extracellular matrix regulation of metabolism and implications for tumorigenesis. Cold Spring Harb. Symp. Quant. Biol. *76*, 313–324.

Gray, M.A., Choy, C.H., Dayam, R.M., Ospina-Escobar, E., Somerville, A., Xiao, X., Ferguson, S.M., and Botelho, R.J. (2016). Phagocytosis Enhances Lysosomal and Bactericidal Properties by Activating the Transcription Factor TFEB. Curr. Biol. *26*, 1955–1964.

Gual, P., Le Marchand-Brustel, Y., and Tanti, J.-F. (2005). Positive and negative regulation of insulin signaling through IRS-1 phosphorylation. Biochimie *87*, 99–109.

Guertin, D.A., Stevens, D.M., Saitoh, M., Kinkel, S., Crosby, K., Sheen, J.-H., Mullholland, D.J., Magnuson, M.A., Wu, H., and Sabatini, D.M. (2009). mTOR Complex 2 Is Required for the Development of Prostate Cancer Induced by Pten Loss in Mice. Cancer Cell *15*, 148–159.

Gulhati, P., Bowen, K.A., Liu, J., Stevens, P.D., Rychahou, P.G., Chen, M., Lee, E.Y., Weiss, H.L., O'Connor, K.L., Gao, T., et al. (2011). mTORC1 and mTORC2 regulate EMT, motility, and metastasis of colorectal cancer via RhoA and Rac1 signaling pathways. Cancer Res. *71*, 3246–3256.

Gullino, P.M., Clark, S.H., and Grantham, F.H. (1964). The Interstitial Fluid of Solid Tumors. Cancer Res. *24*, 780–797.

Gwinn, D.M., Shackelford, D.B., Egan, D.F., Mihaylova, M.M., Mery, A., Vasquez, D.S., Turk, B.E., and Shaw, R.J. (2008). AMPK phosphorylation of raptor mediates a metabolic checkpoint. Mol. Cell *30*, 214–226.

Haar, E. Vander, Lee, S., Bandhakavi, S., Griffin, T.J., and Kim, D.-H. (2007). Insulin signalling to mTOR mediated by the Akt/PKB substrate PRAS40. Nat. Cell Biol. *9*, 316–323.

Hagiwara, A., Cornu, M., Cybulski, N., Polak, P., Betz, C., Trapani, F., Terracciano, L., Heim, M.H., Rüegg, M.A., and Hall, M.N. (2012). Hepatic mTORC2 activates glycolysis and lipogenesis through Akt, glucokinase, and SREBP1c. Cell Metab. *15*, 725–738.

Hanahan, D., and Weinberg, R.A. (2011). Hallmarks of cancer: the next generation. Cell *144*, 646–674.

Hara, K., Maruki, Y., Long, X., Yoshino, K., Oshiro, N., Hidayat, S., Tokunaga, C., Avruch, J., and Yonezawa, K. (2002). Raptor, a Binding Partner of Target of Rapamycin (TOR), Mediates TOR Action. Cell *110*, 177–189.

Hardy, J. (2006). A Hundred Years of Alzheimer's Disease Research. Neuron *52*, 3–13.

Harrington, L.S., Findlay, G.M., Gray, A., Tolkacheva, T., Wigfield, S., Rebholz, H., Barnett, J., Leslie, N.R., Cheng, S., Shepherd, P.R., et al. (2004). The TSC1-2 tumor suppressor controls insulin-PI3K signaling via regulation of IRS proteins. J. Cell Biol. *166*, 213–223.

He, C., and Klionsky, D.J. (2009). Regulation Mechanisms and Signaling Pathways of Autophagy. Annu. Rev. Genet. *43*, 67–93.

Vander Heiden, M.G. (2011). Targeting cancer metabolism: a therapeutic window opens. Nat. Rev. Drug Discov. *10*, 671–684.

Vander Heiden, M.G., Cantley, L.C., and Thompson, C.B. (2009). Understanding the Warburg effect: the metabolic requirements of cell proliferation. Science *324*, 1029–1033.

Hemesath, T.J., Price, E.R., Takemoto, C., Badalian, T., and Fisher, D.E. (1998). MAP kinase links the transcription factor Microphthalmia to c-Kit signalling in melanocytes. Nature *391*, 298–301.

Hemminki, A., Markie, D., Tomlinson, I., Avizienyte, E., Roth, S., Loukola, A., Bignell, G., Warren, W., Aminoff, M., Höglund, P., et al. (1998). A serine/threonine kinase gene defective in Peutz–Jeghers syndrome. Nature *391*, 184–187.

Hennessy, B.T., Smith, D.L., Ram, P.T., Lu, Y., and Mills, G.B. (2005). Exploiting the PI3K/AKT Pathway for Cancer Drug Discovery. Nat. Rev. Drug Discov. *4*, 988–1004.

Hernandez-Davies, J.E., Tran, T.Q., Reid, M.A., Rosales, K.R., Lowman, X.H., Pan, M., Moriceau, G., Yang, Y., Wu, J., Lo, R.S., et al. (2015). Vemurafenib resistance reprograms melanoma cells towards glutamine dependence. J. Transl. Med. *13*, 210.

Hietakangas, V., and Cohen, S.M. (2008). TOR complex 2 is needed for cell cycle progression and anchorage-independent growth of MCF7 and PC3 tumor cells. BMC Cancer *8*, 282.

Hilpert, K., Winkler, D.F., and Hancock, R.E. (2007). Peptide arrays on cellulose support: SPOT synthesis, a time and cost efficient method for synthesis of large numbers of peptides in a parallel and addressable fashion. Nat. Protoc. *2*, 1333–1349.

Ho, P.C., Bihuniak, J.D., MacIntyre, A.N., Staron, M., Liu, X., Amezquita, R., Tsui, Y.C., Cui, G., Micevic, G., Perales, J.C., et al. (2015). Phosphoenolpyruvate Is a Metabolic Checkpoint of Anti-tumor T Cell Responses. Cell *162*, 1217–1228.

Hoek, K.S., and Goding, C.R. (2010). Cancer stem cells versus phenotype-switching in melanoma. Pigment Cell Melanoma Res. *23*, 746–759.

Holz, M.K., Ballif, B.A., Gygi, S.P., and Blenis, J. (2005). mTOR and S6K1 mediate assembly of the translation preinitiation complex through dynamic protein interchange and ordered phosphorylation events. Cell *123*, 569–580.

Hsieh, A.C., Costa, M., Zollo, O., Davis, C., Feldman, M.E., Testa, J.R., Meyuhas, O., Shokat, K.M., and Ruggero, D. (2010). Genetic dissection of the oncogenic mTOR pathway reveals druggable addiction to translational control via 4EBP-eIF4E. Cancer Cell *17*, 249–261.

Hsieh, A.C., Liu, Y., Edlind, M.P., Ingolia, N.T., Janes, M.R., Sher, A., Shi, E.Y., Stumpf, C.R., Christensen, C., Bonham, M.J., et al. (2012). The translational landscape of mTOR signalling steers cancer initiation and metastasis. Nature *485*, 55–61.

Hsu, C.L., Lee, E.X., Gordon, K.L., Paz, E.A., Shen, W.-C., Ohnishi, K., Meisenhelder, J., Hunter, T., and La Spada, A.R. (2018). MAP4K3 mediates amino acid-dependent regulation of autophagy via phosphorylation of TFEB. Nat. Commun. *9*, 942. doi: 10.1038/s41467-018-03340-7

Huan, C., Kelly, M.L., Steele, R., Shapira, I., Gottesman, S.R.S., and Roman, C.A.J. (2006). Transcription factors TFE3 and TFEB are critical for CD40 ligand expression and thymus-dependent humoral immunity. Nat. Immunol. *7*, 1082–1091.

Hughes, M., Zhang, C., Avis, J.M., Hutchison, C.J., and Clarke, P.R. (1998). The role of the ran GTPase in nuclear assembly and DNA replication: characterisation of the effects of Ran mutants. J. Cell Sci. *111 (Pt 20)*, 3017–3026.

Inoki, K., Li, Y., Zhu, T., Wu, J., and Guan, K.-L. (2002). TSC2 is phosphorylated and inhibited by Akt and suppresses mTOR signalling. Nat. Cell Biol. *4*, 648–657.

Inoki, K., Li, Y., Xu, T., and Guan, K.-L. (2003a). Rheb GTPase is a direct target of TSC2 GAP activity and regulates mTOR signaling. Genes Dev. *17*, 1829–1834.

Inoki, K., Zhu, T., and Guan, K.-L. (2003b). TSC2 mediates cellular energy response to control cell growth and survival. Cell *115*, 577–590.

Inoki, K., Ouyang, H., Zhu, T., Lindvall, C., Wang, Y., Zhang, X., Yang, Q., Bennett, C., Harada, Y., Stankunas, K., et al. (2006). TSC2 integrates Wnt and energy signals via a coordinated phosphorylation by AMPK and GSK3 to regulate cell growth. Cell *126*, 955–968.

Inoue, A., and Zhang, Y. (2014). Nucleosome assembly is required for nuclear pore complex assembly in mouse zygotes. Nat. Struct. Mol. Biol. *21*, 609–616.

Jacinto, E., Loewith, R., Schmidt, A., Lin, S., Rüegg, M.A., Hall, A., and Hall, M.N. (2004). Mammalian TOR complex 2 controls the actin cytoskeleton and is rapamycin insensitive. Nat. Cell Biol. *6*, 1122–1128.

Jacinto, E., Facchinetti, V., Liu, D., Soto, N., Wei, S., Jung, S.Y., Huang, Q., Qin, J., and Su, B. (2006). SIN1/MIP1 Maintains rictor-mTOR Complex Integrity and Regulates Akt Phosphorylation and Substrate Specificity. Cell *127*, 125–137.

Jakhar, R., Paul, S., Bhardwaj, M., and Kang, S.C. (2016). Astemizole–Histamine induces Beclin-1-independent autophagy by targeting p53-dependent crosstalk between autophagy and apoptosis. Cancer Lett. *372*, 89–100.

Jewell, J.L., Kim, Y.C., Russell, R.C., Yu, F.-X., Park, H.W., Plouffe, S.W., Tagliabracci, V.S.,

and Guan, K.-L. (2015). Differential regulation of mTORC1 by leucine and glutamine. Science *347*, 194–198.

Jeyasekharan, A.D., Liu, Y., Hattori, H., Pisupati, V., Jonsdottir, A.B., Rajendra, E., Lee, M., Sundaramoorthy, E., Schlachter, S., Kaminski, C.F., et al. (2013). A cancer-associated BRCA2 mutation reveals masked nuclear export signals controlling localization. Nat. Struct. Mol. Biol. *20*, 1191–1198.

de Jong, B., Molenaar, I.M., Leeuw, J.A., Idenberg, V.J.S., and Oosterhuis, J.W. (1986). Cytogenetics of a renal adenocarcinoma in a 2-year-old child. Cancer Genet. Cytogenet. *21*, 165–169.

Jung, J., Genau, H.M., and Behrends, C. (2015). Amino Acid-Dependent mTORC1 Regulation by the Lysosomal Membrane Protein SLC38A9. Mol. Cell. Biol. *35*, 2479–2494.

Kalderon, D., Roberts, B.L., Richardson, W.D., and Smith, A.E. (1984). A short amino acid sequence able to specify nuclear location. Cell *39*, 499–509.

Kalender, A., Selvaraj, A., Kim, S.Y., Gulati, P., Brûlé, S., Viollet, B., Kemp, B.E., Bardeesy, N., Dennis, P., Schlager, J.J., et al. (2010). Metformin, independent of AMPK, inhibits mTORC1 in a rag GTPase-dependent manner. Cell Metab. *11*, 390–401.

Kamphorst, J.J., Nofal, M., Commisso, C., Hackett, S.R., Lu, W., Grabocka, E., Vander Heiden, M.G., Miller, G., Drebin, J.A., Bar-Sagi, D., et al. (2015). Human pancreatic cancer tumors are nutrient poor and tumor cells actively scavenge extracellular protein. Cancer Res. *75*, 544–553.

Kanai, Y., Segawa, H., Miyamoto, K. i, Uchino, H., Takeda, E., and Endou, H. (1998). Expression cloning and characterization of a transporter for large neutral amino acids activated

by the heavy chain of 4F2 antigen (CD98). J. Biol. Chem. *273*, 23629–23632.

Kauffman, E.C., Ricketts, C.J., Rais-Bahrami, S., Yang, Y., Merino, M.J., Bottaro, D.P., Srinivasan, R., and Linehan, W.M. (2014). Molecular genetics and cellular features of TFE3 and TFEB fusion kidney cancers. Nat. Rev. Urol. *11*, 465–475.

Kim, D.-H., Sarbassov, D.D., Ali, S.M., King, J.E., Latek, R.R., Erdjument-Bromage, H., Tempst, P., and Sabatini, D.M. (2002). mTOR interacts with raptor to form a nutrient-sensitive complex that signals to the cell growth machinery. Cell *110*, 163–175.

Kim, D.-H., Sarbassov, D.D., Ali, S.M., Latek, R.R., Guntur, K.V.P., Erdjument-Bromage, H., Tempst, P., and Sabatini, D.M. (2003). GbetaL, a positive regulator of the rapamycin-sensitive pathway required for the nutrient-sensitive interaction between raptor and mTOR. Mol. Cell *11*, 895–904.

Kim, E., Goraksha-Hicks, P., Li, L., Neufeld, T.P., and Guan, K.-L. (2008). Regulation of TORC1 by Rag GTPases in nutrient response. Nat. Cell Biol. *10*, 935–945.

Kim, J., Kundu, M., Viollet, B., and Guan, K.-L. (2011). AMPK and mTOR regulate autophagy through direct phosphorylation of Ulk1. Nat. Cell Biol. *13*, 132–141.

Kim, K.H., Song, M.J., Yoo, E.J., Choe, S.S., Park, S.D., and Kim, J.B. (2004). Regulatory role of glycogen synthase kinase 3 for transcriptional activity of ADD1/SREBP1c. J. Biol. Chem. *279*, 51999–52006.

Kimura, S., Noda, T., and Yoshimori, T. (2007). Dissection of the Autophagosome Maturation Process by a Novel Reporter Protein, Tandem Fluorescent-Tagged LC3. Autophagy *3*, 452–460.

Kırlı, K., Karaca, S., Dehne, H.J., Samwer, M., Pan, K.T., Lenz, C., Urlaub, H., and Görlich, D.

(2015). A deep proteomics perspective on CRM1-mediated nuclear export and nucleocytoplasmic partitioning. Elife *4*. doi: 10.7554/eLife.11466

Kremer, A. (2011). GSK3 and Alzheimer's disease: facts and fiction…. Front. Mol. Neurosci. *4*, 17.

Kuiper, R.P., Schepens, M., Thijssen, J., van Asseldonk, M., van den Berg, E., Bridge, J., Schuuring, E., Schoenmakers, E.F.P.M., and van Kessel, A.G. (2003). Upregulation of the transcription factor TFEB in t(6;11)(p21;q13)-positive renal cell carcinomas due to promoter substitution. Hum. Mol. Genet. *12*, 1661–1669.

Kuo, C.J., Chung, J., Fiorentino, D.F., Flanagan, W.M., Blenis, J., and Crabtree, G.R. (1992). Rapamycin selectively inhibits interleukin-2 activation of p70 S6 kinase. Nature *358*, 70–73.

Lane, A.N., and Fan, T.W.-M. (2015). Regulation of mammalian nucleotide metabolism and biosynthesis. Nucleic Acids Res. *43*, 2466–2485.

Laplante, M., and Sabatini, D.M. (2012). mTOR Signaling in Growth Control and Disease. Cell *149*, 274–293.

Lasnitzki, A. (1925). Neuere Untersuchungen Uber den Stoffwechsel der Carcinomzelle (Referat). Zeitschrift für Krebsforsch. *22*, 531–535.

Law, B.Y.K., Chan, W.K., Xu, S.W., Wang, J.R., Bai, L.P., Liu, L., and Wong, V.K.W. (2015). Natural small-molecule enhancers of autophagy induce autophagic cell death in apoptosis-defective cells. Sci. Rep. *4*, 5510.

Lawrence, M.S., Stojanov, P., Mermel, C.H., Robinson, J.T., Garraway, L.A., Golub, T.R., Meyerson, M., Gabriel, S.B., Lander, E.S., and Getz, G. (2014). Discovery and saturation

analysis of cancer genes across 21 tumour types. Nature *505*, 495–501.

Lee, D.-F., Kuo, H.-P., Chen, C.-T., Hsu, J.-M., Chou, C.-K., Wei, Y., Sun, H.-L., Li, L.-Y., Ping, B., Huang, W.-C., et al. (2007). IKK beta suppression of TSC1 links inflammation and tumor angiogenesis via the mTOR pathway. Cell *130*, 440–455.

Lee, J.K., Jin, H.K., Park, M.H., Kim, B., Lee, P.H., Nakauchi, H., Carter, J.E., He, X., Schuchman, E.H., and Bae, J. (2014). Acid sphingomyelinase modulates the autophagic process by controlling lysosomal biogenesis in Alzheimer's disease. J. Exp. Med. *211*, 1551–1570.

Levy, C., Khaled, M., and Fisher, D.E. (2006). MITF: master regulator of melanocyte development and melanoma oncogene. Trends Mol. Med. *12*, 406–414.

Li, H., Lin, J., Wang, X., Yao, G., Wang, L., Zheng, H., Yang, C., Jia, C., Liu, A., and Bai, X. (2012). Targeting of mTORC2 prevents cell migration and promotes apoptosis in breast cancer. Breast Cancer Res. Treat. *134*, 1057–1066.

Li, L., Friedrichsen, H.J., Andrews, S., Picaud, S., Volpon, L., Ngeow, K., Berridge, G., Fischer, R., Borden, K.L.B., Filippakopoulos, P., et al. (2018). A TFEB nuclear export signal integrates amino acid supply and glucose availability. Nat. Commun. *9*, 2685. doi: 10.1038/s41467-018-04849-7

Li, Y., Xu, S., Mihaylova, M.M., Zheng, B., Hou, X., Jiang, B., Park, O., Luo, Z., Lefai, E., Shyy, J.Y.-J., et al. (2011). AMPK Phosphorylates and Inhibits SREBP Activity to Attenuate Hepatic Steatosis and Atherosclerosis in Diet-Induced Insulin-Resistant Mice. Cell Metab. *13*, 376–388.

Li, Y., Xu, M., Ding, X., Yan, C., Song, Z., Chen, L., Huang, X., Wang, X., Jian, Y., Tang, G.,

et al. (2016). Protein kinase C controls lysosome biogenesis independently of mTORC1. Nat. Cell Biol. *18*, 1065–1077.

Lindsten, T., Golden, J.A., Zong, W.-X., Minarcik, J., Harris, M.H., and Thompson, C.B. (2003). The proapoptotic activities of Bax and Bak limit the size of the neural stem cell pool. J. Neurosci. *23*, 11112–11119.

Liu, P., Gan, W., Chin, Y.R., Ogura, K., Guo, J., Zhang, J., Wang, B., Blenis, J., Cantley, L.C., Toker, A., et al. (2015). PtdIns(3,4,5)P3-Dependent Activation of the mTORC2 Kinase Complex. Cancer Discov. *5*, 1194–1209.

Long, X., Lin, Y., Ortiz-Vega, S., Yonezawa, K., and Avruch, J. (2005). Rheb binds and regulates the mTOR kinase. Curr. Biol. *15*, 702–713.

Longo, V., Brunetti, O., Gnoni, A., Cascinu, S., Gasparini, G., Lorusso, V., Ribatti, D., and Silvestris, N. (2016). Angiogenesis in pancreatic ductal adenocarcinoma: A controversial issue. Oncotarget *7*, 58649–58658.

Ma, L., Chen, Z., Erdjument-Bromage, H., Tempst, P., and Pandolfi, P.P. (2005). Phosphorylation and Functional Inactivation of TSC2 by Erk: Implications for Tuberous Sclerosisand Cancer Pathogenesis. Cell *121*, 179–193.

MacDonald, M.E., Ambrose, C.M., Duyao, M.P., Myers, R.H., Lin, C., Srinidhi, L., Barnes, G., Taylor, S.A., James, M., Groot, N., et al. (1993). A novel gene containing a trinucleotide repeat that is expanded and unstable on Huntington's disease chromosomes. Cell *72*, 971–983.

Di Malta, C., Siciliano, D., Calcagni, A., Monfregola, J., Punzi, S., Pastore, N., Eastes, A.N., Davis, O., De Cegli, R., Zampelli, A., et al. (2017). Transcriptional activation of RagD GTPase

controls mTORC1 and promotes cancer growth. Science (80-.). *356*, 1188–1193.

Mammucari, C., Milan, G., Romanello, V., Masiero, E., Rudolf, R., Del Piccolo, P., Burden, S.J., Di Lisi, R., Sandri, C., Zhao, J., et al. (2007). FoxO3 Controls Autophagy in Skeletal Muscle In Vivo. Cell Metab. *6*, 458–471.

Manning, B.D., Tee, A.R., Logsdon, M.N., Blenis, J., and Cantley, L.C. (2002). Identification of the tuberous sclerosis complex-2 tumor suppressor gene product tuberin as a target of the phosphoinositide 3-kinase/akt pathway. Mol. Cell *10*, 151–162.

Mansueto, G., Armani, A., Viscomi, C., D'Orsi, L., De Cegli, R., Polishchuk, E. V., Lamperti, C., Di Meo, I., Romanello, V., Marchet, S., et al. (2017). Transcription Factor EB Controls Metabolic Flexibility during Exercise. Cell Metab. *25*, 182–196.

Marchand, B., Arsenault, D., Raymond-Fleury, A., Boisvert, F.-M., and Boucher, M.-J. (2015). Glycogen synthase kinase-3 (GSK3) inhibition induces prosurvival autophagic signals in human pancreatic cancer cells. J. Biol. Chem. *290*, 5592–5605.

Márquez, J., Sánchez-Jiménez, F., Medina, M.A., Quesada, A.R., and de Castro, I.N. (1989). Nitrogen metabolism in tumor bearing mice. Arch. Biochem. Biophys. *268*, 667–675.

Martel, R.R., Klicius, J., and Galet, S. (1977). Inhibition of the immune response by rapamycin, a new antifungal antibiotic. Can. J. Physiol. Pharmacol. *55*, 48–51.

Martignoni, G., Gobbo, S., Camparo, P., Brunelli, M., Munari, E., Segala, D., Pea, M., Bonetti, F., Illei, P.B., Netto, G.J., et al. (2011). Differential expression of cathepsin K in neoplasms harboring TFE3 gene fusions. Mod. Pathol. *24*, 1313–1319.

Martignoni, G., Pea, M., Gobbo, S., Brunelli, M., Bonetti, F., Segala, D., Pan, C.C., Netto, G.,

Doglioni, C., Hes, O., et al. (2009). Cathepsin-K immunoreactivity distinguishes MiTF/TFE family renal translocation carcinomas from other renal carcinomas. Mod. Pathol. *22*, 1016–1022.

Martina, J.A., and Puertollano, R. (2013). Rag GTPases mediate amino acid-dependent recruitment of TFEB and MITF to lysosomes. J. Cell Biol. *200*, 475–491.

Martina, J.A., and Puertollano, R. (2018). Protein phosphatase 2A stimulates activation of TFEB and TFE3 transcription factors in response to oxidative stress. J. Biol. Chem. *293*, 12525–12534.

Martina, J.A., Chen, Y., Gucek, M., and Puertollano, R. (2012). MTORC1 functions as a transcriptional regulator of autophagy by preventing nuclear transport of TFEB. Autophagy *8*, 903–914.

Martina, J.A., Diab, H.I., Lishu, L., Jeong-A, L., Patange, S., Raben, N., and Puertollano, R. (2014). The nutrient-responsive transcription factor TFE3 promotes autophagy, lysosomal biogenesis, and clearance of cellular debris. Sci. Signal. *7*. (309):ra9. doi: 10.1126/scisignal.2004754

Martina, J.A., Diab, H.I., Brady, O.A., and Puertollano, R. (2016). TFEB and TFE3 are novel components of the integrated stress response. EMBO J. *35*, 479–495.

Martini, M., De Santis, M.C., Braccini, L., Gulluni, F., and Hirsch, E. (2014). PI3K/AKT signaling pathway and cancer: an updated review. Ann. Med. *46*, 372–383.

Masri, J., Bernath, A., Martin, J., Jo, O.D., Vartanian, R., Funk, A., and Gera, J. (2007). mTORC2 activity is elevated in gliomas and promotes growth and cell motility via overexpression of rictor. Cancer Res. *67*, 11712–11720.

Mastroberardino, L., Spindler, B., Pfeiffer, R., Skelly, P.J., Loffing, J., Shoemaker, C.B., and Verrey, F. (1998). Amino-acid transport by heterodimers of 4F2hc/CD98 and members of a permease family. Nature *395*, 288–291.

Meacham, C.E., and Morrison, S.J. (2013). Tumour heterogeneity and cancer cell plasticity. Nature *501*, 328–337.

Meares, G.P., and Jope, R.S. (2007). Resolution of the nuclear localization mechanism of glycogen synthase kinase-3: functional effects in apoptosis. J. Biol. Chem. *282*, 16989–17001.

Medina, D.L., Fraldi, A., Bouche, V., Annunziata, F., Mansueto, G., Spampanato, C., Puri, C., Pignata, A., Martina, J.A., Sardiello, M., et al. (2011). Transcriptional activation of lysosomal exocytosis promotes cellular clearance. Dev. Cell *21*, 421–430.

Medina, D.L., Di Paola, S., Peluso, I., Armani, A., De Stefani, D., Venditti, R., Montefusco, S., Scotto-Rosato, A., Prezioso, C., Forrester, A., et al. (2015). Lysosomal calcium signalling regulates autophagy through calcineurin and TFEB. Nat. Cell Biol. *17*, 288–299.

Moloughney, J.G., Kim, P.K., Vega-Cotto, N.M., Wu, C.C., Zhang, S., Adlam, M., Lynch, T., Chou, P.C., Rabinowitz, J.D., Werlen, G., et al. (2016). mTORC2 Responds to Glutamine Catabolite Levels to Modulate the Hexosamine Biosynthesis Enzyme GFAT1. Mol. Cell *63*, 811–826.

Morais, R., Zinkewich-Péotti, K., Parent, M., Wang, H., Babai, F., and Zollinger, M. (1994). Tumor-forming ability in athymic nude mice of human cell lines devoid of mitochondrial DNA. Cancer Res. *54*, 3889–3896.

Moruno-Manchon, J.F., Uzor, N.-E., Kesler, S.R., Wefel, J.S., Townley, D.M., Nagaraja, A.S.,

Pradeep, S., Mangala, L.S., Sood, A.K., and Tsvetkov, A.S. (2016). TFEB ameliorates the impairment of the autophagy-lysosome pathway in neurons induced by doxorubicin. Aging (Albany. NY). *8*, 3507–3519.

Murakami, T., Nishiyama, T., Shirotani, T., Shinoharai, Y., Kan, M., Ishii, K., Kanai, F., Nakazuru, S., and Ebina, Y. (1992). Identification of Two Enhancer Elements in the Gene Encoding the the Mouse Which Are Responsive to Type 1 Glucose Transporter from Serum , Growth Factor , and Oncogenes *. J. Biol. Chem. *267*, 9300–9306.

N'Diaye, E.-N., Kajihara, K.K., Hsieh, I., Morisaki, H., Debnath, J., and Brown, E.J. (2009). PLIC proteins or ubiquilins regulate autophagy-dependent cell survival during nutrient starvation. EMBO Rep. *10*, 173–179.

Ngeow, K.C., Friedrichsen, H.J., Li, L., Zeng, Z., Andrews, S., Volpon, L., Brunsdon, H., Berridge, G., Picaud, S., Fischer, R., et al. (2018). BRAF/MAPK and GSK3 signaling converges to control MITF nuclear export. Proc. Natl. Acad. Sci. *115*. E8868-E8877.

Nicklin, P., Bergman, P., Zhang, B., Triantafellow, E., Wang, H., Nyfeler, B., Yang, H., Hild, M., Kung, C., Wilson, C., et al. (2009). Bidirectional transport of amino acids regulates mTOR and autophagy. Cell *136*, 521–534.

Ohno, M., Segref, A., Bachi, A., Wilm, M., and Mattaj, I.W. (2000). PHAX, a Mediator of U snRNA Nuclear Export Whose Activity Is Regulated by Phosphorylation. Cell *101*, 187–198.

Okosun, J., Wolfson, R.L., Wang, J., Araf, S., Wilkins, L., Castellano, B.M., Escudero-Ibarz, L., Al Seraihi, A.F., Richter, J., Bernhart, S.H., et al. (2016). Recurrent mTORC1-activating RRAGC mutations in follicular lymphoma. Nat. Genet. *48*, 183–188.

Otto Warburg, B., Wind, F., and Negelein, N. (1923). THE METABOLISM OF TUMORS IN THE BODY. The Journal of General Physiology. Biochem. Z. Biochem. Z. Biochem. Z.. Biol. Chem *309*, 397–519.

Palaskas, N., Larson, S.M., Schultz, N., Komisopoulou, E., Wong, J., Rohle, D., Campos, C., Yannuzzi, N., Osborne, J.R., Linkov, I., et al. (2011). 18F-fluorodeoxy-glucose positron emission tomography marks MYC-overexpressing human basal-like breast cancers. Cancer Res. *71*, 5164–5174.

Palm, W., Park, Y., Wright, K., Pavlova, N.N., Tuveson, D.A., and Thompson, C.B. (2015). The Utilization of Extracellular Proteins as Nutrients Is Suppressed by mTORC1. Cell *162*, 259–270.

Palmieri, M., Impey, S., Kang, H., di Ronza, A., Pelz, C., Sardiello, M., and Ballabio, A. (2011). Characterization of the CLEAR network reveals an integrated control of cellular clearance pathways. Hum. Mol. Genet. *20*, 3852–3866.

Palmieri, M., Pal, R., Nelvagal, H.R., Lotfi, P., Stinnett, G.R., Seymour, M.L., Chaudhury, A., Bajaj, L., Bondar, V. V., Bremner, L., et al. (2017). MTORC1-independent TFEB activation via Akt inhibition promotes cellular clearance in neurodegenerative storage diseases. Nat. Commun. *8*. 14338. doi: 10.1038/ncomms14338

Pan, M., Reid, M.A., Lowman, X.H., Kulkarni, R.P., Tran, T.Q., Liu, X., Yang, Y., Hernandez-Davies, J.E., Rosales, K.K., Li, H., et al. (2016). Regional glutamine deficiency in tumours promotes dedifferentiation through inhibition of histone demethylation. Nat. Cell Biol. *18*, 1090–1101.

Pankiv, S., Clausen, T.H., Lamark, T., Brech, A., Bruun, J.-A., Outzen, H., Øvervatn, A.,

Bjørkøy, G., and Johansen, T. (2007). p62/SQSTM1 binds directly to Atg8/LC3 to facilitate degradation of ubiquitinated protein aggregates by autophagy. J. Biol. Chem. *282*, 24131–24145.

Parenti, G., Andria, G., and Ballabio, A. (2015). Lysosomal Storage Diseases: From Pathophysiology to Therapy. Annu. Rev. Med. *66*, 471–486.

Parmigiani, A., Nourbakhsh, A., Ding, B., Wang, W., Kim, Y.C., Akopiants, K., Guan, K.-L., Karin, M., and Budanov, A. V (2014). Sestrins inhibit mTORC1 kinase activation through the GATOR complex. Cell Rep. *9*, 1281–1291.

Parr, C., Carzaniga, R., Gentleman, S.M., Van Leuven, F., Walter, J., and Sastre, M. (2012). Glycogen Synthase Kinase 3 Inhibition Promotes Lysosomal Biogenesis and Autophagic Degradation of the Amyloid- Precursor Protein. Mol. Cell. Biol. *32*, 4410–4418.

Pastore, N., Brady, O.A., Diab, H.I., Martina, J.A., Sun, L., Huynh, T., Lim, J.A., Zare, H., Raben, N., Ballabio, A., et al. (2016). TFEB and TFE3 cooperate in the regulation of the innate immune response in activated macrophages. Autophagy *12*, 1240–1258.

Paul, E., and Thiele, E. (2008). Efficacy of Sirolimus in Treating Tuberous Sclerosis and Lymphangioleiomyomatosis. N. Engl. J. Med. *358*, 190–192.

Pavlova, N.N., and Thompson, C.B. (2016). The Emerging Hallmarks of Cancer Metabolism. Cell Metab. *23*, 27–47.

Pearce, L.R., Huang, X., Boudeau, J., Pawłowski, R., Wullschleger, S., Deak, M., Ibrahim, A.F.M., Gourlay, R., Magnuson, M.A., and Alessi, D.R. (2007). Identification of Protor as a novel Rictor-binding component of mTOR complex-2. Biochem. J. *405*, 513–522.

Peña-Llopis, S., Vega-Rubin-de-Celis, S., Schwartz, J.C., Wolff, N.C., Tran, T.A.T., Zou, L., Xie, X.-J., Corey, D.R., and Brugarolas, J. (2011). Regulation of TFEB and V-ATPases by mTORC1. EMBO J. *30*, 3242–3258.

Perera, R.M., Stoykova, S., Nicolay, B.N., Ross, K.N., Fitamant, J., Boukhali, M., Lengrand, J., Deshpande, V., Selig, M.K., Ferrone, C.R., et al. (2015). Transcriptional control of autophagy-lysosome function drives pancreatic cancer metabolism. Nature *524*, 361–365.

Peterson, T.R., Laplante, M., Thoreen, C.C., Sancak, Y., Kang, S.A., Kuehl, W.M., Gray, N.S., and Sabatini, D.M. (2009). DEPTOR is an mTOR inhibitor frequently overexpressed in multiple myeloma cells and required for their survival. Cell *137*, 873–886.

Peterson, T.R., Sengupta, S.S., Harris, T.E., Carmack, A.E., Kang, S.A., Balderas, E., Guertin, D.A., Madden, K.L., Carpenter, A.E., Finck, B.N., et al. (2011). mTOR complex 1 regulates lipin 1 localization to control the SREBP pathway. Cell *146*, 408–420.

Petit, C.S., Roczniak-Ferguson, A., and Ferguson, S.M. (2013). Recruitment of folliculin to lysosomes supports the amino acid-dependent activation of Rag GTPases. J. Cell Biol. *202*, 1107–1122.

Ploper, D., Taelman, V.F., Robert, L., Perez, B.S., Titz, B., Chen, H.-W., Graeber, T.G., von Euw, E., Ribas, A., and De Robertis, E.M. (2015). MITF drives endolysosomal biogenesis and potentiates Wnt signaling in melanoma cells. Proc. Natl. Acad. Sci. U. S. A. *112*, E420-9.

Polito, V.A., Li, H., Martini-Stoica, H., Wang, B., Yang, L., Xu, Y., Swartzlander, D.B., Palmieri, M., di Ronza, A., Lee, V.M.-Y., et al. (2014). Selective clearance of aberrant tau proteins and rescue of neurotoxicity by transcription factor EB. EMBO Mol. Med. *6*, 1142–1160.

Porstmann, T., Santos, C.R., Griffiths, B., Cully, M., Wu, M., Leevers, S., Griffiths, J.R., Chung, Y.-L., and Schulze, A. (2008). SREBP Activity Is Regulated by mTORC1 and Contributes to Akt-Dependent Cell Growth. Cell Metab. *8*, 224–236.

Puleston, D.J., and Simon, A.K. (2014). Autophagy in the immune system. Immunology *141*, 1–8.

Raben, N., and Puertollano, R. (2016). TFEB and TFE3: Linking Lysosomes to Cellular Adaptation to Stress. Annu. Rev. Cell Dev. Biol. *32*, 255–278.

Raposo, G., and Marks, M.S. (2007). Melanosomes — dark organelles enlighten endosomal membrane transport. Nat. Rev. Mol. Cell Biol. *8*, 786–797.

Rathmell, J.C., Vander Heiden, M.G., Harris, M.H., Frauwirth, K.A., and Thompson, C.B. (2000). In the absence of extrinsic signals, nutrient utilization by lymphocytes is insufficient to maintain either cell size or viability. Mol. Cell *6*, 683–692.

Rebsamen, M., Pochini, L., Stasyk, T., de Araújo, M.E.G., Galluccio, M., Kandasamy, R.K., Snijder, B., Fauster, A., Rudashevskaya, E.L., Bruckner, M., et al. (2015). SLC38A9 is a component of the lysosomal amino acid sensing machinery that controls mTORC1. Nature *519*, 477–481.

Reynolds, M.R., Lane, A.N., Robertson, B., Kemp, S., Liu, Y., Hill, B.G., Dean, D.C., and Clem, B.F. (2014). Control of glutamine metabolism by the tumor suppressor Rb. Oncogene *33*, 556–566.

Roberts, E., Simonsen, D.G., Tanaka, K.K., and Tanaka, T. (1956). Free amino acids in growing and regressing ascites cell tumors: host resistance and chemical agents. Cancer Res. *16*, 970–

978.

Robitaille, A.M., Christen, S., Shimobayashi, M., Cornu, M., Fava, L.L., Moes, S., Prescianotto-Baschong, C., Sauer, U., Jenoe, P., and Hall, M.N. (2013). Quantitative phosphoproteomics reveal mTORC1 activates de novo pyrimidine synthesis. Science *339*, 1320–1323.

Roczniak-Ferguson, A., Petit, C.S., Froehlich, F., Qian, S., Ky, J., Angarola, B., Walther, T.C., and Ferguson, S.M. (2012). The transcription factor TFEB links mTORC1 signaling to transcriptional control of lysosome homeostasis. Sci. Signal. *5*, ra42. doi: 10.1126/scisignal.2002790

Rodriguez-Bravo, V., Pippa, R., Song, W.-M., Carceles-Cordon, M., Dominguez-Andres, A., Fujiwara, N., Woo, J., Koh, A.P., Ertel, A., Lokareddy, R.K., et al. (2018). Nuclear Pores Promote Lethal Prostate Cancer by Increasing POM121-Driven E2F1, MYC, and AR Nuclear Import. Cell *174*, 1200–1215.e20.

Rosenfeldt, M.T., O'Prey, J., Morton, J.P., Nixon, C., MacKay, G., Mrowinska, A., Au, A., Rai, T.S., Zheng, L., Ridgway, R., et al. (2013). p53 status determines the role of autophagy in pancreatic tumour development. Nature *504*, 296–300.

Rousseau, A., and Bertolotti, A. (2016). An evolutionarily conserved pathway controls proteasome homeostasis. Nature *536*, 184–189.

Roux, P.P., Ballif, B.A., Anjum, R., Gygi, S.P., and Blenis, J. (2004). Tumor-promoting phorbol esters and activated Ras inactivate the tuberous sclerosis tumor suppressor complex via p90 ribosomal S6 kinase. Proc. Natl. Acad. Sci. U. S. A. *101*, 13489–13494.

Sabatini, D.M., Erdjument-Bromage, H., Lui, M., Tempst, P., and Snyder, S.H. (1994). RAFT1: A mammalian protein that binds to FKBP12 in a rapamycin-dependent fashion and is homologous to yeast TORs. Cell *78*, 35–43.

Sabers, C.J., Martin, M.M., Brunn, G.J., Williams, J.M., Dumont, F.J., Wiederrecht, G., and Abraham, R.T. (1995). Isolation of a protein target of the FKBP12-rapamycin complex in mammalian cells. J. Biol. Chem. *270*, 815–822.

Salt, I.P., Johnson, G., Ashcroft, S.J., and Hardie, D.G. (1998). AMP-activated protein kinase is activated by low glucose in cell lines derived from pancreatic beta cells, and may regulate insulin release. Biochem. J. *335 (Pt 3)*, 533–539.

Samie, M., and Cresswell, P. (2015). The transcription factor TFEB acts as a molecular switch that regulates exogenous antigen-presentation pathways. Nat. Immunol. *16*, 729–736.

Sancak, Y., Thoreen, C.C., Peterson, T.R., Lindquist, R.A., Kang, S.A., Spooner, E., Carr, S.A., and Sabatini, D.M. (2007). PRAS40 Is an Insulin-Regulated Inhibitor of the mTORC1 Protein Kinase. Mol. Cell *25*, 903–915.

Sancak, Y., Peterson, T.R., Shaul, Y.D., Lindquist, R.A., Thoreen, C.C., Bar-Peled, L., and Sabatini, D.M. (2008). The Rag GTPases bind raptor and mediate amino acid signaling to mTORC1. Science *320*, 1496–1501.

Sancak, Y., Bar-Peled, L., Zoncu, R., Markhard, A.L., Nada, S., and Sabatini, D.M. (2010). Ragulator-Rag complex targets mTORC1 to the lysosomal surface and is necessary for its activation by amino acids. Cell *141*, 290–303.

Sanchez-Cespedes, M., Parrella, P., Esteller, M., Nomoto, S., Trink, B., Engles, J.M., Westra,

W.H., Herman, J.G., and Sidransky, D. (2002). Inactivation of LKB1/STK11 Is a Common Event in Adenocarcinomas of the Lung. Cancer Res. *62*, 3659–3662.

Sarbassov, D.D., Guertin, D.A., Ali, S.M., and Sabatini, D.M. (2005). Phosphorylation and regulation of Akt/PKB by the rictor-mTOR complex. Science *307*, 1098–1101.

Sardiello, M., Palmieri, M., di Ronza, A., Medina, D.L., Valenza, M., Gennarino, V.A., Di Malta, C., Donaudy, F., Embrione, V., Polishchuk, R.S., et al. (2009). A gene network regulating lysosomal biogenesis and function. Science *325*, 473–477.

Sathish, V., Ebenezar, K.K., and Devaki, T. (2003). Synergistic effect of nicorandil and amlodipine on lysosomal hydrolases during experimental myocardial infarction in rats. Biomed. Pharmacother. *57*, 309–313.

Sato, T., Nakashima, A., Guo, L., Coffman, K., and Tamanoi, F. (2010). Single amino-acid changes that confer constitutive activation of mTOR are discovered in human cancer. Oncogene *29*, 2746–2752.

Sauer, L.A., Stayman, J.W., and Dauchy, R.T. (1982). Amino acid, glucose, and lactic acid utilization in vivo by rat tumors. Cancer Res. *42*, 4090–4097.

Saxton, R.A., and Sabatini, D.M. (2017). mTOR Signaling in Growth, Metabolism, and Disease. Cell *168*, 960–976.

Saxton, R.A., Chantranupong, L., Knockenhauer, K.E., Schwartz, T.U., and Sabatini, D.M. (2016). Mechanism of arginine sensing by CASTOR1 upstream of mTORC1. Nature *536*, 229–233.

Schafer, Z.T., Grassian, A.R., Song, L., Jiang, Z., Gerhart-Hines, Z., Irie, H.Y., Gao, S.,

Puigserver, P., and Brugge, J.S. (2009). Antioxidant and oncogene rescue of metabolic defects caused by loss of matrix attachment. Nature *461*, 109–113.

Settembre, C., Di Malta, C., Polito, V.A., Garcia Arencibia, M., Vetrini, F., Erdin, S., Erdin, S.U., Huynh, T., Medina, D., Colella, P., et al. (2011). TFEB links autophagy to lysosomal biogenesis. Science *332*, 1429–1433.

Settembre, C., Zoncu, R., Medina, D.L., Vetrini, F., Erdin, S., Erdin, S., Huynh, T., Ferron, M., Karsenty, G., Vellard, M.C., et al. (2012). A lysosome-to-nucleus signalling mechanism senses and regulates the lysosome via mTOR and TFEB. EMBO J. *31*, 1095–1108.

Settembre, C., De Cegli, R., Mansueto, G., Saha, P.K., Vetrini, F., Visvikis, O., Huynh, T., Carissimo, A., Palmer, D., Jürgen Klisch, T., et al. (2013). TFEB controls cellular lipid metabolism through a starvation-induced autoregulatory loop. Nat. Cell Biol. *15*, 647–658.

Shaffer, A.., Shapiro-Shelef, M., Iwakoshi, N.N., Lee, A.-H., Qian, S.-B., Zhao, H., Yu, X., Yang, L., Tan, B.K., Rosenwald, A., et al. (2004). XBP1, Downstream of Blimp-1, Expands the Secretory Apparatus and Other Organelles, and Increases Protein Synthesis in Plasma Cell Differentiation. Immunity *21*, 81–93.

Shah, O.J., Wang, Z., and Hunter, T. (2004). Inappropriate activation of the TSC/Rheb/mTOR/S6K cassette induces IRS1/2 depletion, insulin resistance, and cell survival deficiencies. Curr. Biol. *14*, 1650–1656.

She, Q.-B., Halilovic, E., Ye, Q., Zhen, W., Shirasawa, S., Sasazuki, T., Solit, D.B., and Rosen, N. (2010). 4E-BP1 is a key effector of the oncogenic activation of the AKT and ERK signaling pathways that integrates their function in tumors. Cancer Cell *18*, 39–51.

Shintani, T., and Klionsky, D.J. (2004). Autophagy in health and disease: a double-edged sword. Science *306*, 990–995.

Sidhar, S., Clark, J., Gill, S., Hamoudi, R., Crew, A.J., Gwilliam, R., Ross, M., Linehan, W.M., Birdsall, S., Shipley, J., et al. (1996). The t(X;1)(p11.2;q21.2) translocation in papillary renal cell carcinoma fuses a novel gene PRCC to the TFE3 transcription factor gene. Hum. Mol. Genet. *5*, 1333–1338.

Silvestrini, M.J., Johnson, J.R., Kumar, A. V., Thakurta, T.G., Blais, K., Neill, Z.A., Marion, S.W., Amand, V. St., Reenan, R.A., and Lapierre, L.R. (2018). Nuclear Export Inhibition Enhances HLH-30/TFEB Activity, Autophagy, and Lifespan. Cell Rep. *23*, 1915–1921.

Son, J., Lyssiotis, C.A., Ying, H., Wang, X., Hua, S., Ligorio, M., Perera, R.M., Ferrone, C.R., Mullarky, E., Shyh-Chang, N., et al. (2013). Glutamine supports pancreatic cancer growth through a KRAS-regulated metabolic pathway. Nature *496*, 101–105.

Song, J.-X., Sun, Y.-R., Peluso, I., Zeng, Y., Yu, X., Lu, J.-H., Xu, Z., Wang, M.-Z., Liu, L.-F., Huang, Y.-Y., et al. (2016). A novel curcumin analog binds to and activates TFEB in vitro and in vivo independent of MTOR inhibition. Autophagy *12*, 1372–1389.

Spada, A.R. La, Wilson, E.M., Lubahn, D.B., Harding, A.E., and Fischbeck, K.H. (1991). Androgen receptor gene mutations in X-linked spinal and bulbar muscular atrophy. Nature *352*, 77–79.

Spampanato, C., Feeney, E., Li, L., Cardone, M., Lim, J.-A., Annunziata, F., Zare, H., Polishchuk, R., Puertollano, R., Parenti, G., et al. (2013). Transcription factor EB (TFEB) is a new therapeutic target for Pompe disease. EMBO Mol. Med. *5*, 691–706.

Steingrímsson, E., Copeland, N.G., and Jenkins, N.A. (2004). Melanocytes and the Microphthalmia Transcription Factor Network. Annu. Rev. Genet. *38*, 365–411.

Suzuki, K., Bose, P., Leong-Quong, R.Y., Fujita, D.J., and Riabowol, K. (2010). REAP: A two minute cell fractionation method. BMC Res. Notes *3*, 294.

Tabernero, J., Rojo, F., Calvo, E., Burris, H., Judson, I., Hazell, K., Martinelli, E., Ramon y Cajal, S., Jones, S., Vidal, L., et al. (2008). Dose- and schedule-dependent inhibition of the mammalian target of rapamycin pathway with everolimus: a phase I tumor pharmacodynamic study in patients with advanced solid tumors. J. Clin. Oncol. *26*, 1603–1610.

Takashima, A. (2006). GSK-3 is essential in the pathogenesis of Alzheimer's disease. J. Alzheimer's Dis. *9*, 309–317.

Tan, A.S., Baty, J.W., Dong, L.-F., Bezawork-Geleta, A., Endaya, B., Goodwin, J., Bajzikova, M., Kovarova, J., Peterka, M., Yan, B., et al. (2015). Mitochondrial Genome Acquisition Restores Respiratory Function and Tumorigenic Potential of Cancer Cells without Mitochondrial DNA. Cell Metab. *21*, 81–94.

Tee, A.R., Manning, B.D., Roux, P.P., Cantley, L.C., and Blenis, J. (2003). Tuberous Sclerosis Complex Gene Products, Tuberin and Hamartin, Control mTOR Signaling by Acting as a GTPase-Activating Protein Complex toward Rheb. Curr. Biol. *13*, 1259–1268.

Thomanetz, V., Angliker, N., Cloëtta, D., Lustenberger, R.M., Schweighauser, M., Oliveri, F., Suzuki, N., and Rüegg, M.A. (2013). Ablation of the mTORC2 component rictor in brain or Purkinje cells affects size and neuron morphology. J. Cell Biol. *201*, 293–308.

Tsun, Z.-Y., Bar-Peled, L., Chantranupong, L., Zoncu, R., Wang, T., Kim, C., Spooner, E., and

Sabatini, D.M. (2013). The folliculin tumor suppressor is a GAP for the RagC/D GTPases that signal amino acid levels to mTORC1. Mol. Cell *52*, 495–505.

Tsunemi, T., Ashe, T.D., Morrison, B.E., Soriano, K.R., Au, J., Roque, R.A.V., Lazarowski, E.R., Damian, V.A., Masliah, E., and La Spada, A.R. (2012). PGC-1a rescues Huntington's disease proteotoxicity by preventing oxidative stress and promoting TFEB function. Sci. Transl. Med. *4.* 142ra97. DOI: 10.1126/scitranslmed.3003799

Tullai, J.W., Chen, J., Schaffer, M.E., Kamenetsky, E., Kasif, S., and Cooper, G.M. (2007). Glycogen synthase kinase-3 represses cyclic AMP response element-binding protein (CREB)-targeted immediate early genes in quiescent cells. J. Biol. Chem. *282*, 9482–9491.

Vega-Rubin-de-Celis, S., Peña-Llopis, S., Konda, M., and Brugarolas, J. (2017). Multistep regulation of TFEB by MTORC1. Autophagy *13*, 464–472.

Vézina, C., Kudelski, A., and Sehgal, S.N. (1975). Rapamycin (AY-22,989), a new antifungal antibiotic. I. Taxonomy of the producing streptomycete and isolation of the active principle. J. Antibiot. (Tokyo). *28*, 721–726.a

Vidal, R.L., Figueroa, A., Court, F.A., Thielen, P., Molina, C., Wirth, C., Caballero, B., Kiffin, R., Segura-Aguilar, J., Cuervo, A.M., et al. (2012). Targeting the UPR transcription factor XBP1 protects against Huntington's disease through the regulation of FoxO1 and autophagy. Hum. Mol. Genet. *21*, 2245–2262.

Vidal, R.L., Matus, S., Bargsted, L., and Hetz, C. (2014). Targeting autophagy in neurodegenerative diseases. Trends Pharmacol. Sci. *35*, 583–591.

Wang, C., Niederstrasser, H., Douglas, P.M., Lin, R., Jaramillo, J., Li, Y., Oswald, N.W., Zhou,

A., McMillan, E.A., Mendiratta, S., et al. (2018). Author Correction: Small-molecule TFEB pathway agonists that ameliorate metabolic syndrome in mice and extend C. elegans lifespan. Nat. Commun. *9*. 2270. doi: 10.1038/s41467-017-02332-3

Wang, L., Harris, T.E., Roth, R.A., and Lawrence, J.C. (2007). PRAS40 regulates mTORC1 kinase activity by functioning as a direct inhibitor of substrate binding. J. Biol. Chem. *282*, 20036–20044.

Wang, Q., Beaumont, K.A., Otte, N.J., Font, J., Bailey, C.G., van Geldermalsen, M., Sharp, D.M., Tiffen, J.C., Ryan, R.M., Jormakka, M., et al. (2014). Targeting glutamine transport to suppress melanoma cell growth. Int. J. Cancer *135*, 1060–1071.

Wang, S., Tsun, Z.-Y., Wolfson, R.L., Shen, K., Wyant, G.A., Plovanich, M.E., Yuan, E.D., Jones, T.D., Chantranupong, L., Comb, W., et al. (2015). Metabolism. Lysosomal amino acid transporter SLC38A9 signals arginine sufficiency to mTORC1. Science *347*, 188–194.

Wang, X., Sato, R., Brown, M.S., Hua, X., and Goldstein, J.L. (1994). SREBP-1, a membrane-bound transcription factor released by sterol-regulated proteolysis. Cell *77*, 53–62.

Warburg, O. (1956). On the Origin of Cancer Cells On the Origin of Cance. Source Sci. New Ser. *123*, 309–314.

Weikel, K.A., Cacicedo, J.M., Ruderman, N.B., and Ido, Y. (2016). Knockdown of GSK3β increases basal autophagy and AMPK signalling in nutrient-laden human aortic endothelial cells. Biosci. Rep. *36*, e00382.

Wen, W., Meinkoth, J.L., Tsien, R.Y., and Taylor, S.S. (1995). Identification of a signal for rapid export of proteins from the nucleus. Cell *82*, 463–473.

Weterman, M.A., Wilbrink, M., and Geurts van Kessel, A. (1996). Fusion of the transcription factor TFE3 gene to a novel gene, PRCC, in t(X;1)(p11;q21)-positive papillary renal cell carcinomas. Proc. Natl. Acad. Sci. U. S. A. *93*, 15294–15298.

Weydt, P., Pineda, V. V., Torrence, A.E., Libby, R.T., Satterfield, T.F., Lazarowski, E.R., Gilbert, M.L., Morton, G.J., Bammler, T.K., Strand, A.D., et al. (2006). Thermoregulatory and metabolic defects in Huntington's disease transgenic mice implicate PGC-1α in Huntington's disease neurodegeneration. Cell Metab. *4*, 349–362.

Wieman, H.L., Wofford, J.A., and Rathmell, J.C. (2007). Cytokine Stimulation Promotes Glucose Uptake via Phosphatidylinositol-3 Kinase/Akt Regulation of Glut1 Activity and Trafficking. Mol. Biol. Cell *18*, 1437–1446.

Wise, D.R., and Thompson, C.B. (2010). Glutamine addiction: a new therapeutic target in cancer. Trends Biochem. Sci. *35*, 427–433.

Wise, D.R., DeBerardinis, R.J., Mancuso, A., Sayed, N., Zhang, X.-Y., Pfeiffer, H.K., Nissim, I., Daikhin, E., Yudkoff, M., McMahon, S.B., et al. (2008). Myc regulates a transcriptional program that stimulates mitochondrial glutaminolysis and leads to glutamine addiction. Proc. Natl. Acad. Sci. U. S. A. *105*, 18782–18787.

Woo, S.-Y., Kim, D.-H., Jun, C.-B., Kim, Y.-M., Haar, E. Vander, Lee, S., Hegg, J.W., Bandhakavi, S., Griffin, T.J., and Kim, D.-H. (2007). PRR5, a novel component of mTOR complex 2, regulates platelet-derived growth factor receptor beta expression and signaling. J. Biol. Chem. *282*, 25604–25612.

Wu, D., and Pan, W. (2010). GSK3: a multifaceted kinase in Wnt signaling. Trends Biochem. Sci. *35*, 161–168.

Wu, H.-M., Jiang, Z.-F., Ding, P.-S., Shao, L.-J., and Liu, R.-Y. (2015a). Hypoxia-induced autophagy mediates cisplatin resistance in lung cancer cells. Sci. Rep. *5*, 12291.

Wu, M., Hemesath, T.J., Takemoto, C.M., Horstmann, M.A., Wells, A.G., Price, E.R., Fisher, D.Z., and Fisher, D.E. (2000). c-Kit triggers dual phosphorylations, which couple activation and degradation of the essential melanocyte factor Mi. Genes Dev. *14*, 301–312.

Wu, T., Wang, M.-C., Jing, L., Liu, Z.-Y., Guo, H., Liu, Y., Bai, Y.-Y., Cheng, Y.-Z., Nan, K.-J., and Liang, X. (2015b). Autophagy facilitates lung adenocarcinoma resistance to cisplatin treatment by activation of AMPK/mTOR signaling pathway. Drug Des. Devel. Ther. *9*, 6421–6431.

Xia, H.-G., Zhang, L., Chen, G., Zhang, T., Liu, J., Jin, M., Ma, X., Ma, D., and Yuan, J. (2010). Control of basal autophagy by calpain1 mediated cleavage of ATG5. Autophagy *6*, 61–66.

Xiao, Q., Yan, P., Ma, X., Liu, H., Perez, R., Zhu, A., Gonzales, E., Burchett, J.M., Schuler, D.R., Cirrito, J.R., et al. (2014). Enhancing astrocytic lysosome biogenesis facilitates Aβ clearance and attenuates amyloid plaque pathogenesis. J. Neurosci. *34*, 9607–9620.

Yang, G., Murashige, D.S., Humphrey, S.J., and James, D.E. (2015). A Positive Feedback Loop between Akt and mTORC2 via SIN1 Phosphorylation. Cell Rep. *12*, 937–943.

Yang, Q., Inoki, K., Ikenoue, T., and Guan, K.-L. (2006). Identification of Sin1 as an essential TORC2 component required for complex formation and kinase activity. Genes Dev. *20*, 2820–2832.

Yang, S., Wang, X., Contino, G., Liesa, M., Sahin, E., Ying, H., Bause, A., Li, Y., Stommel, J.M., Dell'antonio, G., et al. (2011). Pancreatic cancers require autophagy for tumor growth.

Genes Dev. *25*, 717–729.

Ying, H., Kimmelman, A.C., Lyssiotis, C.A., Hua, S., Chu, G.C., Fletcher-Sananikone, E., Locasale, J.W., Son, J., Zhang, H., Coloff, J.L., et al. (2012). Oncogenic Kras maintains pancreatic tumors through regulation of anabolic glucose metabolism. Cell *149*, 656–670.

Yousefi, S., Perozzo, R., Schmid, I., Ziemiecki, A., Schaffner, T., Scapozza, L., Brunner, T., and Simon, H.-U. (2006). Calpain-mediated cleavage of Atg5 switches autophagy to apoptosis. Nat. Cell Biol. *8*, 1124–1132.

Yuan, M., Pino, E., Wu, L., Kacergis, M., and Soukas, A.A. (2012). Identification of Akt-independent regulation of hepatic lipogenesis by mammalian target of rapamycin (mTOR) complex 2. J. Biol. Chem. *287*, 29579–29588.

Yun, J., Rago, C., Cheong, I., Pagliarini, R., Angenendt, P., Rajagopalan, H., Schmidt, K., Willson, J.K. V, Markowitz, S., Zhou, S., et al. (2009). Glucose deprivation contributes to the development of KRAS pathway mutations in tumor cells. Science *325*, 1555–1559.

Zapata, P.A.M., Beese, C.J., Jönger, A., Dalmasso, G., Brady, N.R., and Hamacher-Brady, A. (2016). Time course decomposition of cell heterogeneity in TFEB signaling states reveals homeostatic mechanisms restricting the magnitude and duration of TFEB responses to mTOR activity modulation. BMC Cancer *16*. 355. doi: 10.1186/s12885-016-2388-9

Zhang, C.-S., Hawley, S.A., Zong, Y., Li, M., Wang, Z., Gray, A., Ma, T., Cui, J., Feng, J.-W., Zhu, M., et al. (2017). Fructose-1,6-bisphosphate and aldolase mediate glucose sensing by AMPK. Nature *548*, 112–116.

Zhang, H.H., Lipovsky, A.I., Dibble, C.C., Sahin, M., and Manning, B.D. (2006). S6K1

regulates GSK3 under conditions of mTOR-dependent feedback inhibition of Akt. Mol. Cell *24*, 185–197.

Zhang, J., Lu, J., Chen, D., Cai, Q., Li, T., Wu, L., and Wu, X. (2009). Myocardial autophagy variation during acute myocardial infarction in rats: the effects of carvedilol. Chin. Med. J. (Engl). *122*, 2372–2379.

Zhang, L., Yu, J., Pan, H., Hu, P., Hao, Y., Cai, W., Zhu, H., Yu, A.D., Xie, X., Ma, D., et al. (2007). Small molecule regulators of autophagy identified by an image-based high-throughput screen. Proc. Natl. Acad. Sci. U. S. A. *104*, 19023–19028.

Zhang, T., Zhou, Q., Ogmundsdottir, M.H., Möller, K., Siddaway, R., Larue, L., Hsing, M., Kong, S.W., Goding, C.R., Palsson, A., et al. (2015). Mitf is a master regulator of the v-ATPase, forming a control module for cellular homeostasis with v-ATPase and TORC1. J. Cell Sci. *128*, 2938–2950.

Zhang, Y., Gao, X., Saucedo, L.J., Ru, B., Edgar, B.A., and Pan, D. (2003). Rheb is a direct target of the tuberous sclerosis tumour suppressor proteins. Nat. Cell Biol. *5*, 578–581.

Zhang, Y., and Xiong, Y. (2001). A p53 amino-terminal nuclear export signal inhibited by DNA damage-induced phosphorylation. Science *292*, 1910–1915.

Zhao, J., Brault, J.J., Schild, A., Cao, P., Sandri, M., Schiaffino, S., Lecker, S.H., and Goldberg, A.L. (2007). FoxO3 Coordinately Activates Protein Degradation by the Autophagic/Lysosomal and Proteasomal Pathways in Atrophying Muscle Cells. Cell Metab. *6*, 472–483.

Zhao, J., Zhai, B., Gygi, S.P., and Goldberg, A.L. (2015). mTOR inhibition activates overall protein degradation by the ubiquitin proteasome system as well as by autophagy. Proc. Natl.

Acad. Sci. *112*, 15790–15797.

Zhitomirsky, B., and Assaraf, Y.G. (2015). Lysosomal sequestration of hydrophobic weak base chemotherapeutics triggers lysosomal biogenesis and lysosome-dependent cancer multidrug resistance. Oncotarget *6*, 1143–1156.

Zmijewski, J.W., and Jope, R.S. (2004). Nuclear accumulation of glycogen synthase kinase-3 during replicative senescence of human fibroblasts. Aging Cell *3*, 309–317.

Zoncu, R., Bar-Peled, L., Efeyan, A., Wang, S., Sancak, Y., and Sabatini, D.M. (2011). mTORC1 senses lysosomal amino acids through an inside-out mechanism that requires the vacuolar H(+)-ATPase. Science *334*, 678–683.